# San Rafael Glacier and Northern Patagonia Icefield surface mass balance estimation from different approaches

Gabriela Collao Barrios

Communauté UNIVERSITÉ Grenoble Alpes

# THÈSE

Pour obtenir le grade de

## DOCTEUR DE LA COMMUNAUTÉ UNIVERSITÉ GRENOBLE ALPES

Spécialité : Sciences de la Terre et de l'Univers et de l'Environnement (CESTUE)

Arrêté ministériel : 25 mai 2016

Présentée par


## Gabriela Celeste COLLAO BARRIOS


Thèse dirigée par **Vincent FAVIER**, Enseignant-chercheur, UGA
et codirigée par **Fabien GILLET-CHAULET**, Chargé de Recherches, CNRS

préparée au sein du **Laboratoire Institut des Géosciences de l'Environnement**
dans **l'École Doctorale Terre, Univers, Environnement**

# Estimation du bilan masse de surface du Glacier San Rafael et du Champ du Glace Nord de Patagonie par diverses approches

# San Rafael Glacier and Northern Patagonia Icefield surface mass balance estimation from different approaches

Thèse soutenue publiquement le **23 novembre 2018**,
devant le jury composé de :

**Monsieur VINCENT FAVIER**
PHYSICIEN ADJOINT, OBSERVATOIRE SCIENCES UNIVERS - GRENOBLE, Directeur de thèse
**Monsieur PIERRE RIBSTEIN**
PROFESSEUR, UNIVERSITE PIERRE ET MARIE CURIE, Rapporteur
**Monsieur FRANK PATTYN**
PROFESSEUR, UNIVERSITE LIBRE DE BRUXELLES - BELGIQUE, Rapporteur
**Madame SANDRINE ANQUETIN**
DIRECTRICE DE RECHERCHE, CNRS DELEGATION ALPES, Président
**Madame CECILE AGOSTA**
CHERCHEUSE, CEA DE SACLAY, Examinateur

# Contents

# Introduction

Low-elevation coastal zones, with fast population growth and urbanisation will be strongly impacted by sea-level rise during the next century (*Neumann et al.*, 2015; *Vitousek et al.*, 2017). Future contribution of ice sheets and mountain glaciers to sea-level changes, is already a major threat for these areas and has been the center of interest of the last IPCC Assessment report (AR5) (*Church et al.*, 2013).

After Antarctica, the two main ice-covered bodies of Patagonia, the Northern Patagonia Icefield and the Southern Patagonia Icefield, with 3976 km$^2$ and 13219 km$^2$, respectively (*Davies and Glasser*, 2012), correspond to the largest ice extents in the Southern Hemisphere (*Rignot et al.*, 2003). The icefields have been retreating during the last 40 years (*Aniya*, 1999; *Lopez et al.*, 2010; *Casassa et al.*, 2014) and losing mass with an acceleration during the last decades compared to the mean value over the entire period from the Little Ice Age to present (*Rignot et al.*, 2003; *Glasser et al.*, 2011; *Jacob et al.*, 2012; *Dussaillant et al.*, 2018; *Foresta et al.*, 2018). They are within the largest contributors to sea level rise per unit area in the world (*Gardner et al.*, 2013; *Carrivick et al.*, 2016); *Gardner et al.* (2013) estimated that 11% of the total global contribution came from the Southern Andes between 2003-2009, see Fig. 1.

It is commonly assumed that the wastage of NPI during the last decades was mainly a response to increased ablation caused by atmospheric warming (*Rignot et al.*, 2003; *Rasmussen et al.*, 2007). However, assessing the physical drivers of glacier change is challenging because regional climates are the product of complex interactions between oceanic, atmospheric, and land-surface processes with varying timescales, and because a recent ice velocity mosaic (*Mouginot and Rignot*, 2015) in addition to ice velocity modelling revealed that the icefield is also potentially sensitive to dynamical changes. Moreover, the direct impact of climate change on glacier behavior should be evident in the surface mass balance (SMB), which has been estimated by downscaling atmospheric reanalyses with more or less complex models (*Koppes et al.*, 2011; *Schaefer et al.*, 2013), but SMB distribution and variation are still largely unknown.

Indeed, studies propose an increasingly positive SMB over the whole NPI since the 1980's, which is hard to justify because this increase is in contradiction with the unabated

rates of mass loss of the NPI. Since insignificant variations were observed in velocities (*Mouginot and Rignot*, 2015), these changes have not likely been compensated by an increased ice discharge. Actually, the temporal and spatial changes of the modelled SMB are poorly constrained in the accumulation zone, where no long-term meteorological data is available. Moreover, the reliability of reanalysis products is poor over Patagonia (*Nicolas and Bromwich*, 2011), and largely impacted by assimilation of satellite datasets in 1979 (*Kistler et al.*, 2001a; *Uppala et al.*, 2005a). SMB estimates are fragile and conclusions on the role of temperature in Patagonia are still submitted to debate. As a consequence, obtaining robust conclusions on SMB and ice dynamics estimates is still important in Patagonia in order to retrieve the cause of retreat.

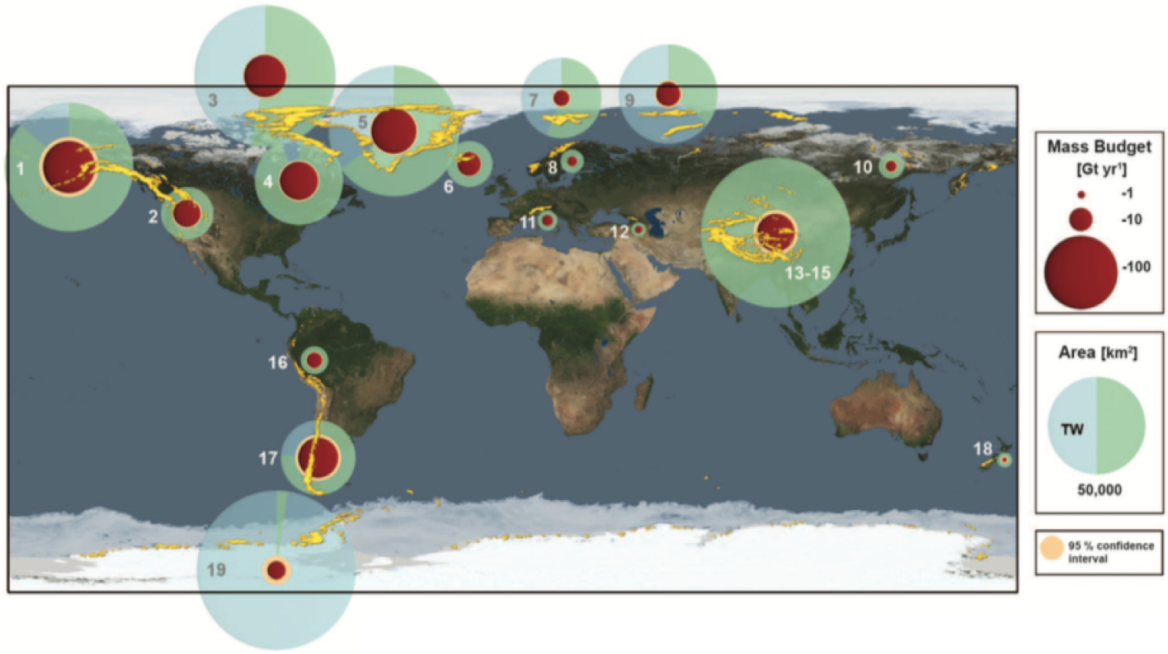


Figure 1: Regional glacier mass changes and tidewater glaciers areas from *Gardner et al.* (2013). Red circles are 2003–2009 regional glacier mass changes, and blue/green circles are regional glacier areas with tidewater basin fractions, in blue. The numbers correspond to different regions, within which 17 is the Southern Andes.

This PhD thesis found its first fundaments in trying to retrieve more accurate mean climate settings, surface mass balance and ice dynamics in Patagonia. However, due to the lack of data available in the area, it focuses on a modeling approach based on physical models for both the atmosphere and the ice dynamics. The main objective of these studies is to retrieve consistency between the changes in the SMB, the ice dynamics, and the final calving fluxes.

The downscaling modeling of climate and SMB in Patagonia suffers from the lack of field data to validate it. The weather stations used for validation are generally located in

the low-lying areas around the icefield, but none of the stations are located on NPI. Few ablation data are available, and accumulation has almost never been measured. Hence, the models which have been applied (*Koppes et al.*, 2011; *Schaefer et al.*, 2013) were mainly validated with data from the ablation zone only (*Ohata et al.*, 1985a) but without important constraints in the accumulation zone. Precipitation enhancement caused by the orography is also hard to assess, and models generally propose extremely high precipitation values, except in one study based on a very high resolution approach (*Koppes et al.*, 2011) based on a 1-D orographic precipitation model (*Smith and Barstad*, 2004a; *Roe*, 2005a). Further modeling studies are thus still necessary to accurately process the SMB and its variations.

Glacier ice dynamics is a direct physical adaptation of the ice to the valley configuration, the bottom surface sliding conditions, to the surface mass balance and to calving fluxes at the front. A physically-based ice-flow model enables us to know whether values of the surface mass balance are compatible with modelled ice fluxes, and to simulate the diffusion of the observed thinning to finally estimate the committed mass loss induced by the current glacier imbalance. Here, we proposed to study San Rafael Glacier (SRG), located in the north-western part of NPI, using a recent ice velocity mosaic that revealed fast flow regions extending far into the plateau and accumulation area (*Mouginot and Rignot*, 2015) and the ice thickness from *Gourlet et al.* (2016).

In a study published in *Journal of Glaciology* (*Collao-Barrios et al.*, 2018) this approach was used to test accumulation values given in the literature by *Schaefer et al.* (2013) and *Koppes et al.* (2011), in order to estimate whether they were in agreement with an ice-flow modelling study performed with the full-stokes model Elmer/Ice and constrained by satellite observations. A simplified spatial distribution of the surface mass balance was proposed, which does not accurately represent the distribution of surface elevation changes, but which should allow for constraining a surface mass balance model with regional scale modeling. This step is necessary to determine the climate variations that produced recent glacier wastage.

Even if changes in the ice dynamics may have largely impacted NPI, a direct link between the glacier and climate change should be retrieved in changes of the SMB. Climate change may impact accumulation, ablation or both.

Changes in regional climate over Patagonia may have impacted solid precipitation, accumulation, and ablation through melting and/or sublimation. To estimate these impacts, it is necessary to compute the surface energy balance (SEB) on the icefield. Obtaining an accurate vision of changes in the SEB and the SMB, which are permanently exchanging and receiving feedbacks with the turbulent atmosphere, is complex and requires a full representation of the airflow at the icefield scale. Regional atmospheric circulation models

with high resolution are necessary to take into account complex topography where spatial changes in atmospheric forcings are very strong in time and space.

Here, we use the MAR (Modèle Atmosphérique Régional *Gallée and Schayes* (1994)) forced by ERA-Interim to evaluate the distribution of the atmospheric variables over NPI, and to assess their impact on the variations of the SMB. After a review of the available data from automatic weather stations installed on the icefield and at low elevations, of albedo values available from MODIS images, and from stakes on NPI, the surface mass balance and surface energy balance obtained from the MAR are analyzed in detail. Finally, we estimate whether temperature or precipitation changes may have explained recent changes in the total mass balance of NPI.

This study presents in Chapter 1 a characterization of Patagonia and its climate including a review of climatic trends and relations with atmospheric climatic modes. This is followed by a description of the Patagonian cryosphere and a review of the evolution of the Patagonian icefields (surface area, mass balance, surface mass balance and ice dynamics) from different sources, with the objective of relating ice mass changes and climate based on available information.

Chapter 2 presents a new approach to constrain SRG surface mass balance using a physically-based ice-flow model during the period 2000-12. Initially, the model is calibrated using available data of surface velocity and the rate of surface elevation change from previous studies. Afterwards, the surface mass balance function compatible with modelled ice fluxes is selected and the surface mass balance is obtained running the model forward in time. Finally, the committed mass loss induced by the current glacier imbalance is estimated simulating the diffusion of the observed thinning.

The estimation of the surface mass balance of NPI through regional atmospheric dynamics is presented in Chapter 3. First, I describe the model and the methods used to adapt and validate the model to the NPI region. Then, I present the results of the model and the sensitivity of the SMB to some important parameters. Afterwards, the SMB trends of San Rafael Glacier and NPI are analyzed and linked to climatic trends and atmospheric modes.

Finally, I present a conclusion about the contribution of the new results obtained on Patagonian mass loss increase and its relationship with climate. This last chapter ends with the perspectives and future applications of the methodologies and results achieved in this study.

# Chapter 1

# Context

In this chapter I present a description of Patagonia, its climate and the extent of the cryosphere, then I review the climatic trends and icefield variations as given in the literature. The goal is to characterize the evolution of Patagonian glaciers (surface area, mass balance, surface mass balance and ice dynamics) with available informations and associated ice mass changes in relation to climate.

## 1.1 General description

Patagonia is located in South America, in the southern part of Chile and Argentina from 40°S to the Strait of Magellan at 52°S - 54°S. This strait connects the Pacific and the Atlantic Oceans and separates the Patagonian region from the islands of the Tierra del Fuego (Fig 1.1). The mountains and the western zone are steep and hardly accessible areas, characterized by a low population density (less than 2 people/km$^2$). The main economic activities are tourism and traditional sheep farming. The name of Patagonia comes from the name given to the indigenous population of the region, called "Patagones" by Hernando de Magallanes, due to their height compared to the Europeans at that time.

This region is geographically divided by the Andes into the so called "Western" and "Eastern" Patagonia. The western side extends from the Pacific Ocean to summits and passes located at altitudes exceeding 1500 m above sea level (a.s.l.). This side is narrow and, except for the icefields, mainly formed by islands and fjords, covered by temperate rain forests. The eastern side of Patagonia presents very different geographical features. Descending from the highest elevations, glaciers reach wide steppes of flat alluvial and glacial terraces covered by scarce vegetation. The steppes extend to the Atlantic Ocean sea shore.

The Andean mountains in this region are generally reaching altitudes around 1500 m a.s.l., with the highest peak (San Valentin peak) culminating at 4032 m a.s.l. (*Vimeux*

*et al.*, 2008). In these mountains, we find the largest ice extensions of the Southern Hemisphere after Antarctica, which are the Northern and Southern Patagonian Icefields (NPI and SPI , respectively). These Icefields result from the peculiar climatic conditions as described hereafter.

## 1.2 Climate settings

This section first presents a description of the Patagonian climate and its situation with respect to the global atmospheric circulation. Then, I present the recent climatic trends and their links with the large scale climate variability.

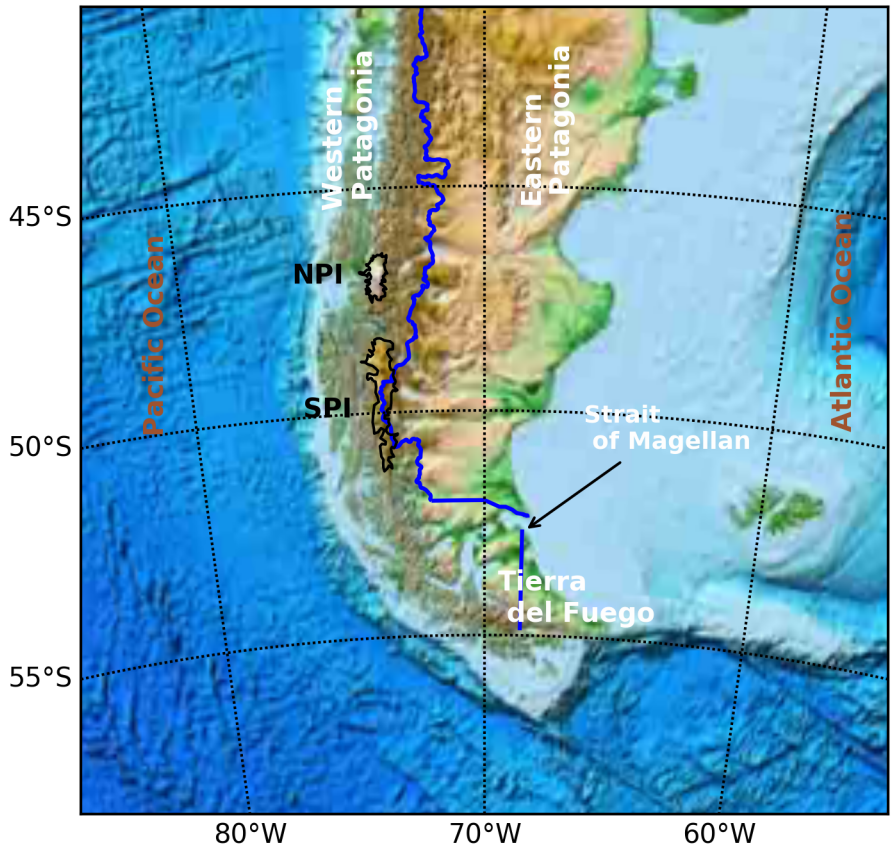


Figure 1.1: Patagonia and the Northern and Southern Patagonian Icefields (NPI and SPI). Blue lines correspond to Chile / Argentina boundary, at the west and east sides, respectively.

### 1.2.1 Mean climate of Patagonia

In the global circulation context, Patagonia is located in the southern part of the mid-latitude Ferrel's cell, near the polar jet stream and hence in the middle of the Westerly winds (Fig. 1.2). Excluding several islands, Patagonia and Tierra del Fuego are the only

large continental masses located between 44°S and the Antarctic Peninsula. The Andes mountains constitute a barrier to the westerly winds, which are forced to ascend along the slopes. Together with the high air humidity of the surface atmosphere associated with the presence of the Pacific Ocean, the especially strong zonal winds observed at these latitudes have a direct influence on Patagonian climate and precipitation (*Garreaud et al.*, 2009).

Precipitation in Patagonia is mainly due to synoptic scale frontal systems related to migratory surface cyclones caused by the baroclinic atmospheric structure. These cyclones travel along the zonal flow, within a narrow latitudinal range known as the storm track (*Garreaud*, 2007). This justifies why a higher precipitation band extends along the western slopes of Patagonia and over the Tierra del Fuego (*Garreaud et al.*, 2009).

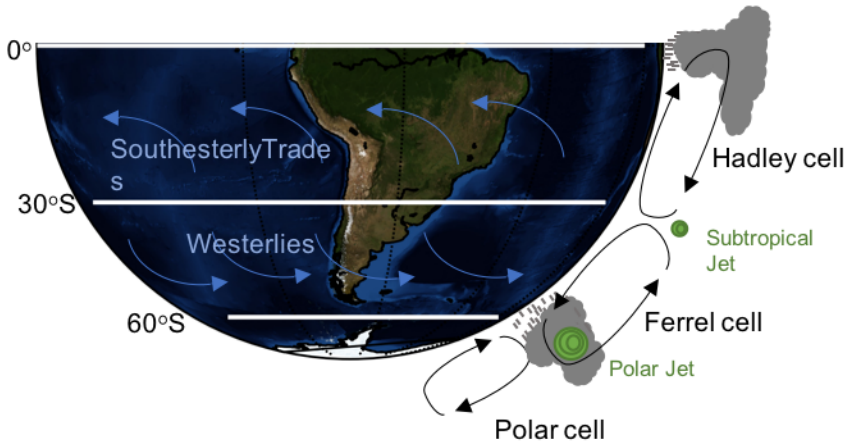


Figure 1.2: Patagonia location in the global circulation cells.

Indeed, the westerly flow advects large amounts of moisture from the southern Pacific Ocean towards the continent. Moisture is lifted upwards over the Andes, leading to large orographic precipitation on the western side of the Andes and a strong westward gradient in precipitation (*Carrasco et al.*, 2002; *Garreaud et al.*, 2012). Climate in Western Patagonia is thus temperate and very humid, with precipitation exceeding 10 m $a^{-1}$ in the mountains. Due to the foehn effect, precipitation decreases quickly on the eastern side of the Andes, with values of less than 0.3 m $a^{-1}$, 100 km away from maximum elevations (*Garreaud et al.*, 2012), see Fig. 1.3. The largest measured annual mean precipitation is 7.2 m $a^{-1}$ at Guarello Station (50.35°S) on the west side of SPI (*Aravena and Luckman*, 2009). For the other stations on the west of the mountain range, values vary between 1.5 to 6.0 m $a^{-1}$. On the east side, measured values are much smaller ($<$0.6 m $a^{-1}$) especially for the stations located to the east of the icefields and at the southern end (*Lopez et al.*, 2010; *Davies and Glasser*, 2012). Seasonal variability of precipitation is small in stations at the east and almost disappears at the stations located on the fjords at the west (*Lopez et al.*, 2010).

Mean annual temperatures in the western valleys of Patagonia varies from 10.3°C at Puerto Montt station at 41.4°S in the north, to 6.1°C at Punta Arenas station at 53.0°S at the southern end. Mean annual temperature is slightly different between coastal and inland stations (*Carrasco et al.*, 2002). There is an important temperature seasonality which is a little less marked on the coast due to ocean influence (*Lopez et al.*, 2010). The monthly average temperatures are between 8 and 14°C in summer and 2 and 6°C in winter. The freezing level and the snowline are generally located between 1000 and 2000 m a.s.l. (*Garreaud et al.*, 2009; *Sagredo and Lowell*, 2012, respectively).

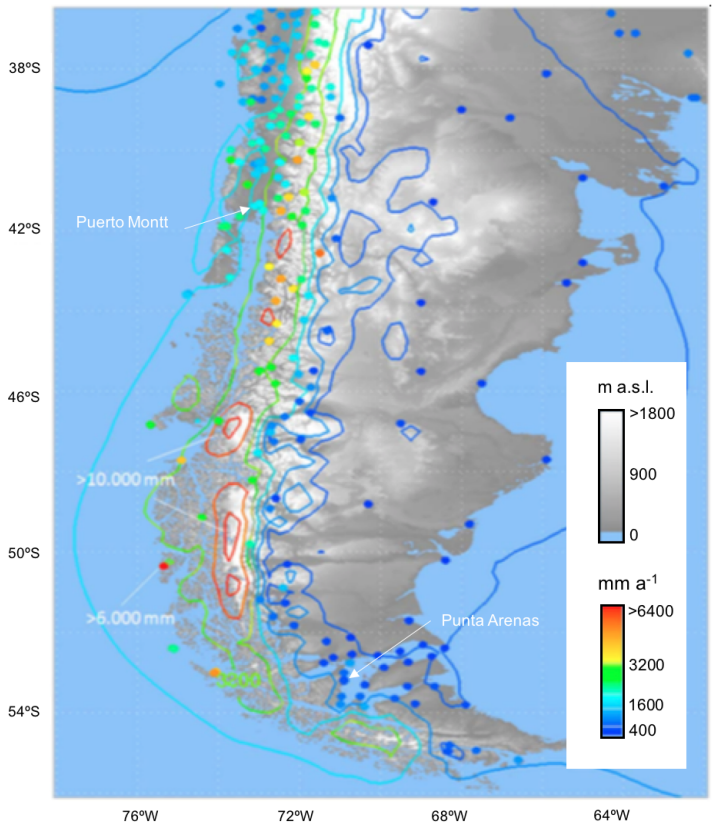


Figure 1.3: Observed and modeled precipitation in Patagonia from *Garreaud et al.* (2014).

### 1.2.2 Climatic trends

Due to the large precipitation gradients and the sparse available observations, describing climatic trends in Patagonia is complex and presents large uncertainties. However, previous studies have given some clues on the climatic trends during the last decades.

*Aravena and Luckman* (2009) analyzed the precipitation patterns in southern South America using precipitation data from 31 weather stations, and described the mean climatic trends, anomalies, and the main modes of variability in the area. They also looked for correlations between regional mean annual precipitation and oceanic circulation indexes. They observed a decrease in precipitation in northern Patagonia (41-44°S) with

changes occurring after 1976. In central Patagonia an increasing precipitation is proposed during the 1960's followed by a decrease at the end of this decade. In southern Patagonia (51-53°S), they detect only small fluctuations with a slight but insignificant increasing trend after 1976, except for one meteorological station located on the western coast in southern Patagonia (Estación Evangelistas), which showed an increasing trend between 1980 and 2000.

Temperature trends between 1979-2006 in the southern Pacific Ocean and along the western coast of South America were studied by *Falvey and Garreaud* (2009), using data from 20 weather stations located between 17.5°S and 47.5°S, from gridded air/sea surface temperature products (ERSST and HadISST) and from MSU microwave sounding units from NOAA. Gridded data showed a cooling trend in surface temperature over the eastern side of South America, along the Pacific Ocean and along the western coast of southern South America, whereas a warming trend is found inland. These trends were confirmed by in-situ data between 17.5°-40°S, which showed a cooling trend in the coastal regions, whereas a warming was observed at inland sites above 150 m a.s.l., with more significant trends observed after 1976-1977. However, stations located on the eastern side of the Andes between 45° and 47.5°S showed a slightly cooling trend over the period 1979-2006. Similar results for the temperature trends between 1930 and 1990 are found by *Villalba et al.* (2003). This analysis showed a climatic shift in 1976/77 with a cooling trend in northern Patagonia at Puerto Montt station and a warming trend at Punta Arenas station.

Results from general circulation models that have participated in the Coupled Model Intercomparison Project Phase 3 (CMIP3), were also analyzed by *Falvey and Garreaud* (2009). The cooling trend was not reproduced by the CMIP3 models, however the models showed a weaker warming trend over the eastern side of the South Pacific Ocean and on the coast than inland. They proposed that the disagreement between models and observations was possibly showing the incapacity of the models to fully capture the SST response to circulation changes in the South-East Pacific. They also suggest that the apparent intensification of the South Pacific Anticyclone resulting from global warming, could explain the cooling trend in the south-eastern Pacific.

As a summary, the warming trend in the eastern zone of Patagonia and Tierra del Fuego is common to all studies. However, only analyses based on observed data and gridded analysis data (ERSST and HadISST) showed the cooling trend at the east of the southern Pacific Ocean and the slight cooling trend in the western side of the continent. Most of the studies coincide in the existence of a negative trend in summer precipitation north of 50°S and a slight but not significant increase to the south. This feature is related to a dipole in variations of zonal wind speeds at this latitude. In winter, the trends are

not clear and annual trends follow those observed in summer.

Patagonian climate and trends are largely influenced by climatic modes impacting the strength and location of the main westerly flow and oceanic conditions. A review of the climate variability related to the main climatic modes is presented in the following section.

### 1.2.3 Links with the large scale climate variability

#### 1.2.3.1 Links with the Southern Annular Mode

Patagonian climate is influenced by climatic modes impacting the strength and location of the main westerly flow, in particular, the Southern Annular Mode (SAM) also called the Antarctic Oscillation (AAO). The SAM is the main mode of climatic variability in the mid- and high latitudes of the Southern Hemisphere. This mode is characterized by an annular structure, with deep and zonally symmetric opposing geopotential height anomalies, located in the polar region and in the mid-latitudes. The SAM structure exists year-round but presents larger impacts during the austral summer (December-January-February). This mode is characterized by different indexes such as the SAM index, the AAO index and the AOI index, which are all different measures of the pressure gradient strength, between the mid- and the high latitudes. The most used index is the one given by *Marshall* (2003), who defined the SAM index as the difference between the zonal mean atmospheric pressures at 40°S (corresponding to the mid-latitudes) and at 65°S (corresponding to the Antarctic boundary). The positive phase of the SAM (SAM+) or the high-index polarity is associated with an increase in the atmospheric pressure gradient. In other words, a SAM+ situation occurs when negative pressure anomalies are observed in the sub-polar low-pressure belt and higher pressure than normal is observed in the subtropical high-pressure region. During a positive phase, the westerlies and the jet stream get stronger and move poleward, associated with an expansion of the Hadley cell and a poleward migration of the dry subtropical belt. Conversely, a negative phase or a low-index polarity means a decrease of the atmospheric pressure gradient between the mid- and the high latitudes. A low index is then associated with a wider westerlies band that expands uncommonly northward.

Since the 1950's, the SAM index has shown an increasing trend towards positive values (*Thompson et al.*, 2011; *Marshall*, 2003). The long term average of the SAM index is now reaching its highest level over the past millenium (*Abram et al.*, 2014). The increase of the SAM positive phase since 1940 is associated with the increase in greenhouse gas concentrations and with the ozone depletion since the 1970's (*Abram et al.*, 2014; *Thompson et al.*, 2011) (see Fig. 1.4). Using temperature proxies in southern South America obtained from tree rings from 33°S to 41°S, *Villalba et al.* (2012) observed

that the increase in the SAM index during 1950-2005 correlates with the warming trend in Punta Arenas in southern South America and some stations in Tasmania and New Zealand.

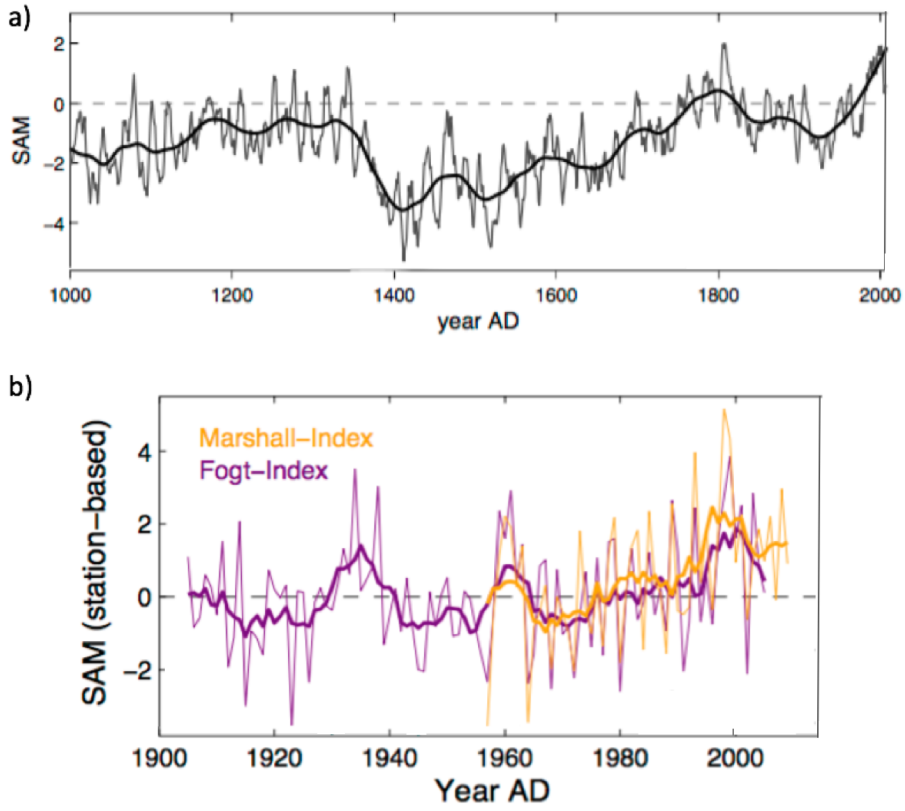


Figure 1.4: SAM index from 1000 AD to present (adapted from *Abram et al.*, 2014).

The influence of the Antarctic ozone hole in the SAM index polarity and Southern Hemisphere climate was studied by *Thompson et al.* (2011). They used reanalysis data, weather station data and results from previous studies to show that the positive trend in the SAM was correlated with a decrease in summer precipitation over the western slopes of the Southern Alps of New Zealand and along the west side of Tasmania. They also showed a SAM-induced increase of the orographic precipitation on the eastern side of the New Zealand Alps and along the Great Dividing Range in southern Australia. For temperature, an increase was observed in New Zealand, whereas cooler situations were observed over the central eastern and subtropical regions of Australia. In southern Patagonia they related the warming trend observed at three weather stations, and the cooling trend in surface air temperature along the southern Pacific Ocean and Patagonia with the changes in the SAM.

Deeper analyses of the SAM impact on climate variations at different time scales in Patagonia are available in *Moreno et al.* (2014, 2018); *Garreaud et al.* (2012); *Garreaud* (2007); *Villalba et al.* (2012) and *Aravena and Luckman* (2009). *Moreno et al.* (2014)

analyzed the correlation between the SAM index and the 850 hPa output from the NCEP-NCAR Reanalysis 1, during the period 1980-2013. They found a negative correlation between the SAM and zonal winds northward of 50°S in summer, but a positive correlation south of this latitude. In winter, the positive correlation is weaker but is extending over all of Patagonia. In this study, a positive correlation between the SAM index and the near surface air temperature at 2m over land (temperature data from the University of Delaware) and at the pressure level of 1000 hPa over the ocean (NECP-NCAR Reanalysis) was found. This correlation is particularly strong in winter and was partially associated with relatively warmer maritime versus land conditions in Patagonia. Moreover, the SAM index was correlated with precipitation data (CPC Merged Analysis of precipitation dataset over the oceans and The University of Delaware dataset over land). A SAM+ index appears correlated with negative anomalies in summer precipitation in Patagonia especially north of 50°S, whereas positive anomalies exist at the south of this latitude and over the ocean. These results are in agreement with the correlation between the SAM and zonal winds expressed earlier in this section, since higher zonal winds lead to higher precipitation amounts.

Following the same line of analysis, *Moreno et al.* (2018) used weather station data and NCEP-NCAR reanlaysis 1 data in southern Patagonia and Tierra del Fuego (50°S - 56°S) and found an important correlation between precipitation and zonal wind speed at 850 hPa. They concluded that the SAM+ index induced a southward shift in the zonal subpolar winds and negative anomalies in precipitation in summer between 40-50°S. This is especially true in the western side of Patagonia.

The occurrence of a drying trend in the northwestern side of Patagonia and of a warming in Tierra del Fuego over 1950-2000 was confirmed using tree ring growth patterns (*Villalba et al.*, 2012). Lower tree growth patterns in north-western Patagonia were linked to a gradual decrease in the water availability, whereas lower tree growth patterns in Tierra del Fuego were associated with warming conditions. Growth patterns were negatively correlated with the SAM index and consistently linked with the associated decrease in precipitation due to the positive trend of the SAM during the last decades.

As a conclusion on the SAM relationship with Patagonian climate, *Garreaud et al.* (2012) analyse the correlation existing between the zonal winds at 850 hPa (ERA-40) and precipitation and surface air temperature given by a dynamical downscaling model (Providing Climates for Impact Studies PRECIS) forced by ERA-40 Reanalyses. They also compared their surface temperature over 1951-2001, with the observed sea surface temperature given by the Haddley Centre Global Sea Ice and Sea Surface Temperature data base (HadlSST). Over the southeast Pacific Ocean, they found a significant positive correlation between zonal wind and precipitation at the annual scale. This correlation in-

creases toward the Patagonian coast. Over the continent there is a positive correlation on the western side of the Andes and a negative correlation on the eastern side. On the other hand, zonal winds and surface atmospheric temperature are not significantly correlated at the annual scale, but only at the seasonal scale. Negative correlation in summer and positive correlation in winter reflects the impact of advection from the ocean to the continent. In *Garreaud* (2007), the author took a closer look at this understanding through the analysis of data from the Climate Prediction Center Merged Analysis of Precipitation (CAMP) and NCEP-NCAR Reanalysis. In this study, the author analyse the relationship between precipitation and circulation covariability in the extra-tropics, and proposed that monthly precipitation anomalies were related with the low- and high-level zonal flows (850 hPa and 300 hPa). Indeed, strong westerlies aloft induce a rapid growth and a fast succession of baroclinic disturbances, inducing an increase of cyclone/frontal precipitation. Associated with the westerly flow, there was enhanced orographic precipitation along the mountain flanks.

As a consequence, the later study allows to conclude that winds were significantly correlated with the SAM. Negative correlations were observed north of 50°S but positive values appeared to the south in summer. This dipole vanishes in winter. A decreasing trend in the westerlies was observed in the northern and central parts of Patagonia but changes were of larger magnitude in winter. This likely justifies that precipitation decreased in western Patagonia at a rate of 300-800 mm/decade in regions located north of 50°S but increased to the south.

#### 1.2.3.2 Links with the PSA, ENSO and PDO/IPO

After the SAM, there are two other modes of Southern Hemisphere atmospheric variability. The second and third EOFs explaining climate variability over the Southern hemisphere mid- to high- latitudes are the Pacific-South American patterns (PSA). They are strongly influenced by El Niño Southern Oscillation (ENSO) (*Mo*, 2000; *Yu et al.*, 2015) and connected to SST and rainfall anomalies in South America and evidence of their impact has been found in tropical and south-eastern zones (*Mo and Paegle*, 2001) and Antarctica (*Yu et al.*, 2015).

Thus, another key mode of climatic variability affecting the Southern Hemisphere is the El Niño Southern Oscillation. ENSO positive phases are associated with positive sea surface temperature anomalies in the tropical, central and East Pacific Ocean. However, the influence of the ENSO is rather limited in the mid-latitudes, and climate in the regions located south of 45°S presents no relationship with the ENSO (*Aravena and Luckman* (2009); *Moreno et al.* (2018)). However, disentangling the relative impacts of ENSO and SAM is relatively difficult since both indexes are significantly correlated, and because

the relationship between both, changed from being weak before the early 1990s to being strong afterward (*Yu et al.*, 2015).

The impact of the Pacific Decadal Oscillation (PDO) on South America and Patagonia has also been studied. The PDO is defined as the leading principal component of monthly SST anomalies in the north Pacific Ocean (>20° N) (*Mantua et al.*, 1997). Several studies have found that the influence of PDO decreases southeastward in South America, and that the PDO has a small influence in Patagonia (*Moreno et al.*, 2014; *Garreaud et al.*, 2009; *Schneider and Gies*, 2004; *Aravena and Luckman*, 2009; *Quintana*, 2004). However, it has been also noted that due to the short data record available, the capability to detect the signal of multidecadal climatic variations such as the PDO is limited (*Aravena and Luckman*, 2009; *Garreaud et al.*, 2009). *Aravena and Luckman* (2009) found that the PDO does not correlate with any of the subregional annual rainfall averages, and is only marginally correlated with the Patagonian plains–Atlantic subregion. *Garreaud et al.* (2009) found that PDO-related anomalies of precipitation and temperature over South America are similar to ENSO but with half of the amplitude and with very low influence in Patagonia and Tierra del Fuego. They also found a relation with the climatic shift in 1976/1977, a relationship that was also found by *Villalba et al.* (2003).

#### 1.2.3.3 Concluding remarks on main climatic modes

As a summary, climate variability in Patagonia and Tierra del Fuego is largely controlled by the SAM variations. For the precipitation, a decreasing trend is described in northwestern Patagonia and positive trends are found in southwestern Patagonia and Tierra del Fuego. Both trends are mainly present during summer but are also significant at annual scale. Regarding the trends in temperature, surface air temperature trends should be linked with the variations in the SAM and with the location and strength of the main zonal winds. However, the impact of SAM on air temperature and SST is not conclusive from the literature, most probably due to the incapacity of global climatic models to simulate the response of SST to circulation changes as pointed out by *Falvey and Garreaud* (2009). The only clear relationship between temperature trends and SAM, based on observations, is the SAM influence on the warming trend in Tierra del Fuego (*Villalba et al.*, 2012).

## 1.3 The Patagonian Icefields

The cryosphere plays a major role in the earth climate system. Glaciers and icecaps are inherently sensitive to temperature and precipitation changes, and are natural proxies of climate variability. In this section, I present a description of the Patagonian Icefields

and give a review of their variations since the Last Glacial Maximum, with a focus on the recent decades. I finally discuss current conclusions on the surface mass balance and dynamical changes, and compare the trends of mass balance proposed in the literature.

### 1.3.1 Characteristics

Patagonia is the largest ice-covered region in the Southern Hemisphere outside of Antarctica (*Rignot et al.* (2003)). Most of the ice is located in two main icefields: the Northern Patagonia Icefield (NPI 3976 km$^2$) and the Southern Patagonia Icefield (SPI 13219 km$^2$) (*Davies and Glasser*, 2012).

Most Patagonian glaciers have been losing mass and retreating for the last 40 years (*Aniya*, 1999; *Lopez et al.*, 2010; *Casassa et al.*, 2014). Estimations of total mass balance from different sources confirm the acceleration of mass losses during the last decades compared to the mean loss observed over the entire period since the Little Ice Age (*Rignot et al.*, 2003; *Glasser et al.*, 2011; *Jacob et al.*, 2012).

The NPI is located between 46.5°S and 47.5°S (Fig.1.5). The equilibrium line altitude (ELA) is between 950 to 1300 m a.s.l. over NPI, leading to an accumulation area ratio (AAR) value of 0.68 (*Rivera et al.*, 2007). This elevation band is characterized by a flat and vast plateau, making the icefield surface mass balance particularly sensitive to shifts in the ELA in response to changes in temperature and accumulation. The NPI is formed by 140 units in the Randolph Glacier (RG) inventory (*Pfeffer et al.*, 2014), including 38 main glaciers of different terminus types: one tidewater calving glacier (San Rafael Glacier (SRG) covering 18% of the total surface area of the NPI), 18 freshwater calving glaciers (64% of the total surface area) and 19 land-terminating glaciers (18% of the total surface area) (*Rivera et al.*, 2007; *Willis et al.*, 2012a; *Pfeffer et al.*, 2014). A recent ice velocity mosaic reveals that fast flow regions extend far into the plateau in the accumulation area, making the icefield also potentially sensitive to dynamical changes (*Mouginot and Rignot*, 2015).

SRG is located in the north-western part of NPI and is the largest glacier with an area of 734 km$^2$ (Fig. 1.5). It covers the entire altitude range of NPI: the highest point of the glacier catchment is San Valentin peak and it ends at sea level in Laguna San Rafael. Laguna San Rafael is connected to the Pacific Ocean through the Témpanos River and Elefantes Fjord. From remotely sensed snowline estimates and surface mass balance modeling studies, the ELA of SRG has been estimated between 905 and 1295 m a.s.l. (*Aniya*, 1988; *Rignot et al.*, 1996; *Rivera et al.*, 2007; *Koppes et al.*, 2011; *Schaefer et al.*, 2013). SRG is among the fastest glaciers in the world with frontal velocities exceeding 7 km a$^{-1}$ (*Willis et al.*, 2012a; *Mouginot and Rignot*, 2015).

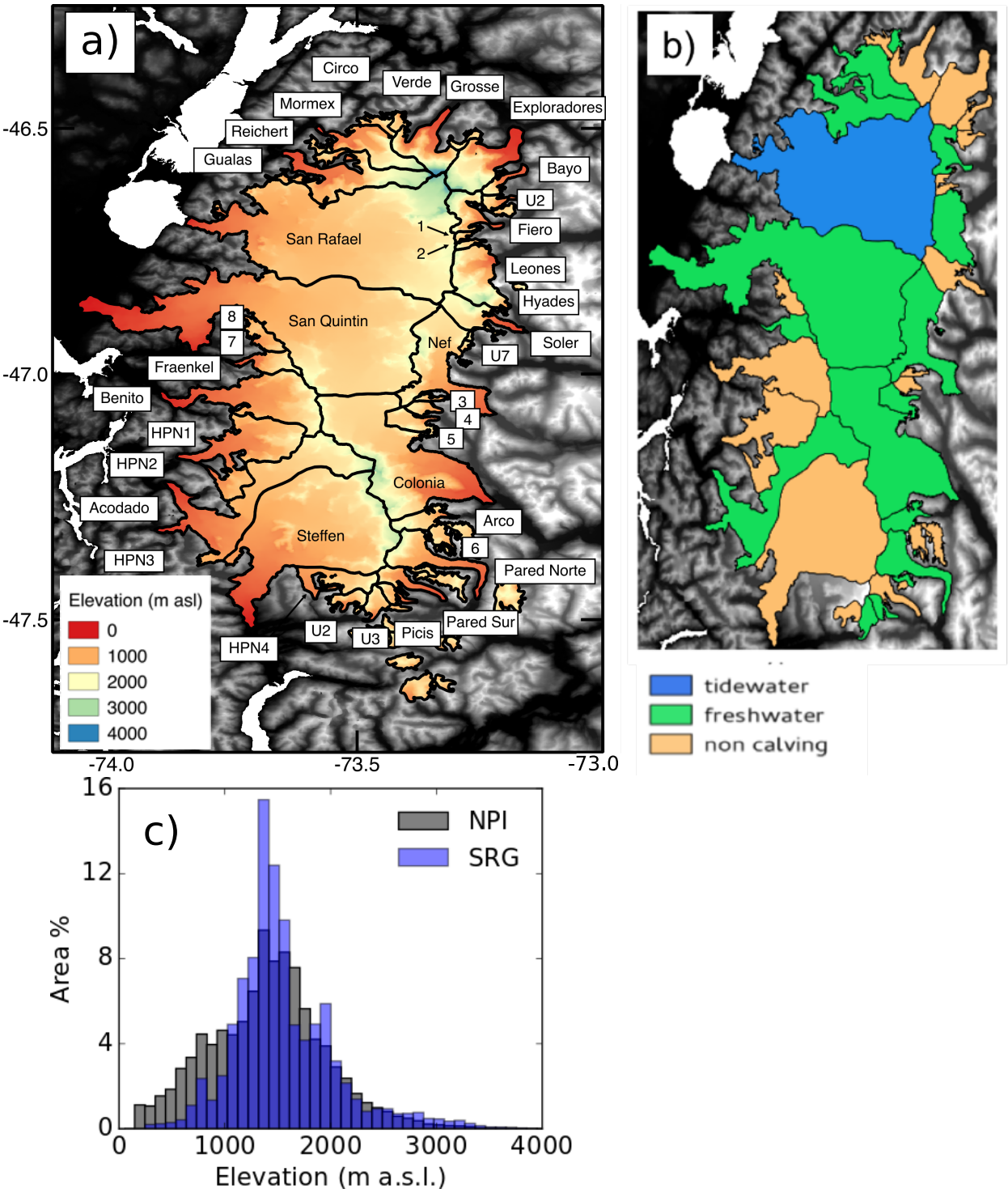


Figure 1.5: Northern Patagogonian Icefield (NPI) a) Topography from SRTM 2000, b) Glacier type, c) Hypsometry of San Rafael Glacier and NPI.

The SPI is located at the south of NPI between 48°S and 51.5°S and centered at 73.5°W (Fig.1.6). This second icefield is approximately 370 km long and 45 km wide. The surface elevation ranges from sea level to the summit of Lautaro volcano (3607 m a.s.l.), one of the four volcanos of SPI. The elevation area distribution of SPI is similar to those of NPI, with a plateau between 1200 and 1800 m a.s.l. The ELA is located

between 650 and 1500 m a.s.l. (*Casassa et al.*, 2014; *Willis et al.*, 2012b; *Aniya et al.*, 1996) leading to an AAR value of 0.71 in 2000 (*Casassa et al.*, 2014). This icefield has 48 major glaciers, Pio XI glacier being the largest glacier with 1221 $km^2$ (*Casassa et al.*, 2014). Most SPI glaciers are calving glaciers (98.6% of the total surface area, with 16 tidewater calving fronts and 30 freshwater calving fronts), whereas SPI presents only 2 land terminus glaciers (1.4 % of the total surface area) (*Casassa et al.*, 2014) (Fig.1.6). Because of these characteristics, SPI is more sensitive to oceanic influence and to complex dynamical processes. The highest velocities have been estimated at the front of calving glaciers, and more particularly at the front of tidewater calving glaciers located on the west side of the icefield (*Sakakibara and Sugiyama*, 2014). Pio XI glacier presents velocities exceeding 4 km $a^{-1}$ (*Sakakibara and Sugiyama*, 2014; *Mouginot and Rignot*, 2015), but the Penguin and Europa glaciers have the maximum estimated velocities with 10.3 and 8.8 km $a^{-1}$, respectively (*Mouginot and Rignot*, 2015).

### 1.3.2 Areal changes since the Last Glacial Maximum

From ice-flow modeling and using geochronologic records collected near NPI, *Hubbard et al.* (2005) estimated that one unique Patagonian Ice Sheet (PIS) was present in the area at the Last Glacial Maximum (LGM). At that time, PIS had an area of about ∼92 000 $km^2$. Using moraines, trimlines and cosmogenic isotope dating, *Boex et al.* (2013) estimated that PIS remained stable until ∼19ky BP when it started to retreat until reaching its current size ∼ 15.5ky BP. They related the rapid shrinkage to regional warming and to the southward migration of the westerlies and to the resulting precipitation changes.

During the Little Ice Age (LIA - around AD 1870 in this region), NPI and SPI areas were 4636 $km^2$ and 14862 $km^2$ respectively (*Davies and Glasser*, 2012). Most of the glaciers from NPI and SPI retreated between 1870 and 2011, with an acceleration during the period 2001-2011 (0.23 $\%a^{-1}$) compared to the period 1870-1986 (0.09 $\%a^{-1}$). Glacier shrinkage at the eastern side of NPI was more pronounced for land-terminating glaciers. However, the large calving glaciers, west of the divide, presented the highest rates of shrinkage. Thus, a small number of large glaciers has been responsible for most of the NPI large areal losses from 1870 to 2011. Over SPI, glacier retreat was larger between 2001 and 2011 than between 1870 and 2011 (0.15 $\%a^{-1}$ compared to 0.07 $\%a^{-1}$). In general, small land terminating glaciers had the highest rates of shrinkage, even though several large calving glaciers also shank significantly. The glaciers located on the eastern side have slightly higher annual rates of shrinkage than those located west of the divide.

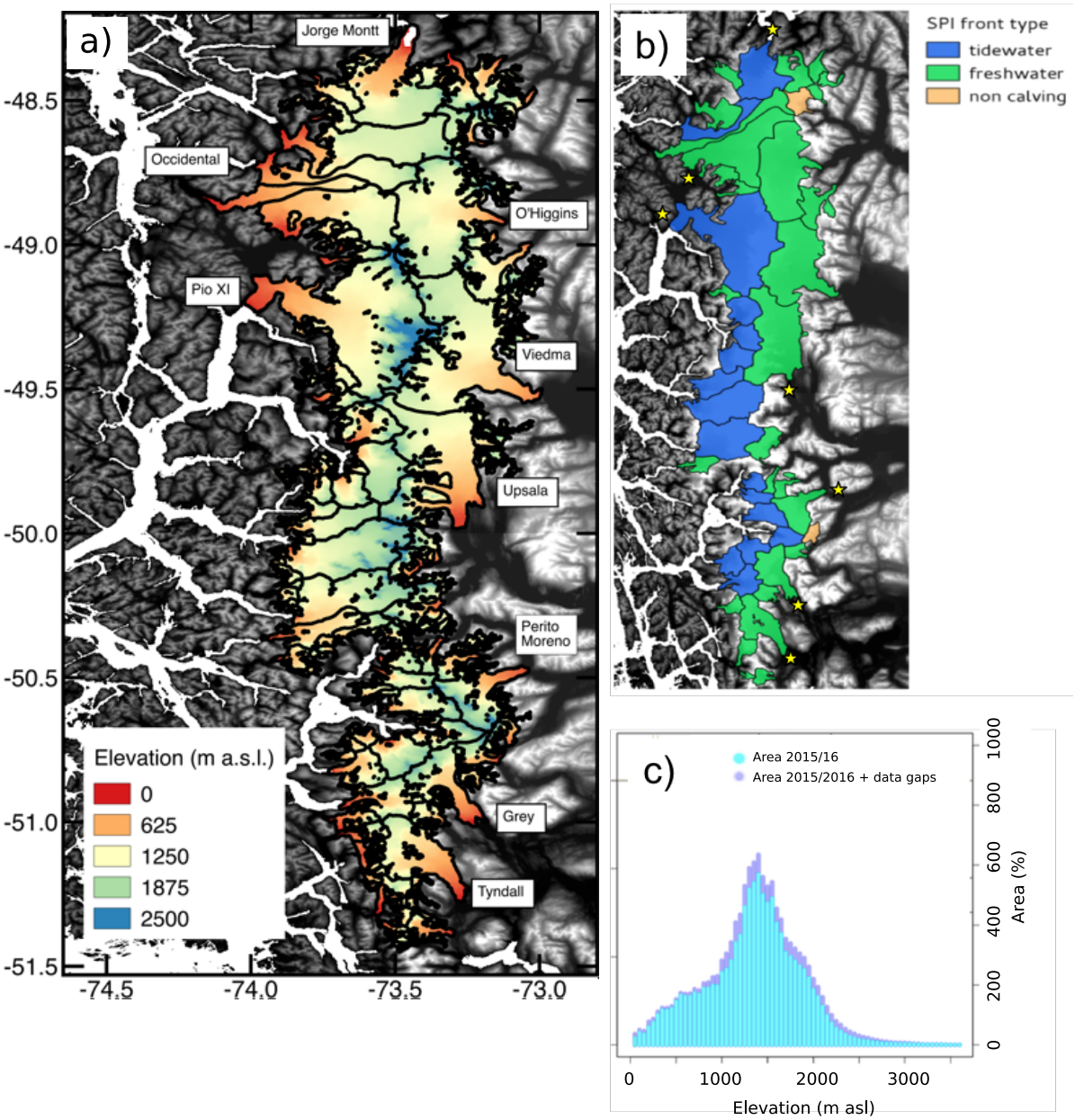


Figure 1.6: Southern Patagogonian Icefield a) Topography from SRTM 2000, b) Glacier type and c) Hypsometry from *Malz et al.* (2018).

Between 1944/45 and 1985/86 most of the glaciers from SPI were retreating, inducing a total area loss of about 200 km$^2$, but few glaciers remained stable and two glaciers advanced (Pio XI and Moreno) (*Aniya*, 1999). On the northeastern side, O'Higgins Glacier displayed the largest retreat of SPI, followed by Upsala Glacier (also located in the east). The glaciers that were calving in fjords in the west retreated slowly, and more particularly those located in the southwestern side of SPI.

*Aniya* (1999) updated the changes for NPI between 1944/45 and 2004/2005 and found a total areal loss of 64 km$^2$. He suggested that the general trends of retreat were very heterogeneous before 1990, and that retreat slowed down after 1990. *Lopez et al.* (2010) also found that most of the glaciers retreated extensively between 1945 and 2005. The

largest retreats were observed for O'Higgins Glacier in the case of SPI (11.6 km) and for San Rafael Glacier in the case of NPI (5.7 km). The shrinkage from 1975 to 2001 reached 3.4±1.5% (140±61 km$^2$) over NPI, and almost 62% of the total area change between 1979 and 2001 took place over glaciers located at its western side (*Rivera et al.*, 2007). In particular, San Rafael Glacier shrank rapidly from 1870 to 1986, and then slowed down until reaching a steady state with a constant front location between 2001 and 2011. San Quintín Glacier experienced a large areal loss (33 km$^2$) between 1979 and 2001 (*Rivera et al.*, 2007). San Quintin and San Rafael presented the most important retreats of NPI after 1990, even if the front of San Rafael Glacier displayed a cycle of stagnation/advance/retreat during the period 1990-2000, as a consequence of a topographic control on the front location. Another study has reported an advance of San Rafael Glacier from 1992 to 1999 (*Aniya*, 2007).

More recent studies (e.g., *Casassa et al.* (2014)) have proposed updates from previous estimates over SPI, proposing a shrinkage of 489±377 km$^2$ between 1986 and 2000. Their results confirmed the general retreat occurring over SPI, demonstrating however that 9 glaciers located in the 49°48' -50°25' S latitude range were relatively stable due to a recent increase in precipitation in the central south sector of SPI. This increase was linked to an intensification of the westerlies (*Marshall*, 2003). However, the trends in areal changes were not only related to mass changes but also to glacier geometry, type, exposition and response time. *Lopez et al.* (2010) also observed that no clear relationship exists with glacier size, surface area nor surface slope, but these authors suggested that the retreat was first controlled by atmospheric warming and that the heterogeneous rate of retreat was due to differences in basin geometry, glacier dynamics and response time. Therefore, *Casassa et al.* (2014) suggested that glacier area did not directly respond to climatic variations. This was confirmed by *Sakakibara and Sugiyama* (2014), who proposed to relate the front retreat and variations of ice velocities over SPI. They found three typical behaviors: i) stable front position and stable ice speed, ii) gradual retreat with deceleration and iii) rapid retreat and large acceleration, with the exception of Pío XI glacier. They related the general retreating trend with the long-term regional warming but also showed that the large retreat of three glaciers was controlled mainly by their ice flow.

#### 1.3.2.1 Summary on areal changes

As a summary, since the LIA, glaciers from the NPI and SPI displayed a large shrinkage. Glacier shrinkage at the eastern side of the NPI and SPI was more pronounced for land-terminating glaciers. Nevertheless, large calving glaciers presented the highest rates of shrinkage at the west of the divide. In particular, San Rafael Glacier shrank rapidly from 1870 to 1986, and then slowed down until reaching a steady state with a constant

front location between 2001-2011.

### 1.3.3 Mass balance changes

#### 1.3.3.1 MB changes until 2000

Due to the lack of in situ glaciological measurements, the mass balance (MB) and volume changes of the Patagonia Icefields have been estimated mainly from geodetic methods based on various data sources (satellite data, aerial photographs) and from gravimetry (*Aniya*, 1999; *Rignot et al.*, 2003; *Rivera et al.*, 2007; *Chen et al.*, 2007; *Glasser et al.*, 2011; *Ivins et al.*, 2011; *Willis et al.*, 2012a,b; *Gardner et al.*, 2013; *Abdel Jaber*, 2016; *Dussaillant et al.*, 2018; *Foresta et al.*, 2018; *Malz et al.*, 2018). Both icefields have shown increasing mass losses since 1945 in comparison with the average mass loss since the Little Ice Age (Fig.1.7 and Table 1.1). If we consider each icefield separately, mass losses have been significantly more important in SPI (above 10 Gt $a^{-1}$) than in NPI with values below 8 Gt $a^{-1}$ (*Aniya*, 1999; *Rignot et al.*, 2003; *Rivera et al.*, 2007; *Willis et al.*, 2012a,b; *Abdel Jaber*, 2016; *Dussaillant et al.*, 2018; *Foresta et al.*, 2018; *Malz et al.*, 2018). This was primarily due to the largest extension of SPI but also to higher punctual thinning and retreat (*Aniya*, 1999). Even if there is a general agreement in the mass loss increase since 1945, the trends on decadal time scales are difficult to asses because of the large uncertainties in the estimates.

In the following I give more details on the different estimates and their uncertainties. To compare among the different studies, all mass changes are given in Gt $a^{-1}$, and have been converted from $km^3$ $a^{-1}$ using an uniform density of 900 kg $m^{-3}$ when needed.

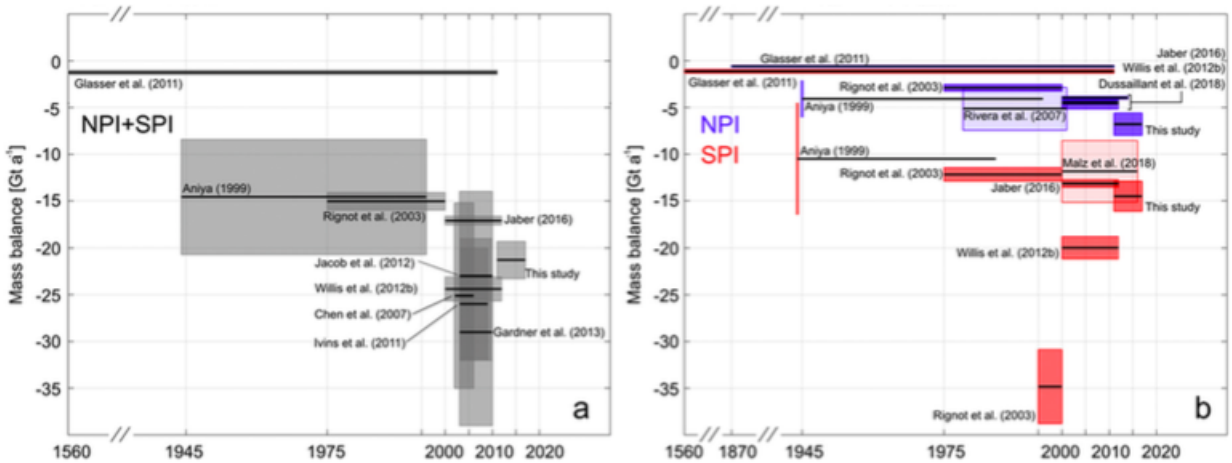


Figure 1.7: Mass balance of NPI and SPI from geodetic and gravimetric methods (from *Foresta et al.* (2018)).

The volume change since the Little Ice Age has been estimated in SPI and NPI using

field observations of the trimline and of the terminal moraine location. These observations allowed to define the boundary and the surface elevation of the glaciers during the LIA. These data were compared to the ASTER GDEM (The ASTER Global Digital Elevation Model, http://www.gdem.aster.ersdac.or.jp/) that offers the actual surface elevation (about 2010), and to glacier boundaries obtained using Landsat and Terra ASTER images from 2002 to more recent years (*Glasser et al.*, 2011). The volume changes only consider variations in the ablation area since the LIA because no evidence of thickening / thinning in the accumulation area was found and the authors assumed that the volume did not change in this area.

Further ice losses were obtained using i) oblique aerial photographs covering the whole NPI from 1944/1945, ii) vertical aerial photographs for Argentinean glaciers and some Chilean glaciers from 1986 for SPI, and iii) hand-held oblique aerial photographs of most of the glacier snouts from different dates (1983, 1986, 1990, 1993 and 1995) (*Aniya*, 1999). The estimations of *Aniya* (1999) have large uncertainties, this is due to the rough estimation of mean changes in the the ablation and accumulation zones based on a few punctual measurements. The rate of mass change of SPI since the Little Ice Age was -1.94±0.44 Gt $a^{-1}$ over the period 1650-2010, whereas its value for both icefields ranged between -8.94 and -20.17 Gt $a^{-1}$ between 1944/45 and 1995/1996 (*Aniya*, 1999).

More recently *Rignot et al.* (2003) proposed MB values of the icefields over the periods 1968/1975-2000 and 1995-2000. They used i) cartography maps from March 1968/75 (the Instituto Geográfico Militar of Chile (IGMch) and Argentina) based on photogrammetric restitution from March 1968/75 and in May 1995 (with local systematic vertical errors of $\pm 3$ $m$ and 4.5 m), and ii) elevation proposed by the Shuttle Radar Topography Mission data (SRTM) from February 2000, which presents a 7-m vertical accuracy (value estimated by comparison between SRTM data and GPS surface reference data on Tyndall and Chico Glaciers). Values proposed by *Rignot et al.* (2003) were of -14.56±5.62Gt $a^{-1}$ for both icefields for the 1968/1975-2000 period. These values have lower uncertainties and are within the range of potential values proposed by *Aniya* (1999). Their estimations correspond to the mass loss observed below 1400 m a.s.l. and due to retreat of the front. Results from *Rignot et al.* (2003) over the period 1975-2000 show that glaciers from NPI and the northern part of SPI thinned more rapidly than those from the southern part of SPI. Thinning was increasing from the highest part of the icefields to the front, especially for SPI.

#### 1.3.3.2 MB since 2000

The development of satellite missions has allowed more frequent estimations of the icefield mass balances since 2000, using different techniques and products. The various

estimates do not always overlap, giving poor confidence in the reported uncertainties.

Over the last decade (2010-2017), the most recent estimation was given by *Foresta et al.* (2018) using CryoSat-2 swath radar altimetry at sub-kilometric spatial resolution. They found a mass balance of -21.29±1.98 Gt $a^{-1}$. This value is slightly lower than the value of -24.4±1.4 Gt $a^{-1}$ given by *Willis et al.* (2012a) for the period 2000-2012 obtained using SRTM-2000 data and ASTER DEMs. *Abdel Jaber* (2016) proposed a lower value of -17.10 ± 0.40 Gt $a^{-1}$ for 2000-2014 using SRTM-2000 and TanDEM-X (TerraSAR-X) data collected between September/October 2013 and January/February 2014. The difference between the previous values is mainly related to a disagreement in ice wastage calculations for SPI, which can be due to a 2m correction applied by *Willis et al.* (2012a) to the SRTM-2000 DEM to consider the penetration of the radar signal within the firn (*Foresta et al.*, 2018). *Abdel Jaber* (2016) did not consider this correction because wet firn in Patagonia should prevent penetration of the signal below the surface. Nevertheless, other uncertainties likely explain this difference between both estimates, since it exceeds 2m. Part of the difference is also related to large losses occurring in 2013 and 2014, which were not considered by *Willis et al.* (2012a).

Table 1.1: NPI + SPI MB changes from literature.

| Source | Method | MB ($km^3a^{-1}$) | MB (Gt $a^{-1}$) | period |
|---|---|---|---|---|
| *Glasser et al.* (2011) | geod. | -2.15±0.48 | -1.94±0.44* | LIA-2010 |
| *Aniya* (1999) | geod. | -9.94 - -22.41 | -8.94 - -20.17* | 1944/45-1995/96 |
| *Rignot et al.* (2003) | geod. | -16.70±0.90 | -14.56±5.62 | 1968/75-2000 |
| *Willis et al.* (2012a) | geod. | -27.11±1.56* | -24.4±1.4 | 2000-2012 |
| *Abdel Jaber* (2016) | geod. | -19.00±0.44 | -17.10±0.40* | 2000-2014 |
| *Foresta et al.* (2018) | geod. | -23.70±2.20 | -21.29±1.98 | 2010-2017 |
| *Chen et al.* (2007) | grav. | -27.90±11.00 | -25.11±9.90* | 2006-2006 |
| *Ivins et al.* (2011) | grav. | -27.90±11.00 | -25.29±9.90* | 2003-2009 |
| *Jacob et al.* (2012) | grav. | -25.56±10.00* | -23.00±9.00 | 2003-2009 |
| *Gardner et al.* (2013) | grav. | -32.00±11.00 * | -29.00±10.00 | 2003-2009 |

* estimated values have been converted between Gt $a^{-1}$ and $km^3a^{-1}$ using an uniform density of 900 $kgm^{-3}$

Estimations from gravimetry methods using data from GRACE may help to reconcile the different volume loss estimates. A mass loss of -25.11±9.90 Gt $a^{-1}$ was given for 2002-2006 by *Chen et al.* (2007), whereas a slightly more negative value of -25.29±9.90 Gt $a^{-1}$ between 2003 and 2009 was estimated by *Ivins et al.* (2011). Nevertheless, *Chen et al.* (2007), *Jacob et al.* (2012), and *Foresta et al.* (2018) pointed out that estimations from GRACE present important uncertainties due to mass corrections included to account for hydrological processes and to the glacial isostatic adjustment associated to the post-LIA

isostatic rebound. As a consequence, many other values using GRACE data exist, as for instance those given by *Jacob et al.* (2012) (-23±9 Gt $a^{-1}$ over the period 2003-2009) or by *Gardner et al.* (2013) (-29±10 Gt $a^{-1}$). Finally values from *Gardner et al.* (2013) were used in the fifth Assessment Report of the IPCC (*Vaughan et al.*, 2013).

#### 1.3.3.3 Focus on NPI

If we focus on wastage of NPI (see Table 1.2), the average loss between the LIA (1870) and 2010 was -0.60± 0.12 Gt $a^{-1}$ (*Glasser et al.*, 2011), with an increase to the range -2.68 to -5.47 Gt $a^{-1}$ between 1944/45 and 1995/1996 (*Aniya*, 1999). *Rignot et al.* (2003) confirmed these estimates and proposed an annual wastage of -2.88±0.36 Gt $a^{-1}$ between 1968/1975 and 2000, whereas more important mass losses (-5.13 Gt $a^{-1}$) were proposed by *Rivera et al.* (2007) over 1979-2001. The latter value was obtained using cartography data from 1974/1975 (compiled by the Instituto Geográfico Militar of Chile (IGM)) and a ASTER DEM from 2001. This value presents a significant source of uncertainty related to the lack of data in the accumulation zone where data were mostly available close to Monte San Valentin. However, the lack of data alone does not justify the existing difference with previous studies because the volume loss was mainly the result of the variations in the ablation area.

For the following decade, the MB values given by four different methods are very similar and range from -3.40 to -4.25 Gt $a^{-1}$ (*Willis et al.*, 2012a; *Abdel Jaber*, 2016; *Dussaillant et al.*, 2018). These values overlap with the estimates from the previous period given by *Aniya* (1999) and *Rivera et al.* (2007) but are higher than those given by *Rignot et al.* (2003). In particular, *Dussaillant et al.* (2018) used two different approaches to compute the MB of the NPI. Their first method was based on a comparison between the SRTM-2000 and a DEM obtained from SPOT5 (Satellite pour l'Observation de la Terre 5) acquired in March 2012. However, in a second approach, the authors deduced volume changes by fitting pixel-based linear elevation trends over 118 DEMs calculated from ASTER stereo images acquired between 2000 and 2012. Comparison of both methods reveals that the C-band SRTM radar signal does not penetrate the NPI snow and firn except for a region above 2900 m a.s.l., which covers less than 1% of the total area, suggesting that *Willis et al.* (2012a)'s assumption was not justified. Finally, *Foresta et al.* (2018) proposed an acceleration of the ice wastage during the last decade, showing the largest rates since the LIA (-6.70±1.16 Gt $a^{-1}$).

The MB of San Rafael Glacier followed the same temporal trend as for NPI (see Table 1.3), showing an acceleration of the mass loss rate after 2000, from -0.09 Gt $a^{-1}$ between 1975 to 2000, to -0.74 Gt $a^{-1}$ between 2000-2012 (*Willis et al.*, 2012a) or -0.77

Gt $a^{-1}$ (*Dussaillant et al.*, 2018) between 2000 - 2011. It is interesting to note that this acceleration of the mass loss coincides with a stabilization of the front between 2000-2012 (*CECs and DGA*, 2012).

Table 1.2: NPI MB changes from literature.

| Source | method | MB ($km^3$ $a^{-1}$) | MB (Gt $a^{-1}$) | period |
|---|---|---|---|---|
| *Glasser et al.* (2011) | geod. | -0.67±0.13 | -0.60±0.12* | LIA-2010 |
| *Aniya* (1999) | geod. | -2.98 - -6.08 | -2.68 - -5.47* | 1944/45-1995/96 |
| *Rignot et al.* (2003) | geod. | -3.2±0.40 | -2.88±0.36* | 1968/75-2000 |
| *Rivera et al.* (2007) | geod. | -5.7 | -5.13 | 1979-2001 |
| *Willis et al.* (2012a) | geod. | -4.06±0.11 | -3.40±0.07* | 2000-2011/12 |
| *Abdel Jaber* (2016) | geod. | -4.40±0.13 | -3.96±0.12* | 2000-2014 |
| *Dussaillant et al.* (2018) | geod. | -4.55±0.41 | -4.10±0.47 | 2000-2014 |
| *Dussaillant et al.* (2018) | geod. | -4.72±0.34 | -4.25±0.31 | 2000-2014 |
| *Foresta et al.* (2018) | geod. | -7.44±1.29 | -6.70±1.16 | 2001-2017 |

* estimated values were converted between Gt $a^{-1}$ and $km^3$ $a^{-1}$ using an uniformed density of 900 kg $m^{-3}$

Table 1.3: SRG MB changes from literature.

| Source | Method | MB ($km^3$ $a^{-1}$) | MB (Gt $a^{-1}$) | period |
|---|---|---|---|---|
| *Rignot et al.* (2003) | geod. | -0.10 | -0.09* | 1968/75-2000 |
| *Willis et al.* (2012a) | geod. | -0.82 | -0.74* | 2000-2012 |
| *Dussaillant et al.* (2018) | geod. | -0.86 | -0.77* | 2000-2014 |

* estimated values were converted between Gt $a^{-1}$ and $km^3$ $a^{-1}$ using an uniformed density of 900 kg $m^{-3}$

#### 1.3.3.4 Focus on SPI

MB values of SPI differ from those observed on NPI. Values present a larger spread depending on the sources with no clear increasing trend during the last decades (Table 1.4). *Glasser et al.* (2011) proposed a mass loss value of -1.13 ± 0.23 Gt $a^{-1}$ for the period 1650-2010, with a slightly larger value of -1.53 ± 0.32 Gt $a^{-1}$ between 1750 and 2010. As for the NPI, volume changes between 1944/45 and 1995/96 were larger (-10.49±4.23 Gt $a^{-1}$, *Aniya* (1999)). A similar total mass loss was proposed over the period 1968/1975-2000 by *Rignot et al.* (2003) (-12.15 ± 0.72 Gt $a^{-1}$), but this analysis was performed using cartography data from the Chilean IGM from 1995-2000, which was covering only 43% of

the SPI area. Extrapolating their results to the entire surface area lead however to a more negative mass loss of -34.83 ± 3.96 Gt $a^{-1}$. This amount is considerably more negative than those from any other geodetic approach. Moreover, if we consider values from both icefields, this gives a total of -37.75 Gt $a^{-1}$, which considerably exceeds the estimations obtained with GRACE (*Chen et al.*, 2007; *Ivins et al.*, 2011; *Jacob et al.*, 2012; *Gardner et al.*, 2013), even if one considers the uncertainty range of the estimates.

For the last two decades, three different estimations of total SPI mass loss have been proposed: *Willis et al.* (2012b) give -20.0±1.2 Gt $a^{-1}$ between February 2000 and March 2012 using SRTM-2000 and ASTER DEMs. This value is significantly more negative than the estimates obtained from SRTM and TanDEM-X DEMs given by *Abdel Jaber* (2016) (-13.14±0.42 Gt $a^{-1}$ between 2000 and 2014) and by *Malz et al.* (2018) (-11.84±3.30 Gt $a^{-1}$ between 2000 and 2015/2016). The latter studies also agreed in the occurrence of a decreasing trend within this period. Finally, another value was proposed by *Foresta et al.* (2018) (-14.50±1.6 Gt $a^{-1}$) for the period 2011-2017. *Malz et al.* (2018) observed that annual surface accumulation in regions located south of 50°S and above the ELA were more positive between 2011/2012 and 2015/2016 than between 2000 and 2011/2012. They proposed that changes in accumulation were related to a potential increase in precipitation at the south of the icefield in 2014 and 2015, which may also partly explain the difference between the estimations of *Malz et al.* (2018) and *Abdel Jaber* (2016).

If we analyze glacier wastage for each unit separately, we observe that most of the glaciers from SPI were losing mass. Upsala glacier presented large mass losses of -2.79±0.2 Gt $a^{-1}$, -2.43 Gt $a^{-1}$ and -2.68±0.4 Gt $a^{-1}$ over 2000-2012 (*Willis et al.*, 2012b), 2000-2015 (*Malz et al.*, 2018) and 2011-2017 (*Foresta et al.*, 2018) respectively. Its neighbour, Viedma glacier, presented slightly less negative mass balances of -1.98±0.09 Gt $a^{-1}$ (*Willis et al.*, 2012b), -1.91 Gt $a^{-1}$ (*Malz et al.*, 2018) and -2.27±0.36 Gt $a^{-1}$ (*Foresta et al.*, 2018) over the same periods. Both glaciers calve in freshwater lakes located at the north-eastern side of SPI and present similar AAR values of 0.65 and 0.67, respectively. The third largest mass loss was observed for Jorge Montt glacier, which is a tidewater glacier located at the north of SPI with an AAR of 0.71. This glacier has been losing mass with values of -1.53 Gt $a^{-1}$ for 1975-2000 (*Rignot et al.*, 2003) increasing to $-2.20 \pm 0.38$ Gt $a^{-1}$ for 2011-2017 (*Foresta et al.*, 2018). In the southern part of SPI, the most important losses were observed on Tyndall and Grey glaciers, which are both freshwater calving glaciers located at the eastern side of SPI. Nevertheless, not all the glaciers presented wastage during the last decades, the main exception being the Pio XI glacier, which is the largest glacier of SPI. This glacier increased in mass between 2011 and 2017 (*Foresta et al.*, 2018) but the causes of this mass gain are not clear yet.

Finally, as suggested before, glacier mass balances presented different trends north and

south of the 49°S- 50°S boundary. This pattern seems to be more pronounced during the last decade. The elevation changes displayed by *Willis et al.* (2012b) were more significant in the low elevation zones of glaciers located in the northern and eastern parts of SPI, with the exception of Pio XI glacier. Conversely, glaciers located in the south-western and southern side of Pio XI showed lower rates of thinning. This pattern was also found by *Abdel Jaber* (2016) and *Malz et al.* (2018) and is even more obvious in *Foresta et al.* (2018) who separately analysed glaciers located south and north of the 49°S boundary. In the latter reference the difference in mass losses between northern and southern parts of SPI are associated to topography differences, because the northern part of SPI is lower and wider. Besides, they propose that part of the difference could come from dynamical differences considering that some of the fastest glaciers, such as Jorge Montt and Upsala glaciers, are located in the northern part of SPI.

Table 1.4: SPI MB changes from literature.

| Source | method | MB ($km^3$ $a^{-1}$) | MB (Gt $a^{-1}$) | period |
|---|---|---|---|---|
| *Glasser et al.* (2011) | geod. | -1.7±0.35 | -1.53±0.32* | 1750-2010 |
| *Glasser et al.* (2011) | geod. | -1.26±0.25 | -1.13±0.23* | 1650-2010 |
| *Aniya* (1999) | geod. | -6.95 - -16.34 | -6.26 - -14.71 | 1944/45-1995/96 |
| *Rignot et al.* (2003) | geod. | -13.5±0.80 | -12.15±0.72* | 1968/75-2000 |
| *Rignot et al.* (2003) | geod. | -38.7±4.40 | -34.83±3.96* | 1995-2000 |
| *Willis et al.* (2012a) | geod. | -22.22±01.33* | -20.00±1.20 | 2000-2012 |
| *Abdel Jaber* (2016) | geod. | -14.60±0.38 | -13.14±0.42* | 2000-2014 |
| *Malz et al.* (2018) | geod. | -13.20±3.60 | -11.84±3.30 | 2000-2015/16 |
| *Foresta et al.* (2018) | geod. | -16.10±1.80 | -14.50±1.60 | 2001-2017 |

* estimated values were converted between Gt $a^{-1}$ and $km^3$ $a^{-1}$ using an uniform density of 900 kg $m^{-3}$

#### 1.3.3.5 General conclusions on icefield MB of both icefields

Glacier wastage since the LIA has been increasingly strong in Patagonia, showing an acceleration after 1945, the last 3 decades being those of largest ice mass losses in Patagonia (*Foresta et al.*, 2018). Nevertheless, large uncertainty of the different methods impede giving the final exact trend of wastage. For instance, *Rignot et al.* (2003) proposed a very large wastage at the end of the $20^{th}$ century, whereas *Willis et al.* (2012b) proposed large wastage at the beginning of the $21^{st}$ century for SPI, but recent compilation of results summarized in *Foresta et al.* (2018) suggests that these extremely high values may have overestimated mass losses. Concerning NPI, the last decade could have been marked by the maximum rates of wastage (*Foresta et al.*, 2018), but again, this conclusion highly relies on how measurement uncertainties are considered in the different studies.

Because the mass balance of the icefield depends on (i) the exchange of mass at the upper free surface, i.e. the surface mass balance (SMB) and on (ii) calving glaciers which represent a direct mass loss to the ocean or lakes, below, I review the literature on SMB and dynamical changes for both icefields. Indeed, the ice flow dynamics control the mass redistribution from the accumulation area to the ablation area, and is crucial for determining the calving flux of glaciers.

### 1.3.4 Surface mass balance changes

The glacier-wide SMBs of different glaciers in Patagonia have been estimated from interpolation of in-situ measurements, from parameterizations such as positive degree day models or from more complex models that reproduce the processes involved in SMB and surface energy balance variations. The last two approaches rely on atmospheric variable inputs that are generally obtained with downscaling methods. Here, I first present the different methodologies used for SMB estimations and then I present the results for NPI and SPI.

There are very few in-situ SMB measurements available over NPI and SPI. The existing data are mainly located in the ablation area of very few glaciers, leading to a large uncertainty in the mean glacier-wide SMB. This justifies why authors rely on downscaling approaches and SMB models of various complexity in order to compute the SMB at the scale of the icefields (*Koppes et al.*, 2011; *Schaefer et al.*, 2013, 2015; *Lenaerts et al.*, 2014; *Mernild et al.*, 2016a).

The SMB of NPI has been previously estimated using different modelling approaches, but results from *Schaefer et al.* (2013) are generally taken as a reference. In their approach, first, the Weather Research and Forecasting (WRF) regional circulation model at 5 km resolution was forced with the NCAR/NCEP reanalysis over the period 2005-2011. These results were then used to build a statistical downscaling method to give regional scale temperature, precipitation and incoming solar radiation over a longer time period (1975-2011). Finally, a 1-D surface mass-balance model based on a degree-day approach was applied with a 0.45 km resolution at the scale of the icefields. The downscaling approach has been validated using data from 16 weather stations located at low elevations ($<$ 427 m a.s.l.) around the icefield. The modeled mean SMB of the entire NPI was calibrated using geodetic MB data from the three largest non-calving glaciers (HPN-1, HPN-4 and Exploradores) and with punctual SMB measurements. These three glaciers presented negative mass balance which were quite well captured by the model. However, they have small accumulation areas and they are not necessarily representative of glaciers presenting a large area on the plateau where most of the accumulation in NPI and SRG takes place. The point SMB measurements were given by 18 ablation stakes below 1200 m a.s.l. (*Ohata*

*et al.* (1985b) and taken by Centro de Estudios Científicos (CECs, Valdivia, Chile), and two values from the accumulation area obtained from shallow firn cores (*Yamada*, 1987; *Matsuoka and Naruse*, 1999). Thus, in general the model results were not well calibrated in the accumulation zone.

Other studies for SPI presented the same uncertainty. For instance, using the same methodology as *Schaefer et al.* (2013), *Schaefer et al.* (2015) computed the SMB of SPI and compared point surface mass-balance with available field data. In the ablation zone, they used a network of ablation stakes implanted on the Perito Moreno glacier between 1995 and 2003 (*Stuefer et al.*, 2007). In the accumulation zone they used data from a tower installed on Chico glacier near the ELA between 1994 and 2002 (*Rivera*, 2004) and SMB estimates from firn cores drilled in four glaciers: Moreno, Tyndall, Chico and PioXI glaciers (*Aristarain and Delmas*, 1993; *Shiraiwa et al.*, 2002; *Schwikowski et al.*, 2006, 2013, respectively). Their estimated SMB were very similar to punctual observation except in two places, where their results were largely exceeding field values. They assumed that the disagreement was due to wind transport of snow.

In another study, *Lenaerts et al.* (2014) used the regional atmospheric climate model RACMO2 forced with the ERA-Interim reanalysis to simulate the climate and SMB of the Patagonian Icefields. They used a 5.5 km resolution and simulated the period from 1979 to 2012. To validate the model, they used precipitation, temperature and wind data from 16 weather stations located in the valleys. The SMB values were validated using punctual accumulation from 2 firn cores from NPI and 5 firn cores from SPI. Comparison with precipitation data showed an overestimation at the western side of the icefield. The SMB average estimation over the whole period were similar to those from firn cores with the exception of 2 sites: on Nef glacier (NPI) the model underestimated the SMB whereas it overestimated it on Moreno glacier (SPI).

Finally, *Mernild et al.* (2016a) used a modeling approach over the entire Andes using SNOWMODEL (*Liston and Elder*, 2006a). In their study, they focused in particular on the NPI and the SPI during the period 1979/80–2013/14. They downscaled the MERRA reanalysis to a 1 km resolution, using an interpolation based on lapse rates with MicroMet, a module from SNOWMODEL (*Liston and Elder*, 2006b; *Mernild et al.*, 2016b). Validation of the model was made using annual SMB values from 7 glaciers from the entire Andes, but only one glacier was located in the Patagonian region (with only 3 years of data). The results showed that the model performances were of reasonable quality, with a determination coefficient $R^2$ of 0.72 and a RMSE of 0.38 m w.e.a$^{-1}$ for the studied sites. The SMB estimated in the Northern Andean region was compared with the results from *Gardner et al.* (2013), showing a good agreement. They also compared the snow cover extent and duration with data given by MODIS products in the southern central Andes

(30°S–40°S), and with individual direct observations of snow depth and densities from the central Andes (30°S–37°S) (*Mernild et al.*, 2016b,c). The validation from these snow variables allowed the authors to assume that there was no significant difference between their model and the observations along the Andes.

#### 1.3.4.1 Surface mass balance of NPI

Over NPI, all studies found very high precipitation and accumulation that result in positive SMB with a small increasing trend (see Table 1.5). In the following, to compare the studies, values in Gt $a^{-1}$ have been converted to m w.e. $a^{-1}$ using an icefield area of 3953 $km^2$ (*Rivera et al.*, 2007).

*Schaefer et al.* (2013) obtained an average annual precipitation between 1975 and 2011 of 8.03±0.37 m w.e. $a^{-1}$ and a total snow accumulation of 4.02 m w.e. $a^{-1}$ over the icefield. Their results showed very high accumulation values of more than 15 m w.e. $a^{-1}$ over the highest zones and a maximum of 24 m w.e. $a^{-1}$ on the peak of Mount San Valentín. On the plateaus of San Rafael and San Quintin glaciers, the estimated accumulation was between 2 and 5 m w.e. $a^{-1}$. The maximum ablation at the front of the glacier was higher than 14 m w.e. $a^{-1}$ whereas it reached 2 to 4 m w.e. $a^{-1}$ on the plateau of San Rafael and San Quintin Glaciers. The SMB on the plateau of NPI was between 2 and 3 m w.e.$a^{-1}$. Over the whole icefield, they found a SMB of 0.21 m w.e. $a^{-1}$ between 2000 and 2009. They found an increasing trend of the annual SMB from the 1970s to the 2000s, mainly due to an increase in accumulation. They explain the increased observed mass loss of NPI between 1975-2000 (*Rignot et al.*, 2003) and 2000-2009 (*Willis et al.*, 2012a) as a consequence of an increase in calving rates. They estimated that calving mass losses increased from 1.78±0.24 $km^3$ $a^{-1}$ between 1975 and 2000, to 3.76±0.44 $km^3$ $a^{-1}$ between 2000 and 2009.

Similarly, *Lenaerts et al.* (2014)'s model results showed very high precipitation with a maximum of more than 10 m w.e. $a^{-1}$. This resulted in a very high glacier-wide SMB of approximately 8 Gt $a^{-1}$ for NPI, much higher than in other studies. The SMB showed a weak positive (insignificant) trend related to a slight atmospheric cooling.

Finally, *Mernild et al.* (2016a) estimated an average precipitation of 6.95±0.34 m w.e. $a^{-1}$ and an average snow accumulation of 3.12±0.15 m w.e. $a^{-1}$ over NPI. The percentage of snow occurrences reached 52% (over the whole icefield). A slight insignificant cooling and a decrease in precipitation were found, in concordance with *Lenaerts et al.* (2014) but opposite to *Schaefer et al.* (2013). However, their results of runoff and ablation had a small trend (-0.05 m w.e. $a^{-2}$). The 35-year mean annual glacier-wide SMB was 0.14±0.49 m w.e. $a^{-1}$ with a small increasing trend.

Table 1.5: NPI SMB from literature.

| Source | Period | SMB (Gt $a^{-1}$) | SMB (m w.e. $a^{-1}$) |
|---|---|---|---|
| *Schaefer et al.* (2013) | 2000-2009 | 0.83* | 0.21 |
| *Lenaerts et al.* (2014) | 1979-2012 | ~8.00** | - |
| *Mernild et al.* (2016a) | 1979/80–2013/14 | 0.55 | 0.14 |

*converted to Gt $a^{-1}$ using 3959 $km^2$ as surface area (*Rivera et al.*, 2007)
**estimated from fig. 11 in *Lenaerts et al.* (2014)

#### 1.3.4.2 Surface mass balance of SPI

Estimations of the SMB of SPI from all studies are much more positive than for NPI with higher precipitation and accumulation amounts (see Table 1.6). *Schaefer et al.* (2015) estimated a very high accumulation of more than 20 m w.e. $a^{-1}$ in the highest zones of SPI. On the plateau their SMB was between 0 to 5 m w.e. $a^{-1}$ and values decreased below -15 m w.e. $a^{-1}$ at the front of the glaciers. They obtained a glacier-wide surface mass gain of 24.93 Gt $a^{-1}$ (equal to a volume gain of 27.7 $km^3$ $a^{-1}$, using ice density of 900 kg $m^3$), with a high interannual variability and an increasing trend (0.054 ± 0.012 m w.e. $a^{-2}$). Their average glacier wide SMB was 2.24 m w.e. $a^{-1}$, with an accumulation of 4.87 m w.e. $a^{-1}$ and an ablation of 2.63 m w.e. $a^{-1}$. The percentage of solid precipitation was 59% with a total precipitation of 8.36 m w.e. $a^{-1}$. They compared their SMB results with the mass loss given by *Rignot et al.* (2003) and *Willis et al.* (2012b) over 1975 - 2000 (16.7 ± 0.9 $km^3$ $a^{-1}$) and 2000-2012 (21.2 ± 0.4 $km^3$ $a^{-1}$) respectively. They explained that the increasing trend in the mass loss of SPI was due to an increase of the calving flux, from 44.4 $km^3$ $a^{-1}$ to 61.3 $km^3$ $a^{-1}$ between 1979 - 2000 and and 2000-2011.

*Lenaerts et al.* (2014)'s model results also showed very high precipitation with a maximum of 30 m w.e. $a^{-1}$, and a very high glacier-wide surface mass gain value around 55 Gt $a^{-1}$, also higher than the other studies. A similar positive trend was also found as in NPI, in agreement with the other studies.

Finally, precipitation given by *Mernild et al.* (2016a) was of 8.13±0.33 m w.e. $a^{-1}$, leading to an accumulation of 4.35±0.21 m w.e. $a^{-1}$ with snow occurrence in 55% of the cases (over the whole icefield). The slight cooling and precipitation decrease found in NPI was found to extend until SPI. Runoff and ablation trends were also small (-0.06 m w.e. $a^{-2}$). The 35-year glacier wide SMB was 1.78±0.36 m w.e. $a^{-1}$ with a small increasing trend of 0.10-0.11 m w.e. $a^{-2}$.

Similar to NPI, *Schaefer et al.* (2015); *Lenaerts et al.* (2014); *Mernild et al.* (2016a) are in concordance in writing that a positive trend was visible over SPI, but they did not relate it to the same reason. While, *Schaefer et al.* (2015) found an increase in

accumulation (precipitation), *Lenaerts et al.* (2014) and *Mernild et al.* (2016a) found a slight atmospheric cooling. *Mernild et al.* (2016a) proposed the occurrence of a slight decrease in precipitation. These differences are probably caused by the different forcings used by the studies.

Table 1.6: SPI SMB from literature.

| Source | Period | SMB (Gt $a^{-1}$) | SMB (m w.e. $a^{-1}$) |
|---|---|---|---|
| *Schaefer et al.* (2013) | 1979-2012 | 24.93* | 2.24 |
| *Lenaerts et al.* (2014) | 1979-2012 | 55.00** | 4.23 |
| *Mernild et al.* (2016a) | 1979/80–2013/11 | 23.14 | 1.78 |

*converted to Gt $a^{-1}$ using 13000 $km^2$ as surface area (*Rignot et al.*, 2003) and using an uniformed density of 900 kg $m^{-3}$
** estimated from fig. 11 in *Lenaerts et al.* (2014)

#### 1.3.4.3 Surface mass balance of San Rafael glacier

Over SRG, two estimations of the surface mass balance exist (see Table 1.7). *Schaefer et al.* (2013) suggested that it was strongly positive (1.6 m w.e. $a^{-1}$ ) and with an increasing trend between 1975 and 2011. At the glacier snout, point surface mass balance was -14.3 m w.e. $a^{-1}$, whereas the maximum was found at the top of the San Valentin peak with 20.8 m w.e. $a^{-1}$. The mean ELA was found to lie at 1203 m a.s.l. The very high accumulation at the San Valentin peak disagrees with the drastically lower values obtained through an ice core (0.2 m w.e. $a^{-1}$ *Vimeux et al.*, 2008). However, the mean accumulation given by the ice core may be site specific, and affected by wind transport. But the very high accumulation obtained by *Schaefer et al.* (2013) is not constrained by any measurement. They compared the SMB with the mass balance estimated by *Willis et al.* (2012a) and obtain a value of 1.85±0.13 $km^3$ $a^{-1}$ for calving losses between 2000 to 2009.

*Koppes et al.* (2011) also estimated the SMB of SRG between 1960-2005 using a downscaling of the NCEP/NCAR reanalysis based on correlations between reanalysis data and daily precipitation and temperature measured by a weather station installed on the shores of Laguna San Rafael, approximately 7 km from the glacier front. To reconstruct the temperature profile over the entire glacier they used daily lapse rates computed from the NCEP/NCAR reanalysis. For precipitation, they used the corrected precipitation and an orographic enhancement factor estimated from a simplified 1-D orographic precipitation model (*Smith and Barstad*, 2004b; *Roe*, 2005b). The ablation was estimated using a PDD model calibrated for ice with ablation stakes measurements from *Ohata et al.* (1985b) and a PDD factor for snow estimated by *Hock* (2003). Hence, as in the previous study, the

model was only calibrated in the ablation zone. They proposed a positive glacier-wide surface mass gain of 0.64 Gt $a^{-1}$ for the entire period (1960-2005) with three sub-periods of very positive (1.26 Gt $a^{-1}$ in 1960-1976), negative (-0.26 Gt $a^{-1}$ in 1977-89) and positive (0.71 Gt $a^{-1}$ in 1990-2005) SMB values. Their SMB has a negavite trend asociated to an increase in ablation and a decrease in accumulation in the second period, and a decrease in accumulation in the last one. The value during the entire period (1960-2005) is much smaller than the estimation from *Schaefer et al.* (2013). Their punctual SMB increases from approximately -16.2 m w.e. $a^{-1}$ at sea level to a maximum of 7.8 m w.e. $a^{-1}$ at 1800 m a.s.l. Above this maximum, punctual SMB decreases to 3 m w.e. $a^{-1}$ at 4000 m a.s.l. The punctual SMB decrease above a certain altitude is a more realistic approach than continuous increase in accumulation, because the precipitable water content in the air is limited. This punctual SMB decrease at high altitudes is the main difference with *Schaefer et al.* (2013) and the reason for lower glacier-wide SMB.

Table 1.7: SRG SMB from literature.

| Source | Period | SMB (Gt $a^{-1}$) | SMB (m w.e. $a^{-1}$) |
|---|---|---|---|
| *Schaefer et al.* (2013) | 1975-2011 | 2.18* | 1.60 |
| *Koppes et al.* (2011) | 1960-2005 | 0.64* | 0.86 |

* converted to Gt $a^{-1}$ using 735 $km^2$ as surface area (*Mouginot and Rignot*, 2015) and using an uniformed density of 900 kg $m^{-3}$

#### 1.3.4.4 Conclusions on Surface mass balance values

The very few in-situ SMB measurements available over the icefields and the data from weather stations at low altitudes were systematically used for all the studies, but modeling approaches rely only on data from the ablation area, with no constraint in the accumulation zone. Due to the large uncertainty in model calibration, mean glacier-wide SMB results present very different values and trends. Nevertheless, *Koppes et al.* (2011) pointed out that constraining accumulation estimations leads to lower values in the accumulation zone and more realistic final glacier-wide SMB values.

### 1.3.5 Dynamical changes

Glacier dynamics drives the calving flux (CF) and ice discharge (D), which can be a significant part of the total mass balance of glaciers (*Cuffey and Paterson*, 2010). As Patagonian Icefields are mainly composed of calving glaciers (82.0% and 98.6% of the surface for NPI and SPI, respectively), CF and D can be important in the icefields. Here, I present the surface velocities to describe the icefield dynamics and a summary of

CF estimations. The objective is to summarize available information on the dynamical changes that can have driven the mass balance changes of the Patagonian Icefields.

The ice discharge, D, is the ice mass flux through a given glacier cross section, often close or at the terminus. Calving is the process by which ice is lost by breaking into pieces at the front. In practice, calving is often used to design the total ablation at the front, including subaerial melting. For a fixed front position, the calving flux exactly compensate the ice discharge, while lower (resp. larger) calving fluxes induce an advance (resp. retreat) of the front. CF and D are sometimes used indifferently and difficult to distinguish in the literature.

Normally, frontal velocity and calving velocity of tidewater calving glaciers are about one order of magnitude greater than those in freshwater calving glaciers (*Warren et al.*, 1995; *Funk and Rothlisberger*, 1989). For NPI, the only tidewater calving glacier (SRG), presents the highest velocities (>7 km $a^{-1}$) of all the glaciers of this icefield. The freshwater calving glaciers present maximum velocities below 2 km $a^{-1}$ (*Willis et al.*, 2012a; *Mouginot and Rignot*, 2015) and among them more than half present velocities below 0.5 km $a^{-1}$ (*Mouginot and Rignot*, 2015). SRG did not show changing velocities at 1-9 km upstream from the front between 2000-2012. However, close to the front very large variations in velocities are present, even if no clear trend can be displayed (*Willis et al.*, 2012a; *Mouginot and Rignot*, 2015), see Fig.1.8. In the case of freshwater calving glaciers, some of them showed accelerations, probably related to surges and frontal lake formation as for San Quintin Glacier. Other glaciers showed more stable velocities (*Willis et al.*, 2012a; *Mouginot and Rignot*, 2015).

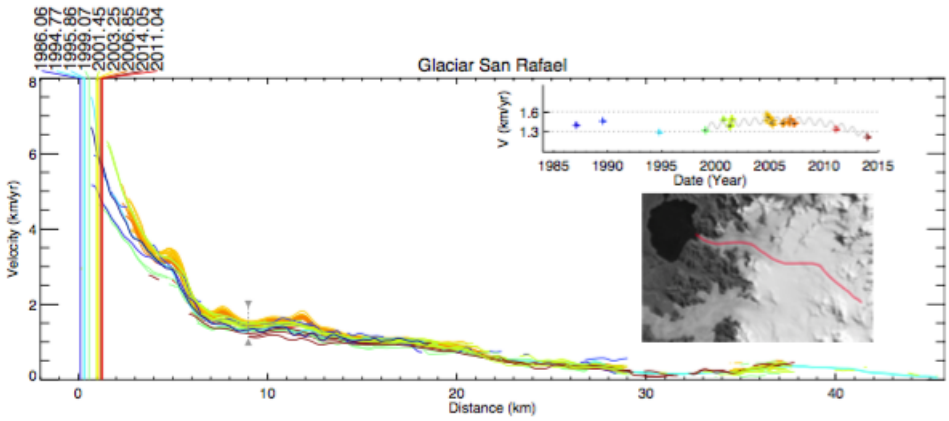


Figure 1.8: San Rafael glacier velocity from *Mouginot and Rignot* (2015) (Fig. S1). Velocities correspond to flow speed along the flow line (red line), with colors blue to red corresponding to 1984 to 2014. The vertical lines indicate the position of the terminus with time. The inset displays the speed versus time at the the grey dashed line location on the main plot.

The highest velocities on SPI correspond to calving glaciers and particularly to tidewater calving glaciers located along the west side of the icefield (*Sakakibara and Sugiyama*,

2014; *Mouginot and Rignot*, 2015). The fastest glaciers are Penguin and Europa glaciers, which have maximum estimated velocities of 10.3 and 8.8 km $a^{-1}$, respectively (*Mouginot and Rignot*, 2015). The estimated velocities of the different glaciers of SPI presented different trends with time. Indeed, *Sakakibara and Sugiyama* (2014) found that 6 glaciers presented stable velocities, 6 glaciers accelerated, and 16 glaciers decelerated during the last 3 decades (1984-2011).

CF and D over long periods are difficult to estimate due to limited velocity data and ice thickness data at the front, and due to the uncertainty in these data. Estimations from the literature are given in Table 1.8 (*Naruse et al.*, 1995; *Warren et al.*, 1995; *Rignot et al.*, 1996; *Warren et al.*, 2001; *Koppes*, 2007; *Koppes et al.*, 2011). In addition, in this study, I provide new estimates of CF for each SPI glacier computed as the average calving velocity times the frontal area. The data used correspond to surface velocity data from *Gourlet et al.* (2016), glacier retreat velocity from *Casassa et al.* (2014) and *Mouginot and Rignot* (2015) and frontal area from the bathymetry given by from the Chilean Navy Hydrographic and Oceanographic Service.

Calving flux estimations are very variable ranging from 0.06 $km^3$ $a^{-1}$ to 3.34 $km^3$ $a^{-1}$ depending on the glaciers. The estimations show smaller CF for freshwater calving glaciers than tidewater calving glaciers as expected. Freshwater CF are within 0.06-2.41 $km^3$ $a^{-1}$ with an average of 0.7 $km^3$ $a^{-1}$. Meanwhile, the estimations of tidewater calving fluxes are between 0.73-2.22 $km^3$ $a^{-1}$ with and average of 1.8 $km^3$ $a^{-1}$. For each glacier, CF estimations have important dispersion. For SRG, CF estimations present variations that exceed 49% even for the same year. These differences among estimations can be related to surface velocity variations or uncertainty in the methods. The average estimation of the CF of SRG is 1.68 $km^3$ $a^{-1}$, much larger than the only estimation available for Nef glacier (0.2 $km^3$ $a^{-1}$) which is a freshwater calving glacier at the east of NPI.

A rough estimation of total calving in the NPI can be made using the average calving flux estimation weighted by tidewater and freshwater calving areas. The result is a NPI total calving of 5.6 $km^3$ $a^{-1}$. On SPI, the CF was estimated even where no water depth measurements were available at the front of glaciers. Here, I roughly assume that the frontal ice height below the surface of water was uniform and equal to 300 m and that the height above the water surface was uniform and equal to 50 m (*Schaefer et al.*, 2015). Given these rough assumptions, the total calving flux estimated for the SPI is 11.2 $km^3$ $a^{-1}$. NPI has a CF 50% lower than SPI which seems reasonable taking into account the differences in total surface area of the icefields, and the difference calving glaciers surface area between both icefields.

Table 1.8: NPI Ice discharge estimations.

| Source | Glacier | Icefiel | Type* | CF($km^3$ $a^{-1}$) | Period |
|---|---|---|---|---|---|
| *Warren et al.* (1995) | SGR | NPI | tw | 0.73 | 1993, 1994 |
| *Rignot et al.* (1996) | SGR | NPI | tw | 1.43 | 1994 |
| *Koppes* (2007) | SGR | NPI | tw | 0.75 | 2005, 2006 |
| *Koppes et al.* (2011) | SRG | NPI | tw | 1.49 | 2001 |
| *Koppes et al.* (2011) | SRG | NPI | tw | 1.79 | 1994 |
| *Koppes et al.* (2011) | SRG | NPI | tw | 3.34 | 1983 |
| *Koppes et al.* (2011) | SRG | NPI | tw | 2.22±0.05 | 2007 |
| *Warren et al.* (2001) | Nef | NPI | fw | 0.2 | 1998 |
| *Warren and Aniya* (1999) | upsala (east) | SPI | fw | 0.14 | 1992/93 |
| *Naruse et al.* (1995) | upsala (west) | SPI | fw | 0.8-1.4 | 1990 |
| *Schaefer et al.* (2015) | Upsala (2 fronts) | SPI | fw | 2.41 0.40 | 2004 |
| this study | Upsala (2 fronts) | SPI | fw | 0.81-0.49 | 1980-2007 |
| *Naruse et al.* (1995) | Perito Moreno | SPI | fw | 0.5-1.0 | 1990 |
| *Schaefer et al.* (2015) | Perito Moreno | SPI | fw | 0.44±0.16 | 2004 |
| *Schaefer et al.* (2015) | Jorge Montt | SPI | tw | 1.20±0.54 | 2004 |
| this study | Jorge Montt | SPI | tw | 2.08-1.20 | 1980-2007 |
| this study | Occidental | SPI | fw | 0.09-0.29 | 1980-2007 |
| this study | Viedema | SPI | fw | 0.34-0.31 | 1980-2007 |
| this study | Grey | SPI | fw | 0.06 | 2000-2007 |
| this study | Tyndall | SPI | fw | 0.09 | 2000-2007 |
| *Schaefer et al.* (2015) | Tyndall | SPI | fw | 0.14 0.08 | 2004 |
| *Schaefer et al.* (2015) | O'Higgins | SPI | fw | 1.78±0.52 | 2004 |
| *Schaefer et al.* (2015) | Pio XI | SPI | fw-tw | 2.69±1.71 | 2004 |

* fw is fresh water calving type and tw is tide water calving type

## 1.4 Conclusions and link with next chapters

The mass loss of the Patagonian icefields showed an increasing trend between 1945 and 2017. This trend is currently not consistent with the stable or increasing SMB estimated for SRG, NPI and SPI during the last decades (1979-2011). However, due to the large uncertainties on SMB estimation in Patagonia it is unclear whether SMB and MB trend differences were real or resulting from MB and SMB uncertainties.

On the other hand, the estimated calving flux, which can be significant for the Patagonian icefields, is still very uncertain. Calving loss trends are very difficult to assess and predict because they not only depend on climatic conditions but also on basal topography.

The possible causes of the increasing mass losses are the increase in calving fluxes or glacier mass adaptation to a long term SMB decrease prior to the beginning of recent reanalysis data (ERA-Interim). A long term decrease in SMB can be associated to climatic changes which are still unclear in the literature, even though the drying trend in the northern part of Patagonia and the warming trend in Tierra del Fuego and east Patagonia would agree with these speculations on SMB long term variations. However, no clear trend was visible in west Patagonia, and still, the changes should have occurred before 1979.

Therefore, direct causes of actual glacier wastage acceleration remain unclear due to the lack of data and observation in the region. In the next chapters, I will estimate SMB and ice discharge of SRG and NPI thanks to a new physical modeling approach. Then I will try to link climate variations with those of the different components of MB. For this task, the study first focuses on SRG ice flow modeling to estimate SRG SMB and D, in order to retrieve a SMB value that agrees with glacier D and MB during the last decade. Finally, I will use regional atmospheric modeling to estimate the SMB of SRG and NPI, and I will analyse the different relationships between SMB and climatic variations.

# Chapter 2

# San Rafael Glacier SMB and D from ice flow modeling

This chapter corresponds to the article "Ice flow modelling to constrain the surface mass balance and ice discharge of San Rafael Glacier, Northern Patagonia Icefield" published in *Journal of Glaciology*, vol. 64, issue 246, August 2018, p. 568-582

**Ice flow modelling to constrain the surface mass balance and ice discharge of San Rafael Glacier, Northern Patagonia Icefield**

G. Collao-Barrios[1], F. Gillet-Chaulet[1], V. Favier[2], Gino Casassa[2 3], E. Berthier [4], I. Dussaillant [4], J. Mouginot [1 5] and E. Rignot [5 6].

[1] Univ. Grenoble Alpes, CNRS, IRD, Grenoble INP, IGE, F-38000 Grenoble, France

[2] Geoestudios, Las Vertientes, Chile

[3] Universidad de Magallanes, Punta Arenas, Chile

[4] CNRS, LEGOS, Université de Toulouse, Toulouse, France

[5] Dept. Earth System Sciences, University of California Irvine, Irvine, CA, USA

[6] Jet Propulsion Laboratory, California Institute of Technology, Pasadena, California, USA

## Abstract

We simulate the ice dynamics of the San Rafael Glacier (SRG) in the Northern Patagonia Icefield (46.7°S, 73.5°W), using glacier geometry obtained by airborne gravity measurements. The full-Stokes ice-flow model (Elmer/Ice) is initialized using an inverse method to infer the basal friction coefficient from a satellite-derived surface velocity mosaic. The high surface velocities (7.6 km $a^{-1}$) near the glacier front are explained by low basal shear stresses (<25 kPa). The modelling results suggest that 98% of the surface velocities are

due to basal sliding in the fast-flowing glacier tongue (>1 km $a^{-1}$). We force the model using different surface mass balance scenarios taken or adapted from previous studies and geodetic elevation changes between 2000-12. Our results suggest that previous estimates of average surface mass balance over the entire glacier ($\dot{B}$) were likely too high, mainly due to an overestimation in the accumulation area. We propose that most of SRG imbalance is due to the ice discharge (-0.83±0.08 Gt a-1) and a slightly positive $\dot{B}$ (0.08±0.06 Gt $a^{-1}$). The committed mass-loss estimate during the next century is -0.34±0.03 Gt $a^{-1}$. This study demonstrates that surface mass-balance estimates and glacier wastage projections can be improved using a physically based ice-flow model.

## 2.1 Introduction

Patagonia is the largest ice-covered region in the Southern Hemisphere outside of Antarctica (*Rignot et al.*, 2003). Most of the ice is locked in two main icefields: the Northern Patagonia Icefield (NPI 3976 $km^2$) and the Southern Patagonia Icefield (SPI 13219 $km^2$) (*Davies and Glasser*, 2012). Most Patagonian glaciers have been losing mass and retreating for the last 40 years (*Aniya*, 1999; *Lopez et al.*, 2010; *Casassa et al.*, 2014). Estimations of total mass balance from different sources confirm the acceleration of mass losses in the last decades compared to mean value over the entire period since the Little Ice Age to present (*Rignot et al.*, 2003; *Glasser et al.*, 2011; *Jacob et al.*, 2012).

The NPI is located between 46.5°S and 47.5°S. It is under the influence of the westerlies (*Garreaud et al.*, 2009) and climate settings are largely influenced by the Southern Annular Mode (SAM) (*Thompson and Wallace*, 2000; *Garreaud et al.*, 2012). The westerly flow transports large amounts of moisture from the southern Pacific Ocean towards the continent. Air parcels are lifted upwards by convection over the Andes entailing orographic precipitation, leading to high precipitation with strong W-E gradients (*Carrasco et al.*, 2002; *Garreaud et al.*, 2012). NPI's climate is thus temperate and very humid, with precipitation exceeding 10 m w.e. in the highest zone (*Garreaud et al.*, 2012). The equilibrium line altitude (ELA) is located around 950 to 1300 m above sea level (a.s.l.) (*Rivera et al.*, 2007). This elevation band comprises a flat and vast plateau, making the icefield surface mass balance particularly sensitive to shifts in the ELA in response to changes in temperature and accumulation. The NPI is formed by 140 units in the RG inventory, including 38 main glaciers of different terminus types: one tidewater calving glacier (San Rafael Glacier (SRG) covering 18% of the total surface area), eighteen fresh water calving glaciers (64% of the total surface area) and nineteen land-terminating glaciers (18% of the surface area) (*Rivera et al.*, 2007; *Willis et al.*, 2012a, and Randolph Glacier Inventory). A recent ice velocity mosaic reveals that fast flow regions extend far into the plateau and

accumulation area, making the icefield also potentially sensitive to dynamical changes (*Mouginot and Rignot*, 2015).

This study focuses on SRG, located in the north-western part, and the largest glacier of NPI with an area of 734 km$^2$ (Fig. 2.1). It covers the entire altitude range of the NPI: the highest point of the glacier catchment is the San Valentin peak at 4032 m a.s.l. (*Vimeux et al.*, 2008) and it ends at sea level in the Laguna San Rafael. Laguna San Rafael is connected to the Pacific Ocean through Tempanos River and Elefantes Fjord. From remotely sensed snowlines and surface mass balance modelling studies, the ELA has been estimated between 905 and 1295 m a.s.l. (*Aniya*, 1988; *Rignot et al.*, 1996; *Rivera et al.*, 2007; *Koppes et al.*, 2011; *Schaefer et al.*, 2013). SRG is among the fastest glaciers in the world with frontal velocities exceeding 7 km a$^{-1}$ (*Mouginot and Rignot*, 2015; *Willis et al.*, 2012a). The terminus position has retreated by more than 10 km since the end of the Little Ice Age in 1870. Since 1990 the retreat has slowed down and since the early 2000's the terminus has been maintained in a nearly stable position in a narrow 2 km wide valley (*Davies and Glasser*, 2012).

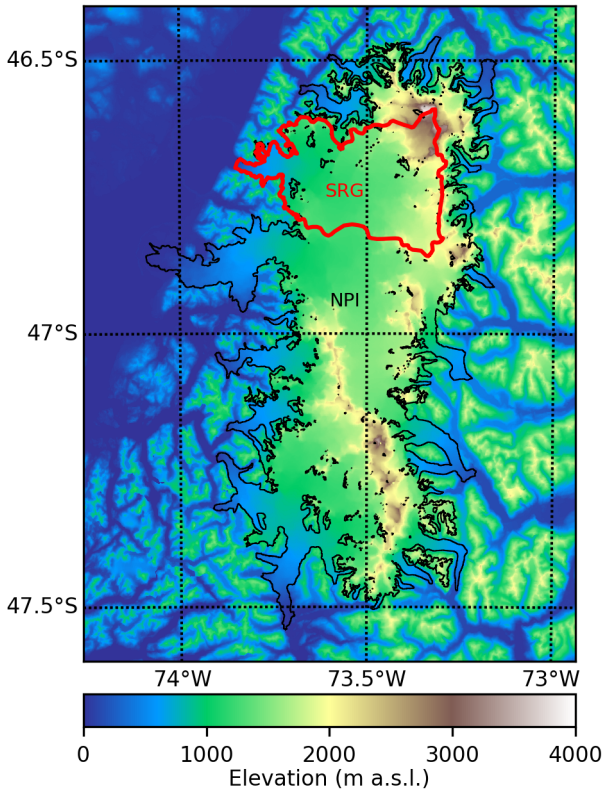


Figure 2.1: Map of the surface elevation of our study area. In black, the outline of the Northern Patagonia Icefield (NPI) from (*Rivera et al.*, 2007). In red, the outline of San Rafael Glacier (SRG) from *Mouginot and Rignot* (2015). Elevations from SRTM-2000. Datum WGS84.

Neglecting volume changes due to advance or retreat of the glacier front and melting at the base in contact with the bed, the total mass balance ($\dot{M}$) of a calving glacier results from the difference between the surface mass balance ($\dot{B}$) and the ice discharge ($\dot{D}$), i.e. $\dot{M} = \dot{B} - \dot{D}$. $\dot{M}$ and $\dot{D}$ can be estimated from remote sensing observations: the total mass balance can be derived from the volumetric change obtained from surface elevations changes measured, for example, by differencing Digital Elevation Models (DEMs). Between 2001 and 2011, SRG has been losing volume at a rate of -0.82±0.06 km$^3$ a$^{-1}$ (-4.06 ±0.11 km$^3$ a$^{-1}$ for the entire NPI) (*Willis et al.*, 2012a). The ice discharge is usually estimated by combining thickness and surface velocity observations. Using surface velocities derived from a 7-day interval pair of ASTER images in the austral fall 2007 and an estimate of the calving front vertical area (from bathymetry measurements *Koppes et al.*, 2011), *Willis et al.* (2012a) calculated $\dot{D}$ =-2.22 km$^3$ a$^{-1}$, a value 60% greater than previous estimates for 1994 (-1.7 km$^3$ a$^{-1}$) (Rignot and others, 1996). However, SRG surface velocities from *Mouginot and Rignot* (2015) do not show a clear temporal trend, except a slight deceleration (20%) after a maximum in 2005 (15% above the 1994 value), at 9 km from the front. $\dot{B}$ is usually estimated by downscaling reanalysis data with more or less complex models (*Koppes et al.*, 2011; *Schaefer et al.*, 2013; *Lenaerts et al.*, 2014). *Schaefer et al.* (2013) found a clearly positive $\dot{B}$ of 1.6 m w e. for 1979-2011. Using the catchment area (734 km$^2$) this corresponds to a $\dot{B}$ value of 1.17 km$^3$ a$^{-1}$ of ice, which is larger than the 0.71 km$^3$ a$^{-1}$ positive value of ice given by *Koppes et al.* (2011) for 1960-2005. *Schaefer et al.* (2013) and *Lenaerts et al.* (2014) suggest that $\dot{B}$ over the whole NPI has been increasing since the 1980's. *Koppes et al.* (2011) also found that $\dot{B}$ over SRG has increased from -0.29±0.21 km$^3$ a$^{-1}$ for the period 1977-89 to 0.79±0.41 km$^3$ a$^{-1}$ for the period 1990-2005. The increase in $\dot{B}$ seems in contradiction to the unabated rates of mass loss. Thus, these previous studies proposed that, the increasing $\dot{B}$ has been compensated by increased ice discharge. However, this is in contradiction with the lack of significant variations in observed velocities by *Mouginot and Rignot* (2015). Further, the absolute value of $\dot{B}$ and its temporal changes are poorly constrained for several reasons: 1) due to the remoteness of the area and the harsh climatic conditions, no long-term meteorological data close to the icefield are available to perform a rigorous climatic study, comprising the reliability of reanalysis products over Patagonia (*Nicolas and Bromwich*, 2011). Moreover, climatic trends in this region are largely impacted by assimilation of satellite datasets in 1979 (*Kistler et al.*, 2001a; *Uppala et al.*, 2005a). 2) Direct surface mass-balance measurements are scarce on NPI and particularly at high elevations (>1000 m a.s.l.) impeding a full validation of the accumulation simulated by the models.

Here we explore a new approach using a physically-based ice-flow model to constrain SRG surface mass balance. First, the model is calibrated using available data of surface

velocity and rate of surface elevation change for the period 2000-12. Then, running the model forward in time enables the selection of $\dot{B}$ values that are compatible with modelled ice fluxes. Finally, the model is used to simulate the diffusion of the observed thinning and to estimate the committed mass loss induced by the current glacier imbalance.

## 2.2 Data and previous estimations

### 2.2.1 Surface mass balance

In this section, we present the initial point surface mass balance functions ($\dot{b}$) used to force our ice-flow model. They are obtained from previous studies results (*Koppes et al.*, 2011; *Schaefer et al.*, 2013). First, we describe the methodology from these two studies, analyze their difference and uncertainties and compare with in-situ measurement available in the literature. Afterward we describe how we obtain the initial $\dot{b}$ functions and the additional function that we explore.

*Schaefer et al.* (2013) used the Weather Research and Forecasting (WRF) regional circulation model forced with data from the NCAR/NCEP reanalysis over the period 2005-2011. These results are used to build a statistical downscaling method to downscale the reanalysis from 1975-2011. Finally, a distributed mass-balance model with a degree-day approach was applied. The downscaling results (temperature, precipitation and incoming solar radiation) were validated with data from 16 weather stations located at low elevations ($<$ 427 m) around the icefield. The modelled mean surface mass balance of the entire NPI was calibrated using geodetic mass-balance data from the three largest non-calving glaciers (HPN-1, HPN-4 and Exploradores) and with point surface mass-balance measurements. These three glaciers presented negative $\dot{B}$ which were well captured by the model. However, these glaciers have small accumulation areas and they do not necessarily represent what happens in the plateau where most of the accumulation in NPI and SRG takes place. The point surface mass-balance measurements were given by 18 ablation stakes below 1200 m a.s.l. (*Ohata et al.* (1985b) and taken by Centro de Estudios Cientificos (CECs, Valdivia, Chile), and two values from the accumulation area obtained by analysing shallow firn cores (*Yamada*, 1987; *Matsuoka and Naruse*, 1999). Thus, in general the model results were not well calibrated in the accumulation zone. *Schaefer et al.* (2013) suggested that the $\dot{B}$ over NPI slightly increased between 1975 and 2011. During this period, the $\dot{B}$ of the San Rafael Glacier was strongly positive with a mean glacier-wide surface mass balance of 1.6 m w.e. $a^{-1}$ (1.19 $km^3$ $a^{-1}$ with ice density of 910 km $m^{-3}$). At the glacier snout, point surface mass balance was as negative as -14.3 m w.e. $a^{-1}$, whereas the maximum was found at the top of the San Valentin peak with

20.8 m w.e. $a^{-1}$. The mean ELA is found to lie at 1203 m a.s.l. The very high accumulation at the San Valentin peak however disagrees with the drastically lower values obtained through an ice core (0.2 m w.e. $a^{-1}$; *Vimeux et al.*, 2008). Even though the mean accumulation given by the ice core may be site specific, this difference between observation and model gives low confidence in the accumulation obtained by *Schaefer et al.* (2013) .

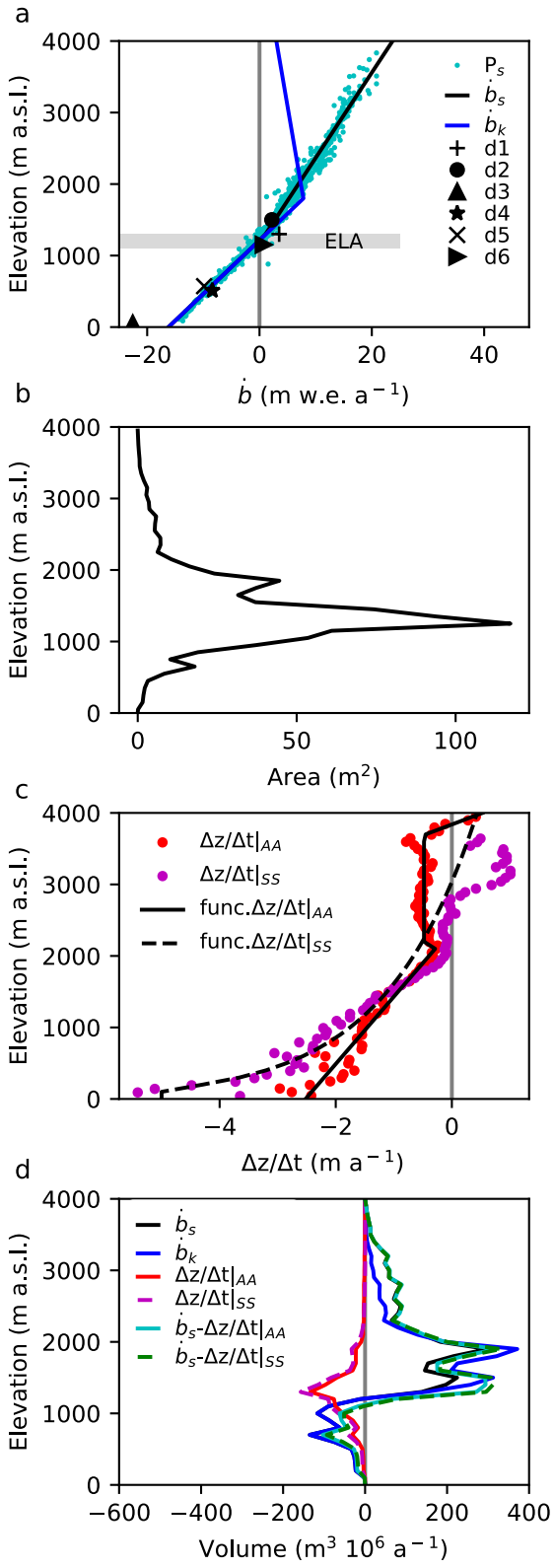


Figure 2.2: a) Distribution of the surface mass balance ($\dot{b}$) from different sources as a function of elevation. $P_S$ correspond to the point surface mass-balance model outputs from *Schaefer et al.* (2013) for SRG, $\dot{b}_s$ is a piece-wise linear regression to these data, $\dot{b}_k$ is mean surface mass balance function of SRG from *Koppes et al.* (2011), represented as a piece-wise linear function and obtain from their figure 8. d1 to d6 are the observed $\dot{b}$ on NPI and listed in Table 2.1. b) SRG hypsometry from the SRTM-2000. c) Surface elevation change in SRG from the two different space-borne geodetic methods (AA and SS, see text) and d) $\dot{b}$ functions and surface elevation changes expressed in volume according to elevation for the two different sources (AA and SS).

On the other hand, *Koppes et al.* (2011) estimated the $\dot{B}$ between 1960-2005 using a downscaling of NCEP/NCAR reanalysis data based on correlations between reanalysis data at a grid point and daily precipitation and temperature measured over one year by a weather station installed on the shores of Laguna San Rafael approximately 7 km from the glacier front. To reconstruct the temperature profile over the entire glacier they used daily lapse rates computed from NCEP/NCAR reanalyses. To reconstruct precipitation, they used the corrected precipitation and an orographic enhancement factor estimated from a simplified 1-D orographic precipitation model (*Smith and Barstad*, 2004b; *Roe*, 2005a). To estimate the ablation amounts, they used a PDD model calibrated for ice with the ablation stake measurements from *Ohata et al.* (1985a) and a PDD factor for snow estimated by *Hock* (2003). Hence, as in the previous study, the model was only calibrated in the ablation zone. They proposed a positive average $\dot{B}$ of 0.71 km$^3$ a$^{-1}$ for the entire period (1960-2005) with three sub-periods of very positive (1.4 km$^3$ a$^{-1}$ in 1960-76), negative (-0.29 km$^3$ a$^{-1}$ in 1977-89) and positive (0.79 km$^3$ a$^{-1}$ in 1990-2005) surface mass balance. The point surface mass balance as a function of surface elevation is shown in Fig. 2.2a; it increases from approximately -16.2 m w.e. a$^{-1}$ at sea level to a maximum of 7.8 m w.e. a$^{-1}$ at 1800 m a.s.l. Above this maximum, $\dot{b}$ decreases to 3 m w.e. a$^{-1}$ at 4000 m a.s.l. (estimated from *Koppes et al.*, 2011).

We compare the point surface mass-balance ($\dot{b}$) field measurements of SRG with these two model estimations: the average between 1975-2011 from *Schaefer et al.* (2013) and the average between 1960-2005 from *Koppes et al.* (2011). In the ablation zone, there is an agreement between measurements and models. However, in the accumulation zone, there is a lack of measurements and results from both studies present strong discrepancies (Fig. 2.2a and Table 2.1). *Koppes et al.* (2011) proposed a lower $\dot{B}$ than *Schaefer et al.* (2013) and took into account a maximum elevation above which the precipitation decreased. However, the lower $\dot{B}$ value in *Koppes et al.* (2011) was not only due to this maximum, but also to the hypsometry of SRG (Fig. 2.2b), and more particularly around the ELA (between 1000-1400 m a.s.l.), where most of the glacier area is concentrated (52% of the area).

Based on these earlier studies, we define two drastically different altitudinal distributions of $\dot{b}$ to force our ice-flow model of SRG. We use the mean annual mass balance function for the period 1960-2005 given by *Koppes et al.* (2011), to define the following functions:

$$\begin{aligned} \dot{b}_k(z_s) &= 0.013 z_s - 16.2 \quad if \quad z_s \leq 1800 \\ \dot{b}_k(z_s) &= -0.0022 z_s - 11.7 \quad if \quad z_s > 1800 \end{aligned} \tag{2.1}$$

From *Schaefer et al.* (2013), is approximated using two linear relationships, below and above the ELA, following the Area Altitude Balance Ratio method (*Osmaston*, 2005a). Using the averaged for the period 1975-2011 (see Fig. 2.2a), we use:

$$\begin{aligned} \dot{b}_s(z_s) &= 0.013 z_s - 16.2 \quad if \quad z_s \leq 1200 \\ \dot{b}_s(z_s) &= 0.0084 z_s - 11.7 \quad if \quad z_s > 1200 \end{aligned} \tag{2.2}$$

Both altitudinal distributions of $\dot{b}$ coincide in the ablation zone. While the values given by *Koppes et al.* (2011) and *Schaefer et al.* (2013), cover slightly different time periods, because they are averaged over period longer than 30 years, we expect that they are good approximation of a mean local climatology for the last decades. In addition to these two altitudinal functions of $\dot{b}$, we explored different surface mass-balance trends with elevation to find a function consistent with the initial ice-flow dynamics. As surface mass balance is well constrained below the ELA, we only vary the parametrisation in the accumulation zone.

### 2.2.2 Glacier geometry

The glacier hypsometric curve as given by the SRTM-2000 DEM is shown in Fig. 2.2b. The glacier has a uni-modal area distribution where most of the area is found in the plateau between 1000 and 2000 m a.s.l. The maximum of the area is at an altitude of 1250 m a.s.l., i.e. close to the ELA. The glacier drainage basin delineation is taken from *Mouginot and Rignot* (2015). They used their surface velocity data to define the ice divide over the plateau where the surface slope is too small to accurately define the divide.

The ice thickness and bedrock topography have been obtained from airborne gravity data (*Gourlet et al.*, 2016). The maximum estimated error is between 38 and 64 m over the NPI plateau and reaches 114 m in the narrow valleys.

### 2.2.3 Volume changes related to surface elevation change

The surface elevation change between 2000 and 2012 ($\Delta z_s/\Delta t$) is calculated with the geodetic method using either multiple ASTER DEMs (*Berthier et al.*, 2016) or by simple DEM differencing applied to a pair of SPOT5 and SRTM DEMs (*Gardelle et al.*, 2013) . Both results agree within errors bars with a mean volume change of -0.80±0.06 km$^3$ a$^{-1}$ and -0.92±0.07 km$^3$ a$^{-1}$, respectively. This is also consistent with the value of -0.82±0.06 km$^3$ a$^{-1}$ from *Willis et al.* (2012a) for the period 2001-2011. The rates of surface elevation changes averaged by 50 m altitude bands are shown in Fig. 2.2c. Data

are thereafter denoted according to their origin as $\Delta z_s/\Delta t|_{AA}$ for the multiple ASTER DEMs and $\Delta z_s/\Delta t|_{SS}$ for the pair of SPOT5 and SRTM DEMs. There is a good agreement between both datasets between 1000 and 2000 m a.s.l. where most of the SRG area lies, while the two datasets differ outside of this range. $\Delta z_s/\Delta t|_{AA}$ leads to lower thinning rates below 1000 m a.s.l., with a minimum of -2.5 m $a^{-1}$ close to the glacier front (-5.0 m $a^{-1}$ for $\Delta z_s/\Delta t|_{SS}$). They also show a slight trend to thinning in the upper reaches. However, due to the hypsometry of the glacier, the volume change is concentrated around 1200 m a.s.l. (Fig. 2.2d).

### 2.2.4 Surface velocities

Surface velocities are derived from SAR and Landsat satellite data using a speckle tracking algorithm, interferometric phase of ascending and descending tracks and feature tracking (*Mouginot and Rignot*, 2015). For best coverage, we use the velocity mosaic from imagery acquired between 1994 and 2014. The mosaic is mostly representative for the dynamic regime in 2004. As no significant trend has been observed in the surface velocities between 2000-12, we consider the mosaic representative for this time interval (Fig. 2.3a). The maximum uncertainty reported here is computed as the 1 sigma error of the distribution of absolute displacement in ice-free areas, and it is 52 m $a^{-1}$ for point velocities.

## 2.3 Methods

This section describes the methodology in two main steps: the ice-flow model initialisation and prognostic simulations. For the model initialisation, we first use an inverse method to constrain the distribution of basal friction using the observed surface velocities. Thereafter, we relax the model using an apparent surface mass balance using the observed surface elevation changes and different $\dot{b}$ functions. We discard the simulations for which the volume changes exceed the surface elevations changes uncertainty. Afterwards, we check that the simulated velocities and surface elevations changes are close to the observation. As the observations used to constrain the model have been collected mostly between 2000 and 2012, after the initialisation, we assume that the model state is representative of this period (study period). Finally, we run 100 years of prognostic simulations using constant forcing to estimate the committed mass loss induced by the initial model imbalance.

Table 2.1: Published point surface mass-balance measurements over the Northern Patagonia Icefield.

| Source | Notation Fig. 2.2a | Glacier | Date | Method | Elevation | b m w.e. $a^{-1}$ |
|---|---|---|---|---|---|---|
| *Yamada* (1987) | d1 | San Rafael leed side | 1985 | firn core stake | 1300 | 3.5 |
| *Matsuoka and Naruse* (1999) | d2 | NPI | 1997 | (winter accu.) | 1500 | 2.20 |
| *Ohata et al.* (1985a) | d3 | San Rafael | 1983 | stake | 50 | -22.57 |
| *CECs and DGA* (2012) | d4 | Nef | Jan-Aug 2012 | stake | 572 | -8.40 |
| *CECs and DGA* (2012) | d5 | Nef | Jan-Aug 2012 | stake | 511 | -9.86 |
| *Geoestudios and DGA* (2014) | d6 | San Rafael | 2013-2014 | stake | 1152 | 0.74 |

### 2.3.1 Model description

To model SRG flow-dynamics, we use the finite-elements full-Stokes three-dimensional ice-flow model Elmer/Ice. Details on the numerical methods and model capabilities can be found in *Gagliardini et al.* (2013). Hereafter, we briefly outline below the main assumptions used in our study.

To compute the velocity, $u = (u_i, u_j, u_k)$, we solve the 3D Stokes equations that comprise the conservation of linear momentum and mass. For the rheological law, we use the non-linear isotropic Glen's flow law, which links the deviatoric stress tensor $\tau$ with the strain-rate tensor $\dot{\epsilon}$ as follows:

$$\tau_{ij} = 2\eta\dot{\epsilon}_{ij} \tag{2.3}$$

The effective viscosity ($\eta$) is equal to:

$$\eta = \frac{1}{2}(A)^{-1/n}\dot{\epsilon}_e^{\frac{1-n}{n}} \tag{2.4}$$

where n is the Glen exponent (taken here equal to 3) and $\dot{\epsilon}_e = (\dot{\epsilon}_{ij}\dot{\epsilon}_{ji}/2)^{0.5}$ is the strain-rate second invariant. The rate factor A is a function of the temperature relative to the pressure melting point, following an Arrhenius Law. The values of all parameters are taken from *Cuffey and Paterson* (2010).

The ice temperature is 0°C over the entire ice column between the front and the ELA

(1200 m a.s.l. according to Schaefer and others, 2013). Above the ELA the thermal regime of the glacier is poorly constrained. Here we assume that the surface temperature varies linearly between 0°C at the ELA and -11.4°C at 3800 m a.s.l., in agreement with the only value given in the upper reaches (measured at 10 m depth by *Vimeux et al.*, 2008). We further assume that the ice temperature is uniform over the local ice column and correspond to the surface temperature. To assess the sensitivity of the model to this assumption we ran several initialization experiments assuming either that the glacier is temperate everywhere or that the temperature is the steady-state solution of the heat equation, with prescribed geothermal heat flux at the bottom boundary and temperature at the upper surface. In agreement with *Seroussi et al.* (2013), we found that the model is weakly sensitive to the thermal regime in the upper zone. The results from all simulations represent the observed velocities with similar accuracy.

The 2D footprint of the model domain, delineated by the red polygon in Fig. 2.1, is meshed using the anisotropic mesh adaptation software Yams (*Frey and Alauzet*, 2005). We use the geometric error estimate given by *Frey and Alauzet* (2005), which provides an upper bound for the interpolation error of a continuous field into piecewise linear elements. This error depends on the second spatial derivatives. The element size is then adjusted to equi-distribute the error over the whole domain. Here we use the observed surface velocities as the reference to estimate the error. The mesh resolution in 2D ranges from 50 m to 500 m. The 2D mesh is then vertically extruded between the bottom and top surfaces using five layers. The thickness of the layer follows a geometric progression. The layer below the surface is two times thicker than the bottom layer. The ice thickness and the bedrock topography of the glacier are taken from *Gourlet et al.* (2016). The surface topography is estimated as the bottom topography plus the ice thickness.

We distinguish four different types of boundary conditions:

(1) At the bottom surface, the ice is in contact with the bed and we apply a linear friction law that relates the tangential basal shear stress ($\tau_b$) to the tangential sliding velocity ($u_b$) as:

$$\tau = \beta u_b \tag{2.5}$$

The friction coefficient $\beta$ is inferred from observed surface velocities using a control inverse method as described in the following section. Normal to the bed ($\boldsymbol{n}$), no outflow is allowed $\boldsymbol{u}.\boldsymbol{n} = 0$.

(2) At the upper surface ($\Gamma_s$), the ice is in contact with the atmosphere and is stress free. The surface elevation is prescribed from the observation in the inverse method (steady state) but is free to evolve in the prognostic simulations following the kinematic equation:

$$\frac{\partial z_s}{\partial t} + u_{s,i}\frac{\partial z_s}{\partial x} + u_{s,j}\frac{\partial z_s}{\partial y} - u_{s,k} = \dot{b} \tag{2.6}$$

where $z_s = z_s(x, y, t)$ is the surface elevation, $u_s = (u_{s,i}, u_{s,j}, u_{s,k})$ is the surface velocity and $\dot{b}$ is the surface mass balance given as a vertical flux.

(3) At the calving front, the ice below sea level ($z_{sl}$) is in contact with the water from the fjord, this leads to the following Neumann condition:

$$\boldsymbol{\sigma.n} = \begin{cases} -\rho_w g(z_{sl} - z)\boldsymbol{n} & if \quad z \leq z_{sl} \\ \mathbf{0} & if \quad z > z_{sl} \end{cases} \tag{2.7}$$

where $\sigma$ is the stress tensor, $\boldsymbol{n}$ is the unit vector in the normal direction, $\rho_w$ is the sea water density and $g$ the norm of the acceleration due to gravity.

(4) Lateral boundaries are taken from the drainage basin delineation and correspond either to artificial ice-ice boundaries in the upper reaches or ice-bed boundaries where the SRG flow is constrained by the topography. Both types are treated with the same conditions, assuming zero in-or outflow ($\boldsymbol{u.n} = \mathbf{0}$) in the normal direction $\boldsymbol{n}$ and free-slip in the tangential directions.

Ice volume changes result from the balance between incoming/outgoing ice fluxes into/from the model domain. Accurate computation of these fluxes is a pre-requisite for the computation of volume changes. Below we give details on the computation of the different fluxes. The glacier-wide surface mass balance ($\dot{B}_0$) used to force the model is computed as the ablation/accumulation flux through the free surface $\Gamma_s$ as:

$$\dot{B}_0 = \int_{\Gamma_s} \dot{b}\boldsymbol{z.n} d\Gamma \tag{2.8}$$

where $\boldsymbol{z}$ is the unit vector in the vertical direction. Because the mesh must have a strictly positive thickness, the free surface equation (Eq. 2.6) is solved with a constraint for the minimal surface elevation for each node, corresponding to a minimal thickness of 10 m. To satisfy this constraint, the model produces an additional mass flux that can be accurately quantified from the residual $R_{zs}$ of Eq. (2.6). The total mass flux through the upper free surface that corresponds to the corrected ($\dot{B}$) is then given by:

$$\dot{B} = \dot{B}_0 + R_{zs} \tag{2.9}$$

This corrected glacier-wide surface mass balance ($\dot{B}$) agrees with the ice flow and will be used hereafter as the glacier-wide surface mass balance.

Since the front is not a free surface, the ice discharge flux ($\dot{D}$) is directly computed as:

$$\dot{D} = \int_{\Gamma} \boldsymbol{u}.\boldsymbol{n} d\Gamma \tag{2.10}$$

where $\Gamma$ is the calving front boundary. As the terminus position is prescribed in the prognostic simulations, this corresponds to the calving flux required to keep a steady calving front location. During the study period the glacier front retreat was slow (220 m between 2000-2012, equivalent to 18 m $a^{-1}$ and 0.004 $km^3$ $a^{-1}$ estimated from *CECs and DGA* (2012) and *Mouginot and Rignot* (2015), suggesting that mass losses resulting from the glacier retreat were negligible in comparison with ice discharge. As discussed in *Gillet-Chaulet et al.* (2012), the non-penetration condition at the bottom and lateral boundaries is enforced as a Dirichlet condition at the nodes, this may result in a non-null ice-flux computed through the boundary elements. Here, we use a definition of the nodal normals consistent with mass conservation so that, globally, the ice-flux through the bottom and lateral boundaries is negligible.

The volume change over the model domain is then given by:

$$\frac{dV}{dt} = \dot{B} - \dot{D} \tag{2.11}$$

We verified that this relation is numerically satisfied within a limit of accuracy of 1% of $dV/Dt$.

## 2.3.2 Model initialization

### 2.3.2.1 Basal friction estimation

Robust physical parameterisations of the basal friction are usually not available and most of the ice-flow models are now equipped with inverse methods to constrain the basal friction coefficient $\beta$ using available surface observations (e.g., *MacAyeal*, 1993; *Morlighem et al.*, 2010; *Gillet-Chaulet et al.*, 2012; *Arthern et al.*, 2015). Here, we use the control inverse method implemented in Elmer/Ice. It consists in minimizing a cost function ($J_0$) that measures the mismatch between observed ($u_H^{obs}$) and simulated ($u_H^{sim}$) horizontal surface velocities obtained from the Stokes solution for a given glacier topography. Importantly, calculations are independent from surface mass balance values and distribution. As the velocity direction is mostly governed by the surface slope, the optimisation of the basal friction will have little effect on the velocity direction. Here $J_0$ measures the differences of the velocity norms and thus does not account for errors in the direction, as follow:

$$J_0 = \int_{\Gamma_s} \frac{1}{2}(|u_H^{obs}| - |u_H^{sim}|)^2 d\Gamma \tag{2.12}$$

The RMS between the model and the observations, expressed in m $a^{-1}$, is defined from $J_0$ as:

$$RMS = \sqrt{2J_0/A_s} \tag{2.13}$$

where $A_s$ is the area of the upper surface. It can be directly compared to the measurement uncertainties to assess the model performance in reproducing the observations.

To prevent overfitting and to improve the conditioning of the problem, we add a Tikhonov regularization term ($J_{reg}$) to the previous cost function. This term penalizes the first spatial derivative of the friction coefficient to avoid the occurrence of high basal friction coefficient gradients. The total cost function is:

$$J_{total} = J_0 + \lambda J_{reg} \tag{2.14}$$

where $\lambda$ is a parameter that controls the smoothness of the friction coefficient (i.e. the larger $\lambda$, the smoother the solution for $\beta$). The best solution is then a balance between a good match to observations and the smoothness of the recovered basal friction field. The optimal value for $\lambda$ is chosen using the L-curve method (e.g., Jay-Allemand and others, 2011).

#### 2.3.2.2 $\dot{b}$ estimation

Once the basal friction is retrieved, following *Välisuo et al.* (2017), the surface mass balance $\dot{b}$, could directly be computed from the free surface kinematic Eq. (2.6), using the observed surface elevation rate of change for $\Delta z_s/\Delta t$. However, this method suffers from unphysical ice-flux divergence-anomalies that arise due to the remaining model uncertainties (*Seroussi et al.*, 2011). To dissipate these anomalies, we run a transient surface relaxation where the surface elevation rate of change is forced to tends to the observation. Practically, in Eq. (2.6) $\dot{b}$ is replaced by the apparent surface mass balance ($\dot{b}_a$) defined as:

$$\dot{b}_a(z_s) = \dot{b}(z_s) - \frac{\Delta z_s}{\Delta_t}(z_s) \tag{2.15}$$

where $\Delta z_s/\Delta t$ is the observed surface elevation rate of change. The kinematic free surface equation used for the relaxation is then written:

$$\frac{\partial z_s}{\partial t} + u_{s,i}\frac{\partial z_s}{\partial x} + u_{s,j}\frac{\partial z_s}{\partial y} - u_{s,k} = \dot{b} - \frac{\Delta z_s}{\Delta t} \tag{2.16}$$

During the relaxation, the free surface and velocities adjust and tend to a steady-state where the free surface is in equilibrium with the apparent surface mass balance ($\frac{\partial z_s}{\partial t} = 0$ in

Eq. 2.16). Because the free surface elevation and velocities evolves during the relaxation they may diverge from the observations. We then test several parametrisations for $\dot{b}$ . If $\dot{b}$ is consistent with the initial flow dynamics and the observed surface elevation rate of change, changes in surface elevation and velocities must remain small, i.e. the same order of magnitude as the estimated uncertainties. The model is relaxed for 100 years; allowing to dissipate divergence anomalies and reaching a quasi-steady state if the initial imbalance is not too large.

The values of $\dot{b}$ and $\Delta z_s/\Delta t$ are then constant in time and depend only on the SRTM-2000 surface elevation ($z_{sSRTM2000}$).

In addition to the reference $\dot{b}$ functions Eqs. (1) and (2), based on the results from *Koppes et al.* (2011) and (*Schaefer et al.*, 2013), we test several parameterisations that differ in the accumulation zone. The function $\dot{b}_{k1300}$ is similar to $\dot{b}_k$ but with a maximal accumulation at 1300 m a.s.l. instead of 1800 m a.s.l in Eq. (2.1). $\dot{b}_{sxx}$ functions are similar to $\dot{b}_s$ except that the maximum accumulation at 4000 m is given by the index $xx$ instead of 23.8 m w.e. a$^{-1}$ in Eq. (2.2).

For each function $\dot{b}$, we determine two apparent surface mass balance fields using the two datasets $\Delta z_s/\Delta t|_{AA}$ and $\Delta z_s/\Delta t|_{SS}$ for the observed surface elevation rate of change (see Eq. 2.17). We use piecewise linear functions for $\Delta z_s/\Delta t|_{SS}$, and a logarithmic function for $\Delta z_s/\Delta t|_{AA}$ as shown in Fig. 2.2c.

$$\begin{aligned} \dot{b}_{aAA}(z_s) &= \dot{b}(z_s) - \frac{\Delta z_s}{\Delta t}|_{AA}(z_s) \\ \dot{b}_{aSS}(z_s) &= \dot{b}(z_s) - \frac{\Delta z_s}{\Delta t}|_{SS}(z_s) \end{aligned} \tag{2.17}$$

To select the surface mass balance scenarios, we first apply a threshold on the average volume change after 100 years. If the model is not biased, we expect that the relaxation will allow local adjustments but should not change the total volume. To define the threshold, we analyse the impact on the volume evolution of using the two forcing fields $\Delta z_s/\Delta t|_{AA}$ and $\Delta z_s/\Delta t|_{SS}$ for a given $\dot{b}$ scenario (Eq. 2.17). After 100 years the difference between the two solutions do not exceed 10 m in average (see fig. 2.4b). Therefore we use a threshold of $\pm 10$ m to select the scenarios. While depending on the relaxation duration the difference between two simulation tends to stabilise after 100 years, as, for the selected scenarios, the simulations approach the steady state. Local changes in surface elevation and velocities are not used to defined a selection criteria but are discussed with the results.

Future prognostic simulations directly start from these 100 year relaxations.

### 2.3.3 Present state of the glacier and committed mass loss

Once the initialization step has been performed, we run the model forward in time using a $\dot{b}$ function in order to simulated the present state of the glacier and to constrain the response of the glacier to the long-term diffusion of the currently observed thinning. We run the model over 100 years with the same configuration and boundary conditions using as spin up the centennial relaxation period (Sect. 2.3.2.2). Importantly, the first time-step of the modelling corresponds to the glacier response to the forcing estimated from observations and represent the period 2000-12. Afterwards, the simulation corresponds to the glacier response if the conditions remains fixed over 100 years. This condition represents the committed mass loss, which provide the minimum dynamical contribution of the glacier to sea level rise in the absence of future changes in the climate or the boundary conditions (e.g. $\dot{b}$ function, basal friction, glacier limits, front position,...) for the next century (*Price et al.*, 2011).

## 2.4 Results

### 2.4.1 Model initialization

#### 2.4.1.1 Basal friction estimation

We performed the optimizing procedure described in Section 2.3.2, and obtained that the optimal regularization parameter is $\lambda = 10^9$. The flow pattern of simulated surface velocities (Fig. 2.3b) is in good agreement with the observations (Fig. 2.3a). The map and histogram of the relative errors are shown in Fig. 2.3c and 2.3d. The error percentage is low in the central and fastest portion of the stream with values below 10%. Errors are lower than 30% in more than 54% of the glacier area. Overall, we note a small positive bias where modelled velocities are larger than the observations. In particular, the error exceeds 100% for 13% of the area (dark green in Fig. 2.3c). This corresponds to mountainous areas with steep slopes and seracs where observed velocities are low ($<$0.1 km $a^{-1}$). In these areas, the model give deformational velocities that exceed the observed values. These values cannot be improved by the inverse method, which only affects the basal sliding component. The RMS error is 104 m $a^{-1}$. This is twice larger than the reported observed velocities uncertainty of $\pm$52 m $a^{-1}$ (*Mouginot and Rignot*, 2015). However, this value is acceptable taking into account that part of the error is due to uncertainties in other model variables (e.g. topography, thermal state,...) that are not controlled by the inverse method. We consider that the model shows a good performance in reproducing the fast flow dynamics covering most of the glacier catchment area.

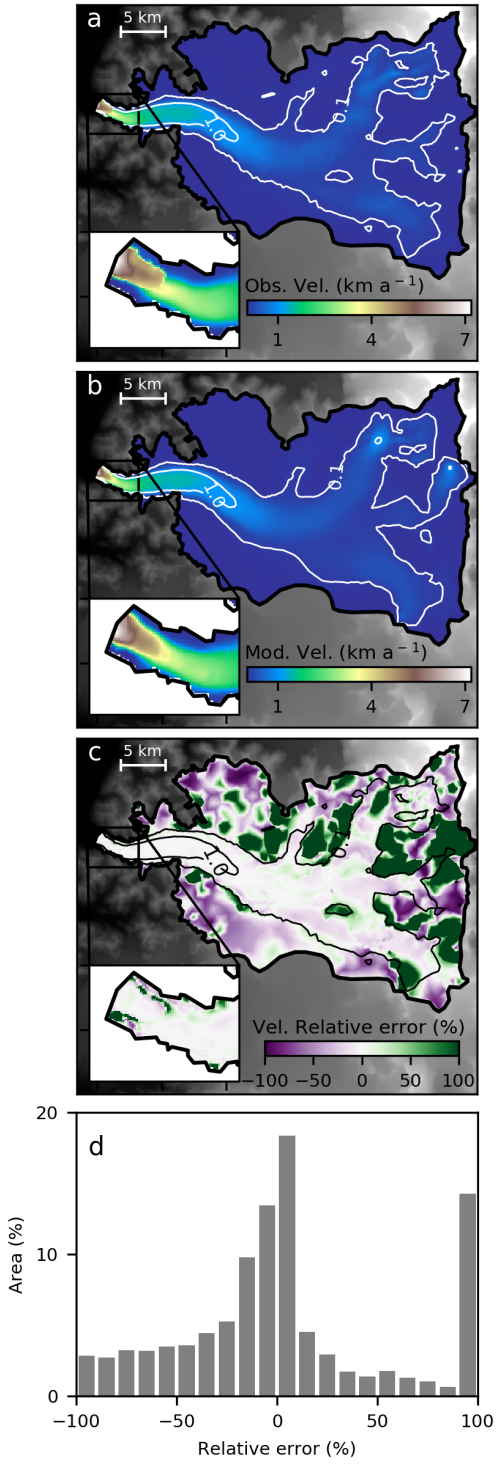


Figure 2.3: a) Observed surface velocities mosaic 1994-2014 and mostly representative of ice surface conditions in 2004 (*Mouginot and Rignot*, 2015) b) Modelled surface velocities c) Relative error and d) Histogram of the relative velocity error (%). White and black contour lines correspond to surface velocities contours (0.1 km a$^{-1}$ and 1.0 km a$^{-1}$).

We find small basal shear stresses (below 25 kPa) in most of the fast flow areas near the glacier front and in the central portion of the stream (Fig. 2.4a). Consequently, the ratio between the slip velocity and the surface velocity, $u_b/u_s$, is above 0.9 over the glacier tongue where velocities exceed 1 km a$^{-1}$ (Fig. 2.4b). Near the glacier front (insets in Fig. 2.3 & 2.4) the slip ratio is close to 1, indicating that surface velocities are good approximations of depth-average velocities. In this area, we also observe narrow bands of higher friction, with basal shear stresses between 50 to 500 kPa, parallel to the lateral boundaries. We suggest that this could be required by the model to compensate the free

slip condition imposed at the lateral boundaries. In the steep zones where we find large relative velocity errors, the inverse method produces large basal shear stresses (>200 kPa) and the sliding velocity is nearly zero showing that the error cannot be reduced by controlling the friction only. In the upper reaches of the glacier with slow flow, the deformation should dominate. Nevertheless, the inverse method is not able to reproduce this behaviour due to the range of velocities below the mean error (<20 m $a^{-1}$) and the only five layers used.

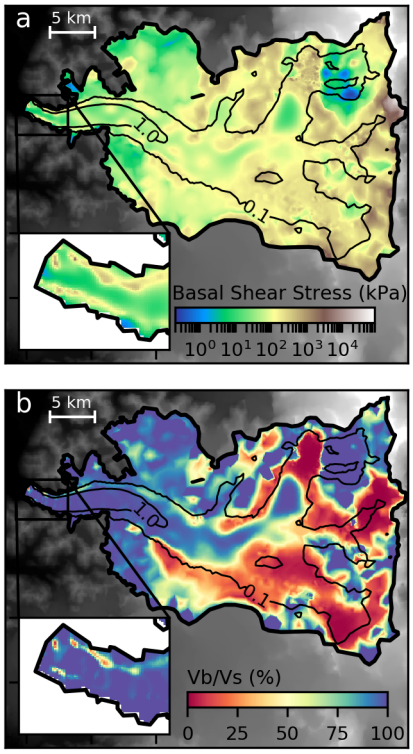


Figure 2.4: a) Basal shear stress and b) Surface/basal velocities ratio (%). Black contour lines correspond to observed surface velocities contours (0.1 km $a^{-1}$ and 1.0 km $a^{-1}$) .

#### 2.4.1.2 $\dot{b}$ estimation

With $\dot{b}_s$ , $\dot{b}_k$ and $\dot{b}_{k1300}$, at the end of the relaxation, the mean thickness change calculated as $\Delta$volume/surface increase to more than >108 m, >76 m and >42 m, which are much higher than the criteria threshold <10 m (Figs. 2.5a & 2.5b). If we look at the surface elevation change, the surface increases by more than 100 m in most of the fast flowing parts, leading to velocities higher than observed and increased ice-flux (see Figs. 2.6a & 2.6b). This suggests that for these scenarios, the accumulation is too high above the ELA to be accommodated by the flow dynamics. As a consequence, we dismiss these scenarios ($\dot{b}_s$ , $\dot{b}_k$ and $\dot{b}_{k1300}$) and try others for which the accumulation is reduced above the ELA.

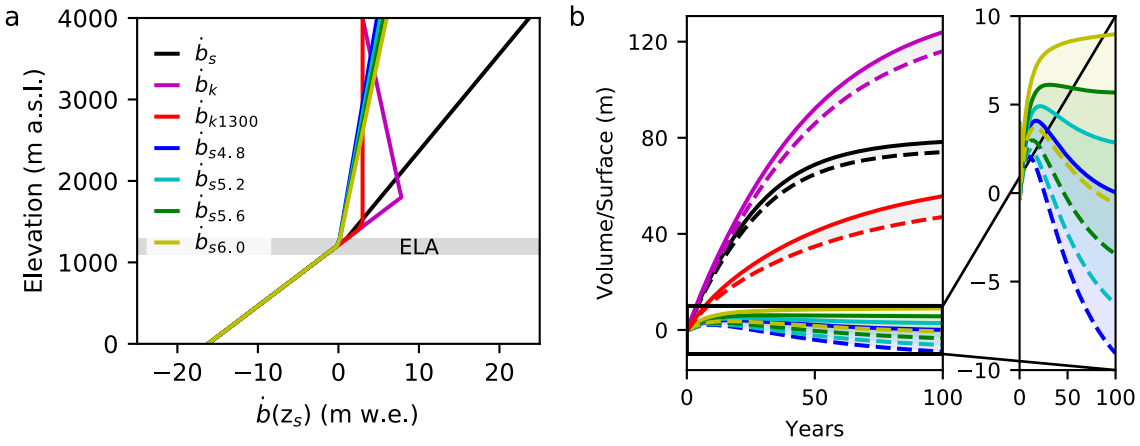


Figure 2.5: a) $\dot{b}$ functions used to force the ice-flow model: $\dot{b}_s$ function (black) from *Schaefer et al.* (2013), $\dot{b}_k$ function (magenta) from *Koppes et al.* (2011), $\dot{b}_{k1300}$ function (red) from *Koppes et al.* (2011) but modified to get an accumulation maximum at 1300 m a.s.l., $\dot{b}_{s4.8}$ (in blue), $\dot{b}_{s5.2}$ (cyan),$\dot{b}_{s5.5}$ (green) and $\dot{b}_{s6.0}$ (in yellow) functions are modified from *Schaefer et al.* (2013) with the indexes corresponding to the maximum surface mass balance at 4000 m a.s.l. b) Relaxation volume changes results expressed in volume/surface, average over the entire glacier, for the different scenarios (same colours legend than a)). Continuous lines correspond to $\Delta z_s/\Delta t|_{AA}$ and the discontinuous lines correspond to $\Delta z_s/\Delta t|_{SS}$.

Among all the tested functions the four mass balance scenarios $\dot{b}_{s4.8}$, $\dot{b}_{s5.2}$, $\dot{b}_{s5.6}$, and $\dot{b}_{s6.0}$ comply with the criteria threshold at the end of the relaxation (Figs. 2.5a & 2.5b). We consider that after 100 years these four scenarios reach the equilibrium because average volume change between two time steps (30 days) is below 0.07 m a$^{-1}$ much smaller than the observed mean surface elevation change, 1.10 m a$^{-1}$ and 1.30 m a$^{-1}$. With the scenarios $\dot{b}_s$, $\dot{b}_k$ and $\dot{b}_{k1300}$ the volume is still increasing after 100 years but the mean surface change has largely exceeded the 10 m threshold. As the selected scenarios are at the equilibrium if we run the model farther in time their increase will be very small and they will continue to be close to 10 m. By the contrary, the $\dot{b}_s$, $\dot{b}_k$ and $\dot{b}_{k1300}$ scenarios will continue to further exceed the threshold. These functions correspond thus to the most realistic scenarios which agree with the dynamics and observed surface elevation rate of change. Hereafter, we refer to them as the selected scenarios.

The scenario $\dot{b}_{S6.0_{AA}}$ shows an acceptable variation of surface elevation. The surface elevation increases by more than 100 m only in a small zone in the highest part of the glacier (above 2500 m a.s.l.) and subsides by up to 140 m in the south east and within two small zones of elevated surface slopes (Figs. 2.6c). The surface elevation changes resulting from the other selected scenarios exhibit similar patterns (not shown). These differences are likely due to the simplified altitudinal dependence chosen for the $\dot{b}$ variants. Surface velocity changes are usually less than 100 m a$^{-1}$ in the upper part of the glacier, except in mountainous zones with steep slopes, seracs and discontinuous ice leading to large changes during the relaxation. The ice is shallow in these areas so we don't expect that

these changes will strongly affect the flux downglacier. There is also an area with velocity changes up to nearly 1 km $a^{-1}$ few kilometres upstream. As it can be seen in Fig. 2.3a, there is a sharp discontinuity in the observed surface velocities in this area. We suspect that this discontinuity comes from the mosaicking and is not a real feature. While the model was forced by these observations during the basal friction inversion, the relaxation insures a continuity of the ice flux and thus smooth this sharp transition. Just at the front, the velocities are very sensitive to the topography, and there is a slight decrease of the velocities during the relaxation.

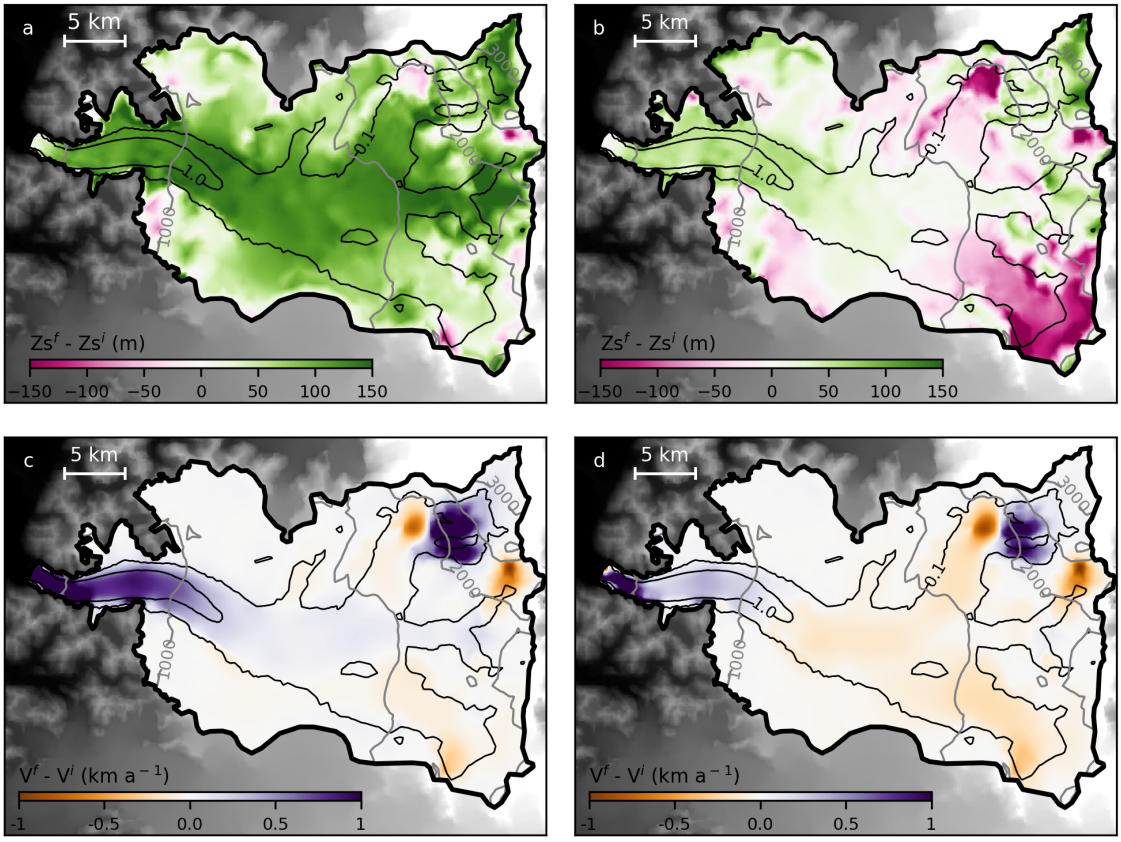


Figure 2.6: Fig. 6. a) Total change in surface elevation ($z_s$) after 100 years of relaxation for mass-balance scenario $\dot{b}_{sAA}$ , b) Same as a) but for scenario $\dot{b}_{s6.0AA}$, c) Surface velocity change after 100 years of relaxation for mass-balance scenario $\dot{b}_{sAA}$ , d) Same as c) but for scenario $\dot{b}_{s6.0AA}$. Gray contour lines correspond to $z_s$ contours every 500 m and black contour lines correspond to observed surface velocities contours (0.1 km $a^{-1}$ and 1.0 km $a^{-1}$). The super-script f means final, at the end of relaxation and i means initial.

The simulated surface velocities that represent the study period forced by the selected $\dot{b}$ function present the same distribution than the observed surface velocities, even though the simulated differ to the observed ones with an RMS below 211 m $a^{-1}$ (see Table A2.4 and Fig. 2.7 that present the results for the scenario $\dot{b}_{S6.0_{AA}}$). Although this RMS is significant, our results are close to observations considering the uncertainties and limitations explained previously.

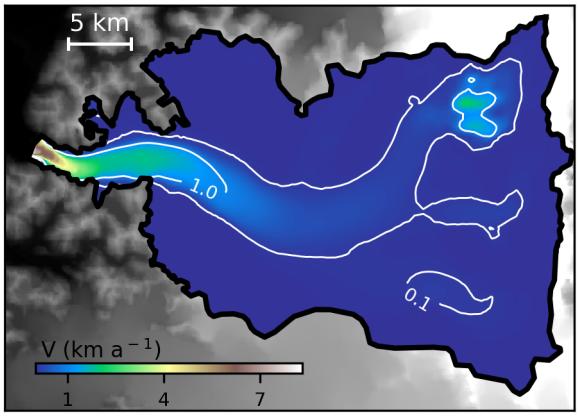


Figure 2.7: Velocity after 100 years of relaxation, for scenario . White contour lines correspond to simulated surface velocities contours (1000 m $a^{-1}$ and 100 m $a^{-1}$).

Table 2.2: RMS between simulated and observed surface velocities from different surface mass balance ($\dot{b}$) forcing.

| $\dot{b}$ functions | RMS (m $a^{-1}$) $\Delta z_s/\Delta t\|_{AA}$ | RMS (m $a^{-1}$) $\Delta z_s/\Delta t\|_{AA}$ |
|---|---|---|
| $\dot{b}_s$ | 326 | 333 |
| $\dot{b}_k$ | 427 | 451 |
| $\dot{b}_{k1300}$ | 265 | 285 |
| $\dot{b}_{s4.8}$ | 188 | 198 |
| $\dot{b}_{s5.2}$ | 192 | 201 |
| $\dot{b}_{s5.6}$ | 196 | 206 |
| $\dot{b}_{s6.0}$ | 200 | 211 |

### 2.4.2 Present state of the glacier

The present state of the glacier is represented by the first time step of the prognostic simulation as explained in the section 2.3.3. The surface mass balance over the entire glacier is $\dot{B}$ = 0.08±0.06 Gt $a^{-1}$, averaged over the four selected scenarios (the error is the standard deviation between the four estimates). The ice discharge estimated from the surface velocity observations and ice thickness is -0.92 Gt $a^{-1}$. The model velocities where slightly larger than the observations at the beginning of the relaxation, resulting in a flux 10% larger at -1.03 Gt $a^{-1}$. To accommodate the ice flux coming from upstream, this value has decreased during the relaxation and, using the selected scenarios, we have $\dot{D} = -0.83 \pm 0.08$ Gt $a^{-1}$.

The computed glacier-wide average volume change that represent the study period is -0.81±0.08 $km^3$ $a^{-1}$. This is close to the value estimated from DEMs ($\Delta z_s/\Delta t|_{AA}$=-0.80±0.06 $km^3$ $a^{-1}$ and $\Delta z_s/\Delta t|_{SS}$=-0.92±0.07 $km^3$ $a^{-1}$ of ice), showing that our simu-

lations capture most of the thinning pattern.

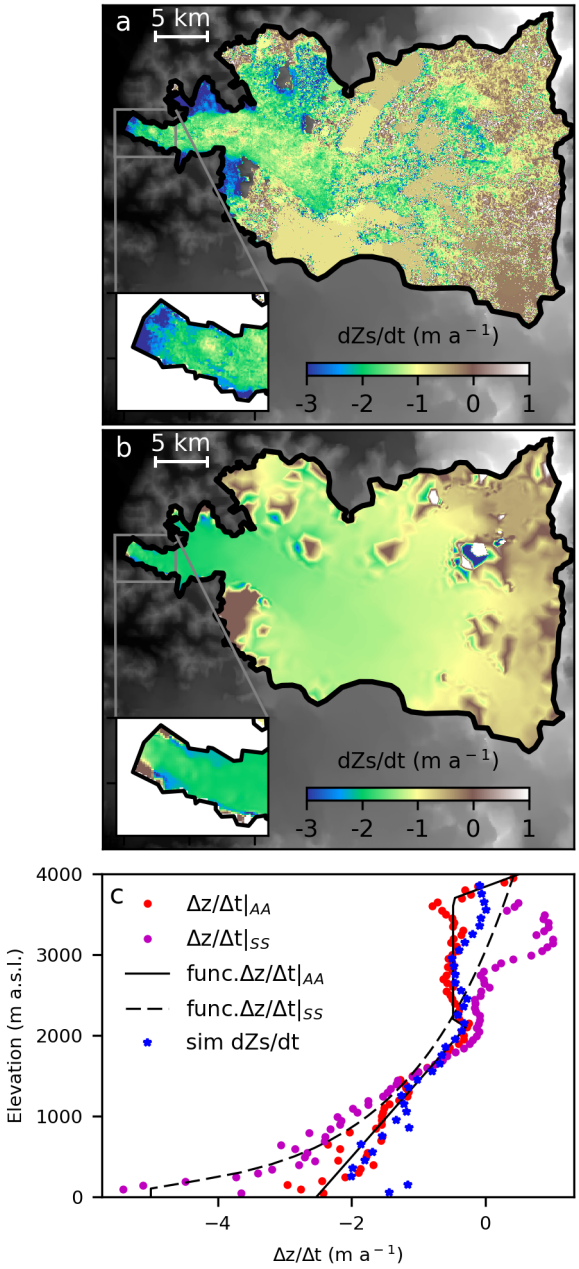


Figure 2.8: a) Observed rate of elevation change from ASTER DEMs b) Simulated rate of elevation change that represents the present state of the glacier (2000-12), for scenario $\dot{b}_{s6.0AA}$ c) Comparison of the rate of elevation change for scenario $\dot{b}_{s6.0AA}$ with the observed values using two space-borne geodetic methods (AA and SS).

The comparison between the distribution of the simulated surface-elevation changes that represent the actual state of the glacier (Figs. 2.8a, 2.8b & 2.8c) and the surface elevation changes estimated by geodetic techniques shows a good agreement. However, a lower simulated thinning compared to the observations appears at the front of the glacier, which may be related to an incorrect bedrock representation at the front in our modelling, to large ablation values at several locations caused by local specific processes

(dust, bedrock protuberances), or to uncertainties in the surface elevation changes estimated with the geodetic techniques. Also, there are some bi-polar features in the elevation change (Fig. 2.8b). These features are in zones of strong slope where the model is not capable of represent the flux and the surface change.

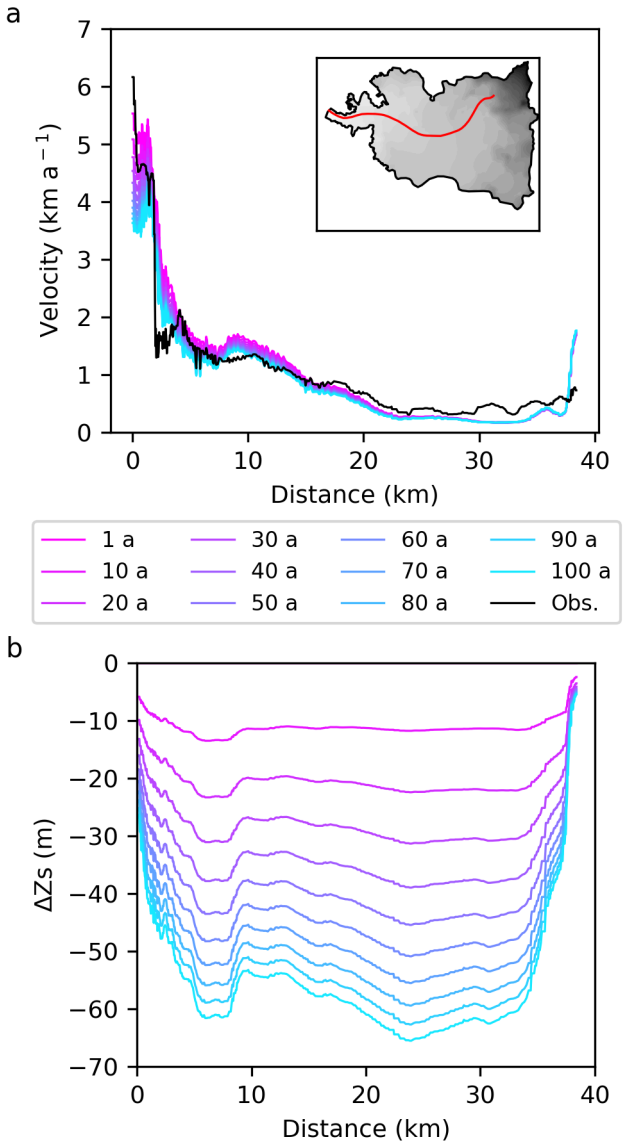


Figure 2.9: a) Velocities along a flow line (located in red in the inset) every 10 years of a 100 years long simulation compared to observed velocities (in black) for scenario $\dot{b}_{s6.0AA}$. b) Change in elevation along this flow line every 10 years for scenario $\dot{b}_{s6.0AA}$.

### 2.4.3 Committed mass-loss results

We now run the model over 100 years forced with the four selected $\dot{b}$ functions and assuming the same configuration and boundary conditions. Assuming both AA and SS surface elevation changes leads to eight different initial conditions for the estimation of the committed mass loss. The simulated and observed velocities along a flow line (Fig. 2.9a) generally show a similar pattern. Yet simulated values near the glacier front are some-

what lower right from the start and decrease further with time. Ice-thickness changes along a flow line (Fig. 2.9b) show a decrease in time, with a maximal decrease at 23.6 km inland, corresponding to an initial altitude of 1206 m a.s.l.

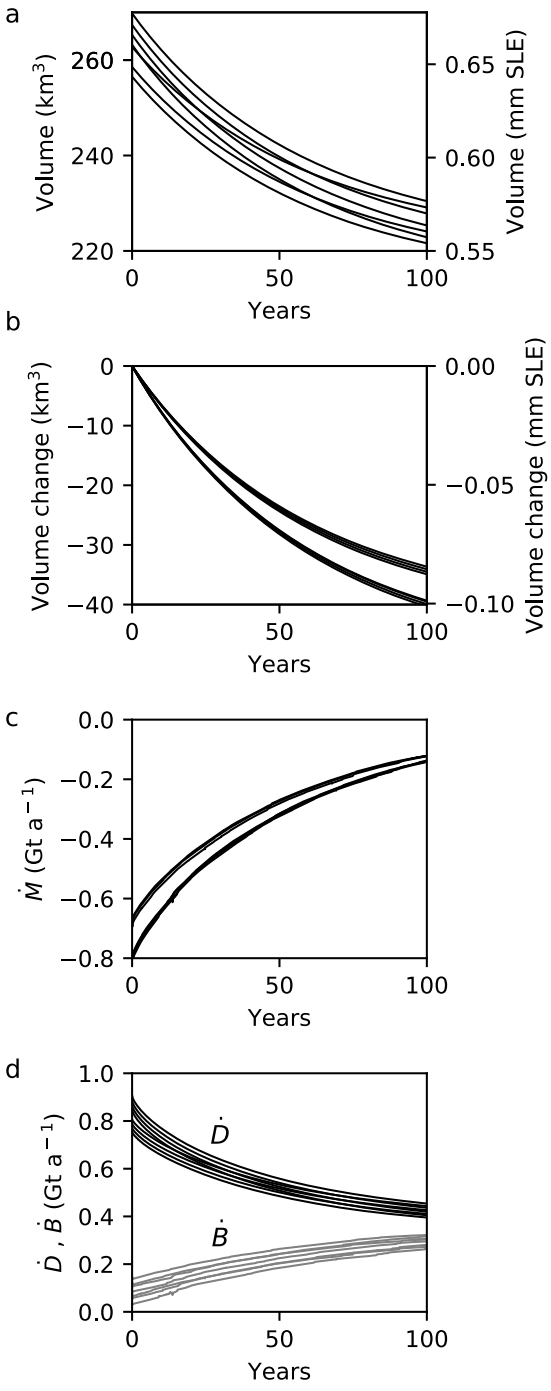


Figure 2.10: Results of the prognostic 100 years simulation for the four selected scenarios and eight initial conditions. Temporal variations of the a) ice volume, b) volume loss c) mass balance ($\dot{M}$), c) ice discharge ($\dot{D}$) and surface mass balance ($\dot{B}$).

The committed mass loss due to the long-term diffusion of the currently observed thinning under constant forcing is equal to -33.7±3.1 Gt (0.093±0.008 mm SLE), after 100 years of simulations (Figs. 2.10a, 2.10b, 2.10c). This corresponds to an annual loss rate of -0.34±0.03 Gt a$^{-1}$ being close to half the value (-0.78±0.06 Gt a$^{-1}$) as reported by *Willis et al.* (2012a). The uncertainty is quantified using the dispersion between the

eight simulations. This result corresponds to the minimum dynamical contribution of the glacier to sea level rise in the absence of future changes during the next century.

Because the forcing is constant in time during this experiment, the initial imbalance decreases with time as the model should tend to a steady state. The most important adjustment is in the ice discharge ($\dot{D}$), which decreases as a result of both thinning and decrease of the velocity at the glacier front. While we don't take into account the surface elevation feedback for the surface mass balance, land terminated margins retreat as a response to the ablation, leading to a reduction of the glaciated area and an increase of the total mass balance $\dot{B}$.

## 2.5 Discussion

Our ice-flow model and satellite observations allow us to constrain the surface mass balance over SRG. Our best estimate of the glacier-wide surface mass balance ($\dot{B}$) is slightly positive during 2000-12 at 0.08±0.06 Gt $a^{-1}$ (0.12 m w.e. $a^{-1}$), which is much lower than in previous studies (Table 2.3). Since our results are in agreement with ice dynamics, we expect our $\dot{B}$ values to be better constrained than in previous studies based on atmospheric models forced by reanalysis with poor calibration in the accumulation zone. However, we are aware that there are uncertainties in the data used in this study. To support higher accumulation, the ice dynamics should be able to export more ice from the accumulation area. We have shown that basal sliding accounts for most of the observed surface velocities in larges areas. The ice flux can then reliably be estimated from the product of the surface velocity with the ice thickness. Because ice is flowing relatively fast, the surface velocities are relatively accurate, so that fluxes higher than what we estimate could be explain only by a low biased ice thickness. Using the same thickness and surface velocity data sets, *Gourlet et al.* (2016) estimated the ice flux crossing a gate at an altitude close to the ELA to be 1.49 $km^3$ $a^{-1}$. Using a gate in a similar location we obtain 1.31 $km^3$ $a^{-1}$. For each simulation, we can estimate the uniform thickness bias at the fluxgate that would be required to obtain the same flux using the same surface velocity observations. For the selected scenarios, the ice thickness should be decreased by 50 m to 74 m. Our accumulation estimates might therefore be biased towards lower values. On the contrary, to accommodate the accumulation from the scenario $\dot{b}_s$, the ice thickness should be increased by 282 m. *Gourlet et al.* (2016) reported thickness errors up to 64 m on the plateau and up to 114 m in narrow valleys. While we can not exclude that our results could be explained by low biased ice thicknesses, the relatively shallow thickness of San Rafael Glacier is consistent with batimetry measurements and is given as a robust feature of the gravimetry inversion (*Gourlet et al.*, 2016) .

Table 2.3: San Rafael glacier-wide average surface mass balance ($\dot{B}$) from different sources and periods

| Source | This study | *Schaefer et al.* (2013) | *Koppes et al.* (2011) |
|---|---|---|---|
| Period | 2000-12 | 1979-2012 | 1990-2005 |
| $\dot{B}$ (Gt a$^{-1}$) | 0.08±0.06 | 1.19 | 0.72±0.37 |
| Area (km$^2$) | 734 | 741 | 728 |

The range of surface areas from the different studies is 13 km$^2$ with a maximum influence of 0.02 Gt a$^{-1}$ on the $\dot{B}$

Regarding the $\dot{B}$ distribution, all the selected $\dot{b}$ functions have much lower accumulation than the $\dot{b}_s$ function from *Schaefer et al.* (2013) and *Koppes et al.* (2011) . Our maximum accumulation at 4000 m a.s.l. is 5.4±0.6 m w.e. a$^{-1}$ while the maximum accumulation predicted by *Schaefer et al.* (2013) is 23.7 m w.e. a$^{-1}$. We also find lower accumulation than *Koppes et al.* (2011) in the elevation range 1000-1400 m a.s.l. where most of the glacier area is (see Fig. 2.2b). However, due to our simplified spatial distribution of the surface mass balance, our results do not accurately represent the distribution of surface elevation changes, and they are only an example of likely $\dot{b}$ function among many other possibilities. Our selected scenarios did not consider that precipitation could decrease above a certain elevation which can explain why, in the model, the surface elevation increased above 2500 m a.s.l (Fig. 2.6c). We do not take into account either the north-south gradient in precipitation (*Garreaud et al.*, 2012) or the effect of blowing snow. *Vimeux et al.* (2008) pointed out the importance of wind transport and erosion at Mont San Valentin. The mass loss in the south-east zone of the glacier (Fig. 2.6c) are compatible with regional patterns in accumulation induced by a precipitation gradient or by snow redistribution by the wind. However, a more detailed representation of surface mass-balance distribution must consider atmospheric variables and modellization is beyond the scope of this study.

The selected $\dot{b}$ functions allow us to check that changes in accumulation just above the ELA have large consequences on the glacier-wide $\dot{B}$ because the San Rafael Glacier is very flat and a large fraction of the glacier area lies around the ELA. Special attention is needed in this zone where data availability is poor (d1, d2 and d6 from Table 2.1) and the only direct measurement over one year is d6 from *CECs and DGA* (2012). Conversely, accumulation at even higher elevation has only a limited impact on the final $\dot{B}$ because only 10% of the glacier surface is located above 2000 m a.s.l. This also suggests that only small variations in the ELA may have a large impact on the final $\dot{B}$ and on the resulting ice dynamics.

The ice discharge resulting from the ice-flow model is consistent with the results from *Koppes et al.* (2011), however it is below the estimation from *Willis et al.* (2012a) and

*Schaefer et al.* (2013), see Table 2.4. During this period (2000-12) the glacier retreat was low, therefore the ice discharge and calving flux are comparable ($<$ 0.1 Gt a$^{-1}$ of difference). On one hand, *Schaefer et al.* (2013) estimated the calving flux as the difference between the total mass balance and $\dot{B}$. Since the $\dot{B}$ is very high in their study, they deduced very high calving flux values. On the other hand, *Willis et al.* (2012a) computed the ice discharge from mean front velocity as 5.29 km a$^{-1}$ using images collected 7-day apart on 28 March and 4 April 2007. The mean front velocity from our model is 3.83 km a$^{-1}$ which is very similar to the average given by *Mouginot and Rignot* (2015). The difference with the *Willis et al.* (2012a) estimate is mainly a result of higher velocities at the borders of the glacier at the front. We have more confidence in the velocity data used in this study because the uncertainty is smaller (52 m a$^{-1}$) than the uncertainty given by *Willis et al.* (2012a) (422 m a$^{-1}$). However, the disagreement confirms that our simulated and observed cross section area close to the front are likely too small compared to the *Willis et al.* (2012a) data. Our ice-discharge results highly depend on the bedrock uncertainty, whereas other components ($\dot{B}$) should be less influenced impacted because ice-flux change at the front hardly propagate to the accumulation zone. Moreover, the first consequences of a higher ice discharge would be a smaller or null thickening in the lower part of the glacier after the relaxation, which would lead to a better agreement between the simulations and the geodetic results (reduction of the green area in the lower part of the glacier in Fig. 2.6c). This potential improvement of surface elevation changes close to the front would also be visible in Fig. 2.8b where we currently observe a small disagreement between simulation and geodetic results below 300 m a.s.l..

Table 2.4: Ice-discharge ($\dot{D}$) estimations.

| Source | This study | *Schaefer et al.* (2013) | *Koppes et al.* (2011) | *Koppes et al.* (2011) | *Willis et al.* (2012a) |
|---|---|---|---|---|---|
| Period | 2000-12 | 2000-09 | 1990-2005 | 2001 | 2007 |
| $\dot{D}$* (Gt a$^{-1}$) | -0.83±0.08 | 1.68±0.11 | 1.04±0.60 | 1.36 | -2.02±0.05 |

* Assuming an ice density of 910 kg m$^{-3}$

SRG glacier is largely in disequilibrium, as demonstrated by the mass loss of the glacier during the last decade, mainly driven by a large ice discharge while the surface mass balance is just slightly positive. As a consequence of this disequilibrium, the glacier will continue to lose mass during the next century even without any further changes in climate and boundary conditions. The resulting committed mass loss after one century will be -33.7±3.1 Gt (-0.34±0.03 Gt a$^{-1}$). The committed mass balance is twice lower than the already observed wastage (see Table 2.5), because recent ice flow was still largely more important than the positive contribution from the $\dot{B}$. However, the ice discharge

will decrease with deceleration and thinning in the lower ablation area. Present rates are not sustained in the future and can therefore not be extrapolated. The committed mass balance result is significant since it corresponds to the minimal contribution of SRG to sea level rise (SLR) over the next century and because it should be considered that the SRG represents 18% of the NPI surface.

Table 2.5: Sea level contribution from earlier studies and committed mass loss from this study.

| Source | *Rignot et al.* (2003)* | *Willis et al.* (2012a)* | This study |
|---|---|---|---|
| Period | 1975-2000 | 2000-11 | 2012-2112 |
| NPI (Gt $a^{-1}$) | 2.91±0.36 | 3.70±0.10 | - |
| San Rafael (Gt $a^{-1}$) | - | 0.78±0.06 | 0.34±0.03 |
| San Rafael (Gt) | - | 7.83±0.55 | 33.7±3.1 |

* Assuming an ice density of 910 kg $m^{-3}$

A further analysis of the ice-flow dynamic variations related to the glacier front location is now planned in order to estimate the influence of front geometry and front depth on the ice discharge of SRG.

Our results show that this new methodology is appropriate independently constrain surface mass balance and ice discharge from fast moving glaciers where ice dynamics is significant. The are many glaciers with these characteristics in Patagonia and other parts of the world as north America and northern Europe where this methodology can improve knowledge on glacier behaviour. We recommend this method when reliable surface velocity and ice thickness data are available. Another point to be consider, that the method computes the ice discharge corresponding to a fixed front and not the calving flux. Therefore, is only applicable during periods of time where the glacier front is stable.

## 2.6 Conclusion

The ice-flow model Elmer/Ice was applied to reproduce the main characteristics of the ice-flow dynamics of San Rafael Glacier. The ice dynamic model initialization demonstrated that a very low basal shear stress (<25 kPa) is inferred along the main stream and that most of the surface velocity is due to basal sliding in the lowest part of the glacier and close to the front. After initialization, the model was used to assess the glacier-wide $\dot{B}$ giving consistent modelled velocities with the observed ice velocities over the period 2000-12. This $\dot{B}$ is slightly positive 0.08±0.06 Gt $a^{-1}$ (0.12 m w.e. $a^{-1}$) and significantly lower than in previous estimations. The modelled ice discharge is -0.83±0.08 Gt $a^{-1}$.

Therefore, the glacier mass loss during this period resulted from an ice discharge larger than the slightly positive glacier-wide surface mass balance. In response to this state of imbalance, San Rafael Glacier is committed to lose ice in the coming decades and the minimum dynamical contribution of the glacier to sea level rise in the absence of future changes during the next century is -33.7±3.1 Gt (0.093±0.008 mm SLE).

Our study demonstrates that a well-calibrated ice-flow model can provide an independent constrain on the poorly known surface mass balance of a large glacier such as San Rafael. The methodology developed in this study can be used on other glaciers in Patagonia where ice dynamics and discharge play an important role in the total mass balance.

# Chapter 3

# SMB from regional climate modeling

## 3.1 Introduction

As explained in previous chapters, the common hypothesis of Patagonian icefields' increasing mass loss is that atmospheric warming is strong in Patagonia (*Rignot et al.*, 2003; *Rasmussen et al.*, 2007) or that ice dynamics remove largely more ice than SMB can offer leading to the icefield instability (*Schaefer et al.*, 2013).

Even if changes in the ice dynamics may have largely impacted NPI, there should be a link between climate change and the glacier MB, retrieved in SMB changes. Climate change may impact accumulation, ablation or both. Indeed, the punctual SMB (in kg $m^{-2}$ $a^{-1}$) at one point is defined as the sum of mass gains and losses at the ice sheet surface:

$$SMB = PR + SU + TR + RU \tag{3.1}$$

where PR is total precipitation (solid and liquid), SU is surface sublimation, TR is drifting snow transport (including erosion, deposition, and sublimation of drifting snow particles), and RU is run-off, the amount of liquid water from melt and rain that is not retained or refrozen in the snowpack. Fluxes are negative when mass is lost at the surface. Variations in regional climate over Patagonia may have impacted solid precipitation occurrences, or induced changes in ablation, through melting and/or sublimation. In order to estimate these feedbacks, computing the incoming/outcoming energy in the ice is necessary, meaning that the surface energy balance (SEB) has to be assessed. The SEB depends on radiation fluxes (short and longwave), turbulent heat fluxes and on the heat storage within the snow cover, or in the ice. Getting an accurate vision of changes in the SEB and the SMB, is not straightforward and requires a full modeling of the airflow at the glacier scale. In complex terrain or topography, where spatial changes in atmospheric forcings are very strong in time and space, this exercise is complex and imposes studies

at a very high resolution, with regional atmospheric circulation models.

Here, I use the MAR (Modèle Atmosphérique Régional, *Gallée and Schayes* (1994)) forced by ERA-Interim to evaluate the distribution of atmospheric variables over NPI, and to assess their impact on the variations of the SMB. To adapt and validate the model to the NPI region, model results, for 2013-2014 and for 2000-2014, are compared to available data from automatic weather stations installed on the icefield and around at lower elevations, albedo values estimated from MODIS images and punctual SMB measurements.

Finally, SMB and SEB obtained from the MAR between 1980 and 2014 are analyzed in detail, to discuss whether temperature or precipitation changes may have explained recent changes in the total mass balance of the NPI.

## 3.2 Regional model description

Regional atmospheric models solve the atmospheric dynamics and surface processes at high resolution (1 km to 20 km) in a physically-based way. They are forced by atmospheric fields from reanalyses or general circulation models at their lateral and top boundaries and by sea surface conditions. Compared to large scale models, they improve the representation of the atmospheric physics, the interaction with the surface in the mid and low troposphere and represent more complex surface characteristics as complex topography and land cover. However, they are dependent on the large-scale circulation patterns defined by the forcing fields.

The model used in this study is the regional climate model MAR. MAR simulates the atmospheric dynamics and is coupled to the 1D surface model SISVAT (*De Ridder and Gallée*, 1998; *Gallée et al.*, 2001). In the following subsections, I describe the main schemes of the atmospheric model and of the land and surface component.

### 3.2.1 Atmospheric model

MAR is a regional climate model that simulates the atmospheric dynamics solving the primitive equations with the hydrostatic approximation and the normalized pressure, $\sigma$, as the vertical coordinate:

$$\sigma = \frac{p - p_t}{p_s - p_t} \tag{3.2}$$

where $p$, $p_s$ and $p_t$ are the pressure, surface pressure and the constant top pressure in the model, respectively.

The vertical sub-cell flux is solved using the E-$\epsilon$ turbulence closure model of *Duynkerke*

(1988), that defines the turbulent mixing length as a function of local flow characteristics. The hydrological cycle is represented by a cloud microphysical model (*Gallée*, 1995) based on the conservation equation for cloud droplet, rain drop, cloud ice crystal and snow flake concentration following *Kessler* (1969) et *Lin et al.* (1983). The model considers the blown snow particles as snow flakes, and sublimation of snow flakes is a function of the air relative humidity. MAR has a detailed radiative scheme based on *Fouquart and Bonnel* (1980) for the solar radiation and *Morcrette* (2002) for the infra-red radiation. The radiative scheme consider cloud proprieties from concentration of cloud droplets and ice crystals at each model level. The convective scheme follows *Bechtold et al.* (2001). The boundary dynamic relaxation assumes a newtonian and diffusion term following *Davies* (1983) and *Marbaix et al.* (2003). The main schemes of the model are represented in Fig. 3.1. A complete description of the atmospheric model can be found in *Gallée and Schayes* (1994) and more information is available on the model website (http://mar.cnrs.fr).

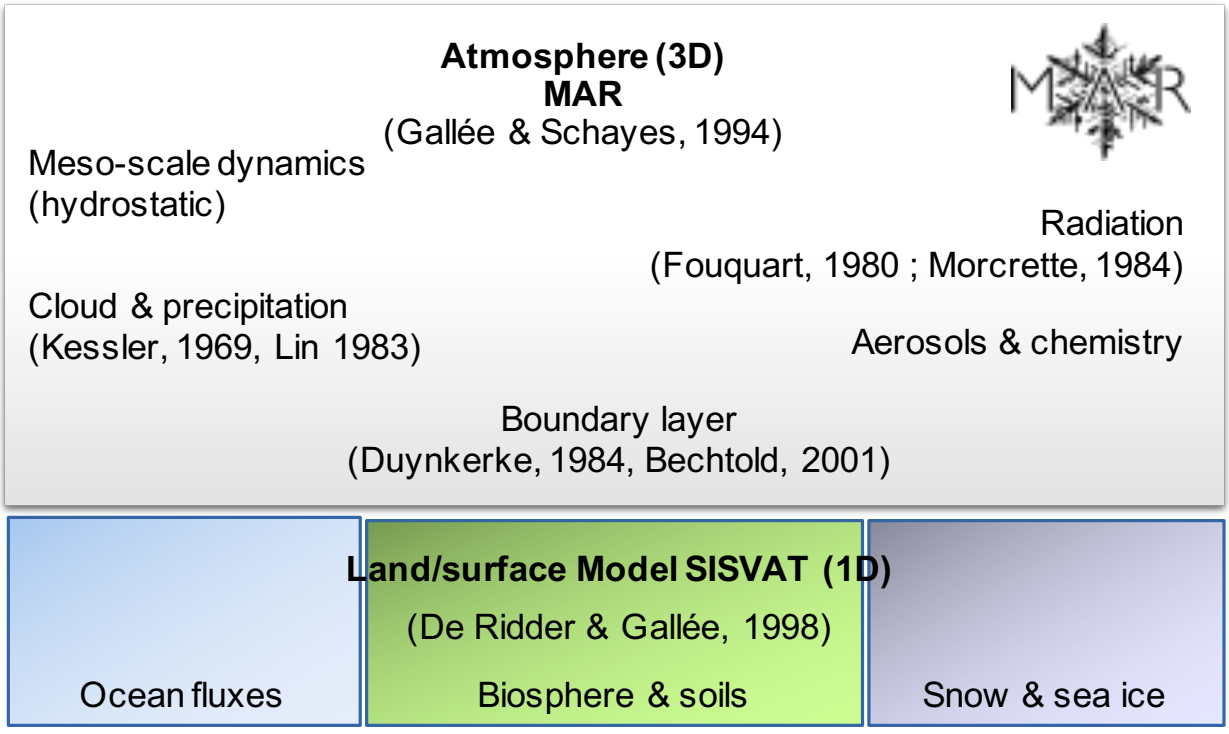


Figure 3.1: MAR model schemes, adapted from *Fettweis* (2006).

### 3.2.2 Land and surface model

The surface 1D model SISVAT (Soil Ice Snow Vegetation Atmosphere Transfer) represents three classes of surface with three different modules for the ocean, soil-vegetation and snow-ice (*De Ridder and Gallée*, 1998; *Gallée et al.*, 2001). The ocean module estimates the sea surface temperature using linear interpolations on the MAR grid. This

module is coupled with the boundary layer of MAR and it solves the flux transfer between the atmosphere and the ocean. The soil vegetation module simulates the heat and moisture transfers over land when there is no snow (*Lefebre*, 2003). The snow-ice module is a multi-layer model that estimates the surface energy balance, surface mass balance and the transfers between the surface, the sea ice, the ice sheet surface, the snow-covered tundra, and the atmosphere. This module is based on the CROCUS model developed in CEN (Centre d'Etudes de la Neige), and the model description can be found in *Brun et al.* (1992).

In the following, I describe the most important schemes of the snow-ice module used to estimate the San Rafael Glacier and NPI surface mass balance and its different components.

The snow-ice module is composed by a group of coupled schemes, that estimate the different processes occurring in the snow pack (Fig 3.2). SISVAT physics, parameterization and validation are presented in *Gallée and Duynkerke* (1997), *Gallée et al.* (2001) and *Lefebre* (2003).

The snow pack is represented by layers with the same characteristics managed by a snow/ice discretization module. The total number of layers changes during the simulation in agreement with new layer formation due to snow falls and snow metamorphism. When enough snow amounts fall on the ground, a new layer is added. The density, dendricity and shericity of each layer is estimated based on CROCUS parameterizations (*Brun et al.*, 1992). The snow pack has a maximum of 20 layers with variable thicknesses, that can split or join to represent the snow pack stratigraphy.

The snow pack surface energy balance is estimated in the thermodynamics scheme which includes calculation of incoming ($F_s$) and reflected ($\alpha F_s$) solar radiation, incoming (Fl) and emitted ($\sigma T_4$) infra-red radiation, turbulent latent ($H_l$) and sensible ($H_s$) heat fluxes, heat from rainfall ($H_{rain}$), the ground heat flux ($Q_g$) and the heat flux from conduction through the snow pack ($H_{cond}$). The geothermal flux is neglected. All fluxes are represented in Fig. 3.2. The turbulent fluxes estimation is based on the similitude theory of *Monin and Obukhov* (1954) following the formulation of *Businger* (1973). It uses the gradient transport theory (*Stull*, 2012) that relates the turbulent fluxes to time-average gradients of wind speed, potential temperature and specific humidity, known as the bulk parameterization. The drag coefficient and roughness length of momentum is a function of the air temperature as proposed in *Amory et al.* (2017).

There is a water balance module that solves the water mass conservation in each snow layer taking into account melting, refreezing, runoff and percolation. The runoff comes from an excess of internal liquid water over the maximum water saturation (*Zuo and Oerlemans*, 1996). When the surface is flat, the liquid water can accumulate at the

surface and decreases the albedo. MAR/SISVAT have also a blowing snow module, which is not used here.

Furthermore, the snow evolution and metamorphism in the snow pack is also simulated in SISVAT and is handled by a module based on CROCUS parameterizations (*Lefebre*, 2003). The snow is characterized by the temperature gradient, liquid water content, density and size, sphericity and dendritic of snow grains. The snow evolves from the fresh snow (dendritic snow) to old snow with its different characteristics depending on the temperature gradient and intermediates processes.

To estimate the radiative balance at the surface of the snow/ice discretization, the albedo is computed according to the characteristics of snow (*Fettweis*, 2006). Depending on the size and form of the snow grain the albedo is estimated following *Brun et al.* (1992) as:

$$\alpha = 0.606 * (\alpha_{0.3-0.8\mu m}) + 0.301 * (\alpha_{0.8-1.5\mu m}) + 0.093 * (\alpha_{1.5-2.8\mu m}) \tag{3.3}$$

$$\alpha_{0.3-0.8\mu m} = 1 - 1.58\sqrt{d} \tag{3.4}$$

$$\alpha_{0.8-1.5\mu m} = 1 - 15.4\sqrt{d} \tag{3.5}$$

$$\alpha_{1.5-2.8\mu m} = 346.3d - 32.31\sqrt{d} + 0.88 \tag{3.6}$$

where $\alpha$ is the albedo of the snow pack. The snow pack albedo depends on the spectral interval albedos with prescribed solar fractions: $\alpha_{0.3-0.8\mu m}$, $\alpha_{0.8-1.5\mu m}$ and $\alpha_{1.5-2.8\mu m}$ are the albedo for the spectral intervals 0.3-0.8, 0.8-1.5 and 1.5-2.8 $\mu m$. $d$ is the optical grain size in meters. The optical grain size is calculated with the CROCUS parameterization (*Brun et al.*, 1992) and is function of dendricity and sphericity. It corresponds to the size of a theoretical snow sample with the same albedo as the one given by the considered snow grain. For dendrictic snow, the albedo decreases when dendricity decreases and for nondendritic snow, the albedo decreases as snow grains get larger (*Lefebre*, 2003).

When the snow depth is below 10 cm, the albedo follows a linear function of the snow depth to simulate a smooth transition from the albedo of snow ($\alpha_{snow}$) to the albedo of ice ($\alpha_{ice}$).

If the ice is uncovered by snow, the surface albedo varies as an exponential function of the water height from the ice albedo to the water albedo ($\alpha_{water} = 0.15$).

The albedo can slightly increase or decrease depending on the cloudiness following *Greuell and Konzelmann* (1994):

$$\alpha = \alpha + 0.05 * (CC - 0.5) \tag{3.7}$$

where $CC$ is the cloudiness parameter that varies between 0 and 1.

Also, the albedo can increase as a function of the solar zenith angle following *Segal et al.* (1991):

$$\alpha = \alpha + max\left\{0; 0.32 * 0.5 * \left(\frac{3}{1 + 4 * cos\theta_{zz}} - 1\right)\right\} \tag{3.8}$$

$$cos\theta_{zz} = max\left(cos80°; cos\theta_z\right) \tag{3.9}$$

where $\theta_z$ is the solar zenith angle.

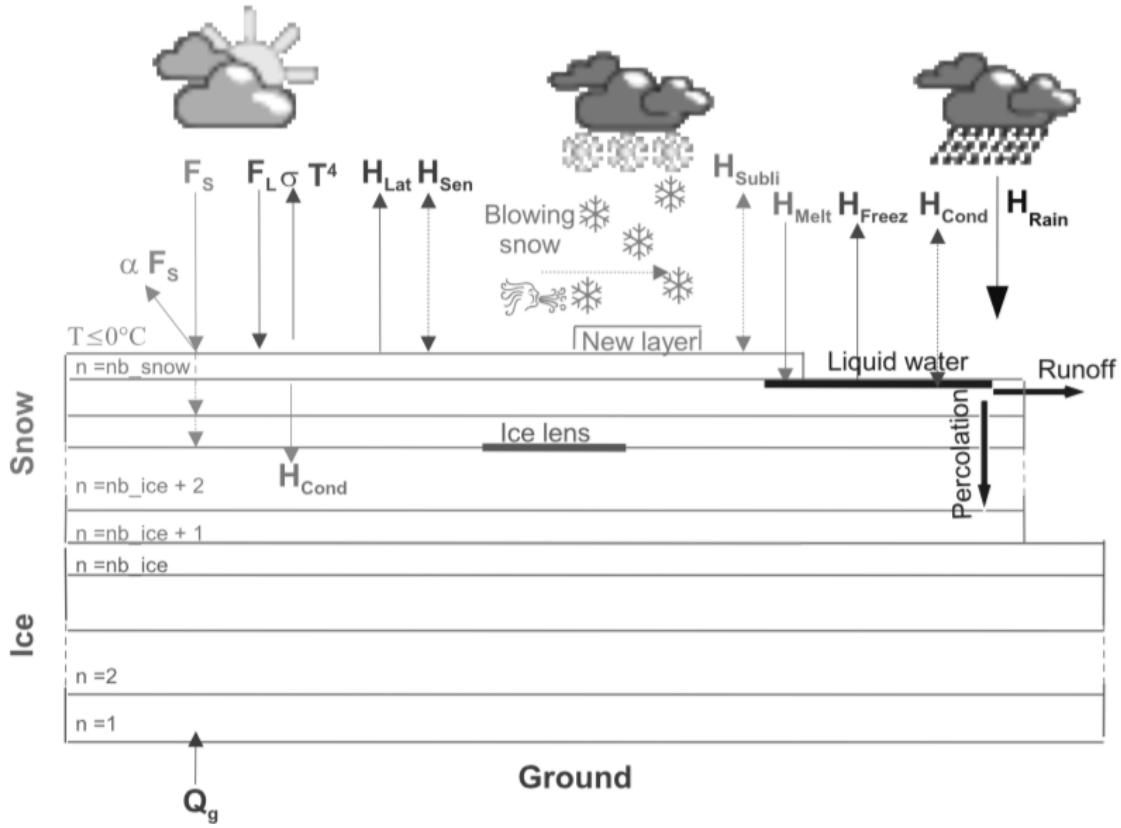


Figure 3.2: snow-ice module of SISVAT. Heat fluxes and mass balance components from *Fettweis* (2006). See text for the definitions.

## 3.3 Methodology

In this section, I describe the model settings, forcings, and the methodology used to adapt and calibrate the model to Patagonia.

### 3.3.1 Model configuration

The model domain is centered on the NPI and extends from the Pacific Ocean to the Argentinian Patagonia, from 78.2°W to 69.2°W and from 44.7°S to 49.3°S (see Fig. 3.3). The troposphere is represented by 23 vertical layers. Different model resolutions are tested in the sensitivity analysis but the final resolution was fixed to 8-km, with 90X160 cells, for the long term simulations.

The topography corresponds to an average on each cell from the 1 arc-minute global relief model ETOPO1 (*Amante*, 2009). Figure 3.3 shows the topography and model domain.

The snow pack has a maximum of 20 layers and is initialized with a spin up simulation of 10 years from 2000 to 2010.

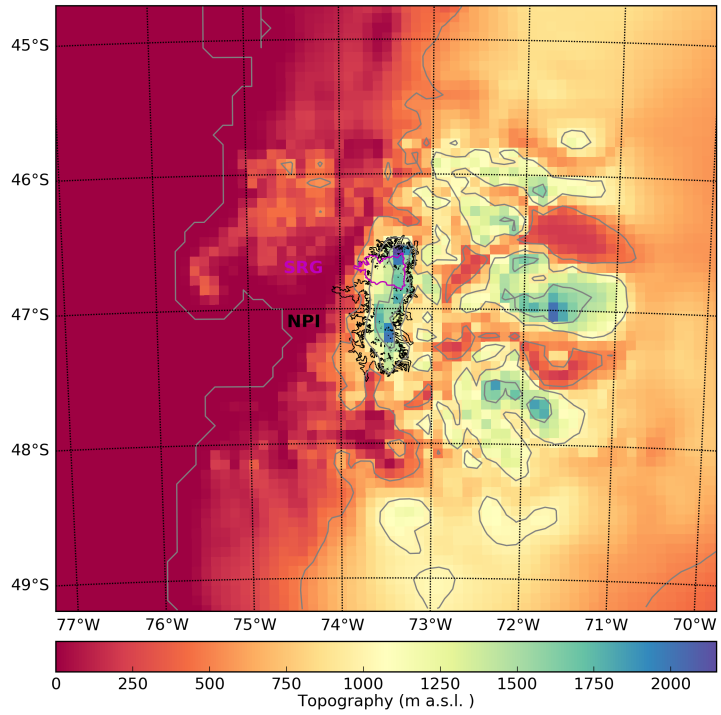


Figure 3.3: Model domain and topography. Black line corresponds to NPI limits and magenta lines correspond to the SRG limits.

### 3.3.2 Large scale forcing

Reanalyses were used to force the regional model. Reanalyses are past states of the atmosphere computed from weather forecast models with an assimilation process. The assimilation combines background information from the model with observations to produce a representation of the state of the atmosphere. The objective is to obtain a physically coherent solution, which is also close to reality (observations). Observations come from many sources: radiosondes, pilot balloons, buoys, ship reports, aircraft and satellites; and

have different spatial resolution, temporal distribution and accuracy. The outputs are the atmospheric variables (wind velocity and direction, temperature, pressure, humidity,...) in a global regularly spaced grid. A reanalysis product uses only one data assimilation scheme and one model to obtain a dynamical atmospheric representation consistent in time. However, the quantity and quality of the assimilated data change over time and can produce artificial trends and shifts.

The reanalysis reliability and accuracy are highly dependent on observational data and consecutively zones with sparse observational data are less reliable. The southern hemisphere and Patagonia are zones with few observations due to the low population and the small land cover compared to the ocean surface (*Nicolas and Bromwich*, 2011). Therefore, reanalysis data in these zones must be taken with caution. In addition, climatic trends in this region are largely impacted by assimilation of satellite datasets since 1979 (*Kistler et al.*, 2001b; *Uppala et al.*, 2005b).

ERA-Interim is an atmospheric reanalysis product from the ECMWF (European Centre for Medium-Range Weather Forecasts) that covers the period from 1979 to present. The reanalysis is available at 6-hour time steps for the atmospheric parameters covering troposphere and stratosphere and 3-hour time steps for the surface parameters. The reanalysis has 60 vertical levels from the surface up to 0.1 hPa and a resolution of 80km equivalent to 0.75 degrees in a regular latitude/longitude grid. Compared to ERA-40, ERA-interim uses an improved model and assimilation system based on IFS (Cy31r2) and four-dimensional variational data assimilation (4D-Var) (*Dee et al.*, 2011).

All the problems due to changes in the observing system have not been circumvented and they can cause changes in mean errors and shifts. An example of shift is found in precipitation over tropical oceans principally, during the period 1992 - 2009, which is due to the assimilation of rain-affected radiances from SSM/I (*Dee et al.*, 2011). In the southern hemisphere, in general, reanalyses have important uncertainties due to the weak in-situ data coverage. As an example, in Patagonia and Tierra del fuego, only 3 or 4 radiosondes are assimilated by ERA-Interim every day, depending on the period, with at least one to three reports available every 2 days on average (*Uppala et al.*, 2005b).

I choose to use ERA-Interim because recent reanalysis inter-comparisons have shown that ERA-Interim is the most reliable contemporary global reanalysis in high southern latitudes, in Antarctica (*Bromwich et al.*, 2011; *Bracegirdle and Marshall*, 2012) and in the Amundsen and Bellingshausen Seas (*Bracegirdle*, 2013) which are close and highly dependent on Southern Ocean conditions as is also the case for Patagonia.

Here, temperature, humidity, wind, atmospheric pressure and sea-surface temperature are used at 6h resolution to force MAR at its lateral and top boundaries.

### 3.3.3 Adapting the model for NPI application

MAR was initially developed to represent the main physical processes driving atmospheric dynamics and to estimate the SMB of the main ice-sheet of Antarctica. Afterwards, it has been used in Greenland, Europe and Africa. Therefore, before using MAR in Patagonia various sets of values for key parameters are tested and a sensitivity analysis is performed. Then, an evaluation of the parameters is obtained by comparing the results to observed data from the icefield plateau and the surrounding valleys. Finally, the best simulation is selected using the previous evaluation.

#### 3.3.3.1 Sensitivity analysis

As one of the main uncertainties in Patagonia is precipitation, the variables and settings which are closely related to precipitation are analyzed. Additionally, because the objective is the estimation of the SMB, the sensitivity to some crucial variables of the snow pack model are also studied. Here, I describe the setup and results are described in section 3.5.

a) Model Resolution

It was shown in the first chapter that Patagonian precipitation is mainly orographic. Therefore, precipitation estimation in Patagonia is highly dependent on topographic representation and model resolution. To analyze this impact, the influence of resolution on precipitation was tested. Since the model is applied assuming the hydrostatic hypothesis, which is not valid for smaller cells than 7 km approximately, it was decided to avoid using resolutions higher than 8 km. Thereafter, simulations with 20 km, 10 km and 8 km of resolutions have been performed. An increase in resolution is associated with a better representation of high mountain elevations, and leads to a precipitation increase over the summits.

b) Humidity input at the boundaries

The water vapor and humidity coming from the Pacific Ocean, at the western model boundary, is the source of precipitable water over Patagonia. Aditionally, the resolution change between large scale and regional scale models generally produce problems in humidity saturation inducing a lack of consistency for precipitation. Therefore, ERA-Interim humidity values used as boundary conditions for the model were enhanced by a relative amount ranging between +0 and +20%. Air humidity at the boundaries can directly impact precipitation and accumulation, but also induces variations in the turbulent heat

fluxes, cloud cover and temperature. It also leads to different amounts of latent heat release during condensation, and to different downward longwave and shortwave radiations.

Simulations were performed with 5 different humidity boundary conditions. The reference simulation uses the humidity given by ERA-Interim; in the 4 other simulations the humidity is enhanced by +5%, +7.5%, +10% and +20%.

c) Snow/rain threshold temperature

A temperature threshold is used to distinguish between snow and rain in the atmosphere, which has important impact on snowfall and accumulation over the icefield. This threshold is expected to vary according to the precipitation conditions (convective/subsidence, frontal, orographic precipitation...) in different regions of the world. In the model this threshold initially given for Antarctica is equal to -1°C. Here, different values of the snow/rain threshold temperature are tested (-1°C, 0°C, 1°C and 2°C), from the initial value of -1°C until 2°C which is a typical value for Patagonia (*Rasmussen et al.*, 2007; *Koppes et al.*, 2011).

d) Albedo of bare ice and of superimposed ice lenses

Albedo is a key parameter for the SMB and SEB since the short wave radiation budget and the energy available for melt are directly related to this variable. The model sensitivity to minimum and maximum albedo values of bare ice and of superimposed ice lenses was tested, because values are expected to vary in different regions due to the presence of different type of dust at the surface. The tested values are given in table 3.1. The quality of the albedo parameterization is checked using albedo estimates from MODIS images.

Table 3.1: Different bare ice and ice lenses albedos use in the sensitivity analysis.

| Simulation | Bare ice min. Alb. | Bare ice max. Alb. | Ice lense Alb. |
|---|---|---|---|
| alb0 | 0.5 | 0.55 | 0.70 |
| alb1 | 0.5 | 0.55 | 0.75 |
| alb2 | 0.6 | 0.65 | 0.75 |
| alb3 | 0.7 | 0.75 | 0.80 |

e) Surface roughness length

Surface roughness length plays a very important role in the turbulent heat fluxes, which are normally the second source of energy on the SEB and accordingly the surface roughness length impact the SMB. In the model, surface roughness length of ageing snow

depends on air temperature. This parameterization was calibrated in Antarctica in order to accurately reproduce the blowing snow fluxes measured at the coast of Adelie Land (*Amory et al.*, 2017).

In many regions of the world including Antarctica, the latent and sensible heat fluxes have opposite signs, and compensate for each other. This leads the sum of heat fluxes to be nearly zero and large uncertainties in the surface roughness length have only small impacts in SEB and SMB.

However, in Patagonia, the latent and sensible heat fluxes very often present both positive values and strongly contribute to melting. In these conditions, the surface roughness length has an important impact in the SMB calculation. For this reason, the sensitivity of the model to surface roughness length is tested.

As in the model turbulent heat fluxes are estimated using the momentum roughness length (Z0m), the model is applied with the typical values of Z0m used for Antarctica, and with reduced values by one and two orders of magnitude.

### 3.3.4 Estimation of glacier-wide SMB

The model estimates the SMB and its components in each cell (8 km resolution) defined as part of the icefield. Due to the difference between the model resolution, glacier fronts geometry and elevation distribution, glacier-wide SMB can not be directly estimated from the SMB values from the cells. Then, to estimate the glacier-wide SMB, I regressed the SMB against elevation values for the cells representing SRG and NPI.

For SRG, the cells that represent the glacier allow to build a piece-wise linear function of SMB versus elevation. Then, using the hypsometry of the glacier separated on bands of 100 m, the total SMB is estimated the area weighted mean surface mass balance of all altitude bands.

The elevations of the cells representing SRG are ranging between 500 m a.s.l. to 2410 m a.s.l. Below this range, I consider that the SMB follows a linear relation with the elevation estimated from the lowest cells. Above 2410 m a.s.l., the SMB is considered constant and equal to the ones computed at 2410 m a.s.l., because precipitation can not increase indefinitely (*Roe*, 2005b; *Houze*, 2012). Therefore, we assumed that accumulation also has a maximum below the summit, i.e. at an elevation of about 2410 m a.s.l..

For NPI, many more cells are available to assess the SMB gradient with elevation than on SRG, and two approaches are used: 1) two linear functions of SMB vs. elevation are fitted for the ablation and accumulation zones and 2) a third-degree polynomial function of SMB vs. elevation is fitted over the whole range of altitudes. Then, we split the glacier hypsometry into bands of 100 m, and the glacier-wide SMB is estimated as weighted SMB average (weighted according to the area of each altitudinal band). The final result

corresponds to the average of both fits and the uncertainty corresponds to the difference between both.

### 3.3.5 Comparison with observations

To compare the observed and simulated precipitation, I use the simulated precipitation that corresponds to the cell where the weather station is located directly without using a lapse rate, because precipitation variation with elevation in the model is highly dependent on location and orientation and no clear linear lapse rate can be found.

However, for the temperature comparison a linear lapse rate is computed between model elevation and temperature for the closest cells around the one that includes the station in use, these lapse rates are used to correct the observed temperatures before comparison.

## 3.4 Observational and remote sensing datasets

In this section, I describe the data used to calibrate and validate the model at a regional scale. This concerns 1) field data from the plateau used to adapt the model, and 2) the precipitation and temperature data from weather stations located around the icefield at low elevation. Then, I describe the methodology to retrieve the albedo from satellite measurements, which is a complementary source of validation of the model.

### 3.4.1 Field data from the icefield

Direct observations of SMB and temperature acquired by Geoestudios and DGA in 2014 during a field campaign on the plateau of SRG are used to assess the accuracy of snow precipitation and ablation in the model. The data correspond to: (i) snow height (SH) acquired on an 18-m high tower installed directly in the snow pack at 1158 m a.s.l. and located at -46.75°W -73.51°N, and (ii) air temperature recorded by an AWS installed at 1197 m a.s.l. and located at -73.60°W -46.71°N. The sensor characteristics are given in Table 3.2.

Table 3.2: Field data recorded on the plateau.

| Data | Period | Sensor | uncertainty |
|---|---|---|---|
| Snow height | 03/09/2013 - 22/08/2014 | Campbell SR50A | 1 cm - 0.4% |
| Air temperature | 03/09/2013 - 22/08/2014 | Campbell 107 Temp. probe | 0.2 °C |

Table 3.3: Weather stations and data.

| N | Name | Lon. Lat. | Elevation (m a.s.l.) | Data (%) |
|---|---|---|---|---|
| s1 | Puerto Chacabuco | -72.82°W -45.46°N | 20 | P(97) |
| s2 | Río Aysen en Pto. A. | -72.6°W -45.4°N | 32 | P(72) |
| s3 | El balseo | -72.5°W -45.4 °N | 25 | P(78) |
| s4 | Teniente Vidal C. Ad. | -72.1°W -45.6°N | 310 | P(100), T(100), $T_{min}$(98), $T_{max}$(100) |
| s5 | Coyhaique Conaf | -72.1°W -45.6°N | 340 | P(81), $T_{min}$(79), $T_{max}$(81) |
| s6 | Coyhaique Esc. Ag. | -72.0°W -45.6°N | 343 | P(81), $T_{min}$(58), $T_{max}$(70) |
| s7 | Coyhaique Alto | 71.6°W -45.5°N | 730 | $T_{min}$(76), $T_{max}$(76) |
| s8 | Balmaceda Ad. | -71.7°W -45.9°N | 517 | P(100), T(98), $T_{min}$(99), $T_{max}$(100) |
| s9 | Villa Cerro Castillo | -72.2°W -46.12 °N | 345 | P(81) |
| s10 | Chile Chico Ad. | -71.7°W -46.6°N | 306 | P(73), $T_{min}$(77), $T_{max}$(74) |
| s11 | Bahía Murta | -72.7°W -46.5°N | 240 | P(87), $T_{min}$(86), $T_{max}$(86) |
| s12 | Lord Cochrane Ad. | -72.6°W -47.2°N | 204 | P(71), T(84), $T_{min}$(83), $T_{max}$(84) |
| s13 | Río Pascua | -73.1°W -48.2°N | 20 | P(71) |

Data (%) is type and percentage of available data for the period 2000-2014. P is monthly mean precipitation, T is monthly mean temperature, $T_{max}$ is the average of monthly maximum temperature and $T_{min}$ is the average of monthly minimum temperature.

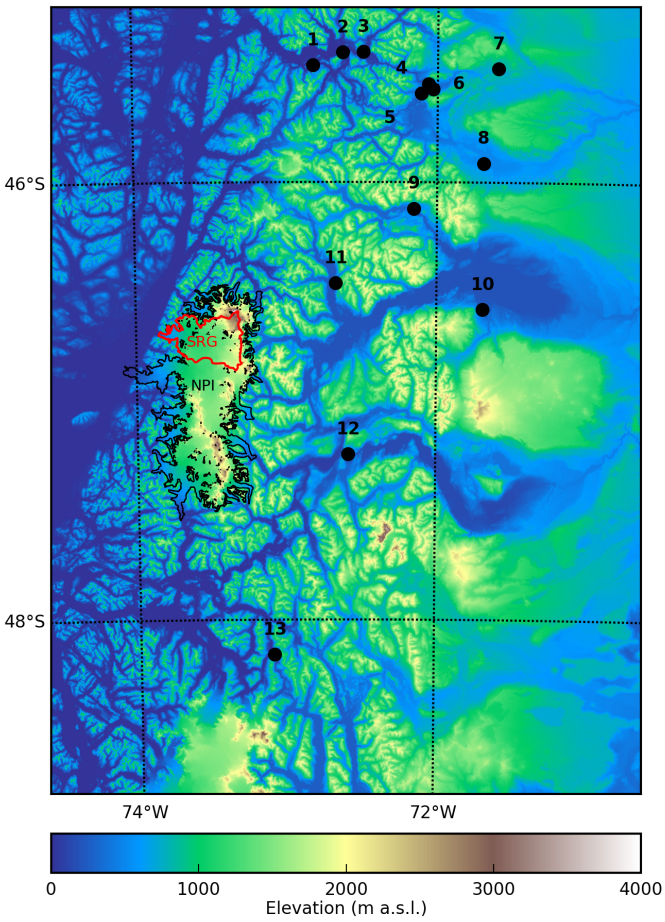


Figure 3.4: Location of weather stations with precipitation and air temperature data. See Table 3.3 for the station characteristics.

### 3.4.2 Weather stations data

Precipitation and temperature data from AWS located at lower elevations around NPI are also used to validate the model. These datasets are obtained from the compiled metadata of CR2 (Center for Climate and Resilience research, Universidad de Chile) for the period 2000-2014.

Precipitation was measured by the DGA (Dirección General de Aguas de Chile) and DMC (Dirección meteorológica de Chile) with standard rain gauge methods (not specified in CR2 metadata). There are large uncertainties associated with precipitation measurements because strong wind and precipitation events commonly occur in Patagonia, and this directly impacts the rain collection in rain gauges. A reference value of the uncertainty of 20% was proposed by *Schneider et al.* (2003), for an unshielded tipping-bucket rain gauge at Puerto Bahamondes in Tierra del Fuego at 53°S with similar climatic conditions as in Patagonia.

Here, monthly precipitation from 12 stations are used, corresponding to stations presenting more than 70% of data available. From these datasets, anomalous data are disregarded, such as constant values or values below a given threshold. The monthly average temperature from 2 stations is also used. These stations are the only ones with more than 50% data coverage over the studied period. To complement these temperature datasets, monthly average of daily maxima and minima from 8 stations are also used. Stations location and characteristics are given in the Table 3.3 and Fig. 3.4.

### 3.4.3 Albedo from satellite observations

The albedo is retrieved from MODIS images using the MODImLab Matlab toolbox. This methodology has been used in previous studies to estimate the albedo in New Zealand, Himalaya and the Alps (*Sirguey et al.*, 2016; *Brun et al.*, 2015; *Davaze et al.*, 2018).

MODIS is an optical sensor of the TERRA-EOS/AM-1 satellite that has been taking near-daily images of the Earth from February 2000 until present. MODIS has 36 spectral bands ranging from 0.459 to 14.385 $\mu m$, and a spatial resolution ranging from 0.25 to 1 km depending on the spectral band.

The data used in this study are the MODIS/TERRA Level 1B C5 products (MOD02QKM, MOD02HKM, MOD021KM, MOD03). They correspond to calibrated radiances at the top of the atmosphere (TOA) and relative geometry parameters such as solar and sensor zenith (see Table 3.4).

Table 3.4: MODIS products characteristics.

| Produc name | Description | Resolution |
|---|---|---|
| MOD02QKM | TOA band 1 and 2 | 250 m |
| MOD02HKM | TOA band 3 to 7 | 500 m |
| MOD021KM | TOA band 8 to 36 | 1 km |
| MOD03 | Geolocation, geometry and topography parameters, such as solar and sensor azimuths and zeniths | 500 km |

MODImLab is an automatized algorithm that uses MODIS L1B data to retrieve snow and ice broadband bihemispherical refectance (albedo) among other products following the methodology developed by *Sirguey* (2009) and *Dumont et al.* (2012). First, the algorithm corrects the radiance measured by MODIS (hemispherical-conical reflectance) for seven spectral bands taking into account the atmospheric effects and the multiple reflections that occur in rugged terrain (*Sirguey*, 2009). Then, a method developed by *Dumont et al.* (2012) is aplied to estimate the broadband bihemispherical refectance from the corrected MODIS radiance. Blue sky albedo is obtained as well as white sky albedo, the latter being the albedo of the same surface under pure diffuse illumination. *Dumont et al.* (2012) and *Sirguey et al.* (2016) estimated that the accuracy of MODImLab albedo is ±10 % under clear-sky conditions. MODImLab also poduces cloud cover maps that are more conservative than the direct MODIS product MOD35 as observed by *Brun et al.* (2015). Moreover, to mitigate the impact of shadows over the glaciers, MODImLab uses the SRTM2000 topography (90 m resolution) to estimate the sky obstruction by the surrounding topography and to correct the impact of shadows (*Sirguey*, 2009).

The albedo used in this study is the white sky albedo, because it makes it possible to compare albedo maps obtained at different periods of the year when the solar zenith angle is not the same. Albedo maps (30 m resolution) were finally obtained from each processed MODIS image. MODImLab was executed by L. Davaze. Then we checked the cloud cover maps and manually selected the albedo maps without clouds, filtering for errors in the cloud recognition. After selection, a total of 114 albedo maps under clear sky conditions were obtained over SRG for the period 2010-2014. The Fig. 3.5 shows an example of the albedo maps.

#### 3.4.3.1 Glacier and icefield geometry data

The SRTM2000 (30 m resolution) was used to obtain the glacier and icefield surface elevation. The glacier and icefield hysometry was used to estimate the surface mass

balance as described in section 3.3.4.

The NPI outlines were taken from *Rivera et al.* (2007) which correspond to the margins observed in march 2001 with a total area of 3953 km$^2$, excluding the nunataks. This outline was chosen because it is the closest to the beginning of the validation period (2000-2014). The SRG drainage basin delineation is taken from *Mouginot and Rignot* (2015), who used their surface velocity data to define the ice divide over the plateau where the surface slope is too small to accurately define the divide. Therefore, this likely corresponds to the best glacier delineation available on the plateau.

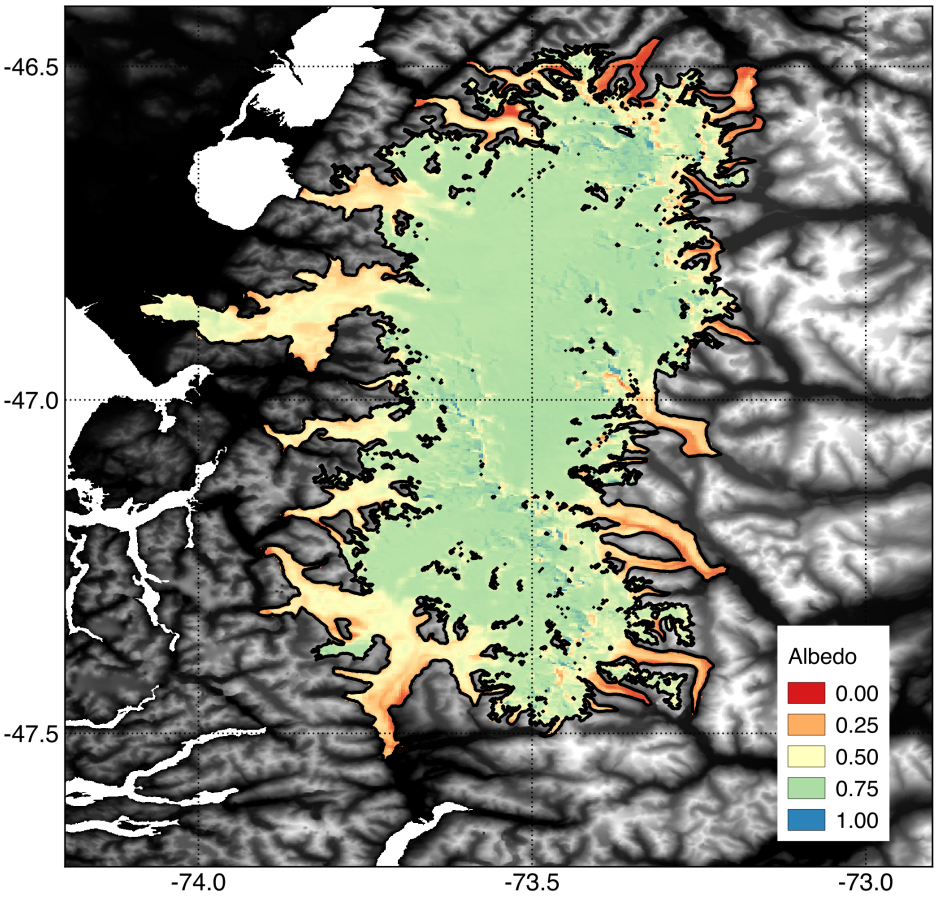


Figure 3.5: Albedo from MODImLAB 24/02/2012.

### 3.4.4 Punctual SMB data on the icefield

There are 6 punctual SMB measurements on NPI that were used to validate the model results. Their chatacteristics are given in Table 3.5.

Table 3.5: Published point surface mass-balance measurements over the Northern Patagonia Icefield.

| Source | Nom. | Glacier | Date | Method | Elevation (m a.s.l.) | b (m w.e. $a^{-1}$) |
|---|---|---|---|---|---|---|
| *Yamada* (1987) | d1 | San Rafael leed side | 1985 | firn core stake (winter accu.) | 1300 | 3.5 |
| *Matsuoka and Naruse* (1999) | d2 | NPI | 1997 | | 1500 | 2.20 |
| *Ohata et al.* (1985a) | d3 | San Rafael | 1983 Jan-Aug | stake | 50 | -22.57 |
| *CECs and DGA* (2012) | d4 | Nef | 2012 Jan-Aug | stake | 572 | -8.40 |
| *CECs and DGA* (2012) | d5 | Nef | 2012 | stake | 511 | -9.86 |
| *Geoestudios and DGA* (2014) | d6 | San Rafael | 2013-2014 | stake | 1152 | 0.74 |

## 3.5 Results and discussion

This section presents the SMB sensitivity to variations in the key parameters described previously. It is followed by an evaluation of the different simulations used in the sensitivity analysis using observational data: (i) Snow height and temperature on the plateau are evaluated during the period 2013-2014. (ii) Precipitations and temperature in the valleys are evaluated during 2000-2014 and (iii) The uncertainty of the SMB estimation is then discussed by comparing similar simulations. Using the results from the evaluation the best simulation is selected and its characteristics and SEB are analyzed in details.

Thereafter, with the paremeterization from the selected simulation, the SMB for the period 1980-2014 is simulated. From these results, the temporal average and trends are discussed. Then, the trends in the SMB are analyzed and related to climate trends in Patagonia. Finally, our results are compared with those from previous studies.

### 3.5.1 Sensitivity analysis

#### 3.5.1.1 Model resolution

As explained in the methods, simulations with 20 km, 10 km and 8 km resolutions have been performed. On NPI, San Valentin peak is the highest summit reaching 4032 m a.s.l. In the model grid, this peak is represented by a cell with elevations of 2003, 2340 and 2410 m a.s.l. for the 20 km, the 10 km and the 8 km simulations, respectively. A maximum annual precipitation of 3.8, 4.1 and 4.4 m $a^{-1}$ is found on San Valentin Peak for 20 km, 10 km and 8 km resolution respectively (Fig. 3.6). For the highest resolutions (10 km

and 8 km), two separated precipitation maxima are displayed associated to the presence of San Valentin at the north and Cerro Arenales at the south, and differences between the western and eastern sides of the icefield are observed. As precipitation continuously increases until 8 km resolution, this resolution is chosen, because it covers the largest range of elevations and orographic precipitation within the limits of the hydrostatic hypothesis.

#### 3.5.1.2 Humidity input at the boundaries

Humidity increase results in higher accumulation caused by a snow height increase in the accumulation zone due to the increase in solid precipitation (table 3.6). However, SMB changes result from the paradoxical variations of accumulation and ablation associated with the average increase in humidity.

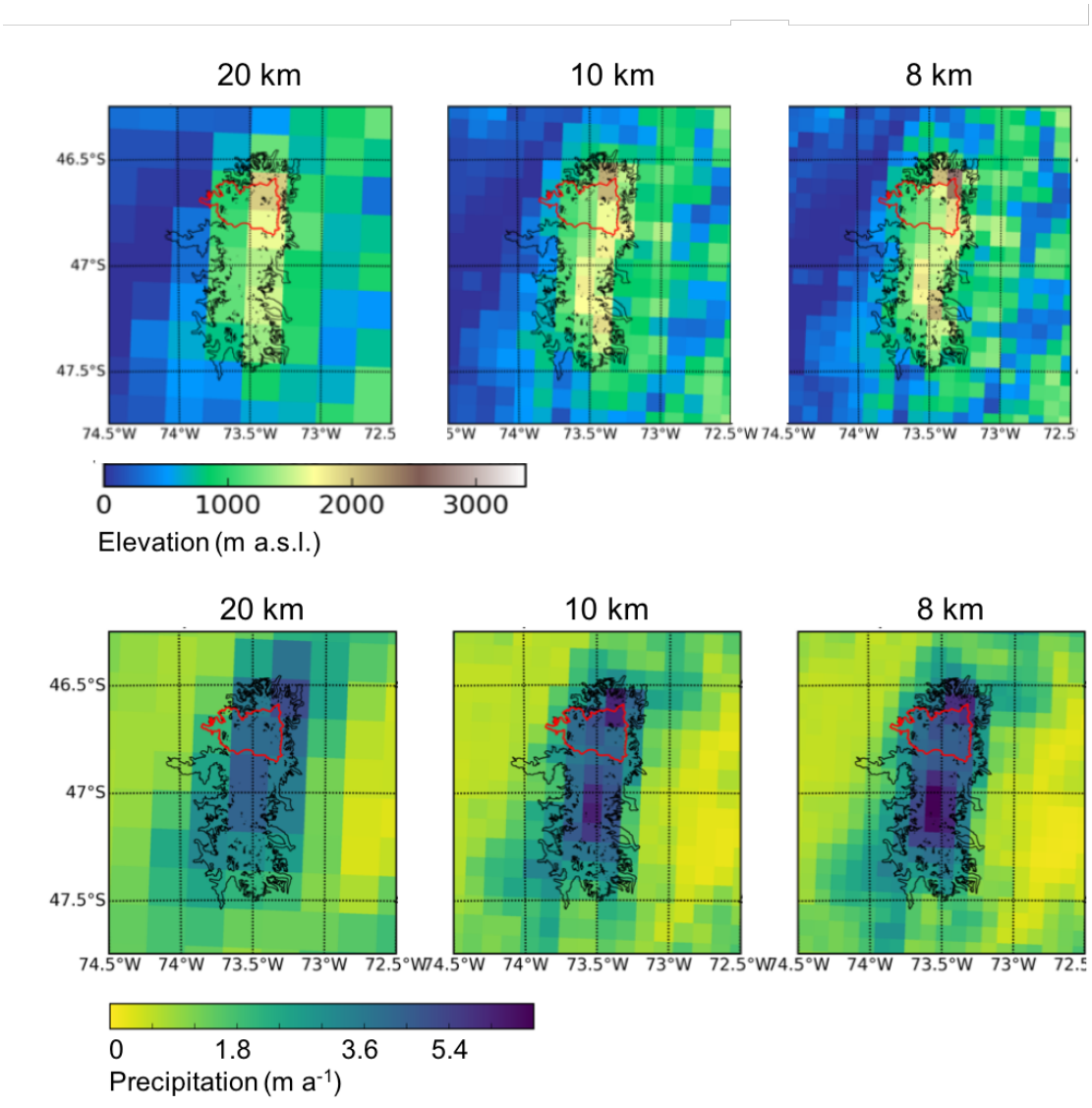


Figure 3.6: Elevation (Top) and 2012 yearly precipitation (bottom) for grid resolutions of 20 km, 10 km and 8 km (from left to right).

Indeed, (i) an enhanced mean humidity leads to more continuous small precipitation amounts during the days characterized by a lack of frontal activity. However, this increase in humidity has no impact on the number of days with frontal activity, i.e., when humidity is already close to 100% and precipitation is already significant. During frontal activity, the model already partially removes the additional humidity input introduced at the lateral boundaries before the fronts reach the Andes. Hence, changing humidity amounts at the boundary do not strongly impact solid precipitation amounts, and our sensitivity test does not reproduce the impact of changes in precipitation with time, which are related to variations in the intensity and in the frequency of strong frontal events. (ii) Conversely, larger humidity amounts induce increased cloud cover and downward longwave radiation. This strongly impacts ablation at low elevations. When large humidity inputs are introduced in the model, this effect has larger impact on the SMB than precipitation changes. As a consequence, this analysis does not offer the sensitivity of SMB to precipitation changes.

As a result of these two competing processes, the total glacier-wide SMB initially increases with the increase in humidity until +7.5% and then decreases due to the increase in melt. These paradoxical effects can be seen in Fig. 3.7 that shows the punctual SMB as a function of elevation.

#### 3.5.1.3 Snow/rain threshold temperature

Changes in the snow/rain threshold temperature also impact solid precipitation and snow accumulation (Table 3.7). As shown in Fig. 3.8, the difference between the simulations decreases with elevation until being almost zero at 2410 m a.s.l. where temperature almost never exceeds 2°C.

Additionally, there is a feedback between snowfall and albedo variations, especially in the ablation zone, where bare ice albedo and melting conditions tend to induce warmer conditions than over the fresh snow cover leading to an higher impact of the snow/rain threshold temperature on the punctual SMB values.

#### 3.5.1.4 Albedo of bare ice and superimposed ice lenses

Small changes in the albedo parameterization also result in important variations in the SMB of SRG. The difference in the glacier-wide SMB reaches 0.85 Gt $a^{-1}$ between the two extreme simulations (see Table 3.8). Changes in the SMB caused by the albedo parameterization are visible at all elevations (Fig. 3.9) showing that the SMB is very sensitive to albedo.

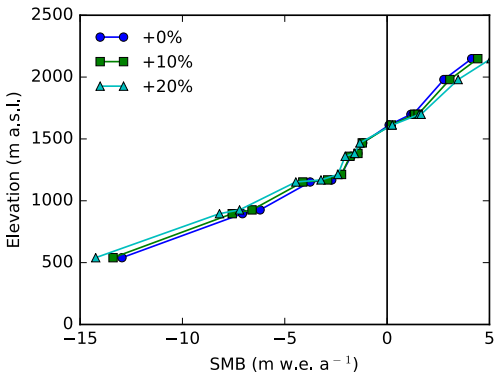


Figure 3.7: Sensitivity of the punctual SMB values versus altitude for different humidity inputs at the boundaries.

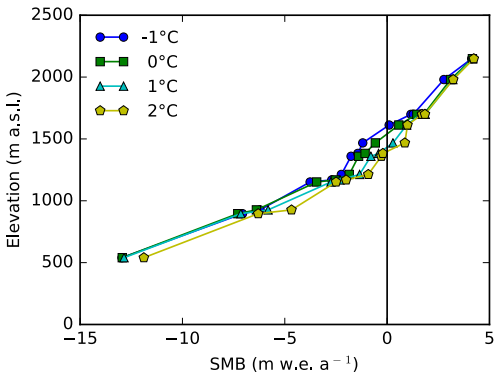


Figure 3.8: Sensitivity of the punctual SMB values versus altitude for different snow/rain threshold temperature values.

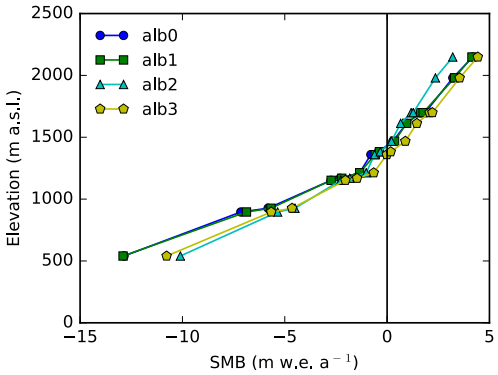


Figure 3.9: Sensitivity of the punctual SMB values versus altitude for different albedo parameterizations.

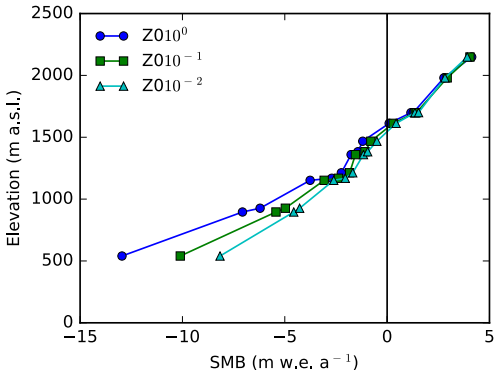


Figure 3.10: Sensitivity of the punctual SMB versus altitude for different surface roughness length.

Table 3.6: SRG SMB, melt and accumulation sensitivity to humidity at the boundaries.

| Sim. | SMB Gt $a^{-1}$ | Melt Gt $a^{-1}$ | Accu. Gt $a^{-1}$ |
|---|---|---|---|
| +0.0 H% | -1.92 | 4.77 | 3.09 |
| +5.0 H% | -1.63 | 5.02 | 3.70 |
| +7.5 H% | -1.64 | 5.13 | 3.82 |
| +10.0 H% | -1.95 | 5.57 | 3.95 |
| +20.0 H% | -2.10 | 6.12 | 4.41 |

Table 3.7: SRG SMB, melt and accumulation sensitivity to snow/rain threshold temperature.

| Sim. | SMB Gt $a^{-1}$ | Melt Gt $a^{-1}$ | Accu. Gt $a^{-1}$ |
|---|---|---|---|
| 0 °C | -1.50 | 5.26 | 4.08 |
| 1°C | -0.89 | 5.19 | 4.61 |
| 2°C | -0.41 | 5.00 | 4.90 |

Table 3.8: SRG SMB sensitivity to albedo parameterization changes.

| Simulation | SMB Gt $a^{-1}$ |
|---|---|
| alb0 | -0.89 |
| alb1 | -0.83 |
| alb2 | -0.72 |
| alb3 | -0.04 |

Table 3.9: SRG SMB sensitivity to momentum roughness length values.

| Simulation | SMB Gt $a^{-1}$ |
|---|---|
| Z0m*$10^{0}$ | -1.92 |
| Z0m*$10^{-1}$ | -1.39 |
| Z0m*$10^{-2}$ | -1.07 |

#### 3.5.1.5 Surface roughness length

The SMB is also very sensitive to the surface roughness length (see table 3.9). A decrease of one order of magnitude induces a SMB decrease of 28%. Because turbulent latent and sensible heat fluxes are often both positive during the melting period, these fluxes induce a high energy source at the glacier surface. Regarding the punctual SMB values at different altitudes (see Fig. 3.10) the impact is very strong at low elevations and decreases with elevation, because positive SEB, and hence melting, are less frequent at high elevations.

#### 3.5.1.6 Summary

As a conclusion, the SMB variations are first controlled by albedo variation, SMB varies by 98% between the simulation alb0 and alb3. Secondly, the snow/rain threshold temperature variation has a large impact on the SMB, since variations from 0°C to 2°C induced changes of +73% in the glacier-wide SMB. Then, surface roughness length is the third parameter that impacts SMB. A 2 order reduction in the magnitude of the surface roughness length has an impact of 44% on the SMB. And finally, changes in the humidity at the boundaries have smaller impacts on SMB. Humidity at the boundaries has a paradoxical impact on the glacier-wide SMB since low and high elevations are impacted differently. The maximun impact on SMB is +15% when the humidity is increased by +7.5%.

A combination of these changes amplifies the impacts. This is particularly true when humidity and snow/rain temperature threshold are both changed: if humidity is increased by +20% and the snow/rain temperature is taken as +2°C, then the increase in SMB is 109%. The combination of these two variables produces enhanced snowfall and accumulation on the plateau that induces larger differences in the glacier-wide SMB.

These results show that temperature has a large impact on the SMB, but that this effect is largely indirect, since it is caused by the occurrence (or not) of snowfall. Snowfall has an important role for the SMB because it impacts both the accumulation and ablation (through albedo changes).

### 3.5.2 Evaluation of the simulations with the observations

The results of the simulations are compared with snow height and temperature measurements on the plateau for the period 2013-2014 and with precipitation and temperature in the valleys for the period 2000-2014 ( see Table 3.10).

Table 3.10: Description and evaluation of the simulations. Comparison of simulations with observed snow height (SH), SMB and precipitation.

| Name | Configuration | | | | SH | | Precip. | | SMB |
|---|---|---|---|---|---|---|---|---|---|
| | H | $T_{s/r}$ | Alb. | Z0 | RMS (m) | Dif. (m) | RMS (m w.e.a$^{-1}$) | Dif. (m w.e.a$^{-1}$) | SRG (Gt a$^{-1}$) |
| sim0 | +0.0% | -1°C | alb0 | $*10^0$ | 2.47 | 4.39 | 0.74 | -0.235 | -1.92 |
| sim1 | +0.0% | 0°C | alb0 | $*10^0$ | 2.48 | 4.16 | 0.74 | -0.235 | -1.50 |
| sim2 | +0.0% | 1°C | alb0 | $*10^0$ | 1.99 | 3.04 | 0.74 | -0.235 | -0.89 |
| sim3 | +0.0% | 2°C | alb0 | $*10^0$ | 1.79 | 2.80 | 0.74 | -0.235 | -0.41 |
| sim4 | +0.0% | 1°C | alb1 | $*10^0$ | 1.83 | 2.82 | 0.74 | -0.235 | -0.83 |
| sim5 | +0.0% | 1°C | alb2 | $*10^0$ | 1.87 | 3.01 | 0.74 | -0.235 | -0.72 |
| sim6 | +0.0% | 1°C | alb3 | $*10^0$ | 1.36 | 2.25 | 0.74 | -0.235 | -0.04 |
| sim7 | +0.0% | 2°C | alb3 | $*10^0$ | 1.30 | 2.14 | 0.74 | -0.235 | 0.20 |
| sim8 | +0.0% | -1°C | alb3 | $*10^{-1}$ | 2.18 | 3.98 | 0.74 | -0.235 | -1.39 |
| sim9 | +0.0% | -1°C | alb3 | $*10^{-2}$ | 2.07 | 3.80 | 0.74 | -0.235 | -1.07 |
| sim10 | +5.0% | 0°C | alb3 | $*10^0$ | 2.16 | 4.00 | 0.73 | -0.231 | -1.63 |
| sim11 | +5.0% | 2°C | alb3 | $*10^{-1}$ | 0.97 | 1.68 | 0.73 | -0.231 | 0.72 |
| sim12 | +5.0% | 2°C | alb3 | $*10^{-2}$ | 0.90 | 1.49 | 0.73 | -0.231 | 1.03 |
| sim13 | +7.5% | 0°C | alb3 | $*10^0$ | 1.95 | 3.70 | 0.72 | -0.047 | -1.64 |
| sim14 | +7.5% | 2°C | alb3 | $*10^{-1}$ | 0.92 | 1.57 | 0.72 | -0.047 | 0.78 |
| sim15 | +7.5% | 2°C | alb3 | $*10^{-2}$ | 0.66 | 1.26 | 0.72 | -0.047 | 1.18 |
| sim16 | +10.0% | 0°C | alb3 | $*10^0$ | 2.14 | 3.90 | 0.74 | 0.143 | -1.95 |
| sim17 | +10.0% | 2°C | alb3 | $*10^{-1}$ | 0.87 | 1.54 | 0.74 | 0.143 | 0.86 |
| sim18 | +10.0% | 2°C | alb3 | $*10^{-2}$ | 0.61 | 1.21 | 0.74 | 0.143 | 1.22 |
| sim19 | +20.0% | 0°C | alb3 | $*10^0$ | 2.50 | 4.27 | 1.28 | 1.010 | -2.10 |
| sim20 | +20.0% | 2°C | alb3 | $*10^{-1}$ | 0.46 | 0.75 | 1.28 | 1.010 | 1.25 |
| sim21 | +20.0% | 2°C | alb3 | $*10^{-2}$ | 0.31 | 0.45 | 1.28 | 1.010 | 1.53 |

SH Dif. is the difference between observed and modeled snow height at the end of the observation period
SH RMS is the root mean square error between observed and modelled snow height during the observation period
Precip. Dif. is the difference between observed and modeled accumulated precipitation at the end of the observation period, averaged between all the stations with precipitation data
Precip. RMS is the root mean square error between observed and modeled monthly precipitation during the observation period, averaged between all the station with precipitation data

For all the simulations, the correlations between observed and modeled daily surface heights are significant (with a correlation coefficient of $R>0.6$ and a p-value $p<0.001$). This shows that the model is able to accurately simulate snowfall, snow densification and snow ablation. However, only few simulations offer surface height changes that fit with observations over the whole observation period. In particular, only one simulation gives similar surface heights until the end of the study period (the simulation sim21, see SH

dif. in Table 3.10). The lowest root mean square (RMS) values computed between observed and modeled values are obtained for simulations accounting for increased humidity boundaries (sims: 11, 12, 14, 15, 17, 18, 20 and 21). These simulations also lead to differences lower than 2 m between modeled and observed surface heights at the end of the study period.

Moreover, the simulated and observed precipitation in the valleys are also in better agreement if humidity inputs at the boundaries are increased (see precip. RMS and Dif. in Table 3.10). The most consistent results are obtained when an increase of 7.5% in humidity inputs is considered, the second best simulation is obtained with an increase of +5.0%, whereas the third best is obtained for an increase of +10%.

Table 3.11 shows the evaluation of the different simulations with the daily temperature on the plateau during the period 2013-2014 (see section 3.4.1 for the location and data characteristic), monthly average temperature for the stations 4 and 8 in the valleys and monthly maxima and minima temperature for eight stations in the valleys during the period 2000-2014 (see Table 3.3 for the station characteristics).

The temperature evaluation shows that all the simulations offer significant correlations with observations on the plateau. All the simulations offer correlation coefficients above 0.88 at a daily time scale, and RMS values ranging between 1.47°C and 1.69°C. On average the temperature is only 0.22°C to 0.84°C higher than the observation. However, better results are obtained on the plateau for simulations presenting higher humidity inputs.

Table 3.11: Evaluation of simulations and comparison with observed daily temperature on the plateau (T1), monthly average temperature at stations s4 and s8 and average values for the eight stations with monthly maxima and minima temperature data.

| Name | Daily av. T1 | | Monthly av. s2 - s8 | | Monthly max. average 8 stations | | Monthly min. average 8 stations | |
|---|---|---|---|---|---|---|---|---|
| | RMS | Dif. | RMS | Dif. | RMS | Dif | RMS | Dif. |
| sim0 to sim9 | 1.6 | 0.8 | 0.7 - 0.8 | 0.4 - -0.3 | 2.3 | -1.0 | 1.5 | -0.1 |
| sim10 to sim12 | 1.6 | 0.7 | 0.7 - 0.8 | 0.4 - -0.3 | 2.2 | -1.0 | 1.5 | -0.2 |
| sim13 to sim15 | 1.6 | 0.7 | 0.7- 0.8 | 0.4 - -0.3 | 2.1 | -0.8 | 1.6 | 0.3 |
| sim16 to sim18 | 1.5 | 0.5 | 0.8- 0.9 | 0.3 - -0.4 | 2.0 | -0.8 | 1.6 | -0.5 |
| sim19 to sim21 | 1.5 | 0.2 | 0.8 - 1.0 | -0.1- -0.7 | 1.7 | -0.4 | 1.9 | -1.2 |

RMS is the root mean square error between the observed and modeled temperatures
Dif. is the average difference between the observed and modeled temperatures

Temperatures in the valleys are also very well represented at monthly and yearly time scales, the correlation coefficients are above 0.87 for the two stations s4 and s8 in Table 3.3. The RMS range between 0.7°C and 1.0°C and difference are below 0.7 °C. This difference is small considering the model resolution (8 km).

Among the simulations, those including more humidity are in better agreement with

observations from station s4, whereas simulations with less humidity are in closer agreement with temperature observed at station s8.

Because the maximum and minimum temperatures are available at a larger number of stations around NPI than for the mean temperature, we also analyzed temperature extremes. Simulated temperature maxima show high correlations with observations in the valleys (R always above 0.83, $p<0.001$), with RMS values ranging between 1.6°C and 3.3°C. The mean differences between observed and modeled temperature are always ranging between -2.5°C and 1.2°C for both minima and maxima. Even if the differences are larger than for the mean observed temperature, these differences are small, showing the good agreement between the model and the observations in terms of temperature. Finally, simulations with more humidity give more accurate results in the case of maxima whereas simulations with less humidity are closer to observations in terms of minima (see table 3.11).

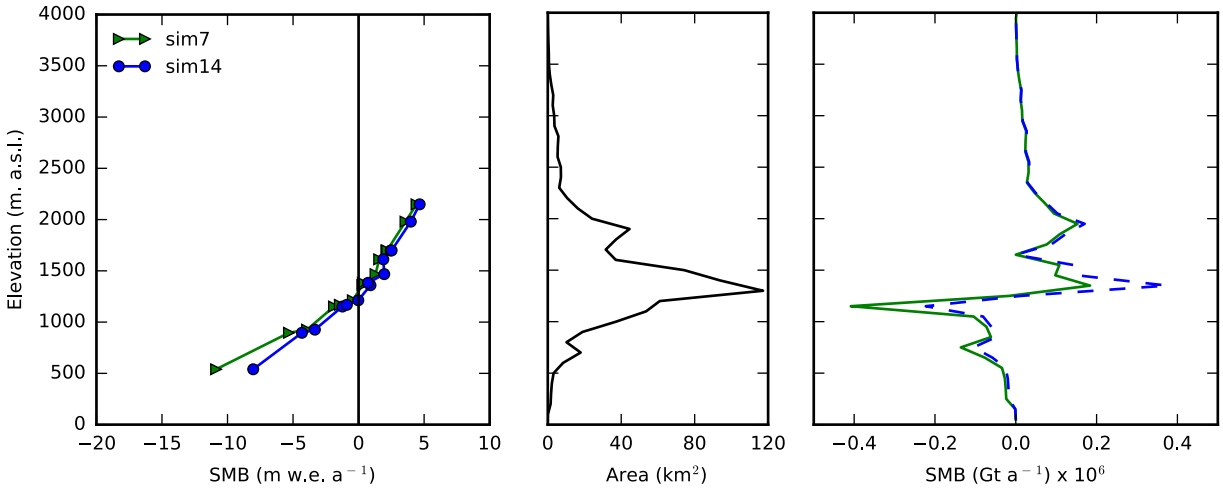


Figure 3.11: SMB results for sim14 and sim7 during the period 2013-2014. Punctual SMB versus elevation in sim14 and sim7 (left), SRG hypsometry (center) and SMB in Gt $a^{-1}$ for each elevation range (right).

The glacier-wide SMB of SRG from the different simulations over the period (2013-2014) cover a wide range of values from -1.92 to 1.53 Gt $a^{-1}$ with a standard deviation equal to 1.23 Gt $a^{-1}$ (Table 3.10).

As already stated, very small changes in accumulation on the plateau can have large impacts on the glacier-wide SMB. To illustrate this efects we show the punctual SMB as function of the altitude for the simulation 7 and 14 in Fig. 3.11. The glacier wide SMB for these two simulations are respectively 0.20 Gt $a^{-1}$ and 0.78 Gt $a^{-1}$.

We observe that the simulation sim7 presents lower punctual SMB than the simulation 14 at all elevations, and the largest difference is observed at the lowest locations. However,

the zone inducing the largest differences in the glacier-wide SMB is located between 1200 and 1600 m a.s.l.. This altitude range corresponds to the plateau and thus to the largest area (53%, see Fig. 3.11center and left). This analysis shows that simulations with similar performance when compared to the weather stations can have large differences in terms of glacier wide SMB.This shows the difficulty in assessing the glacier wide SMB with a unique simulation, even if it has been calibrated with the available observations.

### 3.5.3 Selection and description of the best simulation

Here, we give more details on the comparison of the model with the observations. For this, we select a simulation using the results from the previous section.

The selected simulation is sim14, in which humidity input was increased by 7.5%, the minimum albedo was increased (see albedo changes proposed in option 3), the snow/rain temperature threshold was taken equal to 2°C and the surface roughness length was decreased by one order of magnitude. This simulation is a compromise between accurate surface height changes (RMS $<$ 1 m) and a good representation of precipitation amount (i.e., minimum difference between observed and observed precipitation in low lying areas, with RMS = 0.74 m w.e. $a^{-1}$, as shown in table 3.10). Considering temperature, the simulation sim14 is not the best one, but it is still within the best ones if we only refer to measurements done over the plateau (The mean difference with observations is only 0.7°C). Mean, maximum and minimum temperature values are correctly reproduced in the valleys, and this simulation is only within the middle quality ones (see table 3.11). Finally, compared to other simulations that also fulfill these criteria: sim14 is the closest to the punctual SMB in-situ data (not shown) and albedo is improved with respect to other albedo configurations, as shown hereafter.

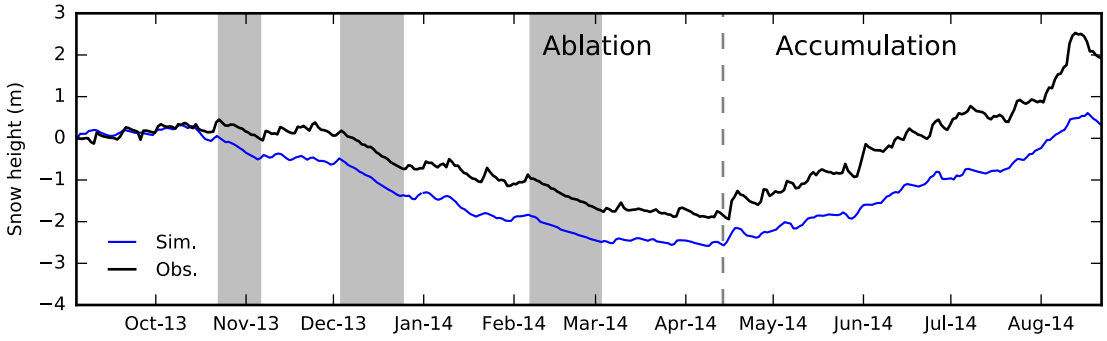


Figure 3.12: Observed and simulated snow height for the selected simulation (sim14). Grey areas correspond to the main ablation periods and dotted line separates the ablation and accumulation period.

#### 3.5.3.1 Surface height changes

Surface height changes given by sim14 are compared with observations in Fig. 3.12. The three largest ablation events are reproduced with an accurate timing. However, the cumulative ablation bias when ablation stops at the beginning of March is already 0.6 m. After this date, we observe that a period with stable surface height conditions is correctly reproduced. Then, at the middle of April, when accumulation starts to increase, the occurrence of snowfall is correctly reproduced, but slightly lower accumulation amounts are simulated, leading to a cumulative accumulation of 2.91 m of snow at the end of winter, versus 3.87 m for the observation. The final surface height difference, at the end of the observed period, between observation and simulation is 1.57 m. However, this difference might be accounted for by the possible differences in density existing between modeled and simulated snow layers, and the potential impact of snow erosion or deposition processes at the study site, which are not considered in this simulation with MAR.

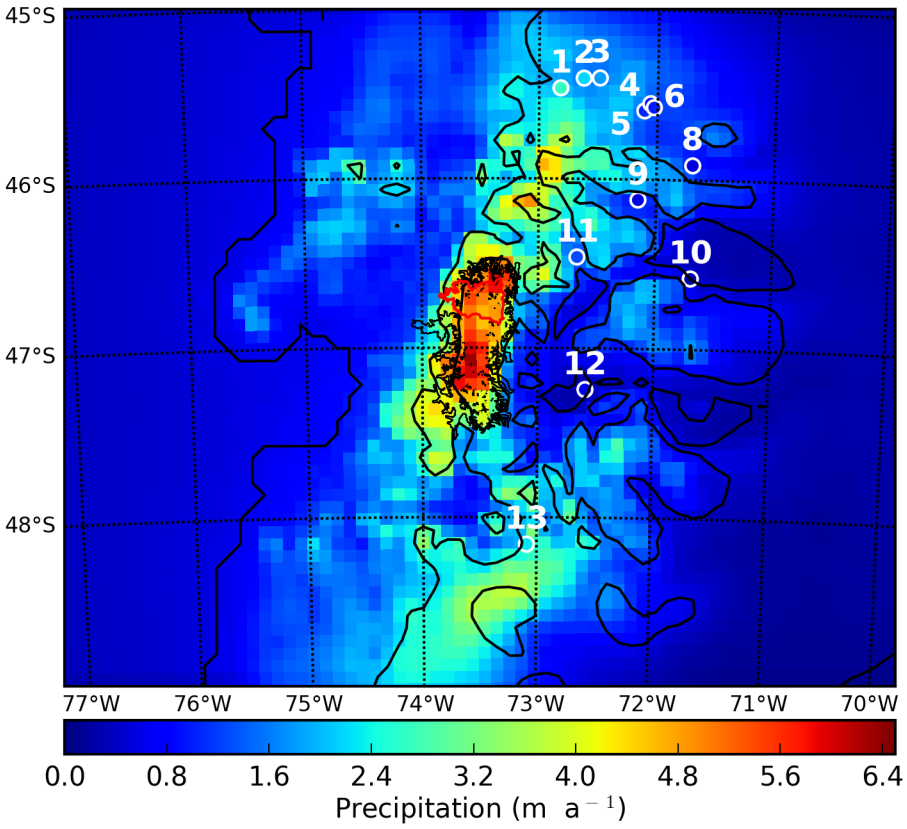


Figure 3.13: Mean annual precipitation: selected simulation (background) and weather station observation (circles).

#### 3.5.3.2 Monthly and annual average precipitation

The simulated annual average precipitation, for the period 2000 to 2014, is presented in Fig 3.13. We observe that orographic precipitation at the western side of NPI induces high precipitation at cells of highest elevation, associated with the highest peak of NPI (6.3 m $a^{-1}$ at 2410 m a.s.l.). The annual average precipitation observed at the stations located close to the ocean is larger in the simulation than at station 1,2,3 and 13 (see Fig. 3.13), whereas annual average precipitation is generally well represented elsewhere with average yearly discrepancies within -0.4 and -0.8 m $a^{-1}$ (see table in appendix). The sub-estimation of precipitation by the model at the west is mainly due to the topography and resolution of the model, because the model does not represent the narrow valleys at the end of which these stations are located, and the simulated precipitation appears to fall in regions located at the west (i.e. closer to the ocean) in the model compared to the observations. An example of this effect occurs for station 3, El Balseo (see Fig. 3.13 and Fig 3.14).

The foehn effect occurring at the eastern side of NPI is correctly represented by the model. MAR proposes much smaller precipitation at the eastern than at the western side, and modeled precipitation is in agreement with observations from the weather stations (see values for stations 4 - 11, in Fig. 3.13). The differences in mean annual precipitation at these stations range between -0.3 and 0.4 m $a^{-1}$. An example is the observed precipitation at station 9 (Villa Cerro Castillo) wich is overestimated by the model (0.3 m $a^{-1}$, see Fig. 3.15).

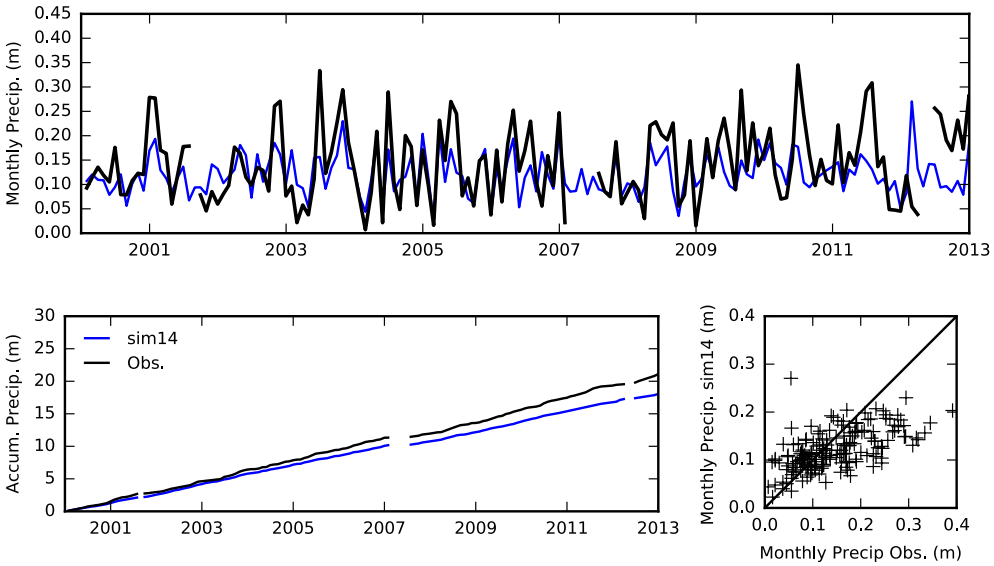


Figure 3.14: Precipitation form the selected simulation and observations at station 3 (El Balseo). Monthly precipitation (top), monthly accumulated precipitation (bottom left) and comparison between monthly observed and modeled precipitation (bottom right).

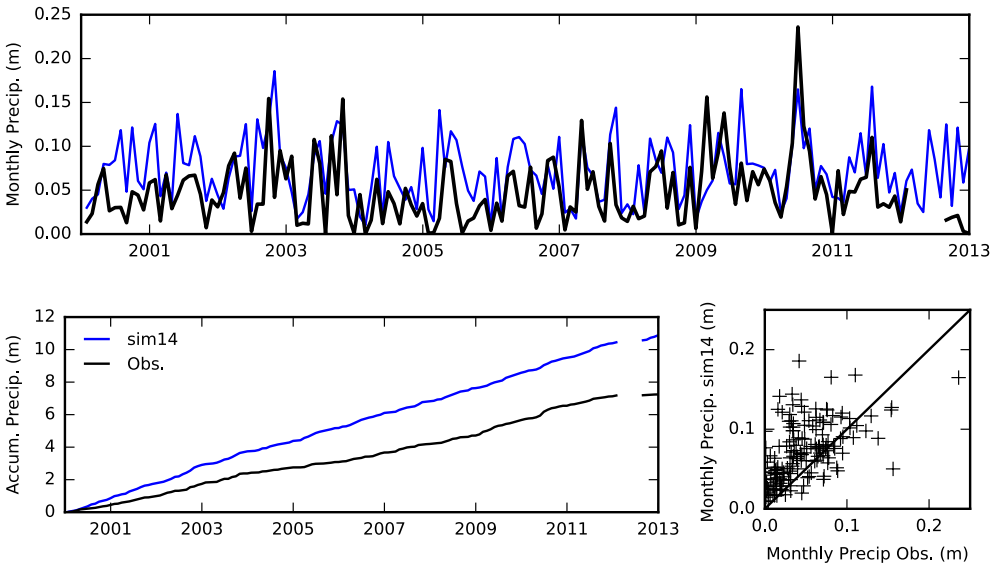


Figure 3.15: Precipitation from the selected simulation and observations at station 9 (Villa Cerro Castillo). Monthly precipitation (top), monthly accumulated precipitation (bottom left) and comparison between monthly observed and modeled precipitation(bottom right).

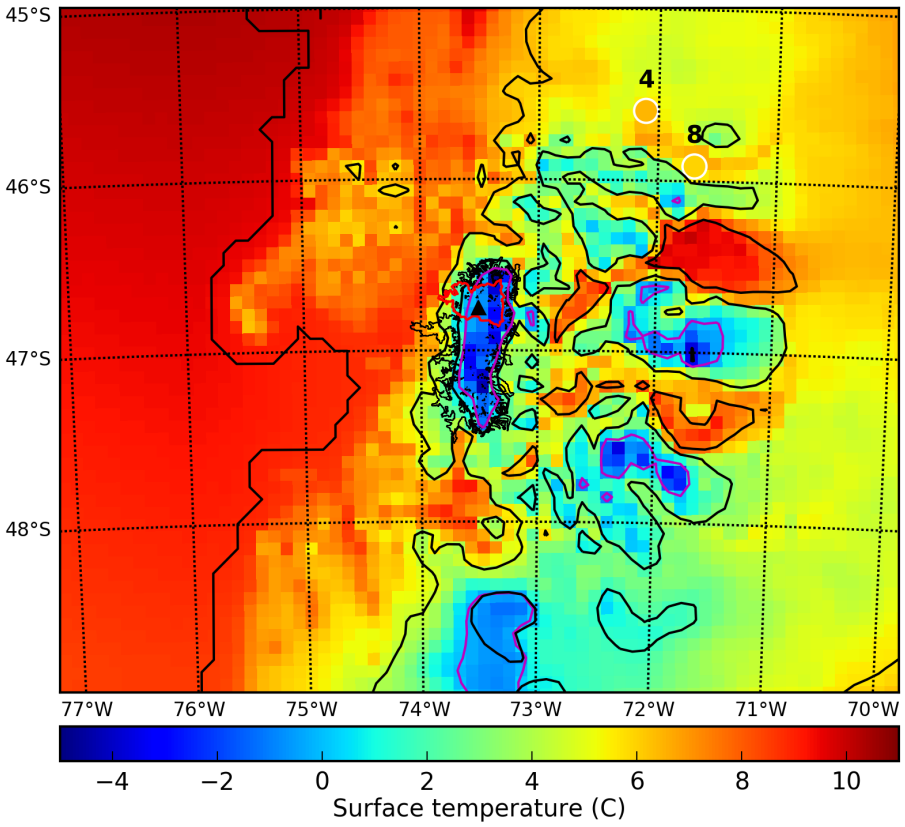


Figure 3.16: Mean annual surface air temperature simulated by MAR (in sim14) and observed at station 4 and station 8. The black triangle corresponds to the location of temperature observations on NPI plateau.

#### 3.5.3.3 Air temperature

The spatial distribution of the mean annual surface air temperature, and its relationship with elevation is correctly reproduced by the model (Fig. 3.16). Very low elevation areas located close to the Pacific Ocean present the highest temperature over the domain (around 8-11°C), whereas minimum temperatures are found for the highest cells (-4.6°C at 2410 m a.s.l.). The mean temperature simulated at s4 and s8 stations is equal to 6.1°C and 6.3°C respectively, and is very close to the observed temperature (6.5°C and 6.0°C, respectively). As described before, the modeled temperature is highly correlated with observations (R≥0.87). Maximum and minimum temperature values are also close to observations with differences below 1.0 °C for 5 of the 8 stations studied here (tables and figures in appendix).

The temperature simulated on the plateau (-0.9°C) is very similar but somewhat lower than the observed one (-1.5°C, Fig. 3.17). The main difference comes from some extremely cold days, which are incorrectly represented by the model. The model also overestimated some very warm days during summer.

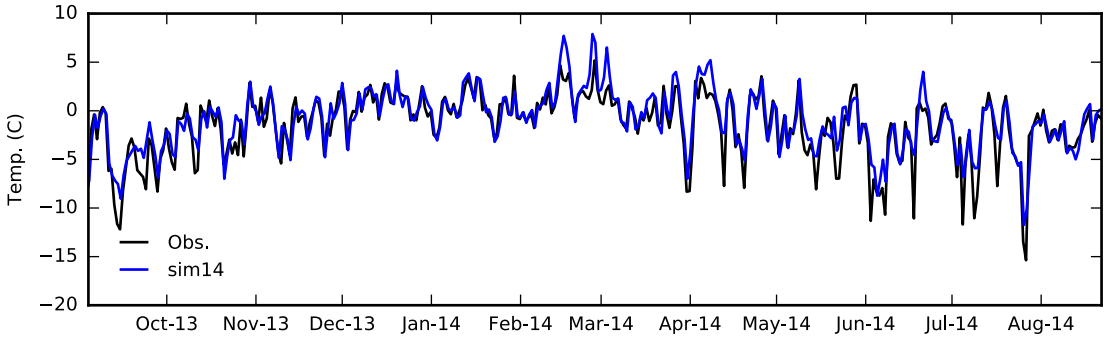


Figure 3.17: Simulated (in sim14) and observed daily temperature on the plateau.

#### 3.5.3.4 Surface albedo

The albedo simulated by the model is compared to the one given by the MODIS images (Section 3.4.3). Validation of MAR albedo is done for an area located close to the ELA, and close to the snow tower on the SRG plateau (Fig. 3.18). Comparisons between MODImLab and MAR albedo values is done over 2013-2014 for the selected simulation (sim14) and the sim1 (hereafter referred to as the reference simulation) to cover the different ranges of simulated albedos. The main difference between these two simulations, is a higher albedo of sim14 in the periods of high ablation, which makes the difference in total ablation at the end of the period. But on average the differences are not very large, with an average albedo of 0.75 and 0.79 for sim14 and sim1, respectively.

Albedo from the selected simulation (sim14) is slightly closer to the observations than the albedo given by sim1 (see Fig. 3.18 and Fig. 3.19), however the difference is not significant. In both simulations the variations of albedo range within those displayed by MODImLab estimations (RMS = 0.004 and RMS = 0.005 respectively), demonstrating that the model accurately calculates this parameter. Nevertheless, there is a discrepancy that can have an impact on the modeled SMB. The simulated albedos are never very high (<0.89) while albedo from MODImLab reaches 0.91. This difference is due to the temporal resolution difference between the simulated albedo (daily average) and the albedo from MODIS (instantaneous).

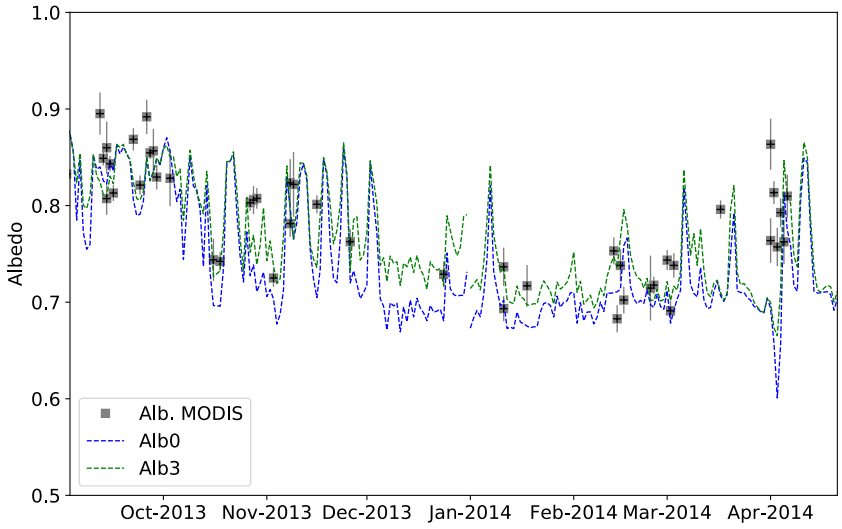


Figure 3.18: Temporal variations of simulated daily albedo from the selected simulation (sim14 and the reference simulation (sim1), and albedo obtained with MODImLab at at 14h-15h Local Time (LT).

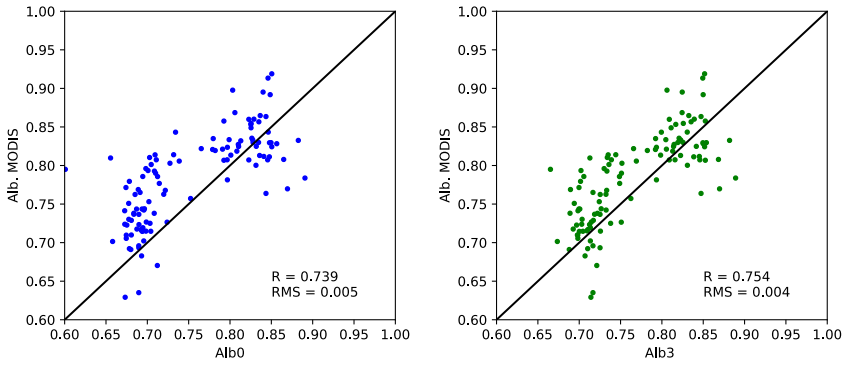


Figure 3.19: Comparison between simulated daily albedo from the selected simulation (sim14 and the reference simulation (sim1), and albedo obtained with MODImLab at 14h-15h Local Time (LT)., sim1 (right), and sim14 (left).

#### 3.5.3.5 Mean surface energy balance

This section presents the description and analysis of the energy fluxes and SEB on the NPI, using the results from the selected simulation during the years 2013-2014.

MAR computes the energy fluxes and the SEB over snow and ice for any cell with more than 1% of ice. Comparison of fluxes at different elevations allows describing changes in ablation processes over the glacier, even if biases in turbulent heat fluxes and outgoing longwave radiation may be found at low elevations when surfaces covered by ice are negligible and rock surfaces induce a warm bias in the low atmosphere, due to the difference between the model resolution (8 km) and glacier tongue widths of 1-2 km. Indeed, the cells at the lowest parts of NPI are a combination of ice, rocks and land, but ice corresponds to a very limited percentage of the cells.

The comparison of mean energy fluxes demonstrate that the net shortwave radiation budget is the first main energy input at the surface, suggesting that albedo is a key variable of the SEB of NPI (see Table 3.12). The contribution of turbulent heat fluxes is positive at any elevation, even if the turbulent sensible heat flux decreases with elevation due to air cooling and is slightly negative above the ELA (Fig. 3.20). The solid condensation is significant at all elevations, and almost compensates for cooling of the surface caused by the net longwave radiation energy sink. Indeed, net longwave radiation is negative, suggesting that incoming longwave radiation is close to 260-280 W m $^{-2}$ over the glacier, in spite of the warm, cloudy and wet conditions of Patagonia. Nevertheless, this value highly depends on the way the MAR computes the radiation budget in the atmosphere, and in particular the impact of clouds. Finally, the turbulent sensible heat flux is weak and decreases with elevation until reaching negative values in the accumulation zone of the glacier. The SEB computed by the MAR for NPI is very similar to the one modeled with the same model on Cook Ice Cap at Kerguelen (*Verfaillie*, 2018), where climate conditions are alike because they are located at the same latitude, giving confidence to the results.

Table 3.12: Mean energy fluxes during the period 2013-2014.

| $SWT$ | $LWT$ | $H_l$ | $H_s$ | Total |
|---|---|---|---|---|
| W m$^{-2}$ | W m$^{-2}$ | W m$^{-2}$ | W m$^{-2}$ | W m$^{-2}$ |
| 42 | -36 | 29 | 10 | 45 |

$SWT$ is net short wave radiation, $LWT$ is net long wave radiation, $H_l$ is turbulent latent heat flux and $H_s$ is turbulent the sensible heat flux

Albedo variations control the temporal (Fig. 3.18) and spatial changes (Fig. 3.20) of ablation. Albedo variations are directly related to snowfall occurrences, and this relationship largely imposes changes of the net short wave radiation (SWT) with elevation, and

the ELA. This link largely justifies the strong relationship between snowfall amounts and the SMB at the scale of the glacier. Additionally, as albedo variations are closely related to the phase of precipitation, they are also linked to temperature.

#### 3.5.3.6 Summary

In conclusion, taking into account the coarse resolution of the model (8 km), the selected simulation (sim14) offers a correct representation of surface height, temperature and albedo variations on the plateau. Mean observed precipitation and temperature and their variations are accurately reproduced by the model in the surroundings of NPI. The selected simulation parameterization is used to simulated the long term SRG and NPI SMB, from 1980-2014.

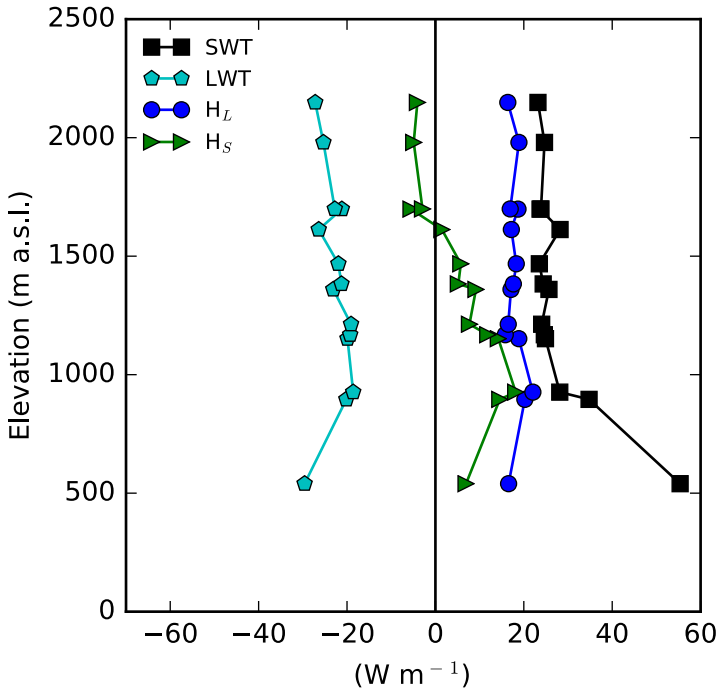


Figure 3.20: Mean energy fluxes versus altitude for SRG during the period 2013-2014.

### 3.5.4 Reconstruction of the 1980-2014 NPI and SRG surface mass balance

#### 3.5.4.1 Average results

This subsection presents the mean modeled SMB over the entire period 1980-2014, using the sim14 parameterization.

During the period 1980-2014, the mean punctual SMB values were -10.0 m w.e. a$^{-1}$ at 201 m a.s.l. and 4.8 m w.e. a$^{-1}$ at 2410 m. a.s.l.. These elevations correspond to the

lowest and highest cells of the model grid (see Fig. 3.21). The equilibrium line altiude (ELA) was 1257 m a.s.l..

Melting amounts decreased with elevation, and changed from -10.5 m w.e. $a^{-1}$ at 201 m a.s.l. to 0.1 m w.e. $a^{-1}$ at 2410 m a.s.l.. The accumulation was very low (<0.1 m w.e. $a^{-1}$) in the lowest zones and increased until reaching 4.7 m w.e. $a^{-1}$ at 2410 m a.s.l.. Solid condensation (and not sublimation) was 0.27 m w.e. $a^{-1}$ at 201 m a.s.l. and 0.08 m w.e. $a^{-1}$ at 2410 m a.s.l. with only small changes with elevation, as a consequence of high humidity amounts even though solid condensation was weaker on the eastern side of NPI due to the foehn effect.

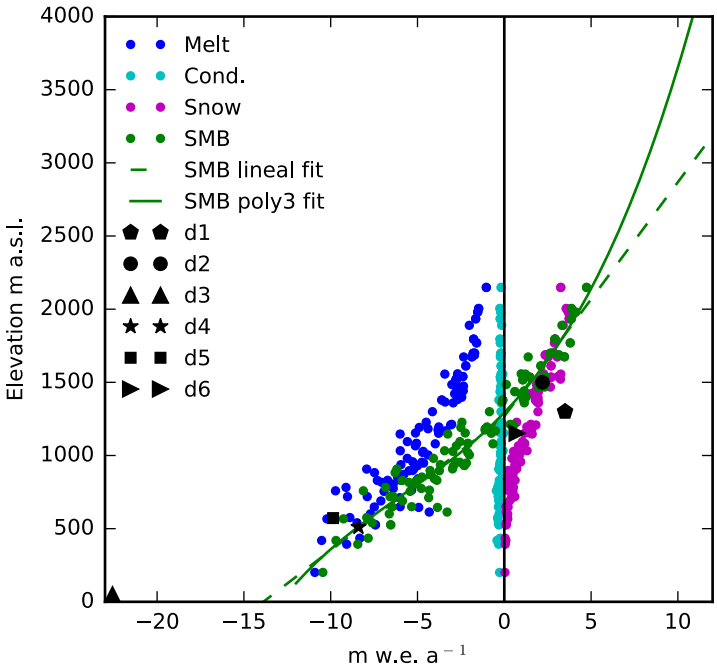


Figure 3.21: SMB, melt, snow fall and sublimation of NPI versus altitude, during 1980-2014. The green solid line corresponds to the third-degree polynomial fit and the dotted line corresponds to linear fits in the ablation and accumulation zones, d1 to d6 correspond to in-situ measurements describe in Table 3.5.

As was explained in the methods, a piece-wise linear function between the punctual SMB values and altitude is used in order to compute the glacier-wide SMB of SRG. Two distinct lines are fitted in the ablation and in the accumulation zones as proposed by *Osmaston* (2005b). A third-degree polynomial fit is also applied to the SMB over the entire range of altitude, because this is more in agreement with the shape of the SMB variation and the slight decrease of precipitation at high elevations. The glacier-wide SMB are computed using these equations and elevation from SRTM2000. The SMB map from the polynomial method is presented in Fig. 3.22. The interpolation uncertainty corresponding to punctual SMB values was estimated with the RMS between results and the fitted line, and is equal to 0.5 m w.e. $a^{-1}$.

The comparison with the punctual SMB in-situ measurements (Table 3.5 and Fig. 3.21) shows an acceptable agreement between observed and simulated values taking into account the model resolution with differences <3.5 m w.e. $a^{-1}$, except for one very negative measurement in the ablation zone.

Differences between the north vs. south and west vs. east sides of the icefield were identified by fitting linear trends in each region separately. The only significant difference is between the ablation zones of the north-western and the north-eastern sides of NPI (Fig. 3.23). In these areas, the punctual SMB at the same altitude are lower on the east side due to increased melting associated with the foehn effect. The linear trend computed in the ablation zone of the north-western side of NPI has the same slope as on the north-eastern side, but the ELA is shifted 163 m downward and is located at 1211 m a.s.l. instead of 1375 m a.s.l..

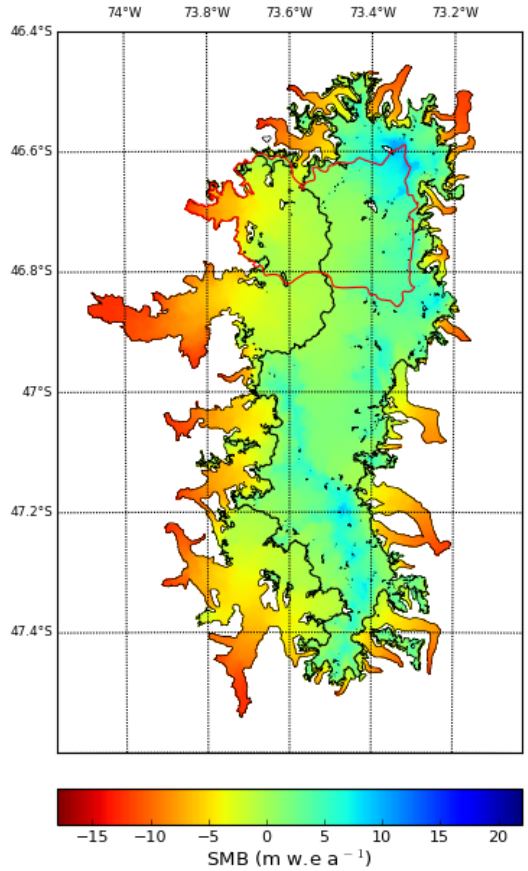


Figure 3.22: Mean SMB interpolated with the third-degree polynomial method (1980-2014). The red line corresponds to the SRG basin and the black line corresponds to the ELA.

The SMB has been computed for NPI, SRG and the 3 biggest non-calving glaciers of the icefield. The results are compared to the MB given by the geodetic methods from *Dussaillant et al.* (2018) and *Willis et al.* (2012a) for the period, in Table 3.13. For Exploradores and HPN4 glaciers, the SMB estimates given by the MAR are slightly less

negative than the MB, but for HPN1 glacier, the SMB and MB are very similar and within the uncertainty range of both SMB interpolation and geodetic calculations. Differences are likely due to the model resolution and uncertainties, in particular because modeling the SMB in the low elevation areas requires high resolution due to the size of valley glaciers with a 1-2 km width. With respect to the differences between the non-calving glaciers, MAR results can capt this difference, with much more negative values at HPN1 than at Exploradores and HPN4. Values are also closer to *Willis et al.* (2012a) than *Dussaillant et al.* (2018). Therefore, for non-calving glaciers, our calculations reflect that MAR is able to accurately reproduce the MB changes and main differences observed between glaciers of NPI.

As a conclusion, if we make the strong assumption that model and observation uncertainties are limited, the differences between the SMB and MB of NPI should reflect the total calving flux of the icefield. Here, we compute a calving flux of 0.95-1.34 m w.e. $a^{-1}$ for NPI, that is 3.76-5.30 Gt $a^{-1}$ during the period 2000-2012. For SRG, calving flux estimated from the difference between MB and SMB is very small and equal to 0.28-0.35 m w.e. $a^{-1}$ (0.21-0.27 Gt $a^{-1}$).

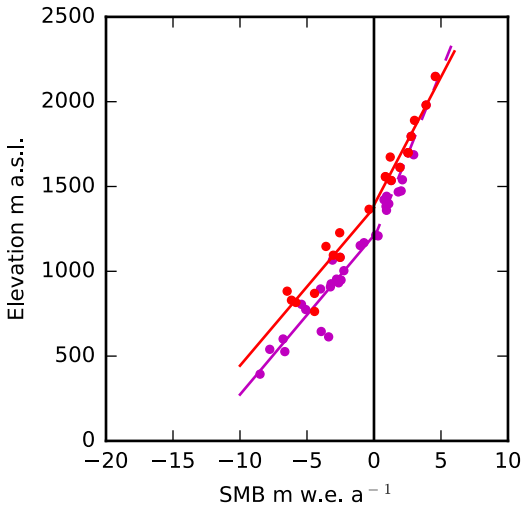


Figure 3.23: SMB at the NW (magenta points) and NE (red points) versus altitude, during 1980-2014. The lines are the linear fits in the ablation and accumulation zones for each region, NW (magenta) and NE (red).

### 3.5.4.2 Temporal trends

The annual glacier-wide SMB of NPI over the period 1980-2014 showed a slight increasing trend with time of 0.05 Gt $a^{-2}$ (Fig. 3.24) but with important inter-annual variations (standard deviation of 6.1 Gt $a^{-2}$). The considerable difference from year to year demonstrates the high sensitivity of the SMB to meteorological conditions. This

slightly increasing trend was common to the four quadrants of NPI (trends in the north-western, north-eastern, south-western, south-eastern sectors are 0.02, 0.04, 0.01 and 0.01 Gt $a^{-2}$, respectively).

Focussing on SRG, where results are better constrained, a slightly increasing trend is observed (0.02 Gt $a^{-2}$). This change was due mainly to decreasing melting (-0.01 Gt $a^{-2}$) and stable accumulation amounts. Temperature and zonal wind speed were both slightly increasing (See Fig 3.25), leading to a slight increase in total precipitation.

The annual SMB of SRG and its main components (melting and snowfall; sublimation is negligible) are compared with the annual values of the main meteorological variables (temperature, precipitation, and wind speed). The correlations between SMB and melting or SMB and snowfall are similar, demonstrating that accumulation and ablation had similar key impacts on the final SMB (see Table 3.14 and Figs 3.26 and 3.27). Moreover, air temperature and zonal wind speed over the glacier also presented a significant correlation with the SMB (R=0.63; p<0.001) and (R=0.6; p<0.001) respectively) demonstrating again the key influence of temperature on accumulation and melt, and the particularly strong contribution of orographic precipitation to the total precipitation on the icefield (*Garreaud et al.*, 2009).

More generally, significant correlations (p<0.001 except for correlation between SAM and zonal wind) are found between accumulation and temperature (Fig. 3.28), but also between temperature and total precipitation. Accumulation (and precipitation) are also related to the zonal wind speed (see Table 3.15). These relationships are expected because winds coming from the Pacific Ocean control climate over Patagonia, and have a key control on the ratio of snow/rain falling on the icefield.

To analyze the relationship with large scale atmospheric circulations and surface state, the atmospheric conditions (air temperature and zonal wind) in a rectangular domain (46°S - 48°S and 77°W - 76°W) at the same latitude over the Pacific Ocean are correlated with the SMB of SRG. Correlation coefficients are significant (R=0.81, $p < 0.001$) and (R=0.51, $p=1.7\times10^{-3}$) for temperature and wind speed respectively, showing the close relationship between the SMB and the conditions observed over the Pacific Ocean.

Finally, the SMB variations are compared with climatic index of the main atmospheric modes in the studied region, i.e. the SAM-index estimated by NOAA following *Gong and Wang* (1999) (https://www.esrl.noaa.gov), and El Niño-index (El Niño3.4 index estimated by NOAA *Rayner et al.* (2003)). A significant correlation is found between the SAM index and zonal wind speed over SRG (Fig. 3.29) and in the ocean. This relation is related to the link existing between the pressure gradient between the mid-latitudes and the polar zone, the baroclinic intensity and the zonal winds in the region. Finally, no significant correlation is found with other indexes, and in particular with El Niño events.

Table 3.13: SMB results and MB from geodetic methods.

| SMB | SMB 2000-2012 | MB* 2000-2012 | MB 2000-2012 |
|---|---|---|---|
| | | *Dussaillant et al.* | *Willis et al.* |
| source | this study | (2018) | (2012a) |
| | m w.e.a$^{-1}$ | m w.e. a$^{-1}$ | m w.e. a$^{-1}$ |
| NPI | -0.09± 0.05 | -1.25±0.09 | -0.86 |
| SRG | 0.65±0.03 | -0.93±0.25 | -1.0 |
| Exploradores | -0.36± 0.24 | -1.01± 0.12 | -0.56 ±0.63 |
| HPN1 | -2.16 ±0.07 | -2.30± 0.24 | -2.19 ± 0.52 |
| HPN4 | -0.20± 0.20 | -1.38± 0.15 | -0.54 ± 0.61 |

* The MB correspond to the ASTER method from (*Dussaillant et al.*, 2018), which have the highest % of measured area on the glaciers

Table 3.14: Average glacier-wide values and temporal trends of different variables over SRG between 1980 and 2014.

| Variable | g-w* | Trend | R | p |
|---|---|---|---|---|
| SMB (Gt a$^{-1}$) | 0.86 | 0.02 | - | - |
| Melt (Gt a$^{-1}$) | 3.81 | -0.01 | 0.85 | $2.1\times10^{-10}$ |
| Accum. (Gt a$^{-1}$) | 5.10 | 0.01 | 0.91 | $7.5\times10^{-14}$ |
| Total Precip. (Gt a$^{-1}$) | . 6.71 | -0.02 | 0.43 | $9.5\times10^{-3}$ |
| Temp. (°C) | -1.5 | 0.01 | 0.63 | $6.2\times10^{-5}$ |
| Wind. (m s$^{-1}$) | 4.5 | 0.01 | 0.61 | $1.3\times10^{-4}$ |

∗ g-w are average glacier-wide values during the period 1980-2014, Accum. is accumulation, Trend is the annual trend, R is Pearson's correlation coefficient and p is the statistical significance of Pearson's correlation coefficient

Table 3.15: Correlation between the SMB of SRG and glacier-wide average of different variables and indexes during the period 1980-2014.

| Correlations | R | p |
|---|---|---|
| Accumulation - Zonal wind | 0.76 | $1.5\times10^{-7}$ |
| Total precip. - Zonal wind | 0.58 | $2.8\times10^{-4}$ |
| Accumulation -Temp. | -0.61 | $1.4\times10^{-4}$ |
| Total precip. - Temp. | -0.58 | $3.1\times10^{-4}$ |
| SAM index - Zonal wind | 0.37 | $4.1\times10^{-2}$ |
| SAM index - Zonal wind (Ocean) | 0.50 | $4.0\times10^{-3}$ |
| SMB - Temp. (Ocean) | 0.81 | $5.5\times10^{-9}$ |
| SMB - Wind. (Ocean) | 0.51 | $1.7\times10^{-3}$ |

(ocean) refers to average over a rectangular domain in the ocean at the same latitude than the NPI (46°S - 48°S and 77°W - 76°W), R is Pearson's correlation coefficient and p is the statistical significance of Pearson's correlation coefficient.

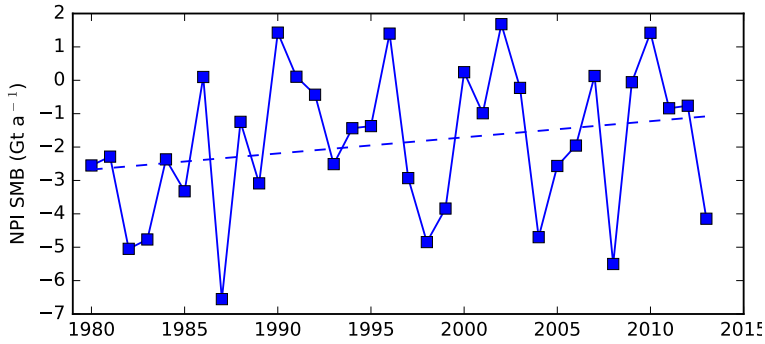


Figure 3.24: Annual values of the SMB of NPI between 1980 and 2014. The dotted line corresponds to the linear trend.

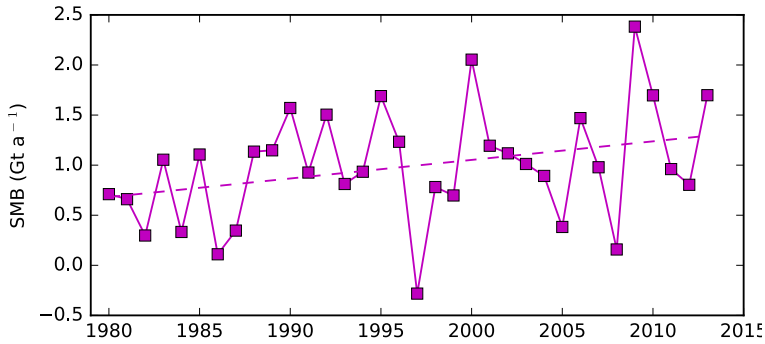


Figure 3.25: Annual values of the SMB of SRG between 1980 and 2014. The dotted line corresponds to the linear trend.

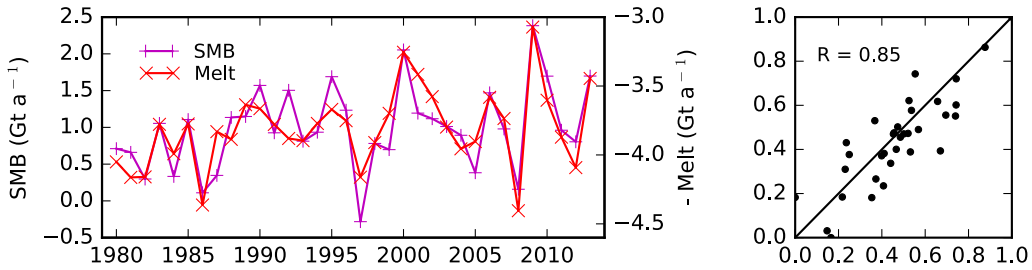


Figure 3.26: Annual SMB and melt over SRG during the period 1980-2014. Temporal variations (left) and comparison between normalized values of SMB versus melt (right).

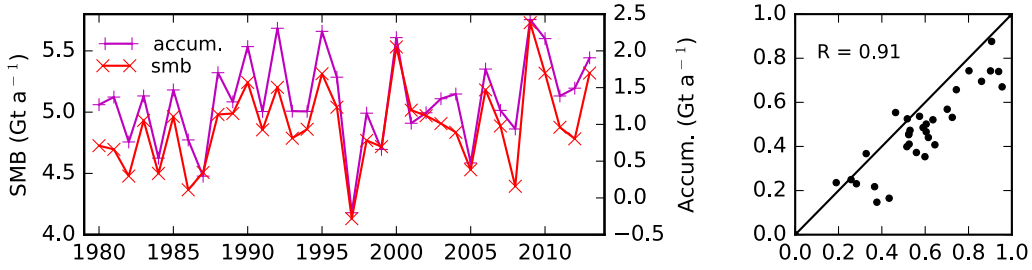


Figure 3.27: Annual SMB and accumulation over SRG during the period 1980-2014. Temporal variations (left) and comparison between normalized values of SMB versus accumulation (right).

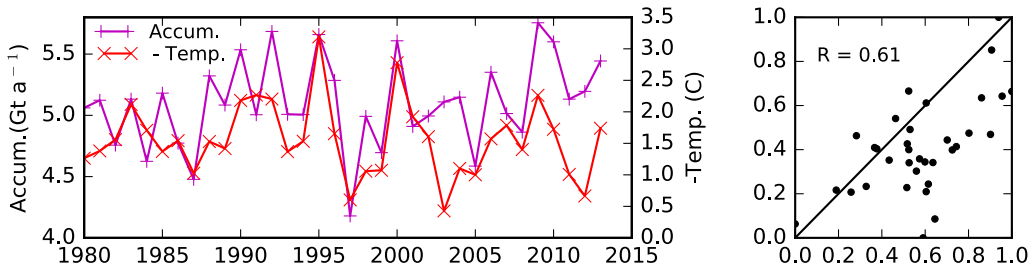


Figure 3.28: Annual temperature and accumulation of SRG between 1980 and 2014. Temporal variations (left) and comparison between normalized values of temperature versus accumulation (right).

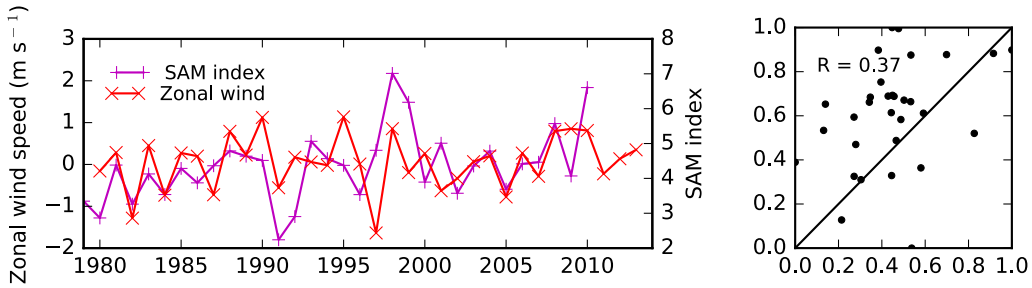


Figure 3.29: Annual SAM-index and average zonal wind over SRG between 1980 and 2014. Temporal variations (left) and comparison between normalized values of SAM-index versus zonal wind (right).

#### 3.5.4.3 Comparison with previous SMB estimations

The glacier-wide SMB of SRG estimated with the selected simulation over the period 2000-2012 is 0.65 Gt $a^{-1}$, much higher than the value of 0.08 Gt $a^{-1}$ estimated in the previous chapter with the ice-flow inverse method. This suggests that the selection process, mainly based on accumulation measurements from the tower, may be biased because of density differences with the model, or to snow deposition caused by the wind. Another explanation may be that the selected simulation may differ from the best simulation in agreement with the ice dynamics. However, as has been shown in section 3.5.2 slight changes on SMB around the ELA elevation have important impact in glacier-wide SMB, leading to uncertainty on the simulation selection.

The comparison with previous studies shows that during the period 1990-2005, SRG glacier-wide SMB from this study (0.84 $Gta^{-1}$ ) is 18% higher that the result from *Koppes et al.* (2011) (0.71 $Gta^{-1}$). On the other hand, with respect to the result from *Schaefer et al.* (2013) the result from this study is 44% lower, for a similar period. *Schaefer et al.* (2013) estimated a SMB equal to 2.18 $Gta^{-1}$ during the period 1975-2011 and the SMB obtain from MAR is 0.96 $Gta^{-1}$ for the period 1980-2011.

For NPI, the glacier wide SMB estimations from this study are much lower than the estimations from *Schaefer et al.* (2013), *Lenaerts et al.* (2014) and *Mernild et al.* (2016a).

We obtain negative SMB of -1.84 Gt $a^{-1}$ and -0.09 Gt $a^{-1}$ during the periods 1980-2014 and 2000-2012, respectively, while previous studies obtained positive SMB (0.55 Gt $a^{-1}$ 1979/80-2013/2014 (*Mernild et al.*, 2016a), 0.83 Gt $a^{-1}$ during 2000-2009 (*Schaefer et al.*, 2013) and ∼8.00 Gt $a^{-1}$ during 1979-2012 (*Lenaerts et al.*, 2014)). However, the slight increasing trend is in agreement with *Schaefer et al.* (2013) and *Mernild et al.* (2016a). The causes of the increase are related to decreasing melting while *Lenaerts et al.* (2014) and *Mernild et al.* (2016a) related the increasing SMB with a slight cooling. The slight precipitation decrease is in concordance with the results from *Mernild et al.* (2016a).

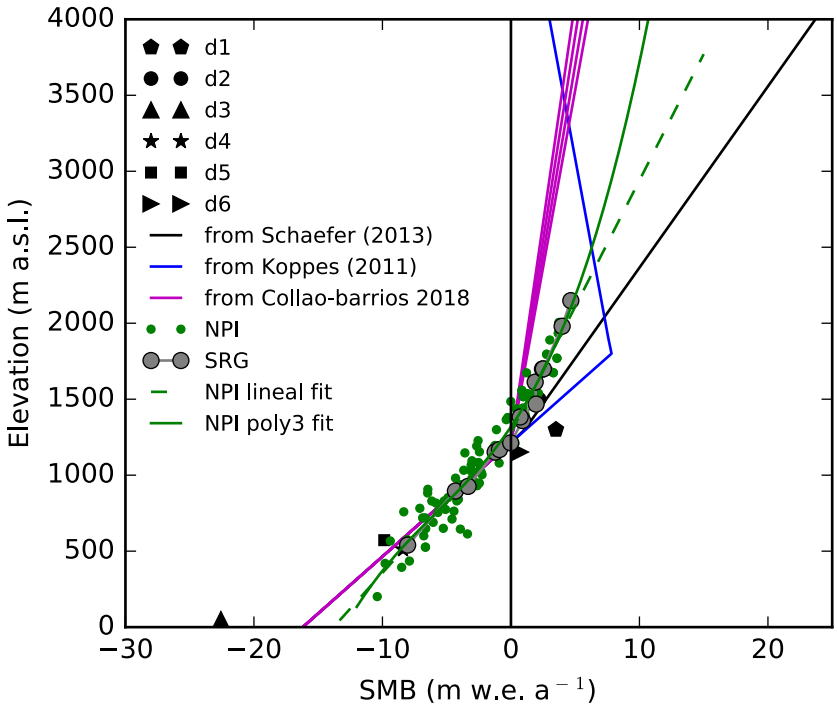


Figure 3.30: Punctual SMB versus elevation for NPI and SRG during the period 1980-2014. Comparison of results from present and previous studies.

The punctual SMB of SRG and NPI during the period 1980-2014 are close to those from previous studies, see Fig. 3.30. In the ablation zone all results are very similar but the results for NPI and SRG from MAR are sightly less negative below 600 m a.s.l. The ELA is also similar for all studies, and located from 1210 to 1320 m a.s.l. The most important differences are in the accumulation zone, where the results from the ice dynamics proposed the smallest accumulation values. The second lowest accumulation value results from MAR and then the results from *Schaefer et al.* (2013) and *Koppes et al.* (2011) propose a larger accumulation. Above 1800 m a.s.l., all the studies differ much more, because *Koppes et al.* (2011)'s model accounts for a decrease in available precipitable water in the atmosphere, this approach gives more realistic results than a continuously increasing accumulation. However, reproducing this limit in precipitation

requires a detailed representation of topography and a very high resolution which was not possible assuming the hydrostatic hypothesis in MAR. However, MAR already displays only a small increase in precipitation at high elevations, even with a 8 km resolution.

## 3.6 Conclusion

In this chapter, regional atmospheric modelling with MAR (Modèle Atmosphérique Régional) (*Gallée and Schayes*, 1994)) forced by ERA-Interim was done to estimate the SMB on SRG and NPI. The methodology focused on the adaptation and validation of the model to obtain a correct representation of ablation, accumulation and of albedo variations on the plateau. Data from weather stations located in the valleys were used for the validation of precipitation and temperature given by the model. For the albedo, we used values obtained from the MODImLab toolboxes. Finally, accumulation was validated using data collected by a snow tower installed on the plateau of SRG. Model results are in agreement with observed data and with the estimated albedo from MODIS images, and offer an accurate representation of regional climate in the area.

As part of the adaptation methodology, we have analyzed the sensitivity of the modeled SMB to humidity at the boundaries, and to the albedo parameterization, to the surface roughness length, and to the snow/rain temperature threshold. We have shown the important role of albedo on ablation and SMB, and the significant combined impact of humidity and snow/rain temperature threshold on accumulation and SMB. The latter shows the indirect effect of temperature in solid precipitation and accumulation. After the adaptation, we selected the simulation giving the best agreement with the available data. However, the analysis of the selected simulation demonstrated that data available to validate the model are still not sufficient to ensure an accurate estimation of glacier-wide SMB due to the sensitivity of the SMB to small changes on the plateau.

During the entire period 1980-2014, the average SMB for SRG and NPI are 0.86 Gt $a^{-1}$ and -1.84 Gt $a^{-1}$, respectively, with very high inter-annual variations of 1.4 and 6.1Gt $a^{-1}$ showing the high sensitivity of the SMB to variations in climatic conditions. This high sensitivity is related to SRG and NPI hypsometry and the extensive plateau where most of the area lies, because small changes in temperature-ablation and snowfall-accumulation in this zone have a large impact on the glacier-wide SMB.

SRG and NPI SMB have slightly increasing trends of 0.02 Gt $a^{-2}$ and 0.05 Gt $a^{-2}$ over the whole period. The increasing trends are due mainly to decreasing melting and stable accumulation. There is an increase in zonal wind speed and temperature that leads to an increase in precipitations but not in snowfall.

Accumulation and ablation present similar correlations with the SMB ($R > 85$). Tem-

perature and zonal wind are also significantly correlated with the SMB ($R > 61$). Then, the most important relationships are found between 1) accumulation and zonal wind, 2) total precipitation and zonal wind and 3) accumulation and temperature. Again, this reflects the indirect role of temperature on accumulation. Finally, considering the main modes of climatic variability, the SAM presents a significant correlation with zonal wind. However, no significant relationship was found with the El Niño index (El Niño3.4 index).

This modelling study finally gives the first negative SMB value for NPI ever proposed in the literature for recent decades. This value is much lower than the positive ones given in previous studies (*Schaefer et al.*, 2013; *Lenaerts et al.*, 2014; *Mernild et al.*, 2016a). This difference is mainly due to smaller accumulation in the highest zones of the icefields. This situation seems to be more reasonable and accurate than previous estimates, because the model has been validated with snow height data measured on the plateau, and because the SMB variations with elevation have been validated over SRG using stake data. Moreover, we verified that the SMB of the 3 biggest non-calving glaciers of NPI were close to the MB values given by geodetic estimates. This negative SMB in addition to the ice discharge can be the cause of wastage of NPI since 1980. Nevertheless, more in-situ data are still necessary to verify this assumption.

The SMB value of SRG given in the present study is between those given by the ice dynamics inversion (Chapter 2) and by *Koppes et al.* (2011) and *Schaefer et al.* (2013). The difference with results from the ice dynamics inversion can be due to a bias in our atmospheric modelling approach, in which we considered the snow height changes over the plateau as the main constrain for model calibration. However, our results at the level of the tower may be biased due to (i) different densification between the model and observations (because observations on the plateau correspond to snow height measurements, a not to changes in water equivalent), (ii) larger accumulation at the site of the tower due to snow deposition associated to snow transport by the wind. The difference may also be due to (iii) uncertainties existing in the ice flow model inversion.

Finally, our results indicate that more constrained estimations from atmospheric modelling should offer an SMB value closer to the actual SMB. This would close the mass budget between mass balance, surface mass balance and ice discharge. Nevertheless, this study contributes new estimations of SMB of SRG and NPI and improves the understanding of the impact of climate variables on SMB in Patagonia.

# Chapter 4

# Conclusions and perspectives

In the introduction the robustness of the commonly assumed assumption that the wastage of the NPI was mainly related to increased ablation caused by atmospheric warming (*Rignot et al.*, 2003; *Rasmussen et al.*, 2007) was questioned. Indeed, atmospheric downscaling modelling studies of glacier surface mass were suffering from the lack of field data to validate them. Accumulation has almost never been measured and observational data were missing to validate the increasing calving losses hypothesis.

Retrieving the physical drivers of Patagonian glacier change is challenging because of the few data available, making regional climate and ice dynamics modelling studies necessary. Here, it was proposed to study San Rafael Glacier, and to test accumulation values given in previous studies using the full-stokes ice flow model Elmer/Ice constrained by satellite observations. The results demonstrated that accumulation values proposed by *Schaefer et al.* (2013) and *Koppes et al.* (2011) on SRG were too high to allow consistency with the ice dynamics. For this task, the most up-to-date distributed data of surface velocities, bedrock elevation and SMB were used (*Mouginot and Rignot*, 2015; *Gourlet et al.*, 2016; *Schaefer et al.*, 2013; *Koppes et al.*, 2011).

This study was the first contribution in which a full-Stokes ice flow model such as Elmer/Ice (*Gagliardini et al.*, 2013) was applied to a glacier in Patagonia. The approach includes an initialization using an inverse method that infers the basal friction coefficient using a satellite-derived surface velocity mosaic. The results gave insight into the processes that control the SRG motion, as for instance the very high surface velocities (7.6 km $a^{-1}$) near the glacier front, which were explained by low basal shear stresses (<25 kPa), and small difference between basal and surface velocities due to basal sliding in the fast-flowing glacier tongue (>1 km $a^{-1}$).

The results allowed estimating the causes of SRG imbalance, which is due to the large ice discharge (-0.83±0.08 Gt $a^{-1}$) compared to a slightly positive glacier-wide SMB (0.08 ± 0.06 Gt $a^{-1}$). In its current state, the glacier size and SMB are not in equilibrium,

and the glacier is committed to retreat in the future, even if climate remains unchanged. The committed mass-loss estimated over the next century is -0.34 ± 0.03 Gt $a^{-1}$, but this likely constitutes a minimum in the future global climate change situation.

Results from the dynamics modelling demonstrated that previous estimates of average surface mass balance over the entire glacier were likely overestimating accumulation at high elevations. A new estimation from atmospheric modelling was proposed, and particular attention was given to accumulation and climatic variability. We applied the MAR (Modèle Atmosphérique Régional) (*Gallée and Schayes*, 1994)) forced by ERA-Interim to evaluate the distribution of the SMB at the scale of the SRG and NPI. Here, the focus was to correctly reproduce the accumulation on a tower, the albedo and the temperature conditions over the icefield plateau. With this objective, albedo values at the scale of NPI estimated with MODImlab using MODIS images were used to validate the albedo on the plateau. After adaptation and validation, MAR results offered a good agreement with accumulation and ablation over the plateau, but also with temperature and precipitation in the low valleys. Adaptation imposes forcing the MAR with higher humidity at the boundaries and changing the albedo parametrization, the surface roughness length and the snow/rain temperature threshold.

During the period 1980-2014 the average SMB for SRG and NPI are 0.86 Gt $a^{-1}$ and -1.84 Gt $a^{-1}$, respectively, with very high inter-annual variations of 1.4 and 6.1Gt $a^{-1}$ because of the high sensitivity of the SMB to variations in climatic conditions. This corresponds to the first negative estimation of the SMB of NPI. Our value seems more accurate than the values given in previous studies, because our SMB has been validated with the SMB of SRG and with the MB data from the 3 biggest non-calving glaciers of NPI. This negative SMB in addition to the ice discharge can be the cause of the icefield wastage since the 1980s. Nevertheless, the analysis of the uncertainty from the selected simulation has shown that data available to validate the model are still not sufficient to ensure an accurate estimation of glacier-wide SMB due to the sensitivity of the SMB to small changes on the plateau and more in-situ data are necessary to verify these results.

The model was then used to analyze the surface energy balance (SEB) at the glacier surface, demonstrating the key role of albedo and of shortwave radiative forcings. Indeed, the occurrence of solid precipitation has large impacts on accumulation, ablation and on the final glacier-wide surface mass balance. This link also justifies the highly significant correlations between melting and SMB, and between temperature and SMB. The second most important influx is related to the turbulent heat fluxes which are both positive, as observed in other locations at the same latitudes. This highlights the interest of obtaining accurate surface roughness length estimations or accurate turbulent heat fluxes measurements in the future. Finally, the net long-wave radiation is negative and largely

depends on cloud cover. However, validation of the MAR outputs with field data is still needed, since incoming longwave radiation are strongly related to cloud processes in the model.

The analysis of whether temperature or precipitation changes may have explained recent changes in the total mass balance of the NPI demonstrates that the SMB largely depends on melting and snowfall changes in almost the same degree, and that temperature and wind speed are also closely related to SMB.

However, the model also showed that changes in solid precipitation associated with an increase in humidity at the boundaries and the snow/rain temperature threshold of the model are the first order variable combination that explained the glacier SMB sensitivity. Thus, past conditions with solid precipitation may have also explained larger glaciers in the area, and current instability may result from having glacier fronts located well below the altitude allowing current glacier equilibrium. Since precipitation decrease in the Kerguelen Islands (located at similar latitude 49.33°S 69.33°W), for instance, reached 50% in few decades, these changes may have justified much larger glaciers during the LIA. Changes in precipitation may have occurred before 1979, explaining why they are not visible in the reanalysis data.

The comparison of the surface mass balance (SMB) at the scale of SRG obtained from the two methods still shows some discrepancies. The SMB from the atmospheric model is slightly higher than those obtained with the ice flow model. Validation of the atmospheric model on non-calving glaciers of NPI confirms that simulations with lower accumulation give more accurate results in term of glacier-wide mass balance, suggesting that accumulation on the plateau is too high. The reasons of this are unexplained. However, our model calibration may be biased because densification may be different between the model and the observations, or because accumulation at the tower may partly be caused by snow deposition associated with snow transport by the wind, which is not included in the model. Nevertheless, using these results gives insight into the contribution of each process in the imbalance of SRG.

The snow model validation is thus still important, as the snow density has only been tested with data from two dates (not shown). The albedo variations caused by superimposed ice lenses have been shown to be very strong, and should be calibrated more accurately in the field. Moreover, the firn is progressively filled by percolating water, leading to a progressive disappearance of the firn in the model. For instance, disappearing of snow layer is not linear in the model since deep layers are thicker than at the surface.

This study demonstrates that well-calibrated ice flow and regional atmospheric circulation models can provide independent constraints on the poorly known surface mass

balance of a large glacier such as San Rafael or NPI.

## Perspectives

Some prospects for the methodology developed in this study are presented in the following lines. First, we discuss future uses of the inverse method used to retrieve the SMB in agreement to ice flow of SRG during the period 2000-2012. The same model could be used to simulate previous periods with different geometry, especially of the front, with similar settings – for example the state of the glacier before 1983, when the glacier extended further into the wide part of the fjord characterized by deeper waters (*CECs and DGA*, 2012; *Koppes et al.*, 2011). The simulations with different front geometry will allow for analysis of the dependency of the ice discharge on the glacier geometry, corresponding to different periods of the San Rafael Glacier.

Additionally, the friction coefficient inferred with the inverse method using one velocity mosaic map is used as the average state of the glacier during 2000-2012, because velocities have not changed significantly during this period. However, this fixed friction coefficient could have been estimated for other conditions if more velocity maps were available. This would allow to use the different results of basal friction coefficient to study the sensitivity to variations in this parameter. Furthermore, we use a linear basal friction law but it would be interesting to test other friction laws. Indeed, more complex laws exits, which evolve with time and present a pressure-dependent friction law as proposed by *Schoof* (2005) and *Gagliardini et al.* (2007).

Moreover, the accuracy of the method may be discussed. As the uncertainty is related to the ice thickness and surface velocity, one way to improve the accuracy would be to use other sources of data when more data become available.

In addition, ice thickness and surface ice velocities are still not accurate enough to simulates the entire NPI icefield using the same methodology. Nevertheless, when data will be available, performing new simulations at the scale of the whole NPI could be interesting to analyze the different dynamics between glaciers and compare the surface elevation changes obtained with the results from geodetic methods. Then, the most obvious prospect would be to apply this methodology to SPI where calving flux and ice discharge have a very significant role due to the large number of tidewater glaciers.

With respect to the atmospheric model, it would be interesting to test the sensibility of the SMB to changes in temperature. We demonstrated in the results, that this variable directly influences ablation but also has an important impact on the solid/liquid precipitation rate. Furthermore, another interesting test would be to simulate the transport of snow by the wind and analyze the effect on the SMB. A new module of snow trans-

port based on the snowpack/aeolian snow transport parameterization presented in *Amory et al.* (2015) has been implemented. Here, we cannot ensure that the use of this process may improve our results because the resolution of the model over NPI is still too low (8 km), but a correct representation of the wind and of the blowing flow at high resolution may offer more accurate results.

Moreover, a useful application would be to run the model with future scenarios. Despite the uncertainty, this would allow us to have an idea of the impact that climate change can have on the SMB of SRG and NPI. Moreover, MAR could be run at the scale of the whole Patagonian region to include SPI. Nevertheless, obtaining more in-situ data at least on precipitation and accumulation at high elevations ($>$ 1200 m a.s.l.) to validate the model in order to reduce the uncertainty would be preferable.

Finally a natural prospect would be to couple the atmospheric and ice flow models to conduct hindcast simulations and jointly validate the models by using independent observations of the glacier dynamics and mass balance.

However few challenges must be tackled to achieve this goal. First, both models, as processes-based models, are time consuming for computation, limiting the number of simulations that can be achieved to explore the uncertainties. Efficient ensemble methods with few members will have to be developed to efficiently sample the uncertainties. Second, the ice thickness measurement coverage is increasing and new inverse methods are in development to better asses the ice thickness distribution (*Farinotti et al.*, 2017). Finally, accurate physically based modeling of calving is still a challenge for ice flow models. If progress has been made at the scale of individual glaciers without much observation data (*Nick et al.*, 2013; *Morlighem et al.*, 2016; *Todd et al.*, 2018; *Cook et al.*, 2018), this remains challenging at the scale of an entire icefield. However, for past simulation, this problem can be circumvented by prescribing the front positions, as proposed in (*Haubner et al.*, 2018).

# Bibliography


Abdel Jaber, W. (2016), Derivation of mass balance and surface velocity of glaciers by means of high resolution synthetic aperture radar: application to the patagonian icefields and antarctica, Ph.D. thesis, Technische Universität München.

Abram, N. J., R. Mulvaney, F. Vimeux, S. J. Phipps, J. Turner, and M. H. England (2014), Evolution of the Southern Annular Mode during the past millennium, *Nature Climate Change*, *4*(7), 564–569, doi:10.1038/nclimate2235.

Amante, C. (2009), Etopo1 1 arc-minute global relief model: procedures, data sources and analysis, *http://www. ngdc. noaa. gov/mgg/global/global.html*.

Amory, C., A. Trouvilliez, H. Gallée, V. Favier, F. Naaim-Bouvet, C. Genthon, C. Agosta, L. Piard, and H. Bellot (2015), Comparison between observed and simulated aeolian snow mass fluxes in adélie land, east antarctica, *The Cryosphere Discussions*, *9*(4), 1373–1383.

Amory, C., et al. (2017), Seasonal variations in drag coefficient over a sastrugi-covered snowfield in coastal east antarctica, *Boundary-Layer Meteorology*, *164*(1), 107–133, doi:10.1007/s10546-017-0242-5.

Aniya, M. (1988), Glacier inventory for the northern patagonia icefield, chile, and variations 1944/45 to 1985/86, *Arctic and Alpine Research*, *20*(2), 179–187, doi:10.2307/1551496.

Aniya, M. (1999), Recent glacier variations of the hielos patagónicos, south america, and their contribution to sea-level change, *Arctic, Antarctic, and Alpine Research*, *31*(2), 165–173.

Aniya, M. (2007), Glacier variations of Hielo Patagónico Norte, Chile, for 1944/45-2004/05, *Bulletin of glaciological research*, *24*, 59–70.

Aniya, M., H. Sato, R. Naruse, P. Skvarca, and G. Casassa (1996), The use of satellite and airborne imagery to inventory outlet glaciers of the southern patagonia icefield, south america, *Photogrammetric Engineering and Remote Sensing*, *62*(12), 1361–1369.

Aravena, J.-C., and B. H. Luckman (2009), Spatio-temporal rainfall patterns in Southern South America, *International Journal of Climatology*, *29*(14), 2106–2120, doi:10.1002/joc.1761.

Aristarain, A. J., and R. J. Delmas (1993), Firn-core study from the southern patagonia ice cap, south america, *Journal of Glaciology*, *39*(132), 249–254, doi:10.3189/s0022143000015914.

Arthern, R. J., R. C. A. Hindmarsh, and C. R. Williams (2015), Flow speed within the Antarctic ice sheet and its controls inferred from satellite observations, *Journal of Geophysical Research: Earth Surface*, *120*(7), 1171–1188, doi:10.1002/2014JF003239.

Bechtold, P., E. Bazile, F. Guichard, P. Mascart, and E. Richard (2001), A mass-flux convection scheme for regional and global models, *Quarterly Journal of the Royal Meteorological Society*, *127*(573), 869–886, doi:10.1002/qj.49712757309.

Berthier, E., V. Cabot, C. Vincent, and D. Six (2016), Decadal region-wide and glacier-wide mass balances derived from multi-temporal ASTER satellite digital elevation models. Validation over the Mont-Blanc area, *Frontiers in Earth Science*, *4*, doi:10.3389/feart.2016.00063.

Boex, J., C. Fogwill, S. Harrison, N. F. Glasser, A. Hein, C. Schnabel, and S. Xu (2013), Rapid thinning of the late pleistocene patagonian ice sheet followed migration of the southern westerlies, *Scientific Reports*, *3*(2118), doi:10.1038/srep02118.

Bracegirdle, T. J. (2013), Climatology and recent increase of westerly winds over the amundsen sea derived from six reanalyses, *International Journal of Climatology*, *33*(4), 843–851.

Bracegirdle, T. J., and G. J. Marshall (2012), The reliability of antarctic tropospheric pressure and temperature in the latest global reanalyses, *Journal of Climate*, *25*(20), 7138–7146.

Bromwich, D. H., J. P. Nicolas, and A. J. Monaghan (2011), An assessment of precipitation changes over antarctica and the southern ocean since 1989 in contemporary global reanalyses, *Journal of Climate*, *24*(16), 4189–4209.

Brun, E., P. David, M. Sudul, and G. Brunot (1992), A numerical model to simulate snow-cover stratigraphy for operational avalanche forecasting, *Journal of Glaciology*, *38*(128), 13–22, doi:10.3189/s0022143000009552.

Brun, F., M. Dumont, P. Wagnon, E. Berthier, M. Azam, J. Shea, P. Sirguey, A. Rabatel, and A. Ramanathan (2015), Seasonal changes in surface albedo of himalayan glaciers from modis data and links with the annual mass balance, *The Cryosphere*, *9*(1), 341–355.

Businger, J. A. (1973), Turbulence transfer in the atmospheric surface layer, pp. 67–100, AMS, Boston, Massachusetts.

Carrasco, J. F., G. Casassa, and A. Rivera (2002), Meteorological and climatological aspects of the Southern Patagonia Icefield, in *The Patagonian Icefields*, pp. 29–41, Springer US.

Carrivick, J. L., B. J. Davies, W. H. James, D. J. Quincey, and N. F. Glasser (2016), Distributed ice thickness and glacier volume in southern south america, *Global and Planetary Change*, *146*, 122–132.

Casassa, G., J. L. Rodríguez, and T. Loriaux (2014), A new glacier inventory for the Southern Patagonia Icefield and areal changes 1986–2000, in *Global Land Ice Measurements from Space*, edited by J. S. Kargel, G. J. Leonard, M. P. Bishop, A. Kääb, and B. H. Raup, pp. 639–660, Springer Berlin Heidelberg.

CECs and DGA (2012), *Variaciones recientes de glaciares en respuesta al cambio climático: características glaciológicas de los glaciares San Rafael, Nef y Colonia, Campo de Hielo Norte*, vol. S.I.T. 302, Dirección General de Aguas, Ministerio de Obras Públicas, Santiago, Chile.

Chen, J. L., C. R. Wilson, B. D. Tapley, D. D. Blankenship, and E. R. Ivins (2007), Patagonia Icefield melting observed by Gravity Recovery and Climate Experiment (GRACE), *Geophysical Research Letters*, *34*(22), L22,501, doi:10.1029/2007GL031871.

Church, J., et al. (2013), *Sea Level Change. In: Climate Change 2013: The Physical Science Basis. Contribution of Working Group I to the Fifth Assessment Report of the Intergovernmental Panel on Climate Change*, Cambridge University Press, Cambridge, United Kingdom and New York, NY, USA.

Collao-Barrios, G., F. Gillet-Chaulet, V. Favier, G. Casassa, E. Berthier, I. Dussaillant, J. Mouginot, and E. Rignot (2018), Ice flow modelling to constrain the surface mass balance and ice discharge of san rafael glacier, northern patagonia icefield, *Journal of Glaciology*, *64*(246), 568–582.

Cook, S., J. Astrom, T. Zwinger, B. K. Galton-Fenzi, J. S. Greenbaum, and R. Coleman (2018), Modelled fracture and calving on the totten ice shelf, *Cryosphere*, *12*, 2401–2411.

Cuffey, K. M., and W. S. B. Paterson (2010), *The physics of glaciers*, 4th edn. ed., Academic Press.

Davaze, L., A. Rabatel, Y. Arnaud, P. Sirguey, D. Six, A. Letreguilly, and M. Dumont (2018), Monitoring glacier albedo as a proxy to derive summer and annual surface mass balances from optical remote-sensing data, *The Cryosphere*, *12*(1), 271–286.

Davies, B., and N. Glasser (2012), Accelerating shrinkage of patagonian glaciers from the little ice age (ad 1870) to 2011, *Journal of Glaciology*, *58*(212), 1063–1084, doi: 10.3189/2012JoG12J026.

Davies, H. C. (1983), Limitations of some common lateral boundary schemes used in regional nwp models, *Monthly Weather Review*, *111*(5), 1002–1012, doi:10.1175/ 1520-0493(1983)111<1002:losclb>2.0.co;2.

De Ridder, K., and H. Gallée (1998), Land surface–induced regional climate change in southern israel, *Journal of Applied Meteorology*, *37*(11), 1470–1485, doi:10.1175/ 1520-0450(1998)037<1470:lsircc>2.0.co;2.

Dee, D. P., et al. (2011), The era-interim reanalysis: Configuration and performance of the data assimilation system, *Quarterly Journal of the royal meteorological society*, *137*(656), 553–597.

Dumont, M., J. Gardelle, P. Sirguey, A. Guillot, D. Six, A. Rabatel, and Y. Arnaud (2012), Linking glacier annual mass balance and glacier albedo retrieved from modis data, *The Cryosphere*, *6*, 1527–1539.

Dussaillant, I., E. Berthier, and F. Brun (2018), Geodetic mass balance of the northern patagonian icefield from 2000 to 2012 using two independent methods, *Frontiers in Earth Science*, *6*, doi:10.3389/feart.2018.00008.

Duynkerke, P. G. (1988), Application of thee– $\epsilon$ turbulence closure model to the neutral and stable atmospheric boundary layer, *Journal of the Atmospheric Sciences*, *45*(5), 865–880, doi:10.1175/1520-0469(1988)045<0865:aottcm>2.0.co;2.

Falvey, M., and R. D. Garreaud (2009), Regional cooling in a warming world: Recent temperature trends in the southeast Pacific and along the west coast of subtropical South America (1979–2006), *Journal of Geophysical Research*, *114*, D04,102, doi:10. 1029/2008JD010519.

Farinotti, D., et al. (2017), How accurate are estimates of glacier ice thickness? results from ITMIX, the Ice Thickness Models Intercomparison eXperiment, *Cryosphere*, *11*(2), 949–970.

Fettweis, X. (2006), Reconstruction of the 1979-2005 greenland ice sheet surface mass balance using satellite data and the regional climate model mar, Ph.D. thesis, Université catholique de Louvain, Louvain-la-neuve, Belgique.

Foresta, L., N. Gourmelen, F. Weissgerber, P. Nienow, J. J. Williams, A. Shepherd, M. R. Drinkwater, and S. Plummer (2018), Heterogeneous and rapid ice loss over the Patagonian Ice Fields revealed by CryoSat-2 swath radar altimetry, *Remote Sensing of Environment*, *211*, 441–455, doi:10.1016/j.rse.2018.03.041.

Fouquart, Y., and B. Bonnel (1980), Computations of solar heating of the earth's atmosphere- a new parameterization, *Beitraege zur Physik der Atmosphaere*, *53*, 35–62.

Frey, P., and F. Alauzet (2005), Anisotropic mesh adaptation for CFD computations, *Computer Methods in Applied Mechanics and Engineering*, *194*, 5068–5082, doi:10.1016/j.cma.2004.11.025.

Funk, M., and H. Rothlisberger (1989), Forecasting the effects of a planned reservoir which will partially flood the tongue of unteraargletscher in switzerland, *Annals of Glaciology*, *13*, 76–81.

Gagliardini, O., D. Cohen, P. Råback, and T. Zwinger (2007), Finite-element modeling of subglacial cavities and related friction law, *Journal of Geophysical Research: Earth Surface*, *112*(F2).

Gagliardini, O., et al. (2013), Capabilities and performance of Elmer/Ice, a new-generation ice sheet model, *Geoscientific Model Development*, *6*(4), 1299–1318, doi:10.5194/gmd-6-1299-2013.

Gallée, H. (1995), Simulation of the mesocyclonic activity in the ross sea, antarctica, *Monthly Weather Review*, *123*(7), 2051–2069, doi:10.1175/1520-0493(1995)123<2051:sotmai>2.0.co;2.

Gallée, H., and P. G. Duynkerke (1997), Air-snow interactions and the surface energy and mass balance over the melting zone of west greenland during the greenland ice margin experiment, *Journal of Geophysical Research: Atmospheres*, *102*(D12), 13,813–13,824, doi:10.1029/96jd03358.

Gallée, H., and G. Schayes (1994), Development of a three-dimensional meso-$\gamma$ primitive equation model: Katabatic winds simulation in the area of terra nova bay, antarctica, *Monthly Weather Review*, *122*(4), 671–685, doi:10.1175/1520-0493(1994)122<0671:doatdm>2.0.co;2.

Gallée, H., G. Guyomarc'h, and E. Brun (2001), Impact of snow drift on the antarctic ice sheet surface mass balance: possible sensitivity to snow-surface properties, *Boundary-Layer Meteorology*, *99*(1), 1–19.

Gardelle, J., E. Berthier, Y. Arnaud, and A. Kääb (2013), Region-wide glacier mass balances over the Pamir-Karakoram-Himalaya during 1999–2011, *The Cryosphere*, *7*(4), 1263–1286, doi:10.5194/tc-7-1263-2013.

Gardner, A. S., et al. (2013), A reconciled estimate of glacier contributions to sea level rise: 2003 to 2009, *Science*, *340*(6134), 852–857, doi:10.1126/science.1234532.

Garreaud, R. D. (2007), Precipitation and Circulation Covariability in the Extratropics, *Journal of Climate*, *20*(18), 4789–4797, doi:10.1175/JCLI4257.1.

Garreaud, R. D., M. Vuille, R. Compagnucci, and J. Marengo (2009), Present-day South American climate, *Palaeogeography, Palaeoclimatology, Palaeoecology*, *281*(3–4), 180–195, doi:10.1016/j.palaeo.2007.10.032.

Garreaud, R. D., P. Lopez, M. Minvielle, and M. Rojas (2012), Large-scale control on the Patagonian climate, *Journal of Climate*, *26*(1), 215–230, doi:10.1175/JCLI-D-12-00001.1.

Garreaud, R. D., M. Gabriela Nicora, R. E. Bürgesser, and E. E. Ávila (2014), Lightning in Western Patagonia, *Journal of Geophysical Research: Atmospheres*, *119*(8), 2013JD021,160, doi:10.1002/2013JD021160.

Geoestudios, and DGA (2014), *Caracterización física del manto nival en Campo de Hielo Norte en base a mediciones GPR terrestre., S.I.T. 359*, Dirección General de Aguas, Ministerio de Obras Públicas, Santiago, Chile.

Gillet-Chaulet, F., O. Gagliardini, H. Seddik, M. Nodet, G. Durand, C. Ritz, T. Zwinger, R. Greve, and D. G. Vaughan (2012), Greenland ice sheet contribution to sea-level rise from a new-generation ice-sheet model, *The Cryosphere*, *6*(6), 1561–1576, doi:10.5194/tc-6-1561-2012.

Glasser, N. F., S. Harrison, K. N. Jansson, K. Anderson, and A. Cowley (2011), Global sea-level contribution from the Patagonian Icefields since the Little Ice Age maximum, *Nature Geoscience*, *4*(5), 303–307, doi:10.1038/ngeo1122.

Gong, D., and S. Wang (1999), Definition of antarctic oscillation index, *Geophysical research letters*, *26*(4), 459–462.

Gourlet, P., E. Rignot, A. Rivera, and G. Casassa (2016), Ice thickness of the northern half of the patagonia icefields of south america from high-resolution airborne gravity surveys, *Geophysical Research Letters*, *43*(1), 241–249.

Greuell, W., and T. Konzelmann (1994), Numerical modelling of the energy balance and the englacial temperature of the greenland ice sheet. calculations for the eth-camp location (west greenland, 1155 m a.s.l.), *Global and Planetary Change*, *9*(1), 91 – 114, doi:https://doi.org/10.1016/0921-8181(94)90010-8, greenland ice margin experiment (GIMEx).

Haubner, K., et al. (2018), Simulating ice thickness and velocity evolution of upernavik isstrøm 1849–2012 by forcing prescribed terminus positions in issm, *The Cryosphere*, *12*(4), 1511–1522.

Hock, R. (2003), Temperature index melt modelling in mountain areas, *Journal of hydrology*, *282*(1-4), 104–115.

Houze, R. A. (2012), Orographic effects on precipitating clouds, *Reviews of Geophysics*, *50*(1).

Hubbard, A., A. S. Hein, M. R. Kaplan, N. R. Hulton, and N. Glasser (2005), A modelling reconstruction of the last glacial maximum ice sheet and its deglaciation in the vicinity of the northern patagonian icefield, south america, *Geografiska Annaler: Series A, Physical Geography*, *87*(2), 375–391, doi:10.1111/j.0435-3676.2005.00264.x.

Ivins, E., M. Watkins, Dah-Ning Yuan, R. Dietrich, G. Casassa, and A. Rulke (2011), On-land ice loss and glacial isostatic adjustment at the Drake Passage: 2003-2009, *Journal of Geophysical Research - Part B - Solid Earth*, *116*(2), doi:10.1029/2010JB007607.

Jacob, T., J. Wahr, W. T. Pfeffer, and S. Swenson (2012), Recent contributions of glaciers and ice caps to sea level rise, *Nature*, *482*(7386), 514–518, doi:10.1038/nature10847.

Kessler, E. (1969), *On the Distribution and Continuity of Water Substance in Atmospheric Circulations*, pp. 1–84, American Meteorological Society, Boston, MA, doi:10.1007/978-1-935704-36-2_1.

Kistler, R., E. Kalnay, W. Collins, S. Saha, G. White, J. Woollen, M. Chelliah, and W. Ebisuzaki (2001a), The NCEP-NCAR 50-year reanalysis: Monthly means CD- ROM and documentation, *Bulletin of the American Meteorological Society*, *82*(2), 247–268.

Kistler, R., et al. (2001b), The ncep–ncar 50-year reanalysis: monthly means cd-rom and documentation, *Bulletin of the American Meteorological society*, *82*(2), 247–268.

Koppes, M., H. Conway, L. A. Rasmussen, and M. Chernos (2011), Deriving mass balance and calving variations from reanalysis data and sparse observations, Glaciar San Rafael, northern Patagonia, 1950–2005, *The Cryosphere*, *5*(3), 791–808, doi: 10.5194/tc-5-791-2011.

Koppes, M. N. (2007), Glacier erosion and response to climate: From alaska to patagonia, Ph.D. thesis, University of Washington.

Lefebre, F. (2003), Modeling of snow and ice melt at eth camp (west greenland): A study of surface albedo, *Journal of Geophysical Research*, *108*(D8), doi:10.1029/2001jd001160.

Lenaerts, J. T. M., M. R. van den Broeke, J. M. van Wessem, W. J. van de Berg, E. van Meijgaard, L. H. van Ulft, and M. Schaefer (2014), Extreme precipitation and climate gradients in patagonia revealed by high-resolution regional atmospheric climate modeling, *Journal of Climate*, *27*(12), 4607–4621, doi:10.1175/JCLI-D-13-00579.1.

Lin, Y.-L., R. D. Farley, and H. D. Orville (1983), Bulk parameterization of the snow field in a cloud model, *Journal of Climate and Applied Meteorology*, *22*(6), 1065–1092, doi:10.1175/1520-0450(1983)022<1065:bpotsf>2.0.co;2.

Liston, G. E., and K. Elder (2006a), A distributed snow-evolution modeling system (snowmodel), *Journal of Hydrometeorology*, *7*(6), 1259–1276, doi:10.1175/jhm548.1.

Liston, G. E., and K. Elder (2006b), A meteorological distribution system for high-resolution terrestrial modeling (micromet), *Journal of Hydrometeorology*, *7*(2), 217–234, doi:10.1175/jhm486.1.

Lopez, P., P. Chevallier, V. Favier, B. Pouyaud, F. Ordenes, and J. Oerlemans (2010), A regional view of fluctuations in glacier length in southern South America, *Global and Planetary Change*, *71*(1–2), 85–108, doi:10.1016/j.gloplacha.2009.12.009.

MacAyeal, D. R. (1993), A tutorial on the use of control methods in ice-sheet modeling, *Journal of Glaciology*, *39*(131), 91–98, doi:10.3189/S0022143000015744.

Malz, P., W. Meier, G. Casassa, R. Jaña, P. Skvarca, and M. Braun (2018), Elevation and mass changes of the southern patagonia icefield derived from tandem-x and srtm data, *Remote Sensing*, *10*(2), 188, doi:10.3390/rs10020188.

Mantua, N. J., S. R. Hare, Y. Zhang, J. M. Wallace, and R. C. Francis (1997), A pacific interdecadal climate oscillation with impacts on salmon production, *Bulletin of the american Meteorological Society*, *78*(6), 1069–1080.

Marbaix, P., H. Gallée, O. Brasseur, and J.-P. van Ypersele (2003), Lateral boundary conditions in regional climate models: A detailed study of the relaxation procedure, *Monthly Weather Review*, *131*(3), 461–479, doi:10.1175/1520-0493(2003)131<0461:lbcirc>2.0.co;2.

Marshall, G. J. (2003), Trends in the southern annular mode from observations and reanalyses, *Journal of Climate*, *16*(24), 4134–4143, doi:10.1175/1520-0442(2003)016<4134:titsam>2.0.co;2.

Matsuoka, K., and R. Naruse (1999), Mass balance features derived from a firn core at Hielo Patagónico Norte, South America, *Arctic, Antarctic, and Alpine Research*, *31*(4), 333–340.

Mernild, S. H., G. E. Liston, C. Hiemstra, and R. Wilson (2016a), The andes cordillera. part iii: glacier surface mass balance and contribution to sea level rise (1979-2014), *International Journal of Climatology*, *37*(7), 3154–3174, doi:10.1002/joc.4907.

Mernild, S. H., G. E. Liston, C. A. Hiemstra, J. K. Malmros, J. C. Yde, and J. McPhee (2016b), The andes cordillera. part i: snow distribution, properties, and trends (1979-2014), *International Journal of Climatology*, *37*(4), 1680–1698, doi:10.1002/joc.4804.

Mernild, S. H., G. E. Liston, C. A. Hiemstra, J. C. Yde, J. McPhee, and J. K. Malmros (2016c), The andes cordillera. part ii: Rio olivares basin snow conditions (1979-2014), central chile, *International Journal of Climatology*, *37*(4), 1699–1715, doi:10.1002/joc.4828.

Mo, K. C. (2000), Relationships between low-frequency variability in the southern hemisphere and sea surface temperature anomalies, *Journal of Climate*, *13*(20), 3599–3610.

Mo, K. C., and J. N. Paegle (2001), The pacific–south american modes and their downstream effects, *International Journal of Climatology: A Journal of the Royal Meteorological Society*, *21*(10), 1211–1229.

Monin, A., and A. Obukhov (1954), Basic regularity in turbulent mixing in the surface layer of the atmosphere, ussr, *Tr. Akad. Nauk SSSR Geophiz. Inst.*, *24*(151), 163–187.

Morcrette, J.-J. (2002), Assessment of the ecmwf model cloudiness and surface radiation fields at the arm sgp site, *Monthly Weather Review*, *130*(2), 257–277, doi:10.1175/1520-0493(2002)130<0257:aotemc>2.0.co;2.

Moreno, P. I., I. Vilanova, R. Villa-Martínez, R. D. Garreaud, M. Rojas, and R. D. Pol-Holz (2014), Southern Annular Mode-like changes in southwestern Patagonia at

centennial timescales over the last three millennia, *Nature Communications*, *5*, 4375, doi:10.1038/ncomms5375.

Moreno, P. I., et al. (2018), Onset and Evolution of Southern Annular Mode-Like Changes at Centennial Timescale, *Scientific Reports*, *8*(1), 3458, doi:10.1038/s41598-018-21836-6.

Morlighem, M., E. Rignot, H. Seroussi, E. Larour, H. Ben Dhia, and D. Aubry (2010), Spatial patterns of basal drag inferred using control methods from a full-Stokes and simpler models for Pine Island Glacier, West Antarctica, *Geophysical Research Letters*, *37*(14), doi:10.1029/2010GL043853.

Morlighem, M., J. Bondzio, H. Seroussi, E. Rignot, E. Larour, A. Humbert, and S. Rebuffi (2016), Modeling of store gletscher's calving dynamics, west greenland, in response to ocean thermal forcing, *Geophysical Research Letters*, *43*(6), 2659–2666.

Mouginot, J., and E. Rignot (2015), Ice motion of the Patagonian Icefields of South America: 1984–2014, *Geophysical Research Letters*, *42*(5), 2014GL062,661, doi:10.1002/2014GL062661.

Naruse, R., M. Aniya, P. Skvarca, and G. Gasassa (1995), Recent variations of calving glaciers in patagonia, south america, revealed by ground surveys, satellite-data analyses and numerical experiments, *Annals of Glaciology*, *21*, 297–303.

Neumann, B., A. T. Vafeidis, J. Zimmermann, and R. J. Nicholls (2015), Future coastal population growth and exposure to sea-level rise and coastal flooding-a global assessment, *PloS one*, *10*(3), e0118,571.

Nick, F. M., A. Vieli, M. L. Andersen, I. Joughin, A. Payne, T. L. Edwards, F. Pattyn, and R. S. van de Wal (2013), Future sea-level rise from greenland's main outlet glaciers in a warming climate, *Nature*, *497*(7448), 235.

Nicolas, J. P., and D. H. Bromwich (2011), Climate of west antarctica and influence of marine air intrusions, *Journal of Climate*, *24*(1), 49–67.

Ohata, T., N. Ishikawa, S. Kobayashi, and S. Kawaguchi (1985a), Heat balance at the snow surface in a katabatic wind zone, East Antarctica, *Annals of Glaciology*, *6*, 174–177, doi:10.3189/1985AoG6-1-174-177.

Ohata, T., N. Ishikawa, S. Kobayashi, and S. Kawaguchi (1985b), Heat balance at the snow surface in a katabatic wind zone, east antarctica, *Annals of Glaciology*, *6*, 174–177.

Osmaston, H. (2005a), Estimates of glacier equilibrium line altitudes by the area x altitude, the area x altitude balance ratio and the area x altitude balance index methods and their validation, *Quaternary International*, *138*, 22–31, doi:10.1016/j.quaint.2005.02.004.

Osmaston, H. (2005b), Estimates of glacier equilibrium line altitudes by the area× altitude, the area× altitude balance ratio and the area× altitude balance index methods and their validation, *Quaternary International*, *138*, 22–31.

Pfeffer, W. T., et al. (2014), The Randolph Glacier Inventory: a globally complete inventory of glaciers, *Journal of Glaciology*, *60*(221), 537–552, doi:10.3189/2014JoG13J176.

Price, S. F., A. J. Payne, I. M. Howat, and B. E. Smith (2011), Committed sea-level rise for the next century from Greenland ice sheet dynamics during the past decade, *Proceedings of the National Academy of Sciences*, *108*(22), 8978–8983, doi:10.1073/pnas.1017313108.

Quintana, J. (2004), Factors affecting central chile rainfall variations at interdecadal scales, Ph.D. thesis, Departamento de Geofísica, Universidad de Chile.

Rasmussen, L., H. Conway, and C. Raymond (2007), Influence of upper air conditions on the patagonia icefields, *Global and Planetary Change*, *59*(1-4), 203–216.

Rayner, N., D. E. Parker, E. Horton, C. Folland, L. Alexander, D. Rowell, E. Kent, and A. Kaplan (2003), Global analyses of sea surface temperature, sea ice, and night marine air temperature since the late nineteenth century, *Journal of Geophysical Research: Atmospheres*, *108*(D14).

Rignot, E., R. Forster, and B. Isacks (1996), Mapping of glacial motion and surface topography of Hielo Patagónico Norte, Chile, using satellite SAR L-band interferometry data, *Annals of Glaciology*, *23*, 209–216, doi:10.3189/S026030550001346X.

Rignot, E., A. Rivera, and G. Casassa (2003), Contribution of the Patagonia Icefields of South America to sea level rise, *Science*, *302*(5644), 434–437, doi:10.1126/science.1087393.

Rivera, A. (2004), Mass balance investigations at glaciar chico, southern patagonia icefield, chile, Ph.D. thesis, University of Bristol.

Rivera, A., T. Benham, G. Casassa, J. Bamber, and J. A. Dowdeswell (2007), Ice elevation and areal changes of glaciers from the Northern Patagonia Icefield, Chile, *Global and Planetary Change*, *59*(1–4), 126–137, doi:10.1016/j.gloplacha.2006.11.037.

Roe, G. H. (2005a), Orographic precipitation, *Annual Review of Earth and Planetary Sciences*, *33*(1), 645–671, doi:10.1146/annurev.earth.33.092203.122541.

Roe, G. H. (2005b), Orographic precipitation, *Annu. Rev. Earth Planet. Sci.*, *33*, 645–671.

Sagredo, E., and T. Lowell (2012), Climatology of andean glaciers: A framework to understand glacier response to climate change, *Global and Planetary Change*, *86*, 101–109.

Sakakibara, D., and S. Sugiyama (2014), Ice-front variations and speed changes of calving glaciers in the Southern Patagonia Icefield from 1984 to 2011, *Journal of Geophysical Research: Earth Surface*, *119*(11), 2014JF003,148, doi:10.1002/2014JF003148.

Schaefer, M., H. Machguth, M. Falvey, and G. Casassa (2013), Modeling past and future surface mass balance of the Northern Patagonia Icefield, *Journal of Geophysical Research: Earth Surface*, *118*(2), 571–588, doi:10.1002/jgrf.20038.

Schaefer, M., H. Machguth, M. Falvey, G. Casassa, and E. Rignot (2015), Quantifying mass balance processes on the Southern Patagonia Icefield, *The Cryosphere*, *9*(1), 25–35, doi:10.5194/tc-9-25-2015.

Schneider, C., and D. Gies (2004), Effects of el niño–southern oscillation on southernmost south america precipitation at 53 s revealed from ncep–ncar reanalyses and weather station data, *International Journal of Climatology*, *24*(9), 1057–1076.

Schneider, C., M. Glaser, R. Kilian, A. Santana, N. Butorovic, and G. Casassa (2003), Weather observations across the southern andes at 53 s, *Physical Geography*, *24*(2), 97–119.

Schoof, C. (2005), The effect of cavitation on glacier sliding, in *Proceedings of the Royal Society of London A: Mathematical, Physical and Engineering Sciences*, vol. 461, pp. 609–627, The Royal Society.

Schwikowski, M., S. Brütsch, G. Casassa, and A. Rivera (2006), A potential high-elevation ice-core site at hielo patagónico sur, *Annals of Glaciology*, *43*, 8–13, doi:10.3189/172756406781812014.

Schwikowski, M., M. Schlappi, P. Santibañez, A. Rivera, and G. Casassa (2013), Net accumulation rates derived from ice core stable isotope records of pío xi glacier, southern patagonia icefield, *The Cryosphere*, *7*(5), 1635–1644, doi:10.5194/tc-7-1635-2013.

Segal, M., J. R. Garratt, R. A. Pielke, and Z. Ye (1991), Scaling and numerical model evaluation of snow-cover effects on the generation and modification of daytime

mesoscale circulations, *Journal of the Atmospheric Sciences*, *48*(8), 1024–1042, doi: 10.1175/1520-0469(1991)048<1024:sanmeo>2.0.co;2.

Seroussi, H., M. Morlighem, E. Rignot, E. Larour, D. Aubry, H. Ben Dhia, and S. S. Kristensen (2011), Ice flux divergence anomalies on 79north Glacier, Greenland, *Geophysical Research Letters*, *38*(9), L09,501, doi:10.1029/2011GL047338.

Seroussi, H., M. Morlighem, E. Rignot, A. Khazendar, E. Larour, and J. Mouginot (2013), Dependence of century-scale projections of the Greenland ice sheet on its thermal regime, *Journal of Glaciology*, *59*(218), 1024–1034, doi:10.3189/2013JoG13J054.

Shiraiwa, T., S. Kohshima, R. Uemura, N. Yoshida, S. Matoba, J. Uetake, and M. A. Godoi (2002), High net accumulation rates at campo de hielo patagónico sur, south america, revealed by analysis of a 45.97 m long ice core, *Annals of Glaciology*, *35*, 84–90, doi:10.3189/172756402781816942.

Sirguey, P. (2009), Simple correction of multiple reflection effects in rugged terrain, *International Journal of Remote Sensing*, *30*(4), 1075–1081.

Sirguey, P., H. Still, N. J. Cullen, M. Dumont, Y. Arnaud, and J. P. Conway (2016), Reconstructing the mass balance of brewster glacier, new zealand, using modis-derived glacier-wide albedo, *The Cryosphere*, *10*(5), 2465–2484.

Smith, R. B., and I. Barstad (2004a), A linear theory of orographic precipitation, *Journal of the Atmospheric Sciences*, *61*(12), 1377–1391, doi:10.1175/1520-0469(2004)061<1377:ALTOOP>2.0.CO;2.

Smith, R. B., and I. Barstad (2004b), A linear theory of orographic precipitation, *Journal of the Atmospheric Sciences*, *61*(12), 1377–1391.

Stuefer, M., H. Rott, and P. Skvarca (2007), Glaciar Perito Moreno, Patagonia: climate sensitivities and glacier characteristics preceding the 2003/04 and 2005/06 damming events, *Journal of Glaciology*, *53*(180), 3–16.

Stull, R. B. (2012), *An introduction to boundary layer meteorology*, Springer Netherlands.

Thompson, D. W. J., and J. M. Wallace (2000), Annular modes in the extratropical circulation. Part I: Month-to-month variability, *Journal of Climate*, *13*(5), 1000–1016, doi:10.1175/1520-0442(2000)013<1000:AMITEC>2.0.CO;2.

Thompson, D. W. J., S. Solomon, P. J. Kushner, M. H. England, K. M. Grise, and D. J. Karoly (2011), Signatures of the Antarctic ozone hole in Southern Hemisphere surface climate change, *Nature Geoscience*, *4*(11), 741–749, doi:10.1038/ngeo1296.

Todd, J., et al. (2018), A full-stokes 3-d calving model applied to a large greenlandic glacier, *Journal of Geophysical Research: Earth Surface*, *123*(3), 410–432.

Uppala, S. M., et al. (2005a), The ERA-40 re-analysis, *Quarterly Journal of the Royal Meteorological Society*, *131*, 2961–3012.

Uppala, S. M., et al. (2005b), The era-40 re-analysis, *Quarterly Journal of the royal meteorological society*, *131*(612), 2961–3012.

Välisuo, I., T. Zwinger, and J. Kohler (2017), Inverse solution of surface mass balance of Midtre Lovénbreen, Svalbard, *Journal of Glaciology*, *63*(240), 593–602, doi:10.1017/jog.2017.26.

Vaughan, D. G., et al. (2013), Observations: cryosphere, *Climate change*, *2103*, 317–382.

Verfaillie, D. (2018), Cook ice cap at kerguelen, submmited.

Villalba, R., et al. (2003), Large-scale temperature changes across the southern andes: 20th-century variations in the context of the past 400 years, *Climatic Change*, *59*(177).

Villalba, R., et al. (2012), Unusual Southern Hemisphere tree growth patterns induced by changes in the Southern Annular Mode, *Nature Geoscience*, *5*(11), 793–798, doi:10.1038/ngeo1613.

Vimeux, F., M. Angelis de, P. Ginot, O. Magand, G. Casassa, B. Pouyaud, S. Falourd, and S. Johnsen (2008), A promising location in Patagonia for paleoclimate and paleoenvironmental reconstructions revealed by a shallow firn core from Monte San Valentin (Northern Patagonia Icefield, Chile), *Journal of Geophysical Research-Atmospheres*, *113*, D16,118, doi:10.1029/2007JD009502.

Vitousek, S., P. L. Barnard, C. H. Fletcher, N. Frazer, L. Erikson, and C. D. Storlazzi (2017), Doubling of coastal flooding frequency within decades due to sea-level rise, *Scientific reports*, *7*(1), 1399.

Warren, C., and M. Aniya (1999), The calving glaciers of southern south america, *Global and Planetary Change*, *22*(1-4), 59–77.

Warren, C., D. Benn, V. Winchester, and S. Harrison (2001), Buoyancy-driven lacustrine calving, glaciar nef, chilean patagonia, *Journal of Glaciology*, *47*(156), 135–146.

Warren, C. R., N. F. Glasser, S. Harrison, V. Winchester, A. R. Kerr, and A. Rivera (1995), Characteristics of tide-water calving at glaciar san rafael, chile, *Journal of glaciology*, *41*(138), 273–289.

Willis, M. J., A. K. Melkonian, M. E. Pritchard, and J. M. Ramage (2012a), Ice loss rates at the Northern Patagonian Icefield derived using a decade of satellite remote sensing, *Remote Sensing of Environment*, *117*, 184–198, doi:10.1016/j.rse.2011.09.017.

Willis, M. J., A. K. Melkonian, M. E. Pritchard, and A. Rivera (2012b), Ice loss from the Southern Patagonian Ice Field, South America, between 2000 and 2012, *Geophysical Research Letters*, *39*(17), L17,501, doi:10.1029/2012GL053136.

Yamada, T. (1987), Glaciological characteristic revealed by a 37.6 m deep core drilled al the accumulation area of San Rafael Glacier, the Northern Patagonia lcefield, *Bulletin of glaciological research*, *4*, 59–67.

Yu, J.-Y., H. Paek, E. S. Saltzman, and T. Lee (2015), The early 1990s change in enso–psa–sam relationships and its impact on southern hemisphere climate, *Journal of Climate*, *28*(23), 9393–9408.

Zuo, Z., and J. Oerlemans (1996), Modelling albedo and specific balance of the greenland ice sheet: calculations for the søndre strømfjord transect, *Journal of Glaciology*, *42*(141), 305–317, doi:10.3189/s0022143000004160.

# Appendix

## A1 Comparison between model and observed precipitation

The table and Figures given in this Appendix complete the comparison between the precipitation modelled with MAR and observed at the stations around the icefield (see Sec. 3.5.3.2 Monthly and annual average precipitation).

Table A2.1: Simulated (sim14) and measured precipitation comparison.

| N | Name | R | p | RMS (m $a^{-1}$) | Dif. (m $a^{-1}$) |
|---|---|---|---|---|---|
| s1 | Puerto Chacabuco | 0.62 | 4.0 x $10^{-20}$ | 11.32 | -0.79 |
| s2 | Río Aysen en Pto. A. | 0.72 | 7.0 x $10^{-22}$ | 0.98 | -0.61 |
| s3 | El balseo | 0.57 | 4.1 x $10^{-16}$ | 0.90 | -0.33 |
| s4 | Teniente Vidal C. Ad. | 0.66 | 1.7 x $10^{-23}$ | 0.66 | 0.41 |
| s5 | Coyhaique Conaf | 0.69 | 1.0 x $10^{-21}$ | 0.58 | 0.37 |
| s6 | Coyhaique Esc. Ag. | 0.59 | 8.6 x $10^{-15}$ | 0.68 | 0.32 |
| s8 | Balmaceda Ad. | 0.69 | 1.3 x $10^{-26}$ | 0.59 | 0.48 |
| s9 | Villa Cerro Castillo | 0.55 | 6.8 x $10^{-14}$ | 0.52 | 0.30 |
| s10 | Chile Chico Ad. | 0.58 | 4.7 x $10^{-13}$ | 0.31 | 0.16 |
| s11 | Bahía Murta | 0.71 | 4.6 x $10^{-25}$ | 0.57 | -0.01 |
| s12 | Lord Cochrane Ad. | 0.47 | 2.6 x $10^{-8}$ | 0.61 | -0.39 |
| s13 | Río Pascua | 0.66 | 4.5 x $10^{-17}$ | 0.91 | -0.46 |

R is Pearson's correlation coefficient, p is the statistical significance of on Pearson's correlation coefficient, RMS is the root mean square error between the observed and modeled precipitation and Dif. is the average difference between the observed and modeled precipitation

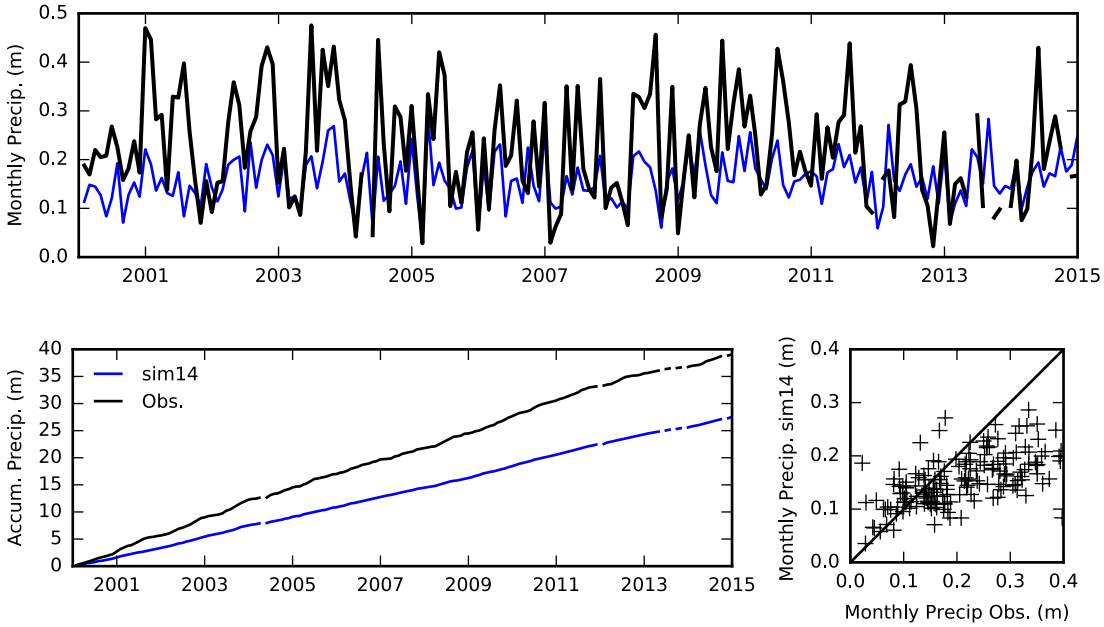


Figure A1.1: Precipitation from the selected simulation and observations at station 1 (Puerto Chacabuco). Monthly precipitation (top), monthly accumulated precipitation (bottom left) and comparison between monthly observed and modeled precipitation (bottom right).

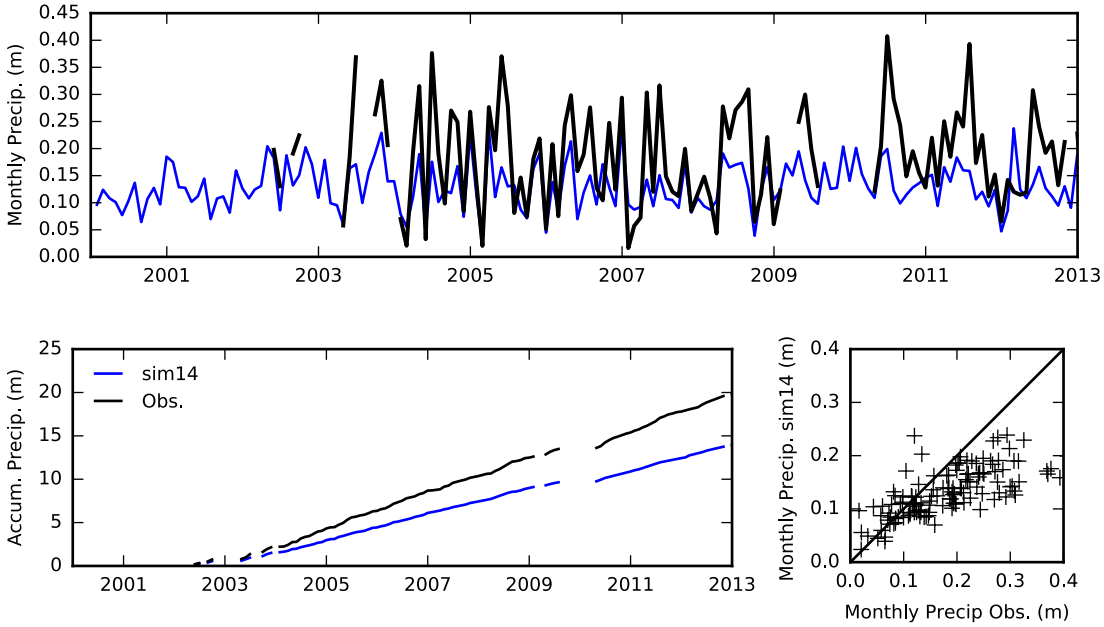


Figure A1.2: Precipitation from the selected simulation and observations at station 2 (Río Aysen). Monthly precipitation (top), monthly accumulated precipitation (bottom left) and comparison between monthly observed and modeled precipitation (bottom right).

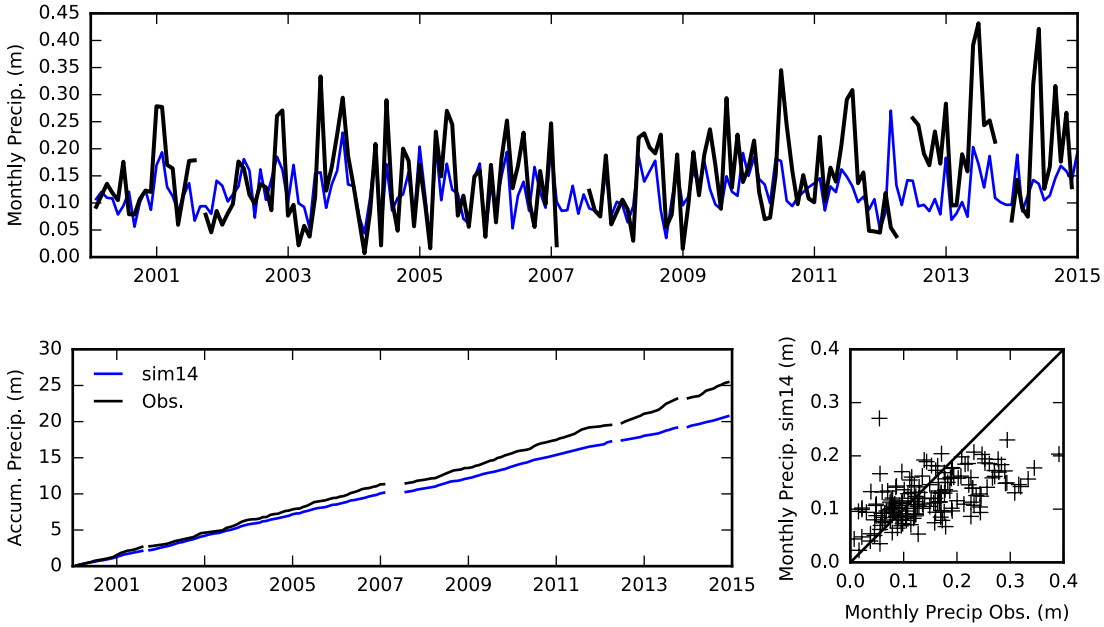


Figure A1.3: Precipitation from the selected simulation and observations at station 3 (El Balseo). Monthly precipitation (top), monthly accumulated precipitation (bottom left) and comparison between monthly observed and modeled precipitation (bottom right).

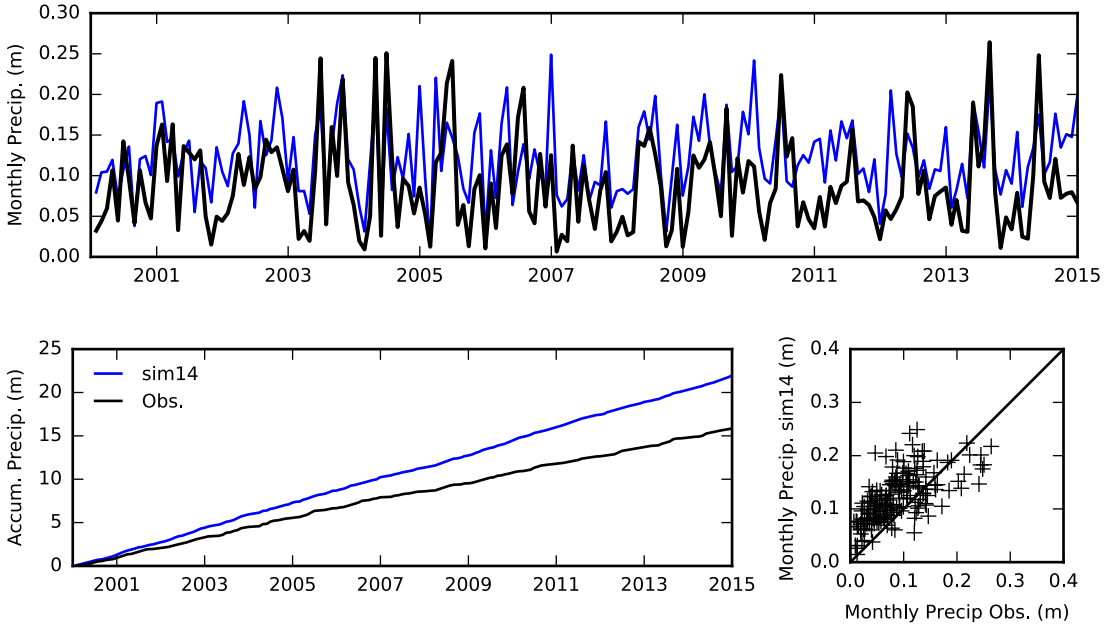


Figure A1.4: Precipitation from the selected simulation and observations at station 4 (Teniente Vidal). Monthly precipitation (top), monthly accumulated precipitation (bottom left) and comparison between monthly observed and modeled precipitation (bottom right).

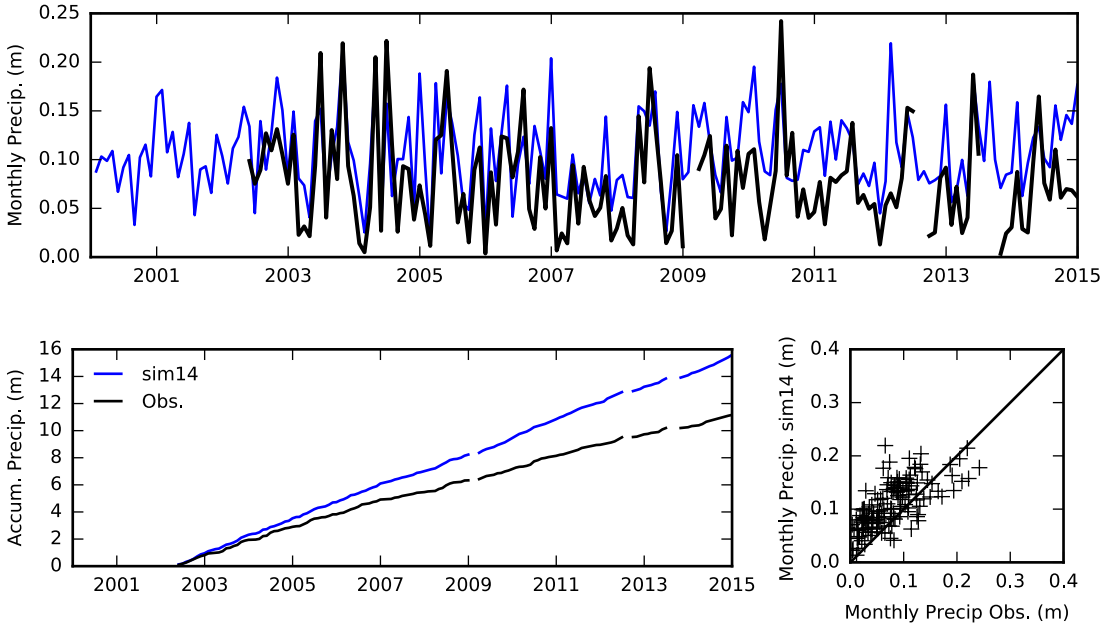


Figure A1.5: Precipitation from the selected simulation and observations at station 5 (Coyhaique Conaf). Monthly precipitation (top), monthly accumulated precipitation (bottom left) and comparison between monthly observed and modeled precipitation (bottom right).

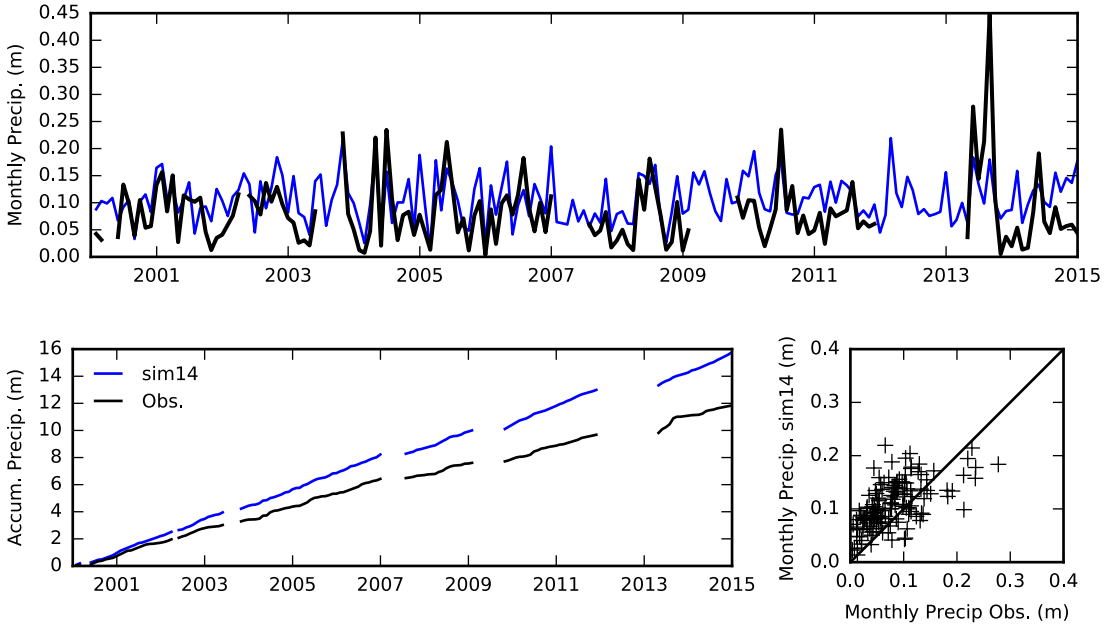


Figure A1.6: Precipitation from the selected simulation and observations at station 6 (Coyhaique Escuela Ag.). Monthly precipitation (top), monthly accumulated precipitation (bottom left) and comparison between monthly observed and modeled precipitation (bottom right).

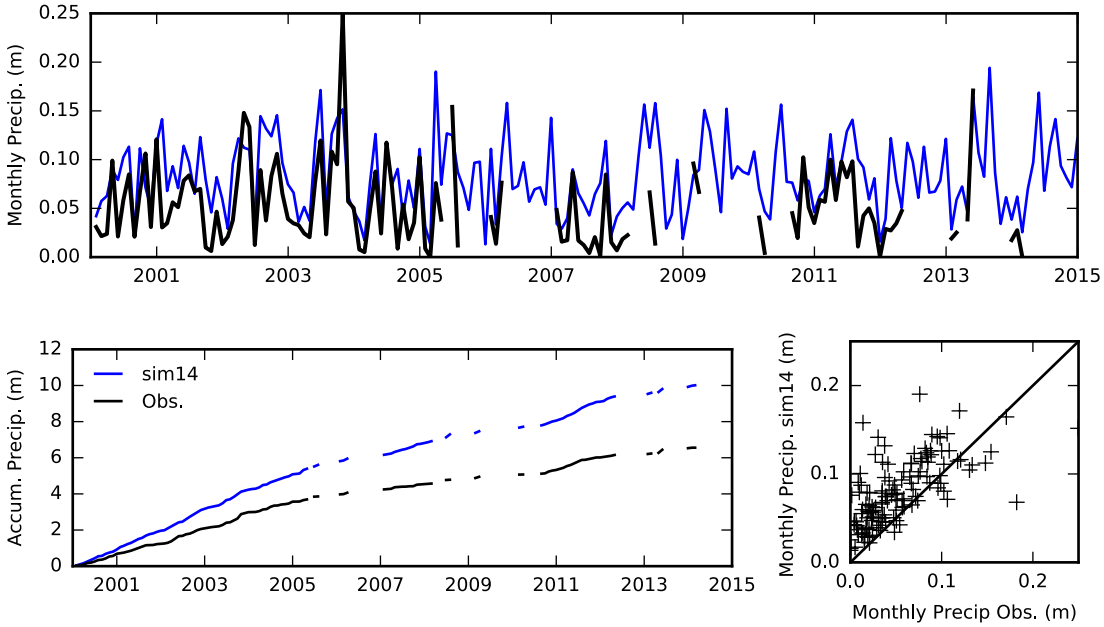


Figure A1.7: Precipitation from the selected simulation and observations at station 8 (Balmaceda Ad.). Monthly precipitation (top), monthly accumulated precipitation (bottom left) and comparison between monthly observed and modeled precipitation (bottom right).

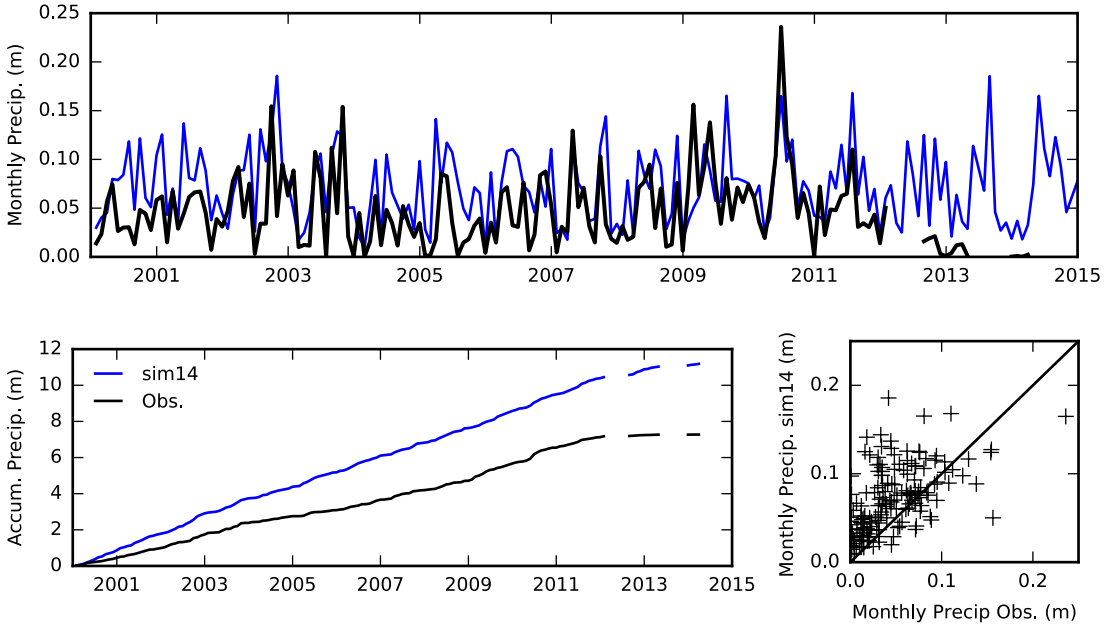


Figure A1.8: Precipitation from the selected simulation and observations at station 9 (Villa Cerro castillo). Monthly precipitation (top), monthly accumulated precipitation (bottom left) and comparison between monthly observed and modeled precipitation (bottom right).

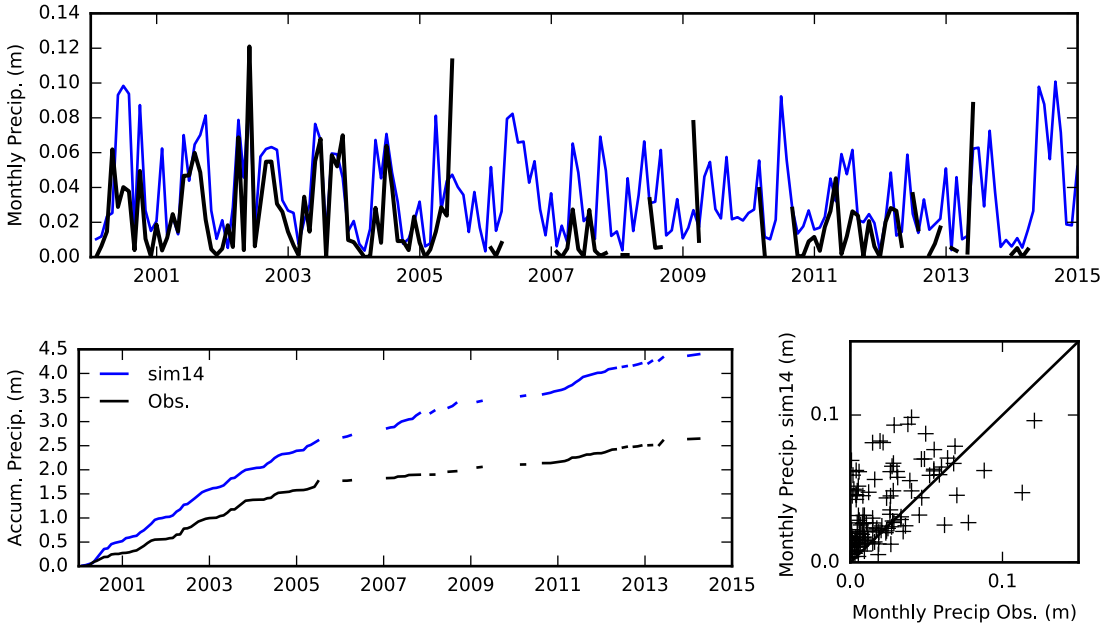


Figure A1.9: Precipitation from the selected simulation and observations at station 10 (Chile Chic Ad.). Monthly precipitation (top), monthly accumulated precipitation (bottom left) and comparison between monthly observed and modeled precipitation (bottom right).

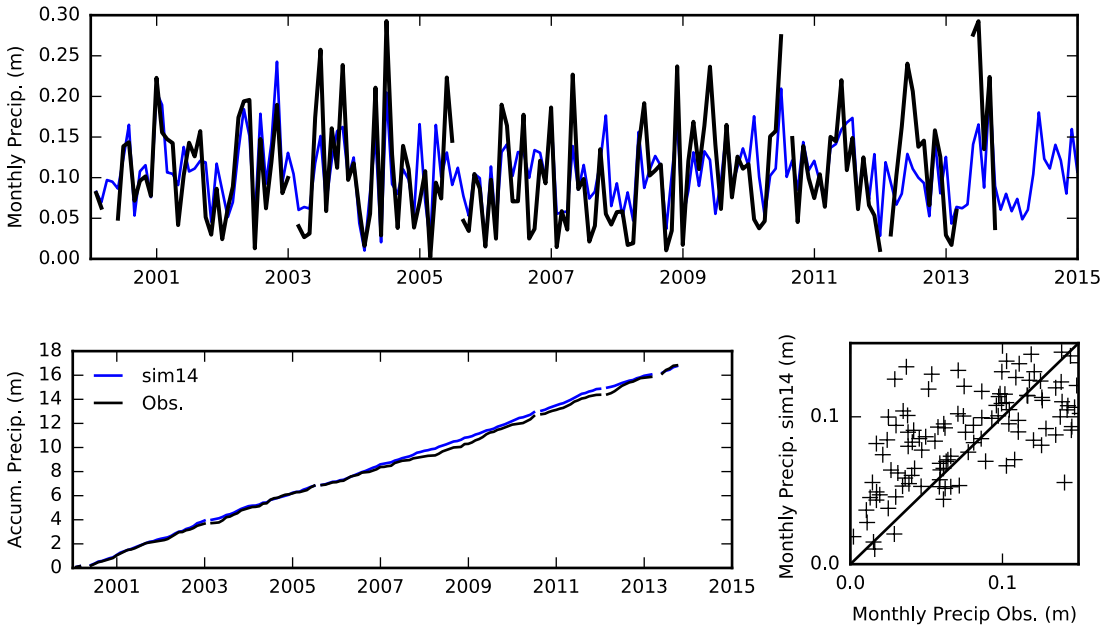


Figure A1.10: Precipitation from the selected simulation and observations at station 11 (Bahía Murta). Monthly precipitation (top), monthly accumulated precipitation (bottom left) and comparison between monthly observed and modeled precipitation (bottom right).

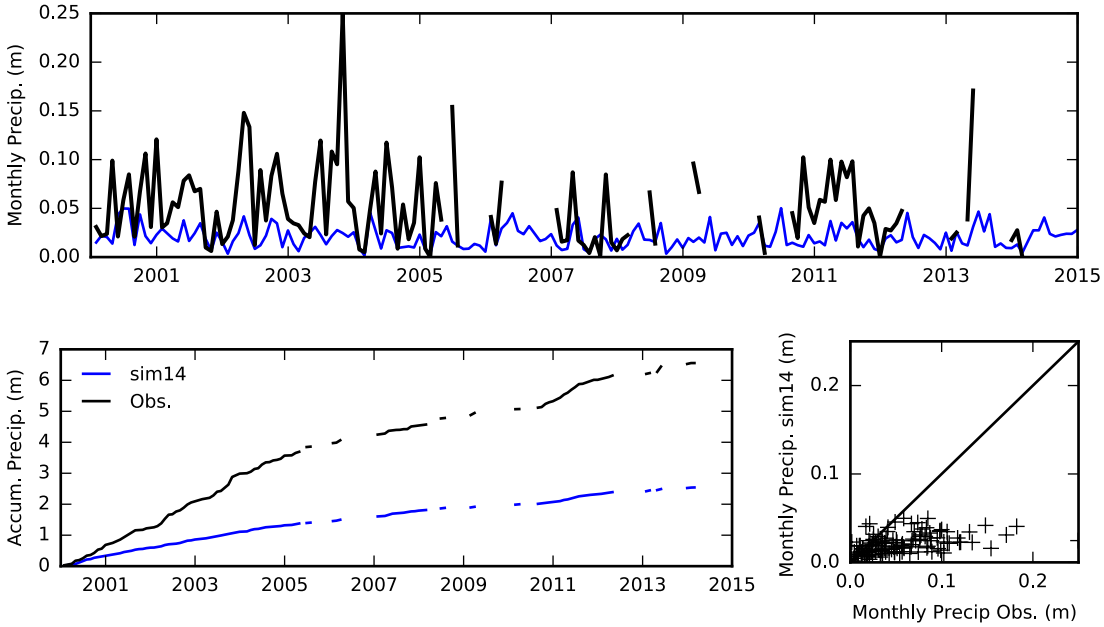


Figure A1.11: Precipitation from the selected simulation and observations at station 12 (Lord Cochrane). Monthly precipitation (top), monthly accumulated precipitation (bottom left) and comparison between monthly observed and modeled precipitation (bottom right).

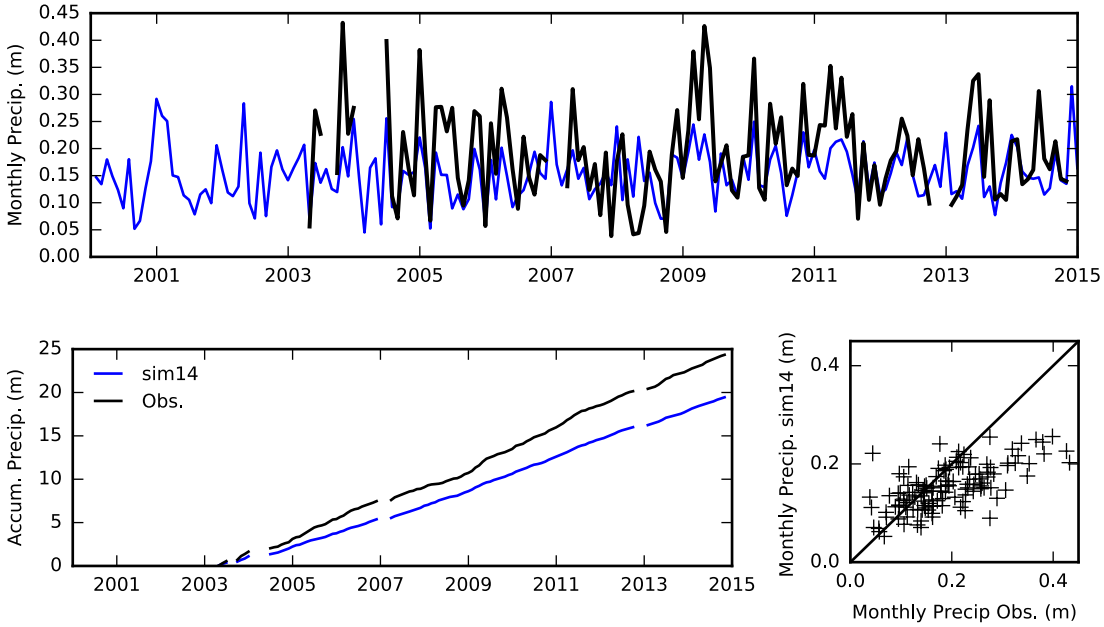


Figure A1.12: Precipitation from the selected simulation and observations at station 13 (Río Pascua). Monthly precipitation (top), monthly accumulated precipitation (bottom left) and comparison between monthly observed and modeled precipitation (bottom right).

# A2 Comparison between model and observed temperature

The table and figures given in this Appendix complete the comparison between the temperature modelled with MAR (sim14) and observed at the stations around the icefield (see Sec. 3.5.3.3 Air temperature).

Table A2.1: Simulated (sim14) and observed temperature comparison, stations with mean monthly temperature.

| N | Name | R | p | RMS (m $a^{-1}$) | Dif. (m $a^{-1}$) |
|---|---|---|---|---|---|
| s4 | Teniente Vidal C. Ad. | 0.89 | 7.6 x $10^{-131}$ | 0.73 | 0.37 |
| s8 | Balmaceda Ad. | 0.99 | 4.3 x $10^{-142}$ | 0.81 | -0.29 |

R is Pearson's correlation coefficient, p is the statistical significance of on Pearson's correlation coefficient, RMS is the root mean square error between the observed and modeled temperatures and Dif. is the average difference between the observed and modeled temperatures

Table A2.2: Simulated (sim14) and observed temperature comparison, stations with mean annual temperature.

| N | Name | R | p | RMS (m $a^{-1}$) | Dif. (m $a^{-1}$) |
|---|---|---|---|---|---|
| s4 | Teniente Vidal C. Ad. | 0.89 | 8.0 x $10^{-6}$ | 0.43 | 0.37 |
| s8 | Balmaceda Ad. | 0.87 | 5.4 x $10^{-5}$ | 0.37 | -0.29 |

R is Pearson's correlation coefficient, p is the statistical significance of on Pearson's correlation coefficient, RMS is the root mean square error between the observed and modeled temperatures and Dif. is the average difference between the observed and modeled temperatures

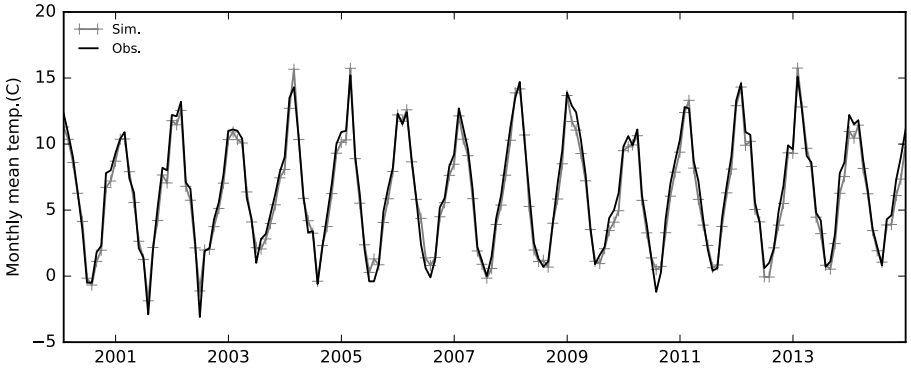


Figure A2.1: Monthly mean temperature from the selected simulation (sim14) and observations at station 4 (Teniente Vidal).

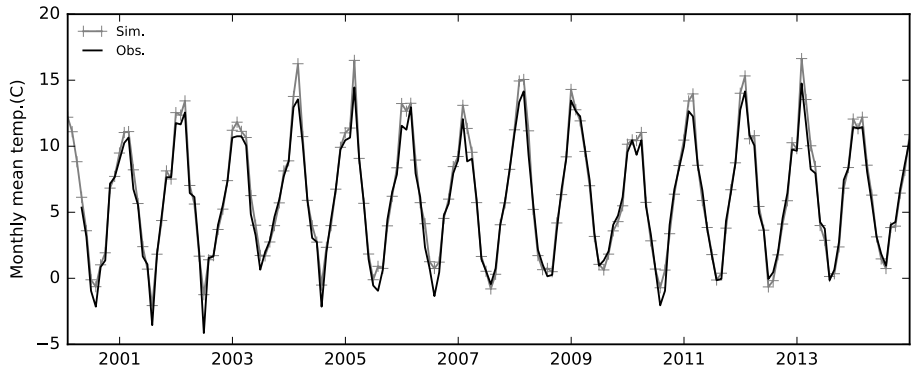


Figure A2.2: Monthly mean temperature from the selected simulation (sim14) and observations at station 8 (Balmaceda Ad.).

Table A2.3: Simulated (sim14) and measured temperature, stations with monthly maxima temperature.

| N | Name | R | p | RMS (m $a^{-1}$) | Dif. (m $a^{-1}$) |
|---|---|---|---|---|---|
| s4 | Teniente Vidal C. Ad. | 1.54 | 1.6 x $10^{-133}$ | 1.54 | 0.96 |
| s5 | Coyhaique Conaf | 2.22 | 2.8 x $10^{-97}$ | 2.22 | -1.35 |
| s6 | Coyhaique Esc. Ag. | 2.06 | 3.0 x $10^{-74}$ | 2.06 | -0.92 |
| s7 | Coyhaique Alto | 3.13 | 2.3 x $10^{-44}$ | 3.13 | -0.23 |
| s8 | Balmaceda Ad. | 1.57 | 8.1 x $10^{137}$ | 1.57 | -0.64 |
| s10 | Chile Chico Ad. | 1.11 | 1.2 x $10^{-116}$ | 1.11 | -0.07 |
| s11 | Bahía Murta | 2.74 | 2.8 x $10^{-102}$ | 2.74 | -2.24 |
| s12 | Lord Cochrane Ad. | 2.52 | 1.2 x $10^{-104}$ | 2.52 | -2.21 |

R is Pearson's correlation coefficient, p is the statistical significance of on Pearson's correlation coefficient, RMS is the root mean square error between the observed and modeled temperature and Dif. is the average difference between the observed and modeled temperature

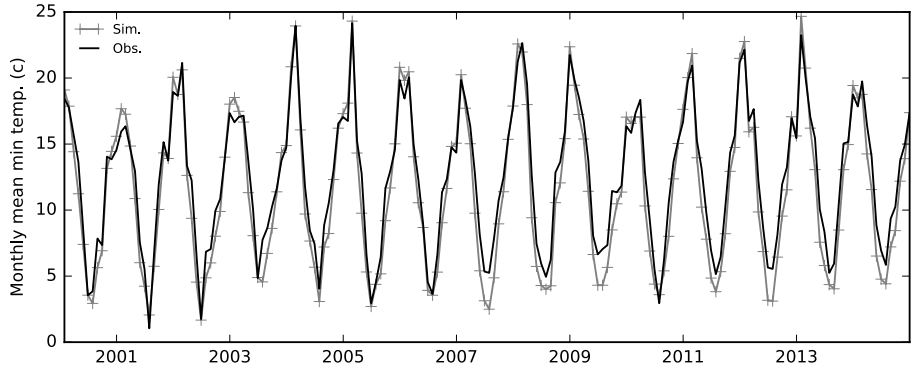


Figure A2.3: Monthly maxima temperature from the selected simulation (sim14) and observations at station 4 (Teniente Vidal C. Ad. ).

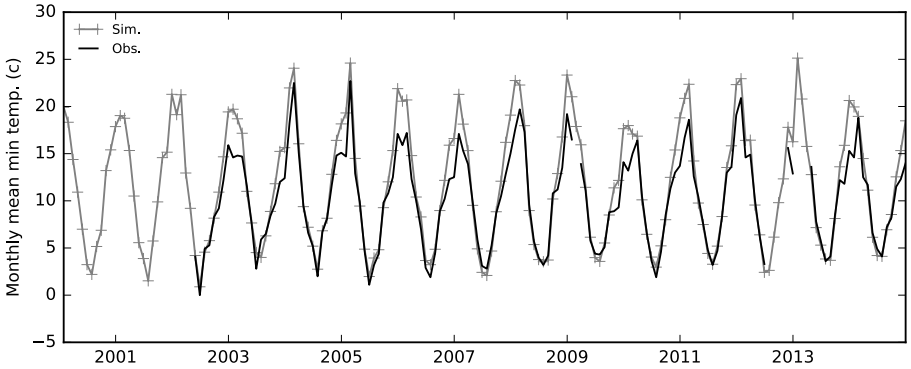


Figure A2.4: Monthly maxima temperature from the selected simulation (sim14) and observations at station 5 (Coyhaique Conaf ).

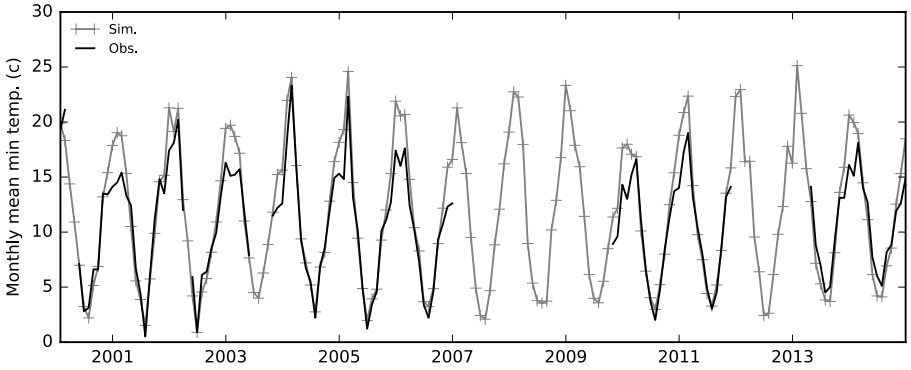


Figure A2.5: Monthly maxima temperature from the selected simulation (sim14) and observations at station 6 (Coyhaique Esc. Ag. ).

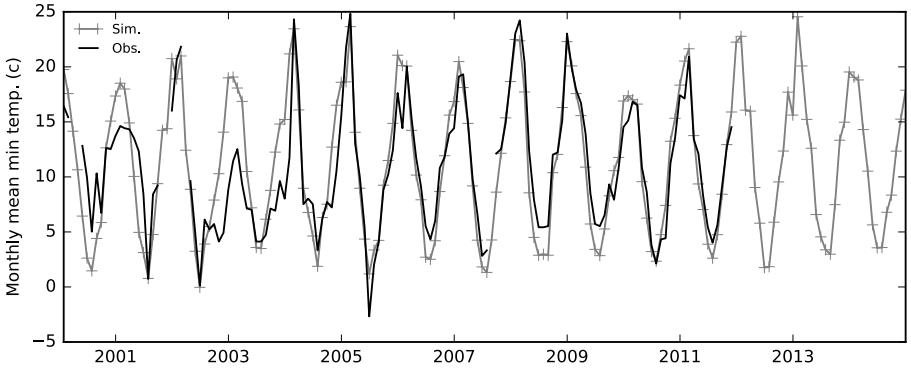


Figure A2.6: Monthly maxima temperature from the selected simulation (sim14) and observations at station 7 (Coyhaique alto).

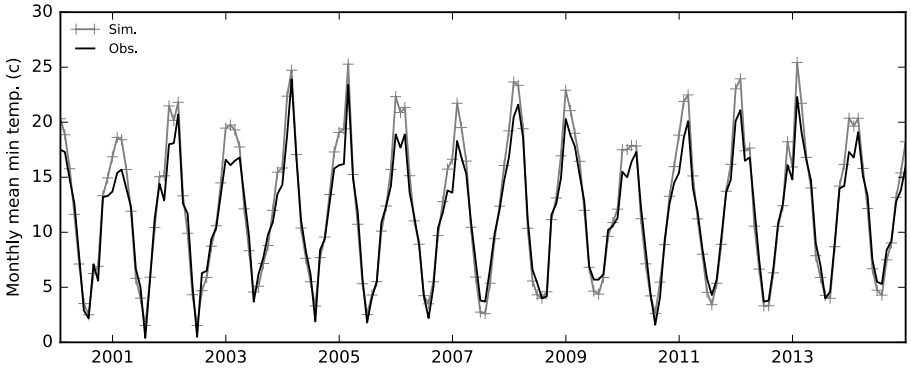


Figure A2.7: Monthly maxima temperature from the selected simulation (sim14) and observations at station 8 (Balmaceda Ad. ).

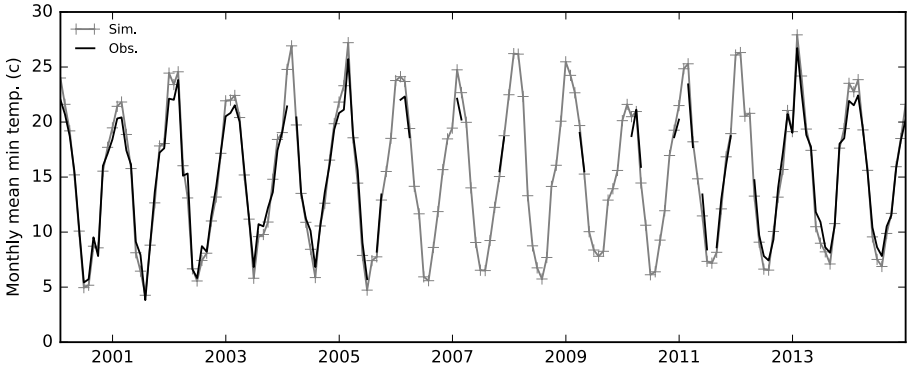


Figure A2.8: Monthly maxima temperature from the selected simulation (sim14) and observations at station 10 (Chile Chico Ad. ).

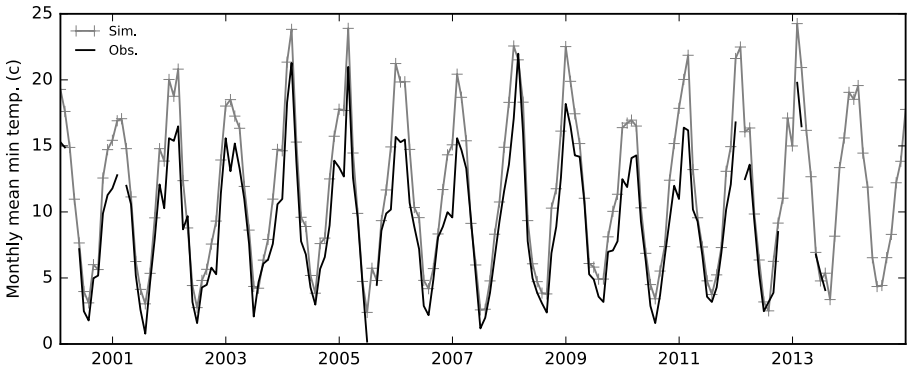


Figure A2.9: Monthly maxima temperature from the selected simulation (sim14) and observations at station 11 (Bahia Murta ).

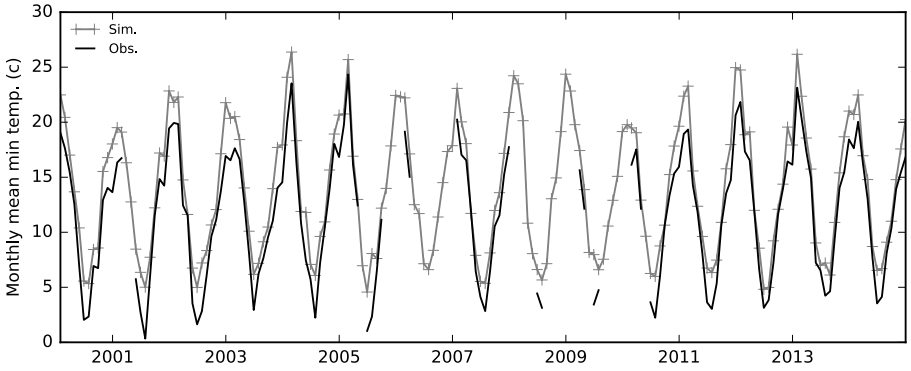


Figure A2.10: Monthly maxima temperature from the selected simulation (sim14) and observations at station 12 (Lord Cochrane Ad. ).

Table A2.4: Simulated (sim14) and measured temperature, stations with monthly minima temperature.

| N | Name | R | p | RMS (m $a^{-1}$) | Dif. (m $a^{-1}$) |
|---|---|---|---|---|---|
| s4 | Teniente Vidal C. Ad. | 0.98 | 1.3 x $10^{-122}$ | 1.20 | 0.97 |
| s5 | Coyhaique Conaf | 0.96 | 1.4 x $10^{-8}$ | 1.65 | -1.37 |
| s6 | Coyhaique Esc. Ag. | 0.95 | 3.4 x $10^{-54}$ | 1.65 | -1.22 |
| s7 | Coyhaique Alto | 0.83 | 8.4 x $10^{-36}$ | 2.53 | -0.45 |
| s8 | Balmaceda Ad. | 0.95 | 1.7 x $10^{-88}$ | 1.14 | 0.18 |
| s10 | Chile Chico Ad. | 0.97 | 3.1 x $10^{-86}$ | 1.62 | -1.35 |
| s11 | Bahía Murta | 0.93 | 9.5 x $10^{-67}$ | 1.25 | -0.43 |
| s12 | Lord Cochrane Ad. | 0.95 | 5.7 x $10^{-78}$ | 1.55 | 0.95 |

R is Pearson's correlation coefficient, p is the statistical significance of on Pearson's correlation coefficient, RMS is the root mean square error between the observed and modeled temperature and Dif. is the average difference between the observed and modeled temperature

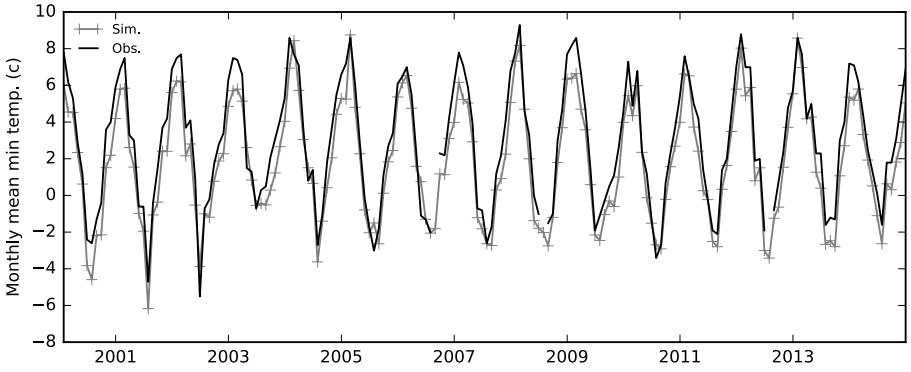


Figure A2.11: Monthly minima temperature from the selected simulation (sim14) and observations at station 4 (Teniente Vidal C. Ad.).

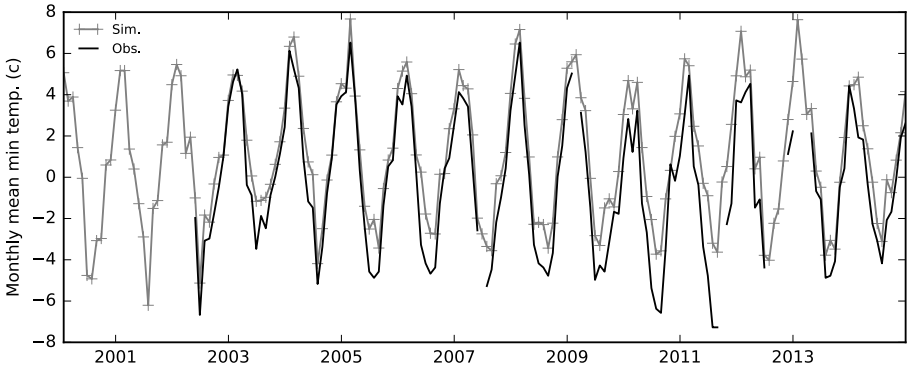


Figure A2.12: Monthly minima temperature from the selected simulation (sim14) and observations at station 5 (Coyhaique Conaf).

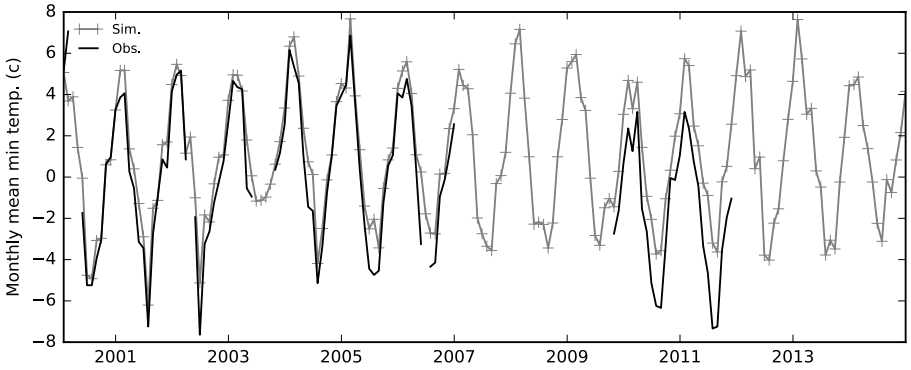


Figure A2.13: Monthly minima temperature from the selected simulation (sim14) and observations at station 6 (Coyhaique Esc. Ag.).

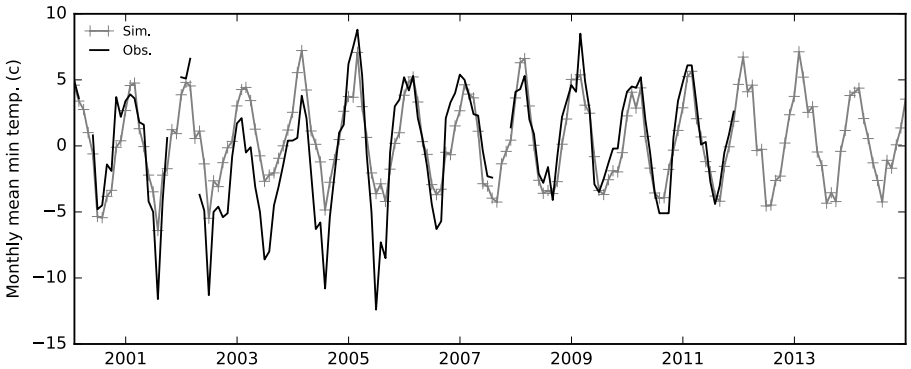


Figure A2.14: Monthly minima temperature from the selected simulation (sim14) and observations at station 7 (Coyhaique alto).

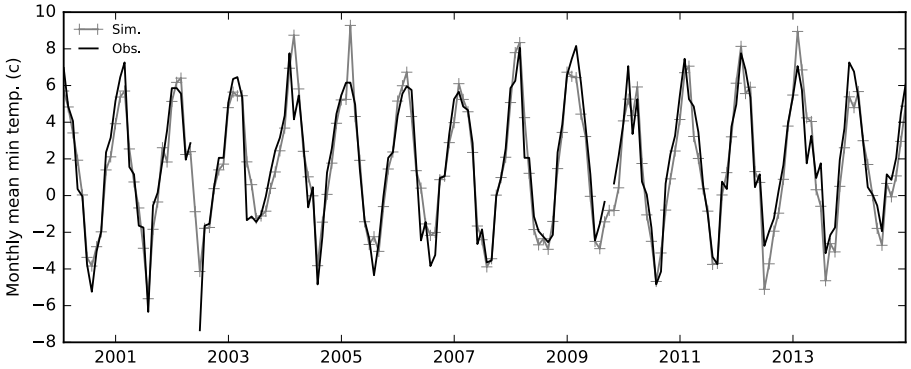


Figure A2.15: Monthly minima temperature from the selected simulation (sim14) and observations at station 8 (Balmaceda Ad.).

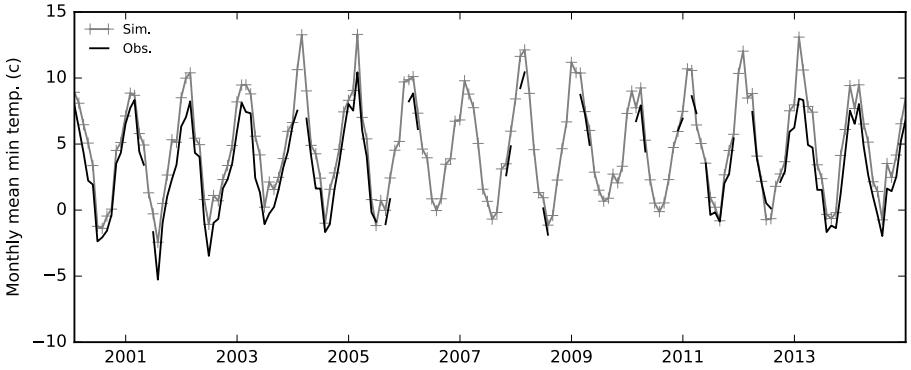


Figure A2.16: Monthly minima temperature from the selected simulation (sim14) and observations at station 10 (Chile Chico Ad.).

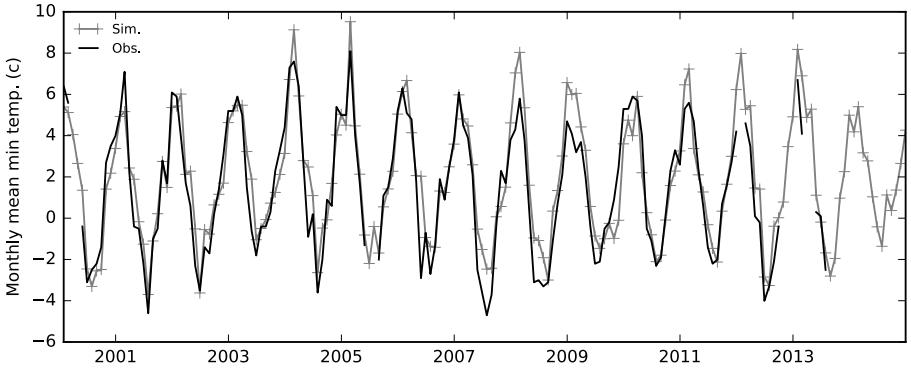


Figure A2.17: Monthly minima temperature from the selected simulation (sim14) and observations at station 11 (Bahia Murta).

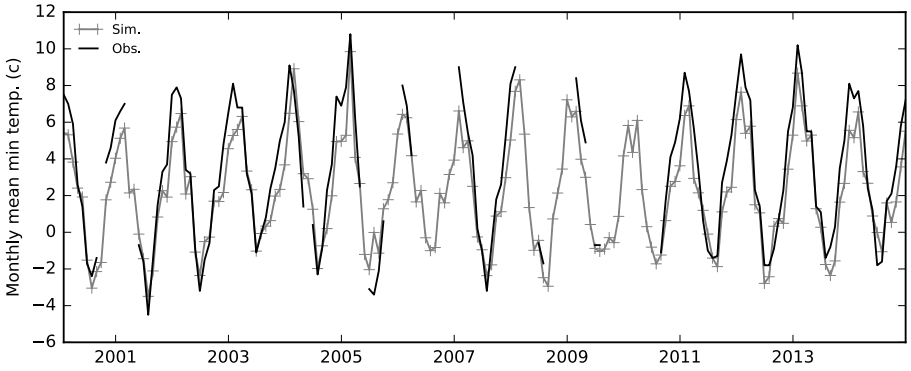


Figure A2.18: Monthly minima temperature from the selected simulation (sim14) and observations at station 12 (Lord Cochrane Ad.).

**Résumé**

Le champ de glace nord de Patagonie (NPI) a connu des pertes de glace accélérées depuis le Petit Âge de Glace (PAG). Cette thèse évalue les conditions climatiques moyennes régnant en Patagonie, ainsi que les bilans de masse de surface et les flux de glace engendrés par la dynamique de la glace du NPI. En raison du manque de données disponibles, l'approche est principalement basée sur des modélisations physiques à la fois des conditions atmosphériques et de la dynamique de l'écoulement des glaciers.

Dans un premier temps, la dynamique du glacier San Rafael (SRG) est modélisée à l'aide du modèle full-Stokes Elmer/Ice. Le modèle d'écoulement est initialisé et contraint à l'aide des données de vitesse de surface et d'altitude du lit rocheux. Le modèle est forcé en considérant diverses paramétrisations et scénarios d'évolution du bilan de masse de surface (BMS) avec l'altitude. Les modélisations visent à retrouver un accord entre bilan de masse total, BMS et dynamique de la glace. Les simulations montrent que les études précédentes ont systématiquement surévalué l'accumulation sur le plateau et à haute altitude. Le déséquilibre du glacier est principalement contrôlé par un flux de glace élevé (-0.83 $\pm$ 0.08 Gt $a^{-1}$) en comparaison du BMS légèrement positif (0.08 $\pm$ 0.06 Gt $a^{-1}$). Nos modélisations permettent d'évaluer que les pertes de glace irréversibles pour le glacier (ou committed mass balance) seront en moyenne de 0.34 $\pm$ 0.03 Gt $a^{-1}$ pour le prochain siècle. Cette valeur est la perte minimale attendue pour ce glacier en réponse au changement climatique futur.

Dans un second temps, nous modélisons le BMS de SRG et de NPI à l'aide d'un modèle de circulation atmosphérique régionale, le modèle MAR. Le modèle est forcé par les reanalyses climatiques ERA-Interim et adapté de façon à reproduire l'accumulation mesurée sur le plateau. Une attention particulière est aussi portée aux valeurs d'ablation et d'albédo. Les températures et précipitations sont validées à l'aide de données provenant des vallées alentour. Entre 1980 et 2014, les valeurs de BMS intégrées à l'échelle du SRG et de NPI était de 0.86 Gt $a^{-1}$ et -1.84 Gt $a^{-1}$, respectivement, associées à une forte variabilité interannuelle (de 1.4 Gt $a^{-1}$ et 6.1Gt $a^{-1}$, respectivement). Cette variabilité dépend directement de celle des températures et des précipitations neigeuses en Patagonie. En raison de l'hypsometrie du SRG, de faibles variations de BMS autour de la ligne d'équilibre ont un impact très fort sur la valeur intégrée de BMS à l'échelle du glacier. Néanmoins, l'obtention de données in-situ d'accumulation est encore nécessaire pour réduire l'incertitude des valeurs de BMS. Ici, les BMS intégrés à l'échelle des trois plus gros glaciers à terminaison terrestre de NPI ont été validés à partir de bilans géodésiques. Ainsi, combinée aux pertes par vêlage, la valeur négative de BMS proposée pour NPI aurait permis la perte de masse du champ de glace depuis les années 80.

Enfin, l'étude du bilan d'énergie de surface révèle que les variations d'albédo contrôlent celles du BMS, car il contrôle le rayonnement de courtes longueurs d'ondes et la fonte du glacier. Les variations d'albédo expliquent indirectement le lien existant entre température et fonte celui-ci étant conditionné par la phase des précipitations sur le plateau. Ainsi, les changements des précipitations neigeuses expliquent les variations de BMS, et nous supposons que les conditions climatiques ayant régné au PAG étaient plus humides et ont permis au glacier de se développer jusqu'à des altitudes trop faibles pour que les glaciers soient stables aujourd'hui.

Cette thèse a ainsi permis d'évaluer les conditions atmosphériques régionales et de mieux contraindre la dynamique des glaciers et les valeurs de BMS du champ de glace NPI. Néanmoins, de nouvelles estimations sont à effectuer en zone d'accumulations de NPI pour contraindre encore le BMS et conclure définitivement sur les causes du recul de NPI depuis le PAG.

**Abstract**

The Northern Patagonia Icefield (NPI) have been losing mass at an accelerated rate during the last decades compared to the mean losses recorded since the Little Ice Age. Here we look for accurate estimates of the mean climate variables, surface mass balance (SMB) and ice dynamics of NPI. Due to the lack of available data in the area, the approach is based on physical models for both the atmosphere and the ice dynamics, in order to properly attribute the components of the glacial mass budget (mass balance, surface mass balance and ice discharge).

First, the San Rafael Glacier (SRG) ice dynamics are modelled using the full-Stokes model Elmer/Ice. The flow model is initialised and constrained using the most up-to-date observations of surface velocities and bedrock elevation. The model is forced with several parametrisations of the altitudinal SMB distribution to obtain consistency between the changes in SMB and ice dynamics. We show that previous studies have proposed excessive accumulation values on the icefield plateau, and that SRG imbalance is largely controlled by a large ice discharge (-0.83 $\pm$ 0.08 Gt $a^{-1}$) compared to a slightly positive glacier-wide SMB (0.08 $\pm$ 0.06 Gt $a^{-1}$). This allows for an estimation of a committed mass loss of 0.34 $\pm$ 0.03 Gt $a^{-1}$ for the next century. This value likely constitutes a minimum wastage in the future global climate change situation.

Second, we model the SMB of the SRG and the NPI using the regional circulation model MAR (Modèle Atmosphérique Regional). This model is forced by the ERA-Interim reanalysis outputs and adapted to accurately reproduce accumulation on the icefield. In addition to accumulation, attention is paid to estimating accurate ablation and albedo values on the plateau. The modelled temperature and precipitation are also validated using data from weather stations in the valleys around the icefield. For the period 1980-2014, the modelled mean SMB of the SRG and the NPI are 0.86 Gt $a^{-1}$ and -1.84 Gt $a^{-1}$, respectively, with a large inter-annual variability of 1.4 Gt $a^{-1}$ and 6.1 Gt $a^{-1}$, which is induced by temperature and snowfall variability. Due to the hypsometry of the SRG, small changes in the punctual SMB around the ELA have impacts over large areas and have significant consequences on the final glacier-wide SMB. However, in-situ data above the ELA are lacking, leading to important uncertainty in accumulation. Nevertheless, our SMB estimates for the 3 largest non-calving glaciers of the icefield are similar to mass balance values given by geodetic techniques. This validation shows that our estimate of SMB, which is the first negative proposed at the scale of NPI, is accurate. Combined with the ice discharge proposed in the first section of this study, this SMB could have contributed to the observed mass loss from the 1980s.

Finally, the study of the surface energy balance given by MAR reveals the key role of the albedo and the shortwave radiation budget in the variations of the SMB. Albedo variations indirectly justify the existing correlations between temperature and melting as air temperature controls the phase of precipitation on the plateau. Thus, changes in solid precipitation explain most of the SMB variations. Consequently, past conditions with higher solid precipitation may have explained larger glaciers in Patagonia. The current instability is possibly a result from the location of glacier fronts which are well below the necessary altitude for equilibrium in the current icefield topography.

This study allows us to conclude that well constrained atmospheric and ice dynamic modelling leads to SMB values which are in better agreement with the mass balance of the icefield. Nevertheless, new field data is necessary to better constrain SMB estimates of the SRG and the NPI in order to improve our understanding of past and future climate change impacts on these glaciers.